12-2011

Synthesis and Computational Studies on Hiv-1 Integrase Inhibitors

Horrick Sharma
University of Tennessee Health Science Center

Synthesis and Computational Studies on Hiv-1 Integrase Inhibitors

DOI
10.21007/etd.cghs.2011.0285

SYNTHESIS AND COMPUTATIONAL STUDIES ON HIV-1 INTEGRASE INHIBITORS

A Dissertation
Presented for
The Graduate Studies Council
The University of Tennessee
Health Science Center

In Partial Fulfillment
Of the Requirements for the Degree
Doctor of Philosophy
From The University of Tennessee

By
Horrick Sharma
December 2011

DEDICATION

I dedicate this dissertation to my loving parents:
Mr. Subhash C. Sharma
Dr. Saroj Sharma
and to my beloved wife:
Pragya Sharma

ACKNOWLEDGEMENTS

I would firstly like to thank my research advisor, Dr. John K. Buolamwini for providing me the opportunity to pursue my graduate studies and for all his help, and guidance throughout my research. I would like to thank him for helping to develop my independent thinking and also for his support, without which, any part of this dissertation would not have been possible. I am also highly indebted to my committee members, Dr. Isaac O. Donkor, Dr. Richard E. Lee, Dr. Duane D. Miller, and Dr. Abby L. Parrill for their time and valuable suggestions throughout my studies.

I would like to thank Dr. Nouri Neamati and his research group at the University of Southern California for all biological *in vitro* studies that they have performed on my synthesized compounds. I also express my gratitude to Dr. Raymond F. Schinazi and his research group at Emory University School of Medicine for carrying out the *in vitro* anti-HIV assays. I am also highly thankful to Dr. Xiaolin Cheng of the Oak Ridge National Laboratory for developing the homology model of a full length HIV-1 IN-DNA complex, which I have used in my computational studies on HIV-1 IN inhibitors. I am thankful to Dr. Ryan Yates at the UTHSC for allowing me to perform the HPLC purity studies in his laboratory.

I must thank Dr. Shivaputra Patil who has initially worked on this project and synthesized few compounds of the chalcone series. I would also like to thank the past and present members of our laboratory: Dr. Chunmei Wang, Shan Sun and Hilaire Playa for all the support and help they have provided throughout my graduate studies.

Finally, I must express my sincere gratitude to my family and friends who have always stood beside me in all my times of joy and despair and, for their constant encouragement and support.

ABSTRACT

HIV-1 integrase (IN) is essential for viral replication and offers a promising target for the development of anti-retroviral drugs. Two decades of extensive research has lead to the recent approval of raltegravir as the first IN inhibitor. Advancement of drug candidate elvitegravir, which is currently in Phase III clinical trial, has furthermore accelerated efforts against this potential target for combating HIV. However, the emergence of resistance against raltegravir and elvitegravir demands exploration of novel chemical scaffolds that could circumvent resistance against currently used HIV-1 IN inhibitors. With the goal of discovering new agents targeting HIV, a novel structural class of HIV-IN inhibitors have been designed and synthesized. Substantial computational studies were also performed that could aid the design and development of potent HIV IN inhibitors.

A part of this dissertation research, covered in Chapter 3, details the design, synthesis, and biological evaluation of 3-keto salicylic acid chalcones as novel HIV-1 IN inhibitors. In the chalcone series, the most active compound, 5-bromo-2-hydroxy-3-[3-(2,3,6-trichloro-phenyl)-acryloyl]-2-hydroxybenzoic acid (**96**) was selectively active against IN strand transfer (ST) with IC_{50} of 3.7 μM. While most of the compounds exhibit ST selectivity, a few were nonselective, such as 5-bromo-3-[3-(4-bromo-phenyl)-acryloyl]-2-hydroxybenzoic acid (**86**), which was active against both 3′-processing (3′-P) and ST with IC_{50} values of 11 ± 4 and 5 ± 2 μM, respectively. The compounds also inhibited HIV-1 replication with potencies comparable to their integrase inhibitory activities. Thus, compounds **96** and **86** inhibited HIV-1 replication with EC_{50} values of 7.3 and 8.7 μM, respectively. Chapter 4 describes the synthesis of structurally related amide derivatives which were designed by modification of the chalcone moiety. In the amide series, the most active compound, 5-bromo-3-[(3-chloro-2,4-difluoro benzyl)-carbamoyl]-2-hydroxy- benzoic acid (**151**), inhibited ST with an IC_{50} of 4 μM. Chapter 5 discloses the synthesis, and biological studies of halogenated phenanthrene β-diketo acids as novel HIV-1 IN inhibitors. The two most active compounds of the series, 4-(8-chlorophenanthren-3-yl)-2,4-dioxobutanoic acid (**179**) and 4-(6-chlorophenanthren-2-yl)-2,4-dioxobutanoic acid (**177**) had ST IC_{50} values of 1.2 and 1.3 μM, respectively, and corresponding 3′-P values of 11.0 and 5.0 μM.

In the last section of the dissertation detailed in Chapter 6, computational studies were conducted with the aim of exploring the possible binding modes of potent IN inhibitors and evaluating the structural requirements for IN inhibition. To determine the physicochemical parameters important for ligand binding, in the first part of this chapter, a PHASE pharmacophore hypothesis was developed and used for molecular alignments in the initial comparative molecular field analysis (CoMFA) and comparative molecular similarity analysis (CoMSIA) 3D-quantitative structure activity relationship (3D-QSAR) modeling of the chalcone derivatives. A recent breakthrough in the field of anti-HIV research was achieved with the crystallization and 3D structure determination of a complete foamy virus IN-DNA complex. To take advantage of the power of structure-based drug design, in the second part of the computational studies, homology models of

HIV-1 IN-DNA were constructed based on the foamy virus IN-DNA complex X-ray crystal structure as template through collaboration with the Oak Ridge National Laboratory. The binding modes of raltegravir and elvitegravir in our homology models were in accordance with their binding modes in their complexes with the foamy virus structure. The homology model was then used for docking and 3D-QSAR studies on our synthesized inhibitors and other integrase inhibitors including the clinically available raltegravir and elvitegravir. Free energy calculations using Molecular Mechanics-Generalized Born Surface Area (MM-GBSA) methods were carried out to rescore and validate the binding modes of HIV-1 integrase inhibitors. 3D-QSAR models derived from this study provided detailed insights into the structural requirements for IN inhibition and established predictive tools to guide further inhibitor design. Linear interaction energy (LIE) calculations were also performed to derive energy parameters contributing to the binding free energies of the IN inhibitors in the data set. These energy parameters were also analyzed to gain insight into the binding modes of raltegravir and elvitegravir as well as to validate the conformations of our synthesized chalcone and amide derivatives. The energy terms were then used as descriptors to develop a linear interaction approximation (LIA) activity model for the inhibition of integration catalytic step. In the next section of the chapter, lead optimization was attempted using structure- and ligand-based drug design tools. RACHEL, a drug optimization software, was used to design an inhibitor with desired binding interactions with the IN active site residues. The hit obtained from RACHEL was used to design a structurally related compound (**157**), the synthesis and activity testing of which has been described in Chapter 4. Docking studies were also performed on the phenanthrene derivatives synthesized in Chapter 5. The docking studies predominantly revealed two binding poses that were distinct from the possible binding modes of clinically used raltegravir and advanced IN inhibitor elvitegravir and, moreover, do not interact significantly with some of the key amino acids (Q148 and N155) implicated in viral resistance. Therefore, this series of compounds can further be investigated as IN inhibitors to circumvent resistance associated with current clinically used HIV-1 IN inhibitors.

TABLE OF CONTENTS

LIST OF TABLES

LIST OF FIGURES

LIST OF SCHEMES

LIST OF ABBREVIATIONS

AIDS	Acquired immunodeficiency syndrome
AZT	Azidothymidine
BBr_3	Boron tribromide
CCD	Central core domain
CoMFA	Comparative molecular field analysis
CoMSIA	Comparative molecular similarity analysis
CTD	Carboxy-terminal domain
DCM	Dichloromethane
DKA	Diketo acid
DMF	Dimethyl formamide
DMSO	Dimethyl sulfoxide
EDCI	Ethyl-3-(3-dimethylaminopropyl)carbodiimide
FDA	Food and drug administration
FIs	Fusion inhibitors
HAART	Highly active anti retroviral therapy
HIV-1	Human immunodeficiency virus-1
HOBT	Hydroxybenzotriazole
IN	Integrase
LEDGF	Lens epithelium-derived growth factor
LIA	Linear interaction energy approximations
LIE	Linear interaction energy
LTR	Long terminal repeat
MM-GBSA	Molecular mechanics/generalized born surface area
NTD	N-terminal domain
PFV	Prototype foamy virus
PIC	Pre-integration complex
rt	Room temperature
ST	Strand transfer
STC	Strand transfer complex
THF	Tetrahydrofuran
vdW	van der Waals
3D-QSAR	Three-dimensional quantitative structure activity relationship
3′-P	3′-processing

CHAPTER 1. INTRODUCTION

HIV/AIDS

Acquired Immunodeficiency syndrome (AIDS) is one of the most devastating infections in human history.[1] Since the first report of this syndrome in 1981, about 30 million people have died from the AIDS-related diseases.[2] The Human Immunodeficiency virus (HIV) was first identified as the causative agent of AIDS in 1983.[3-8] The number of people infected with HIV has increased from 8 million in 1990 to 33 million today, with an addition of 2.6 million new HIV infections each year; making it a major pandemic of the 21st century.[9,10]

There is still neither a cure nor a vaccine available for AIDS and it remains a serious challenge to the scientific and healthcare community.[11] Two decades of tremendous effort has however led to major breakthroughs in combating this dreadful menace.[12-15] Before the discovery of its causative agent most patients died within 2 years of infection. Today, the average longevity has exceeded 22 years due to the current antiretroviral therapy and early diagnosis of patients with AIDS.[16,17] Since the identification of zidovudine (AZT) as the first drug against HIV, remarkable success has been achieved.[18-20] This is reflected by the fact that the number of clinically approved drugs against HIV exceeds the number of drugs for all other viral infection, taken together.[21] Despite this unprecedented achievement, the issues of drug toxicity,[22-27] compliance,[28-30] and more importantly the emergence of drug resistance due to viral mutations have rendered the current therapy ineffective.[31-36] It is thus highly imperative to stay ahead of the virus and develop drugs with novel scaffolds and different mechanisms of action for achieving an effective and sustained success against AIDS/HIV.

The HIV-1 Life Cycle

HIV-1 belongs to the genus lentivirus and is a member of retroviridae, a family of RNA viruses that use an intermediate DNA for replication.[37] The life cycle of HIV (shown in **Figure 1-1**) begins with the attachment of the virus to the host cell membrane.[38] This process involves specific interactions of the viral envelope glycoprotein gp120 with CD4 receptors on the host cell surface. This interaction results in conformational changes that expose the chemokine co-receptors CXCR4 or CCR5 to the viral gp120. The gp120 protein binds to the co-receptors and further leads to conformational changes that expose viral fusion protein gp41 which then fuses with the host cell surface. After fusion and entry of the viral particle into the host cell, the virion is decapsidated to release the viral RNA genetic material and core proteins in a nucleoprotein complex. Viral enzyme reverse transcriptase (RT) then transcribes viral single-stranded RNA to viral double-stranded DNA. Viral integrase (IN) thereafter catalyzes the integration of the viral DNA into the host genome. The process of integration occurs via two catalytic steps viz., the 3′-processing (3′-P) and the strand transfer (ST) which involves integration of the viral DNA into the host genome. The

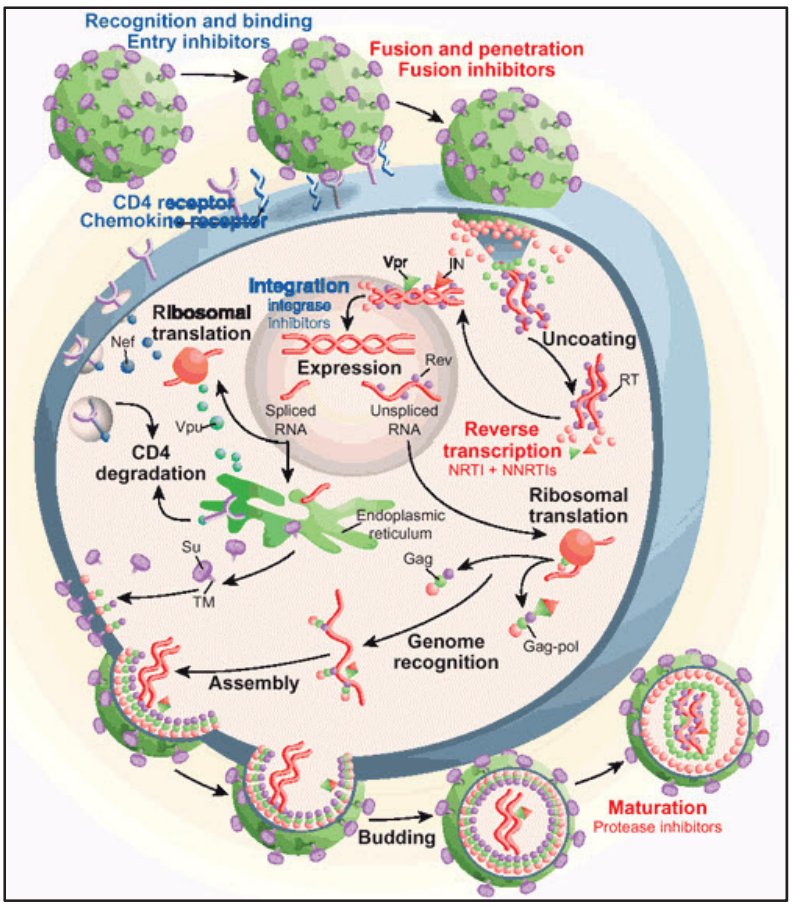

Figure 1-1. Life cycle of HIV-1

(Reproduced with permission from Nature Publishing Group: Pomerantz, R. J.; Horn, D. L. Twenty years of therapy for HIV-1 infection. *Nat. Med.* **2003,** 9, 867-873.)[17]

integrated viral DNA uses the host's cellular machinery to transcribe viral RNA, which then undergoes translation to give viral proteins.[39] The viral genetic material and the gag and gag-pol polyproteins are assembled together in the cytoplasm and the viral particle is budded off from the cell. Finally, during assembly, the viral protease (PR) cleaves the gag-pol polyprotein to generate a mature and functional virion capable of infecting another host cell.

Current Therapy

There are currently 25 drugs approved for anti-HIV therapy. These drugs (shown in **Table 1-1**) belong to seven different classes which include:

1) Nucleoside Reverse Transcriptase Inhibitors (NRTIs)

2) Nucleotide Reverse Transcriptase Inhibitors (NtRTIs)

3) Non-Nucleoside Reverse Transcriptase Inhibitors (NNRTIs)

4) Protease Inhibitors (PIs)

5) Co-receptor Inhibitors (CRIs)

6) Fusion Inhibitors (FIs)

7) Integrase Inhibitors (INs)

Nucleoside Reverse Transcriptase Inhibitors (NRTIs)

Zidovudine (AZT, **1**), a nucleoside analog, was the first anti-HIV drug approved by the FDA.[40] There are currently 7 NRTIs clinically available and 4 more are in advanced Phase II/III clinical trials (**Table 1-2**). NRTIs, shown in **Figure 1-2**, exert their anti-HIV effect by inhibiting the viral enzyme RT. These drugs are deoxyribonucleoside mimic without the 3′-OH group. They require *in vivo* phosphorylation to be transformed to their active triphosphate form, which then acts as an alternate substrate and gets incorporated into the growing DNA, resulting in chain termination.[41]

Nucleotide Reverse Transcriptase Inhibitors (NtRTIs)

Tenofovir (**8**) is currently the only NtRTI (**Figure 1-3**) approved for the treatment of HIV.[42] It also inhibits the enzyme RT. However, it has a phosphonate group incorporated into its structure and hence requires only two phosphorylations to be converted to its active triphosphate form.

Table 1-1. FDA-approved anti-HIV drugs

Class	Generic name	Brand name	Approval year
NRTIs	Zidovudine	Retrovir	1987
	Didanosine	Videx	1991
	Zalcitabine	Hivid	1992
	Stavudine	Zerit	1994
	Lamivudine	Epivir	1995
	Abacavir	Ziagen	1998
	Emtricitabine	Emtriva	2003
NtRTI	Tenofovir disoproxil	Viread	2001
NNRTIs	Nevirapine	Viramune	1996
	Delavirdine	Rescriptor	1997
	Efavirenz	Sustiva	1998
	Etravirine	Intelence	2008
PIs	Saquinavir mesylate	Invirase	1995
	Indinavir	Crixivan	1996
	Ritonavir	Norvir	1996
	Saquinavir	Fortovase	1997
	Nelfinavir	Viracept	1997
	Amprenavir	Agenerase	1999
	Lopinavir+Ritonavir	Kaletra	2000
	Fosamprenavir	Lexiva	2003
	Atazanavir	Reyataz	2003
	Tipranavir	Aptivus	2005
	Darunavir	Prezista	2006
Fusion inhibitors	Enfuvirtide	Fuzeon	2003
Entry inhibitors	Maraviroc	Selzentry	2007
INIs	Raltegravir	Isentress	2007

(Adapted with permission from Nature Publishing Group: Pommier, Y.; Johnson, A. A.; Marchand, C. Integrase inhibitors to treat HIV/AIDS. *Nat. Rev. Drug Discov.* **2005,** 4, 236-248.)[96]

Table 1-2. Clinically advanced anti-HIV agents

Class	Drug	Clinical trials (Phases)
NRTIs	Apricitabine	III
NRTIs	Amdoxovir	II
NRTIs	Elvucitabine	II
NRTIs	Racivir	II
NNRTIs	BILR 355 BS	II
NNRTIs	(+)-Calanolide A	II
NNRTIs	IDX899	I/II
NNRTIs	MIV-150	II
NNRTIs	RDEA806	II
NNRTIs	Rilpivirine	II
CRIs	AK-602	III
CRIs	AMD070	II
CRIs	HGS004	II
CRIs	Ibalizumab (TNX-355)	II
CRIs	PF-232798	II
CRIs	VCH-286	II
CRIs	Vicriviroc	III
FIs	PRO 140	II
EIs	SP01A	III
INIs	Elvitegravir	III
INIs	Dolutegravir	II

(Adapted with permission from American Chemical Society Publisher Ltd.: Mehellou, Y.; De Clercq, E. Twenty-six years of anti-HIV drug discovery: where do we stand and where do we go? *J. Med. Chem.* **2010,** 53, 521-538.)[21]

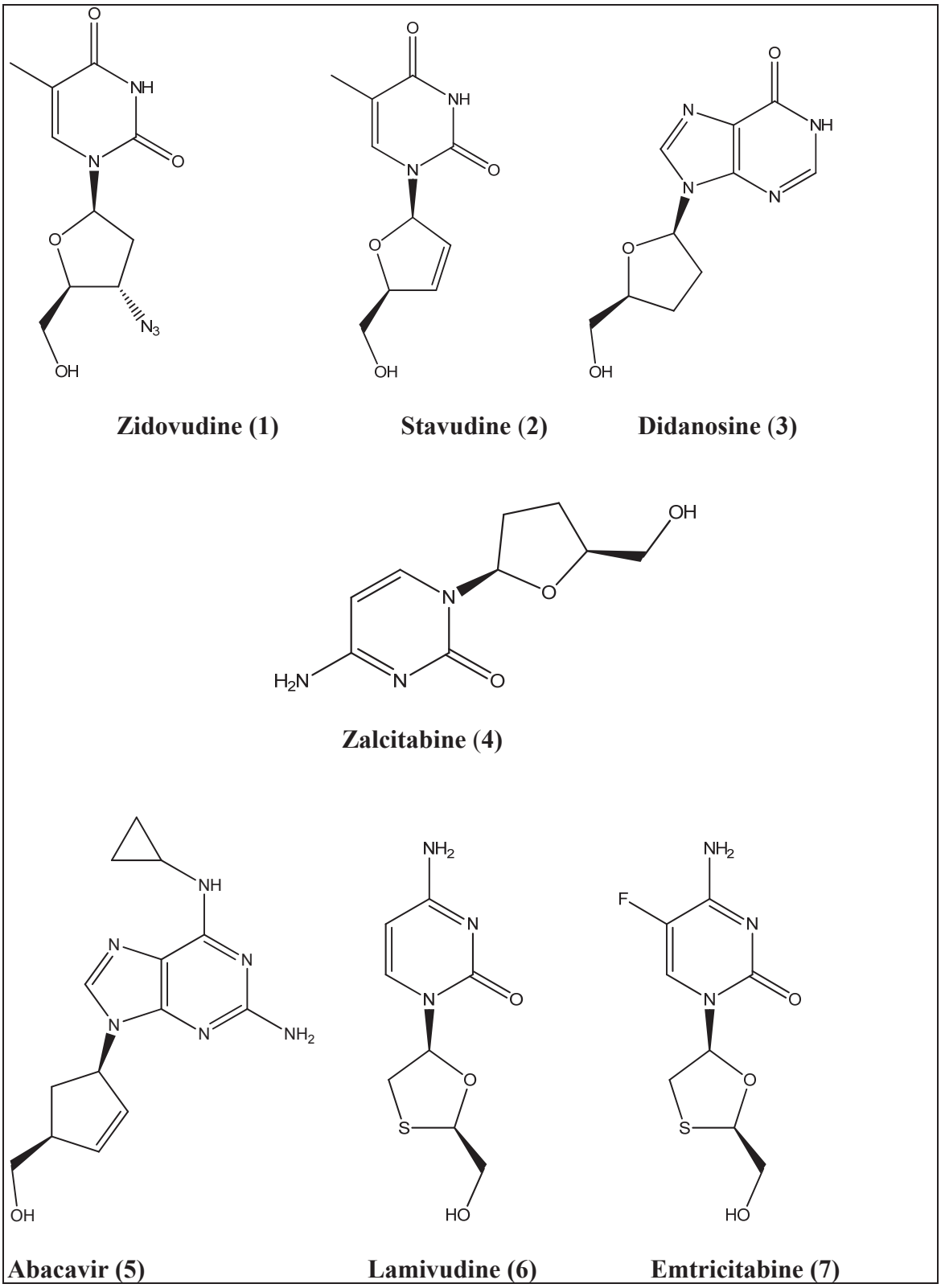

Figure 1-2. Structures of nucleoside reverse transcriptase inhibitors

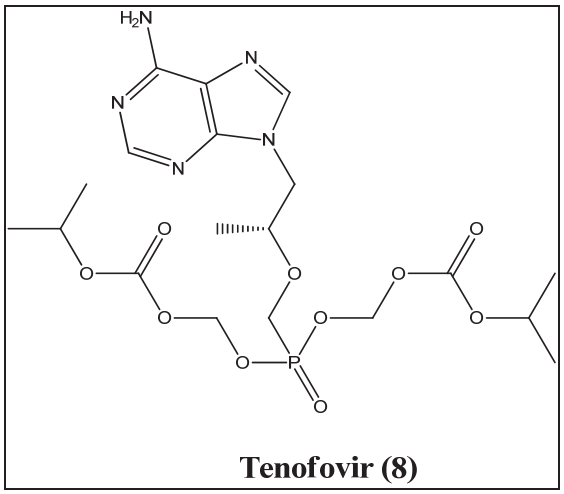

Figure 1-3. Structure of Tenofovir

Non-Nucleoside Reverse Transcriptase Inhibitors (NNRTIs)

Nevirapine (**9**) was the first NNRTI approved in 1996. In contrast to the above two classes, these are non-substrate analogs that bind to an adjacent allosteric site and inhibit RT by a non-competitive mechanism. Three more NNRTIs including Delavirdine, Efavirenz, and Etravirine (**Figure 1-4**) are approved as anti-HIV agents.[43,44] In addition, there are six NNRTIs that are currently under clinical development (see **Table 1-2**).

Protease Inhibitors (PIs)

HIV PR acts at a later stage of viral replication cycle and cleaves the gag and gag-pol precursor polypetides to structural and functional proteins resulting in mature and infectious virions. These drugs act by inhibiting HIV protease and thereby preventing the formation of a mature and infectious viral particle. Protease inhibitors constitute the largest class of HIV/AIDS drugs with 10 approved for anti-HIV therapy.[45,46] The first protease inhibitor approved was saquinavir mesylate (**13**) shown in **Figure 1-5**. Most of these drugs are peptidomimetic transition state analogs and possess a hydroxyethylene moiety as a non-scissile peptide bond isostere.

Co-Receptor Inhibitors (CRIs)

The first step in viral replication involves interactions of the viral glycoprotein gp120 with chemokine receptors on the host cell membrane. Co-receptor inhibitors prevent this interaction and inhibit the entry of virus into the cell.[47] Although a large number of small molecules antagonist have been discovered, maraviroc (**Figure 1-6**) is currently the only approved CCR5 antagonist.

Fusion Inhibitors (FIs)

Synthetic peptides were derived from gp41and targeted as HIV fusion inhibitors. A synthetic peptide, enfuvirtide, is the only fusion inhibitor currently approved. It prevents the fusion of the viral fusogenic peptide gp41 to the host cell membrane thereby preventing viral entry.[48]

Integrase Inhibitors (INIs)

HIV IN is an important enzyme involved in viral replication. It catalyzes the insertion of the viral DNA into the host genome. Since IN has no homologue in human cells, it offers a promising strategy for anti-retroviral drug development. β-Diketo acids and isosteres are the most advanced class to have shown promising HIV-1 IN inhibitory activity.[49] S-1360 (**Figure 1-7**) was the first IN inhibitor to enter clinical trials.[50] Over the last two decades, promising IN inhibitors were designed to incorporate bioisosteres of

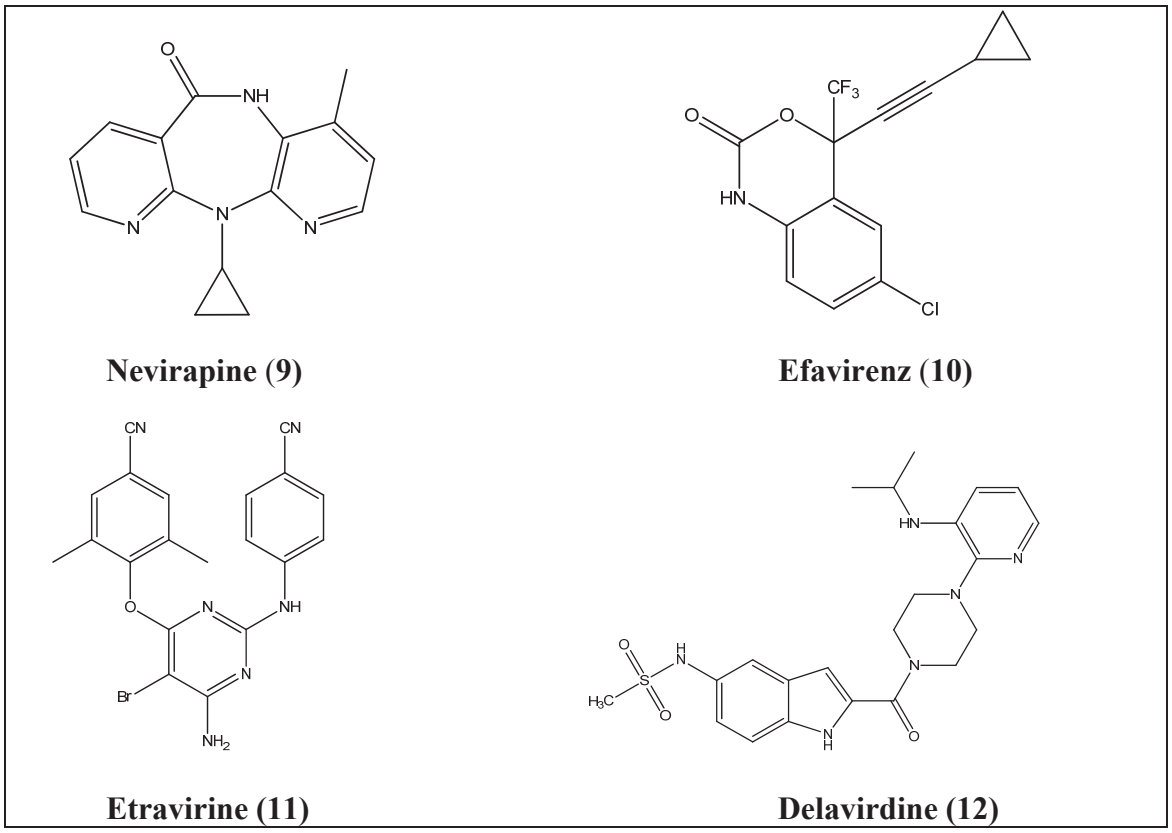

Figure 1-4. Structures of non-nucleotide reverse transcriptase inhibitors

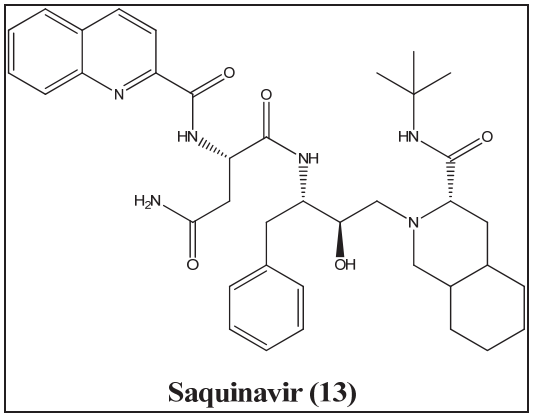

Figure 1-5. Structure of Saquinavir

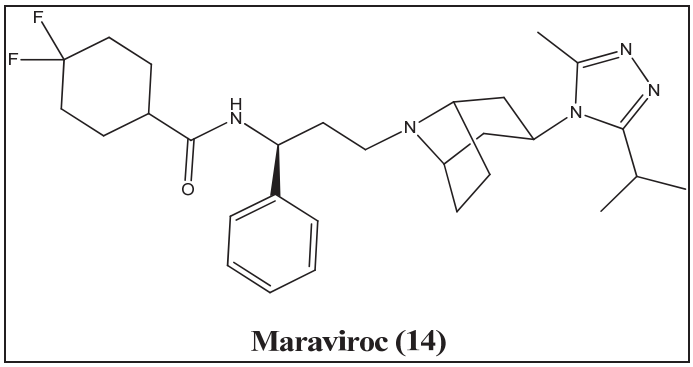

Maraviroc (14)

Figure 1-6. Structure of Maraviroc

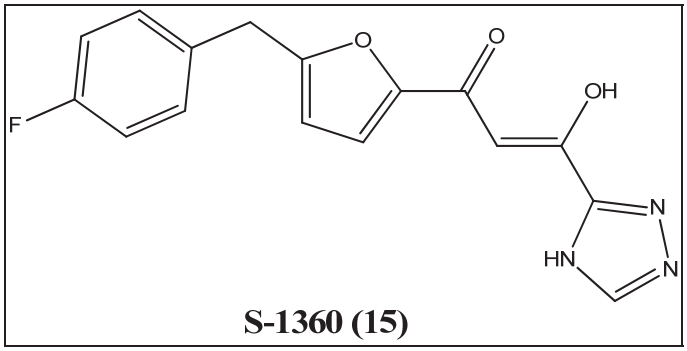

S-1360 (15)

Figure 1-7. Structure of S-1360

diketo acid functionality. Raltegravir (**16**) shown in **Figure 1-8** is currently the only IN inhibitor approved by the FDA[51] and 2 inhibitors elvitegravir and dolutegravir are in Phase III and II clinical trials, respectively.

Resistance to anti-retroviral drugs results due to the high mutational rate of HIV which in turn is caused by a low genetic barrier and a high turnover of the virus. To circumvent viral resistance, the currently available anti-HIV regimens include a cocktails of drugs from two or more classes. FDA-approved anti-HIV drug combinations are listed in **Table 1-3**. The combination therapy called Highly Active Antiretroviral Therapy (HAART), comprises of two NRTIs and one NNRTI and/or a PI. HAART though highly successful in reducing morbidity and mortality, has failed to fully eradicate the virus.[52-55] The emergence of multi-drug resistant viral stains demands development of drugs with novel mechanisms of action. Towards this end, IN has emerged as a promising target with the introduction of raltegravir for the clinical management of AIDS.

HIV Integrase: Structure and Function

Structure of HIV-1 IN

HIV-1 integrase, encoded by the *pol* gene, is an important enzyme in HIV replication. IN is a 288 amino acid 32 kDa protein composed of three distinct domains viz., the N-terminal domain (NTD), the central core domain (CCD), and the C-terminal domain (CTD) (**Figure 1-9**), all of which are required for catalytic activity. The NTD (1-50 amino acids) has a His-His-Cys-Cys (HHCC) zinc-finger motif, which is highly conserved in the IN of retroviruses and retrotransposases. Coordination of this motif with a Zn^{2+} ion stabilizes protein folding and multimerization, which in turn, is required for normal enzymatic activity. The CCD (aa 51-212) contains a catalytic triad of acidic amino acids that are conserved among the members of the super family of polynucleotidyl transferases. The catalytic triad consists of residues D64, D116 and E152 which are involved in chelation with metal ions in the IN active site. Any mutation in any of these residues and/or disruption of this coordination renders the enzyme inactive. It is believed that two divalent ions, Mg^{2+} *in vivo* and Mg^{2+} or Mn^{2+} *in vitro*, are required for catalysis. While D64 and D116 coordinate one Mg^{2+} ion, the second Mg^{2+} ion binds residues D64 and E152. The CTD (aa 213-288) is the least conserved, and bears some structural homology with SH3 DNA binding domains. This lysine-rich positively charged domain has nonspecific but strong DNA binding function. All the three domains, connected by flexible linkers, are prone to homodimerization. Recombinant IN exists in dynamic equilibrium between monomers, dimmers, and tetramers in solution.[56] Earlier *in vitro* studies have reported that while the monomeric form of IN is inactive *in vitro*, the isolated NTD, CCD, and CTD all exist as dimers. In the dimeric form, the IN is capable of catalyzing 3′-P and integration of one viral DNA end. In further studies, IN has been isolated as a tetramer from human cells expressing HIV-1 IN. Electron microscopy, single-particle image reconstruction studies and atomic force microscopy of intact IN-DNA complex have also revealed that IN acts as a tetramer.[57,58] Structural modeling

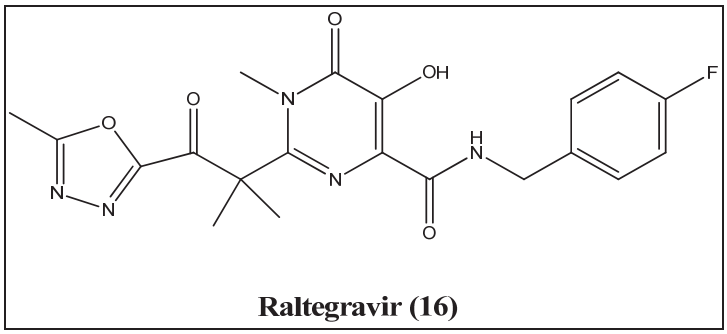

Raltegravir (16)

Figure 1-8. Structure of Raltegravir

Table 1-3. FDA-approved anti-HIV combination therapies

Combination	Components	FDA approval year
Combivir	Zidovudine (300 mg), Lamivudine (150mg)	1997
Trizivir	Abacavir (300 mg), Zidovudine (300 mg), Lamivudine (150mg)	2000
Epzicom	Abacavir (600 mg), Lamivudine (300mg)	2004
Truvada	Tenofovir disoproxil fumarate (TDF) (300 mg), Emtricitabine (200 mg)	2004
Atripla	TDF (300 mg), Emtricitabine (200mg), Efavirenz (600 mg)	2006

(Adapted with permission from American Chemical Society Publisher Ltd.: Mehellou, Y.; De Clercq, E. Twenty-six years of anti-HIV drug discovery: where do we stand and where do we go? *J. Med. Chem.* **2010,** 53, 521-538.)[21]

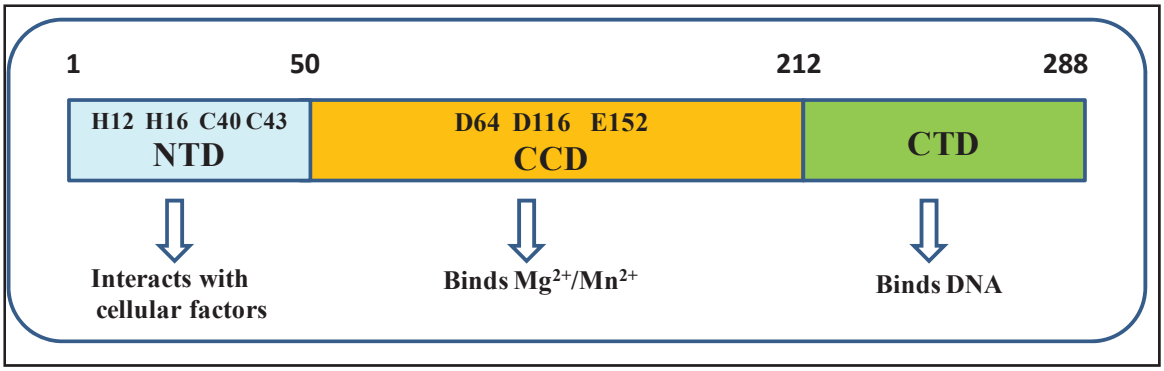

Figure 1-9. Structure of HIV-1 integrase

(Adapted with permission from Nature Publishing Group: Pommier, Y.; Johnson, A. A.; Marchand, C. Integrase inhibitors to treat HIV/AIDS. *Nat. Rev. Drug Discov.* **2005,** 4, 236-248.)[96]

further supports that the tetrameric form of IN catalyzes the insertion of two viral DNA ends into the target DNA. It should be noted that because of the staggered cut, which occurs 5 base pairs apart in a target helical B-form of DNA, the site of integration should be separated by a corresponding distance of 15-18 Å. Thus the active site in a functional integrase should also be separated by a similar distance. However, in the crystal structure of the dimeric CCD, the active sites are found 35 Å apart. It was therefore concluded that in order to maintain a distance of 35 Å at least one tetramer of IN is required to fulfill the complete concerted 'two-ended' ST integration step.[59] Moreover, studies on IN isolated from a nuclear extract and its complex with lens epithelium-derived growth factor (LEDGF) has further indicated that IN exists as a tetramer.[60]

3D structures of individual domains of recombinant HIV-1 IN have been reported by either NMR or X-ray crystallography.[61-80] Because of the poor solubility, full-length wild type HIV-1 IN has yet not been crystallized. The F185K Mutation resulted in substantial improvement in solubility and led to the first crystallization of the CCD. The CCD has five-stranded mixed β-sheet flanked by α- helices. The crystal structures of HIV-1 CCD have been solved for its apo form as well as with different metal-complexes. The available structures however contain only single metal ion and no structure with two metals have yet been reported. A crystal structure of a CCD-inhibitor (5-CITEP) complex has also been reported. The inhibitor showed only indirect, water mediated, contact with the active site Mg^{2+} and no interactions with either Asp64 or Asp116 were observed. Later, it was confirmed that binding mode of 5-CITEP was affected by crystal packing.[81,82] Most of the structures of a CCD have partially resolved flexible loop region (residues Gly140-Gln148). Only two crystal structures (chain B of 1BIS and chain C of 1BL3) have a completely resolved flexible loop, however, the conformations of the active site residues in these structures were different. Although no X-ray crystal structures of the CTD and NTD are available, the structures of these domains have been solved by solution NMR spectroscopy. The solution structure of NTD of HIV-1 revealed that the NTD exists as a homodimer, each monomer of which consists of 4 helices. The NMR resolved structure of CTD also showed the presence of dimeric molecules in which each monomer comprises 5 β-strands, arranged in an antiparallel manner in a β-barrel. Interdomain (CCD-CTD or CCD-NTD) structures of HIV-1 IN have also been crystallized. **Table 1-4** summarizes the reported 3D structures of HIV-1 IN solved by NMR and X-ray crystallography. One of the major limitations of the available structures is that they have only partially resolved inter-domain linker conformations. Furthermore, the absence of two metals in the IN active site and of a full-length HIV IN-DNA complex make the structural information available limited and far from reality. Several studies have been directed to exploring the binding interactions of IN with the viral DNA.[83-88] HIV-1 IN-DNA models were constructed based on the solved two domain (CCD-NTD/CCD-CTD) structures. Although IN is not very selective for the target DNA, it does recognize viral DNA sequence-specifically. The terminal conserved CA dinucleotide is shown to be important for IN binding and catalyzing 3′-P and ST reactions. In addition, *in vitro* mutational studies revealed a region centered 12 bases from the 3′-terminus to be essential in DNA binding in the presence of magnesium cofactor.[89,90] Specific photocrosslinking studies have identified Lys156 and Lys159 as important CCD residues involved in interaction with the viral DNA.[91]

Table 1-4. Crystal structures of HIV-1 IN

Protein	PDB code	Method	Resolution (Å)	Year	Ref.
NTD	1WJA, 1WJB	NMR	N/A[a]	1997	62
NTD	1WJC, 1WJD	NMR	N/A	1997	62
NTD	1WJE, 1WJF	NMR	N/A	1998	64
CCD	1ITG	X-ray	2.30	1994	63
CCD	2ITG	X-ray	2.60	1996	61
CCD	1BHL	X-ray	2.20	1998	66
CCD	1BI4	X-ray	2.50	1998	66
CCD	1BL3	X-ray	2.00	1998	66
CCD	1BIS	X-ray	1.95	1998	67
CCD	1BIU	X-ray	2.50	1998	67
CCD	1BIZ	X-ray	1.95	1998	67
CCD	1B92	X-ray	2.02	1999	68
CCD	1B9D	X-ray	1.70	1999	68
CCD	1B9F	X-ray	1.70	1999	68
CCD	1QS4	X-ray	2.10	1999	69
CCD	1EXQ	X-ray	1.60	2000	70
CCD	1HYV	X-ray	1.70	2001	71
CCD	1HYZ	X-ray	2.30	2001	71
CTD	1IHV	NMR	N/A	1995	72
CTD	1QMC	NMR	N/A	1999	73
NTD-CCD	1K6Y	X-ray	2.40	2001	74
CCD-CTD	1EX4	X-ray	2.80	2000	70
CCD+LEDGF	2B4J	X-ray	2.02	2005	76
CCD	3LPT	X-ray	2.00	2010	77
CCD	3LPU	X-ray	1.95	2010	77
CCD	3L3U	X-ray	1.40	2010	78
CCD	3L3V	X-ray	2.00	2010	78
CCD	3NF6, 3NF8	X-ray	1.90	2011	79
CCD	3NF7	X-ray	1.85	2011	79
CCD	3NF9, 3NFA	X-ray	1.95	2011	79

[a] N/A = not available.

(Adapted with permission from John Wiley and Sons: Jaskolski, M.; Alexandratos, J. N.; Bujacz, G.; Wlodawer, A. Piecing together the structure of retroviral integrase, an important target in AIDS therapy. *FEBS J.* **2009,** 276, 2926-2946.)[80]

Since IN inhibitors target a DNA- IN complex and not a free protein, tremendous efforts are underway to solve a complete HIV IN-DNA complex structure which would accelerate the structure-based design of new HIV-IN inhibitors. In a recent breakthrough, crystal structures of full-length IN from prototype foamy virus in complex with the viral/host DNA (**Figure 1-10**) have been determined.[92-94] Crystal structures of the foamy virus IN-DNA-inhibitor (raltegravir or elvitegravir) complexes have also been published.[92] The structure revealed the retroviral IN as a tetramer tightly bound to the viral DNA. This minimal IN-DNA complex within the pre integration complex (PIC) capable of carrying 3′-P and ST is referred to as intasome. Foamy virus and HIV both belong to the family of retroviruses and super family of polynucleotidyl transferases. They share a conserved triad of acidic residues in the active site and use two divalent metals (Mg^{2+}) for nucleophilic S_N2 catalytic mechanism. A high level of sequence identity in the active sites of the foamy virus and HIV provides a rationale for using the foamy structure as a surrogate for HIV. This structure was used as template and sequence aligned with the secondary structure of HIV-1 to build a model for HIV-1 intasome.[95] The modeled intasome consisted of a pair of IN dimer (forming a tetramer) tightly bound to a molecule of viral DNA. The outer CCDs of the two dimers serve an accessory role to the complex; while the CCDs of the inner subunits of each dimer forms a pair of functional active site which is involved in all protein-protein and protein- DNA interactions. Residues of the active site loop (Gln140-Gln148) and α4 helix are involved in CCD-DNA contacts. Most of the contacts were observed with the backbone of the nontransferred DNA strand, however few specific contacts with the bases are also observed. Apart from the residues previously implicated in DNA binding, Arg20 and Lys266 were identified as new residues which have role in DNA binding and integration.[95] Another crystal structure of the foamy virus intasome shows (**Figure 1-11**) viral DNA-IN in association with the target DNA.[94] Within the intasome, target DNA is placed in a cleft between the two symmetric dimers of the IN. Severe bending of the target DNA makes it possible to position its scissile phosphodiester into the intasome active site, separated by a distance of ~ 27Å. While there are only few direct contacts between target DNA and IN, the phosphodiester backbone is involved in 8 hydrogen-bonds with the main chain amides of IN.[94]

Function and Putative Mechanism of IN

HIV-1 IN is one of the three enymes essential for viral replication, the other two being HIV-1 reverse transcriptase and HIV-1 protease. It catalyzes the integration[96] of the viral DNA into the host genome by two catalytic steps, 3′-P and ST (**Figure 1-12**).[97] In the 3′-P reaction, which occurs in the cytoplasm of an infected cell within a pre-integration complex (PIC), a site specific endonucleolytic activity removes a GT dinucleotide from the long terminal repeat region (LTR) of the viral genome. The terminal nucleotides removed are adjacent to the highly conserved CA dinucleotide at each of the 3′-end of the proviral DNA. Chemically, the reaction involves the nucleophilic activation of a water molecule by the Mg^{2+} ion (coordinated with Glu152 and Asp64); the activated water molecule then subsequently attacks the phosphodiester bond of the viral DNA to generate free 3′-OH ends.

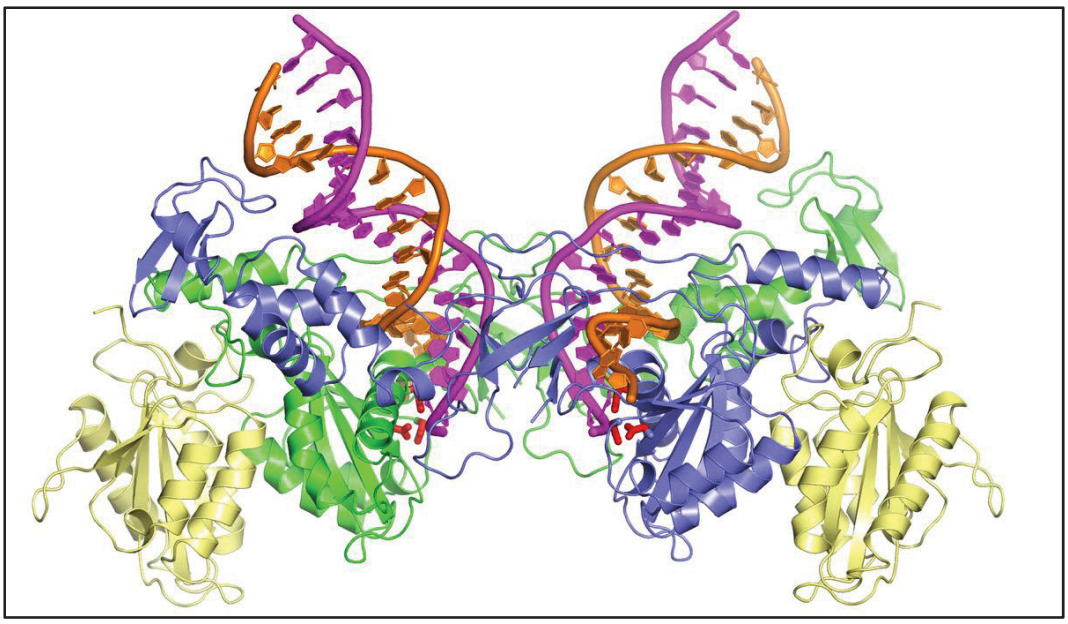

Figure 1-10. Crystal structure of foamy virus integrase-viral DNA complex

The inner subunits of the IN tetramer, engaged with viral DNA, are blue and green; outer IN chains are yellow. The reactive and non-transferred DNA strands are magenta and orange, respectively. Side chains of Asp128, Asp185 and Glu221 active-site residues are red sticks; Zn atoms are grey spheres.

(Reproduced with permission from Nature Publishing Group: Hare, S.; Gupta, S. S.; Valkov, E.; Engelman, A.; Cherepanov, P. Retroviral intasome assembly and inhibition of DNA strand transfer. *Nature* **2010**, 464, 232-236.)[93]

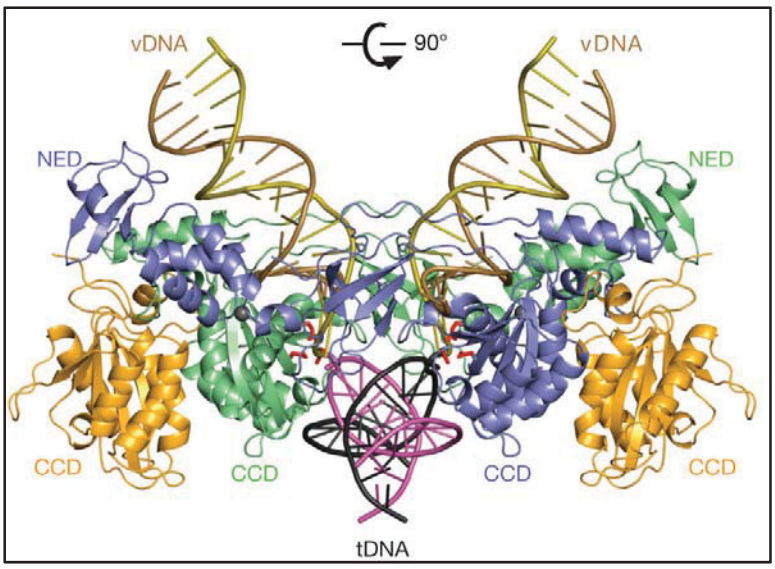

Figure 1-11. Crystal structure of foamy virus IN, viral and target DNA strand transfer complex

Representations of the STC crystal structure, viewed along or perpendicular to the crystallographic two-fold axis, respectively. IN active site carboxylates are shown in red.

(Reproduced with permission from Nature Publishing Group: Maertens, G. N.; Hare, S.; Cherepanov, P. The mechanism of retroviral integration from X-ray structures of its key intermediates. *Nature* **2010**, 468, 326-329.)[94]

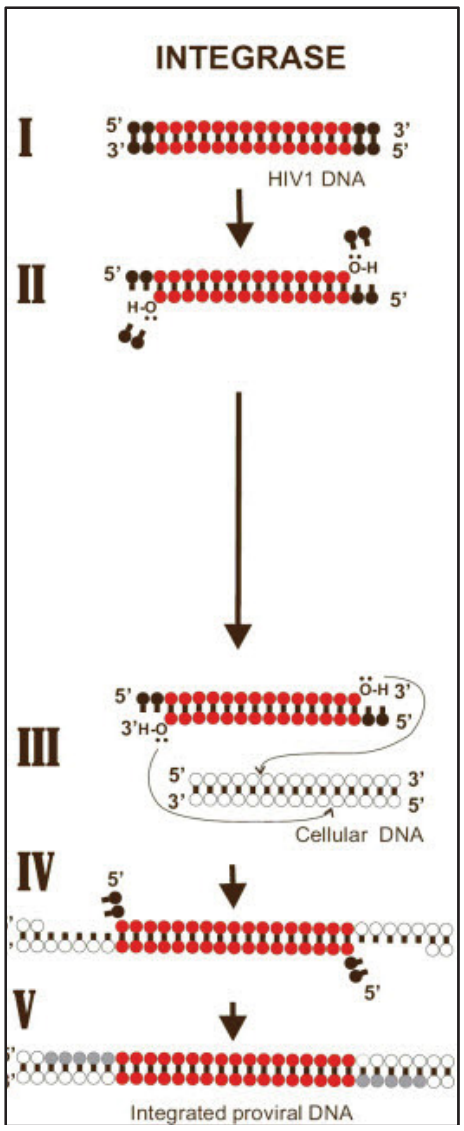

Figure 1-12. Mechanism of integration

(I) Donor DNA; (II) integrase-catalyzed 3′- processing; (III) integrase-catalyzed strand transfer; (IV) product of strand transfer; (V) DNA repair by cellular enzymes.

(Open Access: Savarino, A. In-Silico docking of HIV-1 integrase inhibitors reveals a novel drug type acting on an enzyme/DNA reaction intermediate. *Retrovirology* **2007**, 4, 21.)[97]

The primed viral DNA in association with the viral protein, in a pre-integration complex, then translocates into the nucleus of the host cell. Within the nucleus, viral IN catalyzes the next step of integration, ST. In the process of ST, IN introduces a staggered cut in the target DNA at sites separated by 5 base pairs resulting in overhangs with 5′ phosphorylated ends. IN then performs strand transfer, also called as the 3′ -end joining reaction wherein the primed 3′-ends of the viral DNA are joined to the 5′-ends of the host/target DNA. Chemically, this involves a second nucleophilic attack, this time by the 3′ OH groups at the phosphodiester bond of the host DNA. Finally, host enzymes remove the two mismatched nucleotides at each 5′ end of viral DNA, fill in the single stranded gaps and ligate the remaining ends.

A putative mechanism for inhibition of integration has been proposed based on the recently reported foamy virus crystal structures. For integration to occur, unpairing of the donor DNA is required to expose the scissile phosphodiester bond (for 3′-P) and orient the 3′ OH (for ST) near the IN active site. The model suggests that the terminal adenine (A17) of the reactive DNA strand dissociates from its base pair thymine (T3) in the complementary nontransferred strand, as the terminal bases of the DNA interacts with the CCD, CTD and CCD-CTD linker. The adenine 3′ OH end is then positioned into the active site and is activated by the metal (coordinated between Asp64 and Asp116) to undergo S_N2 nucleophilic attack at the phosphodiester bond of the host DNA. Raltegravir and other IN inhibitors have coplanar metal chelating hetero atoms that coordinate the two divalent metals in the IN active site.[98,99] Furthermore, a halogenated benzyl group which is a common feature of IN inhibitors, according to the model, stacks against the penultimate cytosine of the reactive DNA strand and thereby displaces the terminal 3′-OH out of the active site away from the metal ions. Thus, any disruption of the activation of the nucleophilic 3′-OH or its displacement from the active site upon drug binding inhibits ST step of retroviral integration.[92,100]

HIV-1 IN Inhibitors

HIV-IN does not have a human counterpart making it an attractive target for anti-HIV therapy. During the last two decades of research, large numbers of IN inhibitors have been discovered. However, only few have advanced to clinical trials and only one, raltegravir, has been approved. IN inhibitors can be classified on the basis of those targeting selectively the 3′-P step, those that inhibit both 3′-P and ST, and those that selectively inhibit the ST catalytic step. The most advanced drugs selectively inhibit the ST reaction and have two common structural features viz., a hydrophobic halo benzyl group and a chelating motif capable of binding two Mg^{2+} ions.

In the early efforts, ribozymes were used to cleave HIV-1 IN and oligonucleotides were designed to form triplex DNA to inhibit the integration process.[101-103] These efforts did not yield any potent inhibitor and were not pursued due to their significant risk of toxicity. Nucleotide analogs based on AZT were among the early IN inhibitors reported.[104] Several di-, tri-, and tetra-nucleotides were then examined for their IN inhibitory activities. A G-quartet oligonucleotide composed of deoxyguanosine and

thymidine, zintevir, showed potent HIV-1 IN inhibitory activity and inhibition of viral replication in cell culture.[105] Zintevir, which progressed to Phase I/II clinical trials, was later shown to inhibit viral gp120 binding and prevent viral entry into cells.

DNA-Binding Agents

Several DNA-binding agents were identified to inhibit HIV-1 IN by preventing the interaction of viral DNA with the DNA-binding domain of the enzyme. Benzimidazoles inhibited IN with an overall 50 % inhibitory concentration (IC_{50}) of 5 μM.[106] Minor groove binders like netropsin are also reported to interfere with viral DNA-IN binding. Lexitropsins have also been shown to inhibit IN by binding at the conserved AT sequence in HIV-1 LTR.[107] The fluorescent dye Hoechst 33258 and its derivatives bind in a site-specific and non-covalent manner to the minor groove of DNA. *N,N′*-(methylene-di-4,1-phenylene) *bis*-1-pyrrolidineacetamide was recently reported as novel anti-HIV agent that competes with viral DNA for binding to the IN CCD dimer interface.[108]

Peptides/Proteins

Polyamides prevent the binding of viral DNA to IN and subsequently inhibit IN enzymatic activity. A hexamer peptide (HCKFWW) was identified to be an inhibitor of HIV-1 IN with micromolar affinity.[109] In another study, a 30-mer peptide which corresponds to amino acids 147-175 of HIV-1 IN was shown to inhibit IN activity at a millimolar concentrations but was not active in cell culture.[110] MAP30, luffin, and saporin which are members of the family of ribosome inactivating protein (RIP), have also been reported to have antiviral and anti-IN inhibitory activity.[111]

Polyhydroxylated Aromatic Compounds

Polyhydroxylated aromatic compounds (**Figure 1-13**) were among the first small molecule inhibitors of HIV-IN *in vitro*. They include both natural and synthetic derivatives like flavones, tyrphostins, lignans, anthraquinones, catechols and bis-catechols.[112-116] These compounds possess two aryl groups which are separated by a linker. At least one aryl unit contains two *ortho*-hydroxyl groups meant for chelation with the IN active site metal ions. An example of a potent member of the class of bis-catechols is β-conidendrol (**17**), which selectively inhibited both steps of HIV-1 IN with an IC_{50} of 0.5 μM. However, when tested in cell cultures the *in vitro* inhibition did not translate into antiviral activity. Dicaffeoylquinic acids (DCQAs) represented by *L*-chicoric acid (**18**) and analogs were shown to be active against HIV-1 IN *in vitro*, and to also inhibit HIV-1 replication in tissue culture in the low μM concentration range.[117] Other bis-catechol IN inhibitors include the curcumin derivative rosmarinic acid (**19**).[118] Curcumin analog dicaffeoyl methane (**20**) inhibited ST activity with an IC_{50} of 3.1 μM.[118] One representative IN inhibitor of the catechol series, caffeic acid phenylethyl ester

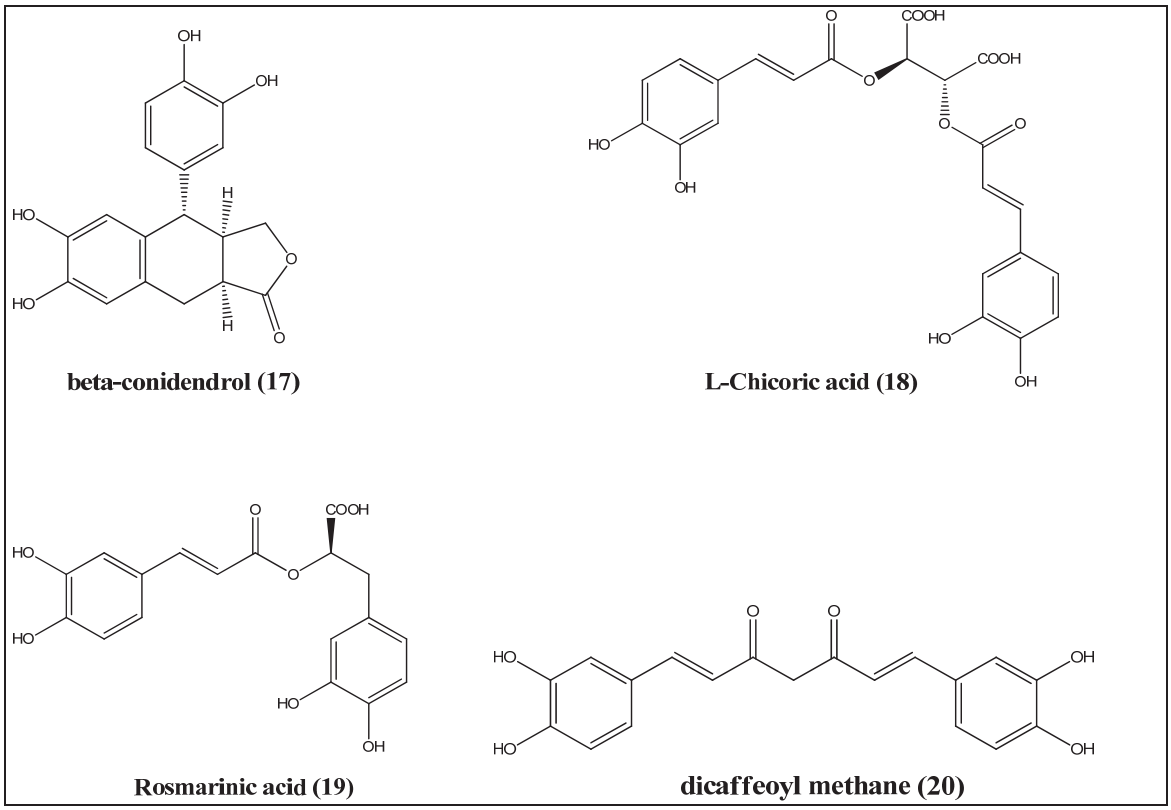

Figure 1-13. Structures of poly-hydroxylated HIV-1 integrase inhibitors

(CAPE, **21**) is shown in **Figure 1-14**.[119] CAPE was the first selective (ten-folds selectively against ST relative to 3′-P) IN inhibitor that also showed weak antiviral activity. From these studies it was inferred that at least one catechol group is required for potent HIV IN inhibitory activity.[119] Compounds without a catechol unit were also investigated for their HIV-IN inhibitory activity. NSC 158393 (**Figure 1-15**, compound **22**) contains four 4-hydroxycoumarin moieties with no catechol substructure and was active against both HIV-1 PR and IN.[120] The utility of polyhydroxylated aromatic compounds as drug candidates is however limited by the fact that their catechol moiety is prone to oxidation *in situ* to a reactive quinone species which may lead to covalent protein modification.

Styryl Quinolines

A novel series of compounds in which a quinoline ring system is attached to a hydroxyl containing aryl group by an ethylenic linker (**Figure 1-16**) was developed as potent HIV-1 IN inhibitors.[121] Although, highly active compounds of the series, including FZ41 (**23**), have a catechol substituent, detailed structure activity relationship (SAR) studies showed that a catechol group was not an absolute pharmacophoric requirement for an IN inhibitor. These compounds were designed to chelate active site divalent metals and were found to inhibit both 3′-P and ST at sub-micromolar levels. They are believed to be competitive inhibitors of the binding of viral DNA to IN. Another study has shown that they prevented the nuclear import of recombinant IN.[122]

Pyranodipyrimidines

Pyranodipyrimidines (**Figure 1-17**) were reported to inhibit HIV-1 integration at low μM concentrations. The most potent compound of the series V-165 (**24**) inhibited recombinant integrase *in vitro* and also HIV-1 replication in cell cultures.[123] V-165 was more active against 3′-P with IC_{50} of 0.17 μM as compared to ST inhibitory IC_{50} value of 16 μM. Time-of-addition experiments indicate that V-165 acts prior to the formation of the pre-integration complex (PIC) suggesting that it prevented the formation of DNA-IN complex by inhibiting the binding of IN to the viral DNA. It was however reported that V-165 was not selective for IN and was found to be active against RT as well.

β-Diketo Acids

The β-Diketo acid pharmacophore was discovered from several fungi derived natural products which were reported as HIV-1 IN inhibitors. These fungal compounds contained a β-hydroxy keto groups which were subsequently modified to a β-diketo acid and its structural analogs.[49,124] Although, not sufficient for activity, the diketo acid functionality was identified as an important requirement for an IN inhibitor. Extensive research was thus directed to incorporate a β-diketo acid functionality, which subsequently became the first representative pharmacophore of potent IN inhibitors. The

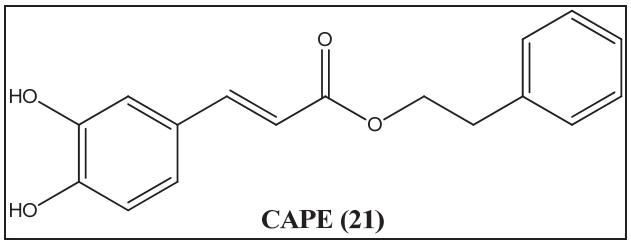

Figure 1-14. Structure of caffeic acid phenyl ester (CAPE)

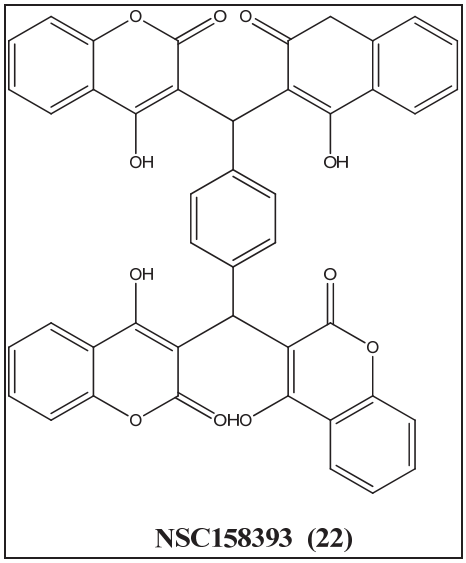

Figure 1-15. Structure of NSC 158393 HIV-1 integrase inhibitor

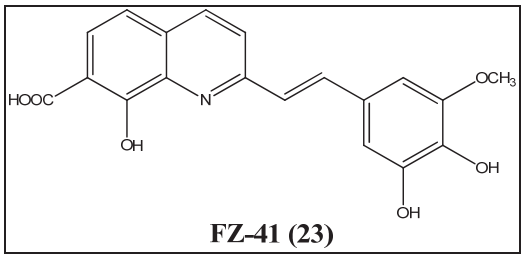

FZ-41 (23)

Figure 1-16. Structure of styryl quinoline integrase inhibitors

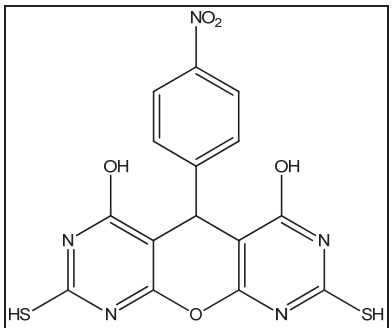

V-165 (24)

Figure 1-17. Structure of pyranodipyrimidine, V-165

coplanar heteroatoms in the β-diketo acid motif were perceived to chelate the divalent metals in the IN active site.[99] In pursuit of β-diketo acid IN inhibitors shown in **Figure 1-18**, researchers at the Shionogi & Co. Ltd discovered 5-CITEP (**25**) which contained a tetrazole as a bioisostere of carboxylic acid. 5-CITEP was highly selective for the ST catalytic step (IC_{50}s of 0.4-4.0 μM for ST vs. 35 μM for 3′-P). Moreover, 5-CITEP was found to be a more potent inhibitor (ST IC_{50} of 0.4 μM) in the presence of Mn^{2+} than Mg^{2+} (ST IC_{50} 4.0 μM). It was also the first integrase inhibitor to have been co-crystallized with the CCD of IN. Subsequently, Merck also discovered β-diketo acid IN inhibitors; the most potent among them were L-731,988 (**26**) and L-708,906 (**27**), which have an acid functionality instead of its isostere tetrazole that was present in 5-CITEP.[50,124] SAR studies have shown that replacement of the lesser acidic tetrazole moiety with a carboxylate substantially improved the ST inhibitory activity in Mg^{2+} suggesting that a carboxylate might be important for metal coordination.[50] L-731,988 and L-708,906 were also highly selective (70-100 folds) for the ST reaction *in vitro*. L-731,988 and L-708,906 have ST IC_{50s} values of 80 nM and 150 nM, respectively, and inhibited HIV-1 replication with micromolar 50 % effective concentration (EC_{50}) values in cell culture. It was again shown that IN inhibition can be divalent-cation dependent. The IC_{50} of L-708,906 for 3′-P was 2.5 μM and 22 μM in Mg^{2+} and Mn^{2+} respectively, while its IC_{50} for ST was comparable with either metal. Another closely related compound from Shionogi, S-1360 (see **Figure 1-7**) showed potent inhibition of integrase in enzymatic assay and displayed antiviral activity in cell culture. Their antiviral activity was proved to be the result of their inhibition of the integration process in viral replication. S-1360 was also selective against ST with IC_{50} value of 20 nM and it became the first IN inhibitor to enter Phase I/II clinical trials.[125] Its progression was however halted due to rapid metabolism of its β-diketo acid functionality and subsequent formation of inactive metabolites. The SAR studies of the diketo acid derivatives revealed that the aromatic moiety is important for potency and ST selectivity. Several diketo acid derivatives were then synthesized with various aromatic systems containing different substitutions. Examples include MA-DKA which had an azido group on the aryl moiety designed for cross linking studies.[126] One of the common aryl ring system present in potent IN inhibitors such as L-731,988 and S-1360 was a *para*-fluorobenzyl group, which was later identified as an important feature of potent ST selective inhibitors. Subsequent modifications were made to incorporate the diketo acid chelating heteroatom into a ring system also leading to potent sub micromolar and nanomolar inhibitory activities.

Naphthyridine Carboxamide

To circumvent the metabolic issues of a free β-diketo acid functionality, the diketoacid motif was embedded into a naphthyridine carboxamide core such that the carboxylic acid was replaced with a lone pair donor atom containing heterocycle. Examples of metabolically stable naphthyridine carboxamides include L-870,810 (**28**), L-870,812 (**29**), and GSK-364735 (**30**) (**Figure 1-19**). L-870,810 and L-870,812 were found to be selective for ST inhibition and inhibited ST activity *in vitro* with potent IC_{50s} of 8-15 nM and 40 nM, respectively. L-870,812 inhibited HIV replication with 95 %

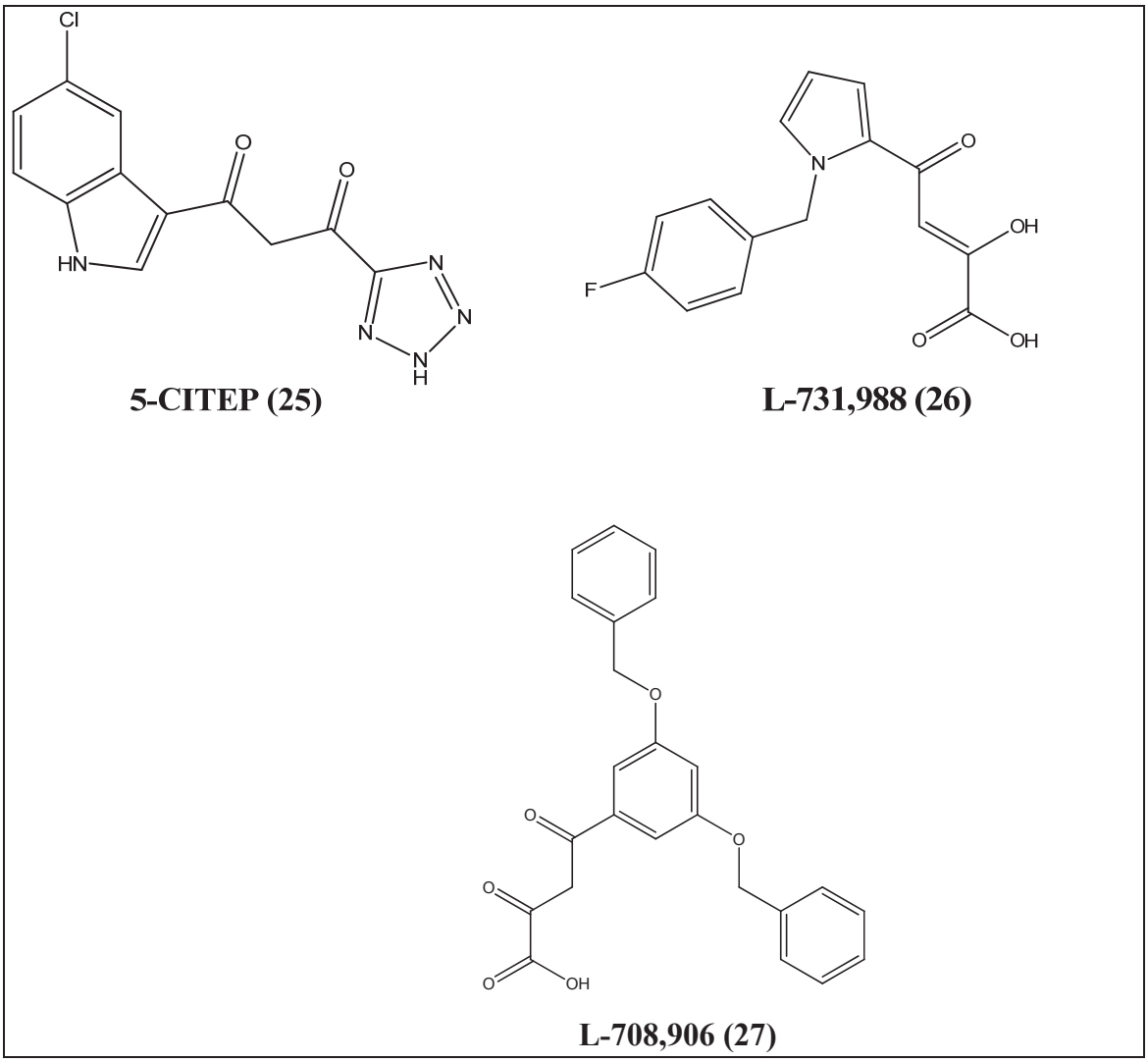

Figure 1-18. Structures of diketo acid HIV-1 integrase inhibitors

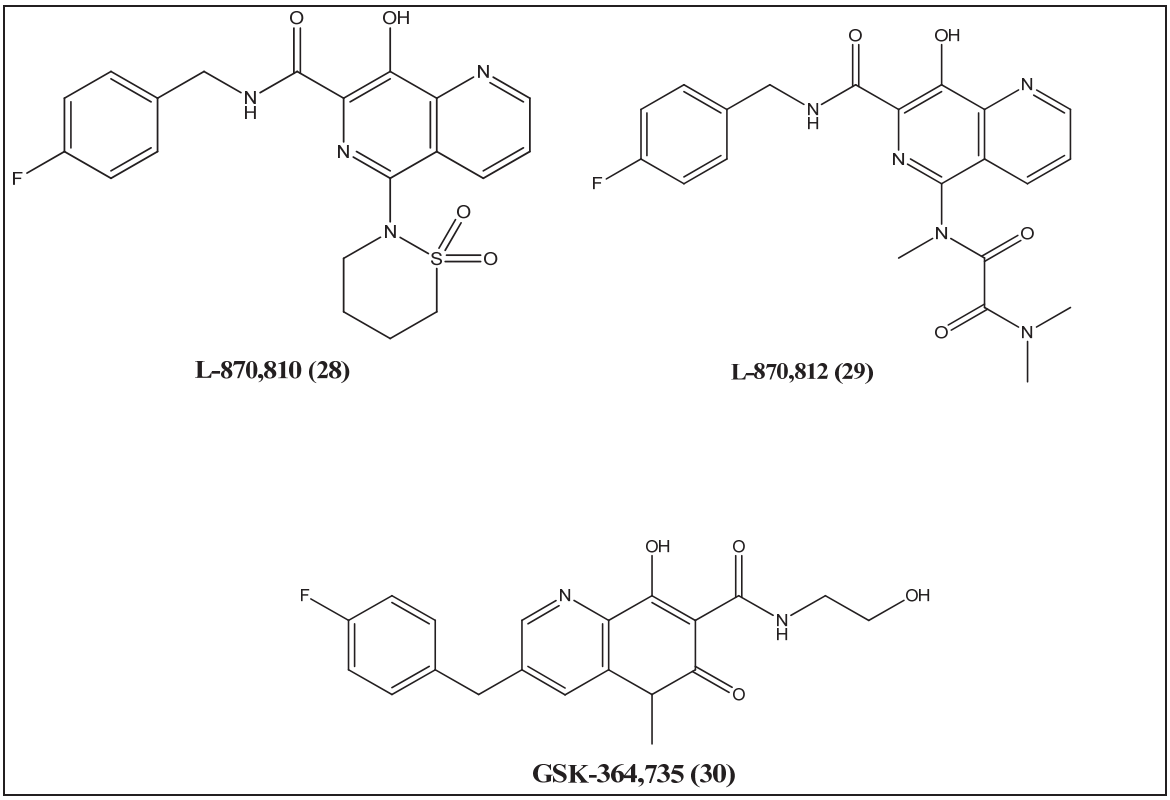

Figure 1-19. Structures of naphthyridine carboxamide HIV-1 integrase inhibitors

inhibition concentration (IC_{95}) of 250 nM and suppressed viral load in rhesus macaques infected with SHIV 89.6P recombinant strain.[127] L-870,810 became the second candidate to enter clinical trials; its progression was however halted because of long-term hepatotoxicity observed in dogs.[128] Furthermore, it also suffered from low bioavailability due to high serum protein binding. L-870,812 also entered clinical trials but its data were not made public and was discontinued probably because of similar *in vivo* profile as L-870,810. Although integrase ST inhibitors were validated for the treatment of HIV, viral resistance against them soon emerged. Mutations T66I and F121Y selectively conferred resistance to diketo acids and naphthyridine carboxamides, respectively. Mutation N155H/S resulted in viral resistance to diketo acids and also showed cross resistance to naphthyridine carboxamides.[129] GSK-364735 showed potent inhibition of ST activity (IC_{50} value of 8.0 nM) of recombinant integrase in enzymatic assay.[130] It also inhibited HIV replication in nanomolar concentrations (1.2 ± 0.4 nM in peripheral blood mononuclear cells and 5 ± 1.0 nM in MT-4 cells). It entered in Phase I clinical trials but its development was halted due to long-term toxicity issues.[130]

Dihydroxypyridopyrazine-1,6-diones

The 1,6- naphthyridine carboxamide core was used to design dihydroxypyridopyrazine-1,6-diones (**Figure 1-20**) as a new class of IN inhibitors such that the diketo functionality was embedded in a pyridinone scaffold.[131] Compound (**31**) showed ST IC_{50} value of 0.10 μM and inhibited HIV replication with EC_{50} value of 0.31 μM. A series of analogs synthesized demonstrated *in vitro* potency, but they did not however offer improved anti-HIV activities.

Pyrazolopyrazinone

A bicyclic system having pyrazolopyrazinone scaffold (**Figure 1-21**) was designed to enforce coplanarity of the metal-chelating atoms.[132] Compound (**32**) had potent ST inhibitory activity value of < 10 nM and inhibited HIV-1 replication with EC_{50} (10% FBS) value of 0.63 μM in cells.

8-Hydroxy-3,4-dihydropyrrolo[1,2-a]pyrazine-1(2H)-ones

The pyridinone ring was substituted with a pyrrole ring (**Figure 1-22**) to design this new class of IN inhibitors.[133] Several halogen substitutions were made on the benzyl group to confer ST selectivity and improve anti-HIV activity. Compound (**33**) had an ST IC_{50} value of 0.04 μM and an anti-HIV CIC_{50} value of 3.23 μM in cells. Another compound of the series, (**34**), showed a potent ST IC_{50} value of 0.01 μM and also inhibited HIV replication in cells with a CIC_{50} value of 0.31 μM. However, it was not metabolically stable and was readily eliminated with a short half-life of 0.5 h. To improve metabolic stability, the ester was replaced by an amide functionality in compound (**35**). Compound **35** inhibited ST activity with similar potency (IC_{50} value of 0.08 μM), but

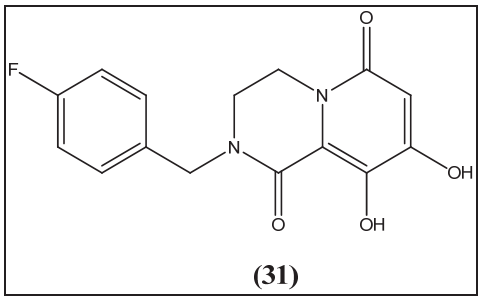

(31)

Figure 1-20. Structure of dihydroxypyridopyrazine-1,6-diones HIV-1 integrase inhibitors

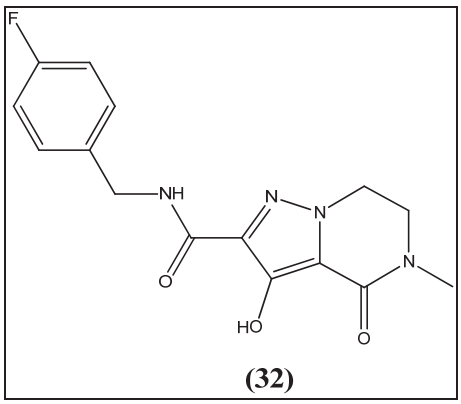

(32)

Figure 1-21. Structure of pyrazolopyrazinone HIV-1 integrase inhibitors

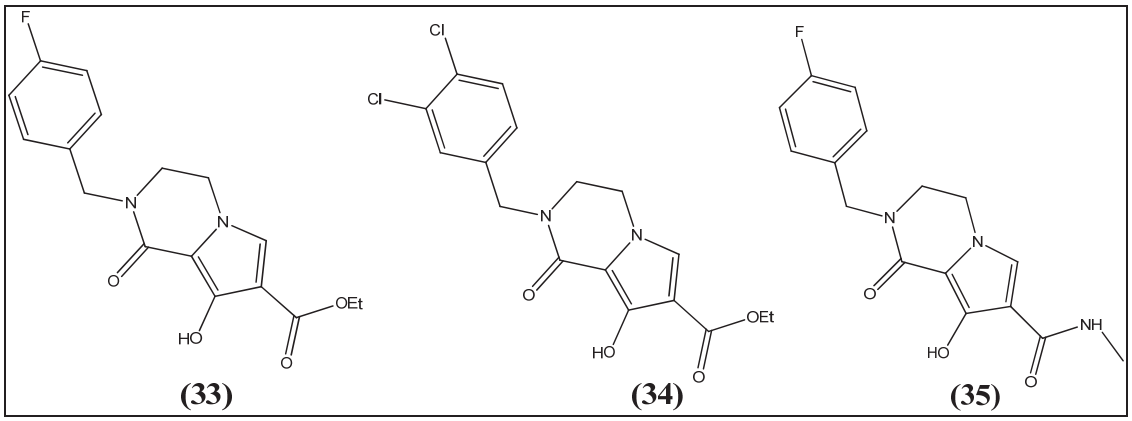

(33) **(34)** **(35)**

Figure 1-22. Structures of HIV-1 integrase inhibitors pyrrolopyrazine carboxamides

showed a marked decrease in the antiviral activity in cell culture (CIC_{50} value of 10 μM). Further modifications of the naphthyridine carboxamide core led to the development of dihydroxy pyrimidine carboxamides (**Figure 1-23**) as a new class of HIV-1 IN inhibitors showing potent nanomolar activity in the ST enzymatic assay.[134,135] The most potent compound (**36**) of this class exhibited an IC_{50} of 80 nM against ST. However, the antiviral activity was lost in the presence of serum (EC_{50} value of 5.0 μM and 59 μM in the presence of 10% and 50% FBS, respectively). The dihydroxy pyrimidine group was optimized to a pyrimidinone scaffold having coplanar chelating atoms, which were meant for coordination with the active site metals. Extensive SAR studies established the *para*-fluoro benzyl as an important group on the carboxamide moiety and the *gem*-dimethyl and oxadiazole substituents were identified as optimal groups in the 2′ position. These efforts lead to the discovery of raltegravir as the first HIV-1 IN inhibitor to be approved for clinical use in AIDS patients.[51] Recently reported 3D structures showed raltegravir in complex with the foamy virus IN and viral DNA. Raltegravir is developed by Merck Research Laboratories and is marketed as Isentress, a twice daily 400 mg oral tablet, and used in combination with other retroviral drugs. Raltegravir showed potent *in vitro* enzymatic inhibition with an IC_{50} of 15 nM in cell based assays in the presence of 50% human serum. Raltegravir is highly selective for IN and did not inhibit other Mg^{2+} dependant enzymes like HCV polymerases, RNaseH, and human α, β, and γ polymerases. Pharmacokinetic studies showed good oral bioavailability in animals (37%-45%).[136] Raltegravir is mainly eliminated through bile and urine via O-glucuronidation of the 5-hydroxyl group of the pyrimidinone ring, and is neither a substrate nor an inhibitor of cytochrome P450. In a 48-week study with 198-naive patients, raltegravir in a combination therapy showed effective reduction of viral load.[137] Although raltegravir is active against several multidrug resistant HIV strains, resistant IN has however emerged.[138,139] The most common mutations include T66I, N155H, Q148H /R, and G140S. N155H and Q148H/R are the two main mutations resulting in 10 and 25 folds of *in vivo* resistance, respectively. Double mutations like Q148H/R/G140S and N155H/E92Q resulted in about 400 and 64 folds decrease in viral susceptibility to raltegravir, respectively.[140] Another pyrimidinone carboxamide that is structurally similar to raltegravir was developed by researchers at Bristol Meyers Squibb. BMS-707035 showed potent *in vitro* activity (IC_{50} of 20 nM). It entered preclinical studies but its development was halted in Phase II clinical trials.[141]

Bicyclic Pyrimidone

Researchers at Merck also incorporated the pyrimidone scaffold into a bicyclic system (**Figure 1-24**) giving compounds with potent ST and antiviral activity.[142] Sulphone and sulfonamide groups were introduced to improve antiviral activity. Some of the representative compounds include **37** and **38**, both of which showed IC_{50} values of 7 nM in ST assay and also inhibited HIV-1 replication with potent nM EC_{50} values in cell culture.

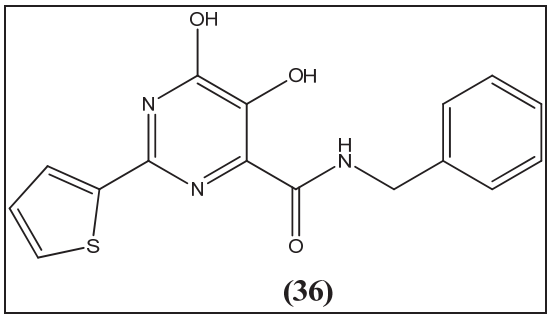

(36)

Figure 1-23. Structure of dihydroxypyrimidine carboxamide HIV-1 IN inhibitors

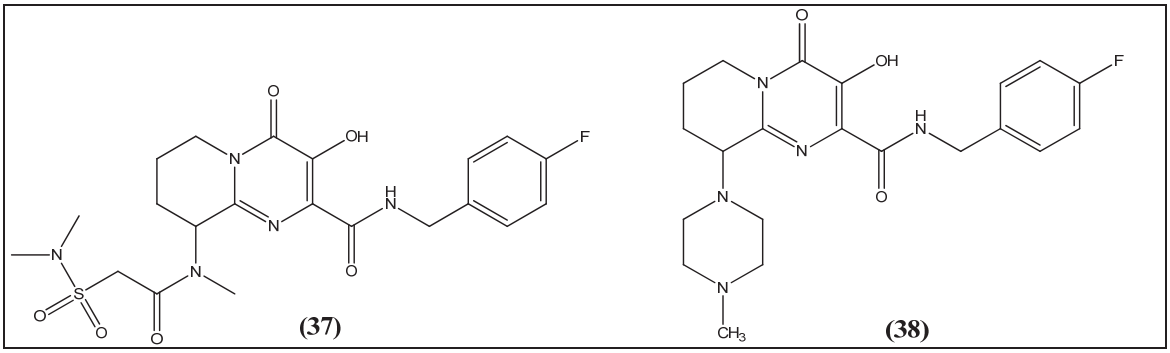

(37) **(38)**

Figure 1-24. Structures of bicyclic pyrimidone HIV-1 integrase inhibitors

4-Quinolone-3-carboxylic Acid

Quinolone carboxylic acid IN inhibitor shown in **Figure 1-25** include elvitegravir (GS-9137, compound **39**), which possesses a novel pharmacophore containing only two coplanar metal-chelating groups.[143] It has also been co-crystallized with foamy virus IN-DNA complex and is shown to bind in a similar mode to raltegravir. Elvitegravir has demonstrated potent inhibitory activity against ST with an IC_{50} value of 7.0 nM. It has also shown potent antiviral activity *in vivo* against HIV-1 mutatants resistant to other retroviral drugs.[143] Elvitegravir is also active against HIV-2 strains, SIV and murine leukemia viruses. It is developed jointly by Japan Tobacco and Gilead Sciences as the next promising IN inhibitor. Elvitegravir has entered into Phase III clinical trials in antiretroviral (ARV) treatment-experienced patients and is also undergoing a Phase II study in subjects never exposed to ARV therapy. It has been found to effectively reduce viral loads and also demonstrated good safety and pharmacokinetic profiles.[144] Elvitegravir has showed good oral bioavailability in rats (34%) and dogs (30%). It is primarily metabolized by cytochrome P450 (CYP) 3A4 while the minor pathways include glucorinidation and oxidative metabolism. Combination therapy with ritonavir, a CYP3A4 inhibitor, has shown to boost elvitegravir concentrations and thus enhancing its efficacy (a 20 fold increase in oral bioavailability) to allow for a once-daily dosing. *In vitro* and clinical data suggests overlapping resistance profile with raltegravir.[145,146] T66I, Q148H/R/K and E92Q mutations conferred resistance to both drugs while S153Y mutation resulted in greater resistance to elvitegravir. T66I and E92Q contributed the most to resistance, with 37 and 36 folds reduced susceptibility, respectively. A comparative study of the enzymatic activity of IN mutant using the dual ST and 3′-P assay showed that the 3′-P step was not significantly affected. Only Q148K mutation was found to severely impair 3′-P, while ST was defective for most of the viral mutants.

Tricyclic IN Inhibitors

Conformational constraints were applied to incorporate the exocyclic carboxamide functionality of raltegravir into a ring system. Thus the pyrazinopyrrolopyridazine class was designed as a coplanar tricyclic core for HIV-1 IN inhibitors. Examples include MK-2048 (**40**) (**Figure 1-26**), which is a promising inhibitor active against both ST and HIV-1 replication at nanomolar concentrations. It is being developed by Merck as a second generation inhibitor to circumvent resistance associated with raltegravir and elvitegravir. Although MK-2048 retained activity against viruses resistant to raltegravir and elvitegravir, a recent study has shown that mutants G118R and G118R, E138K have decreased susceptibility to MK-2048 by two and eight folds, respectively.[147]

Another promising IN inhibitor which is currently undergoing Phase II clinical trials is S/GSK1349572 (dolutegravir, compound **41**) developed by Shionogi and GlaxoSmithKline. Its structure is shown in **Figure 1-27**. It has potent ST IC_{50} of 2.7 nM. Dolutegravir has demonstrated encouraging results in clinical studies. It is being studied as an unboosted inhibitor with a once-daily dosage regimen.[148] GS-9160 (**42**), a

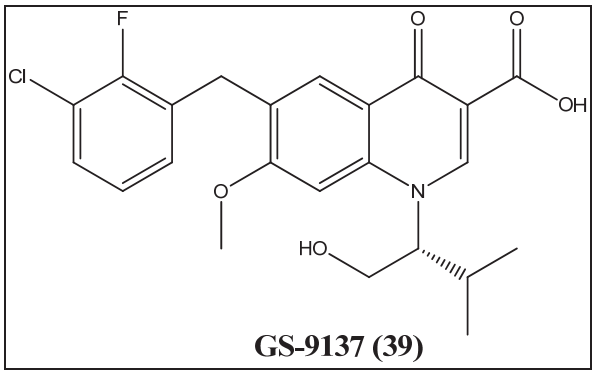

Figure 1-25. Structure of Elvitegravir (GS-9137)

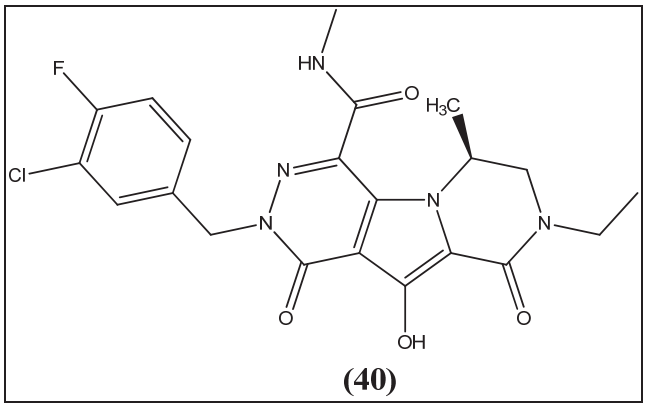

Figure 1-26. Structure of MK-2048

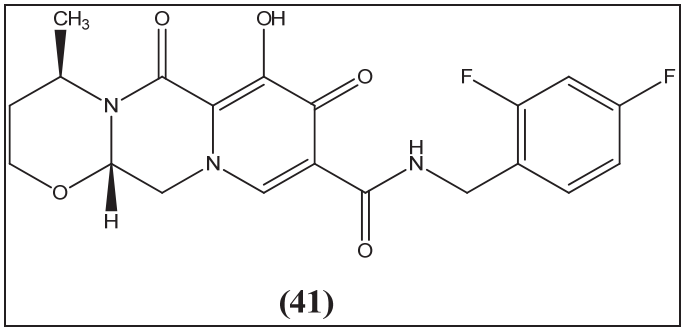

Figure 1-27. Structure of Dolutegravir (S/GSK-1349572)

tricyclic pyrroloquinolone shown in **Figure 1-28**, is a selective ST inhibitor also developed by GlaxoSmithKline. GS-9160 showed an IC_{50} value of 28 nM in ST assay and potent antiviral activity, with EC_{50} in the range 0.7 to 2.0 nM.[148] Its development was halted because of an unfavorable pharmacokinetic profile and failure to achieve effective antiviral activity.[149]

Miscellaneous Classes

Pyrrolinone derivatives (**Figure 1-29**) having coplanar chelating atoms have been reported as HIV-1 integrase inhibitors.[150] Some representative examples of this series include compounds **43**, **44** and **45**, which had ST IC_{50} values of 0.03, 0.037, and 0.08 μM, respectively. Their corresponding antiviral activities (EC_{50}) were 0.18, 0.17, and 0.24 μM, respectively.

Coumarin scaffold containing *N*-benzylcarboxamide derivatives (**Figure 1-30**) were reported as HIV-1 IN inhibitors.[151] Examples include compound **46** which showed moderate ST IC_{50} values of 7.0 μM.

Phenanthrene and anthracene β-diketo acids (**Figure 1-31**) have been reported as potent HIV-1 IN inhibitors by our laboratory.[152] Compounds **47** and **48** exhibited ST inhibitory activities of 0.38 and 0.53 μM, respectively.

Hydrazides (**Figure 1-32**) have been reported to inhibit both 3′-P and ST activities at micromolar levels.[153] Examples include compound **49** which inhibited 3′-P and ST with corresponding IC_{50}s of 6.9 and 1.6 μM.

Tetracyclines derivatives (**Figure 1-33**) have been synthesized as HIV-1 integrase inhibitors.[154] This class of compounds has displayed moderate potencies in micromolar concentrations against ST and against HIV-1 replication in cell cultures. Examples include compounds **50** and **51**.

Quinolinoyl diketo acids (**Figure 1-34**) combine the diketo acid pharmacophore with the quinolone system.[155] They were reported as selective inhibitors of the ST catalytic step. A representative compound of the series (compound **52**) had a ST IC_{50} value of 0.18 μM and antiviral activity EC_{50} of 0.17 μM.

Benzylindole scaffold (**Figure 1-35**) was attached to a diketo acid in compound (**53**).[156] It inhibited ST with an IC_{50} of 0.03 μM but it showed reduced activity against HIV-1 replication with an EC_{50} value of 2.13 μM.

Aryl sulfonamides (**Figure 1-36**) have been reported as HIV-IN inhibitors.[157,158] Examples include 2-mercaptobenzene sulfonamides (**54**) and their cyclic analogue (**55**), which inhibit ST activity at μM concentrations.

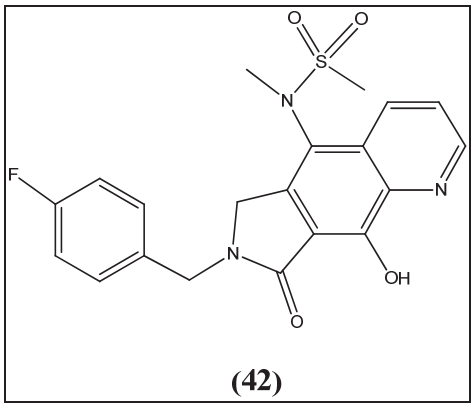

Figure 1-28. Structure of GS-9160

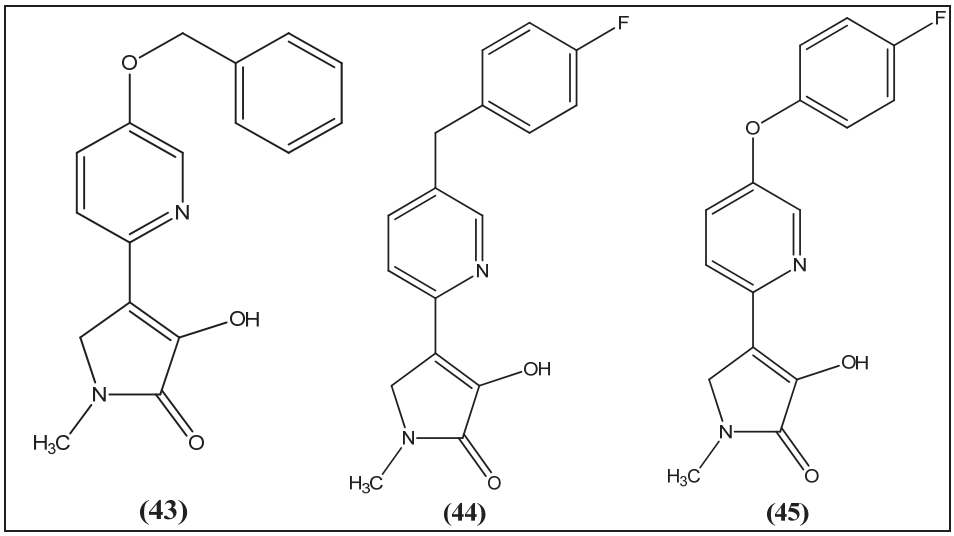

Figure 1-29. Structures of pyrrolinone HIV-1 integrase inhibitors

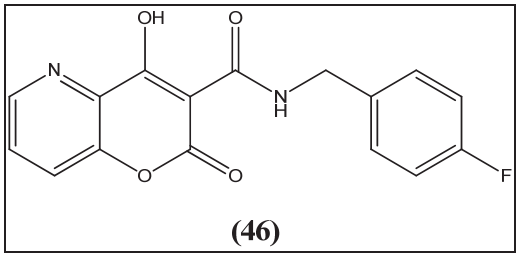

Figure 1-30. Structure of coumarin carboxamide HIV-1 integrase inhibitors

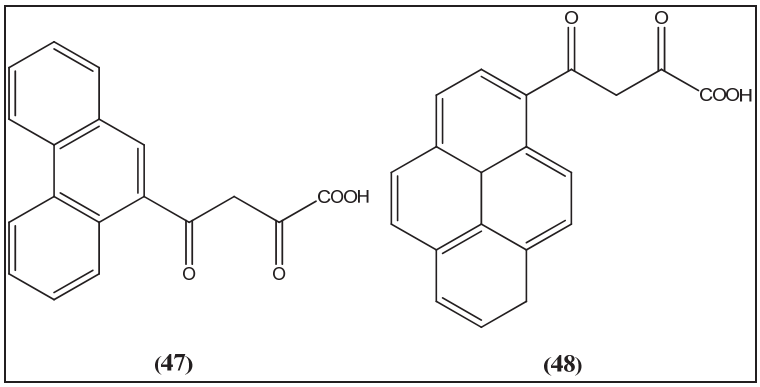

Figure 1-31. Structures of polycyclic β-diketo acid HIV-1 integrase inhibitors

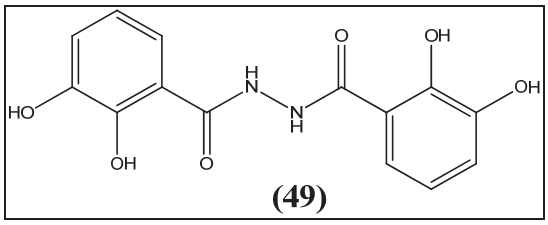

Figure 1-32. Structures of hydrazides HIV-1 integrase inhibitors

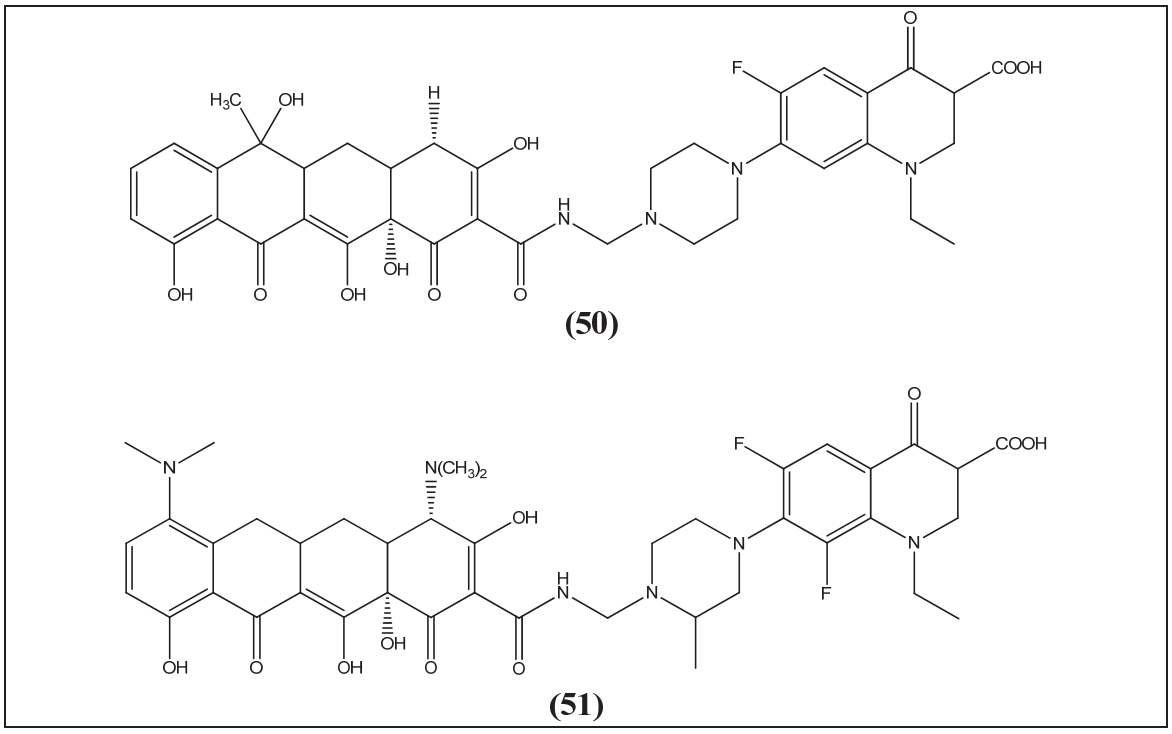

Figure 1-33. Structures of tetracyclines HIV-1 integrase inhibitors

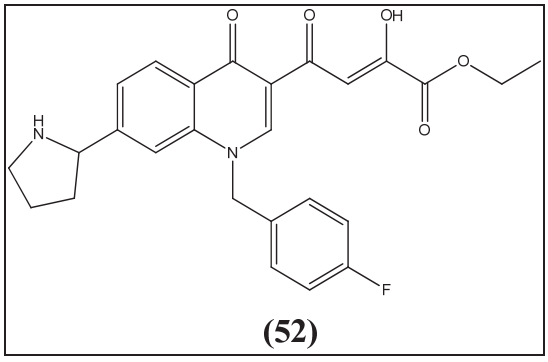

Figure 1-34. Structures of quinolinoyl diketo acids HIV-1 integrase inhibitors

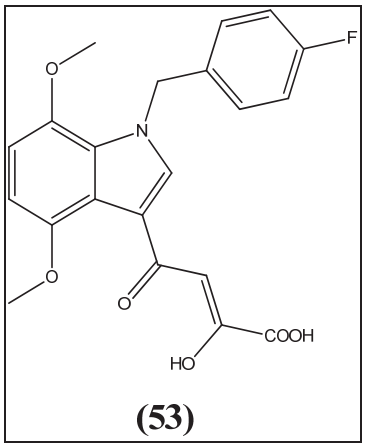

(53)

Figure 1-35. Structure of benzylindole HIV-1 integrase inhibitors

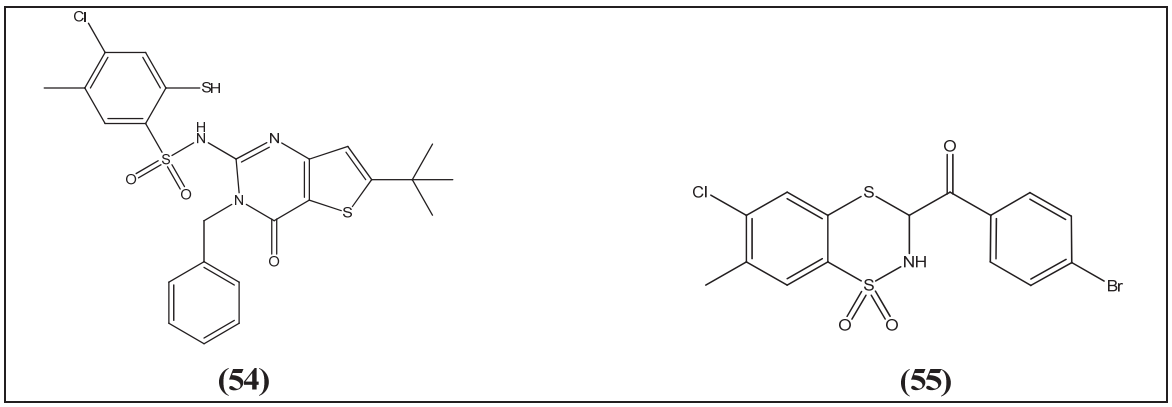

(54) **(55)**

Figure 1-36. Structures of aryl sulfonamides HIV-1 integrase inhibitors

Recently Reported HIV-1 IN Inhibitors

N-1 aryl or benzyl substituted 5-hydroxyquinolone-3-carboxylic acids have been reported as a new series of HIV-1 IN inhibitors.[159] The most active compound (**56, Figure 1-37**) inhibited wild type HIV-1 with an EC_{50} value of 3.1 μM in C8166 cells.

On the basis of the C-2 symmetry present in the naphthyridinone core, a new series of related IN inhibitors have been designed and synthesized.[160] Combining the A/B naphthyridinone type analogs into a single compound inhibited ST in low nM concentrations and significantly improved their antiviral activities. One of the most active compounds (**Figure 1-38**) of the series (**57**) inhibited ST with an IC_{50} of 8 nM and also showed potent antiviral activity, inhibiting HIV-1 replication with an EC_{50} of 3.0 nM.

Ethyl malonate amides functionality has been discovered to inhibit HIV-1 IN.[161] One of the most active compounds of the series (**58**) shown in **Figure 1-39** was active against ST with an IC_{50} of 2.0 μM.

Bicyclic pyrimidinones and 4,5-dihydroxy-1H-isoindole-1,3(2H)-diones classes of IN inhibitors were combined to design tricyclic hydroxy-1H-pyrrolopyridine-trione as a novel class of HIV-1 IN inhibitors.[162] The most active compound (**59**) of the series shown in **Figure 1-40** selectively inhibited ST with an IC_{50} of 9.1 μM. Compound **59** was also shown to be less susceptible to the resistance producing effects of G140S/Q148H, N155H and Y143R mutations than raltegravir.

In another study, a series of caffeoyl-anilides have been reported as dual inhibitors of HIV-1 IN and CCR5 co-receptors.[163] Compound (**60, Figure 1-41**) showed ST IC_{50} of 44.6 μM and antiviral EC_{50} value of 0.90 μM in cell culture.

2-hydroxyisoquinoline-1,3(2H,4H)-diones (**Figure 1-42)** were reported as inhibitors of HIV-1 RT ribonuclease (RNase) H domain and HIV-1 IN.[164] Compound **61** inhibited ST with an IC_{50} of 4.77 μM and was also active against HIV-1 RNase H with an IC_{50} of 61 nM. In another related publication[165] compound **62** showed IC_{50}s of 1.3 μM and 33.6 μM against ST and RT RNase H, respectively.

N-Hydroxydihydronaphthyridinones has been designed and synthesized as potent orally available tricyclic HIV-1 IN inhibitors.[166] Compound **63** shown in **Figure 1-43** inhibited ST with an IC_{50} of 2.9 nM, displayed potent antiviral activity with an EC_{50} of 1.0 nM and, also showed good pharmacokinetic properties.

6-substituted quinolonyl diketo acid HIV-1 IN inhibitors have been reported.[167] Compound **64** shown in **Figure 1-44** was active against ST with an IC_{50} of 50 nM and inhibited HIV-1 replication with EC_{50} of 1.0 μM in TZM-bl cells.

3-Hydroxypyrimidine-2,4-diones were reported as inhibitors of HIV-1 IN and RT.[168] Compound **65** shown in **Figure 1-45** exhibited IC_{50} of 3.5 μM against ST and inhibited HIV-1 replication with EC_{50} of 24 nM. Raltegravir resistant mutants

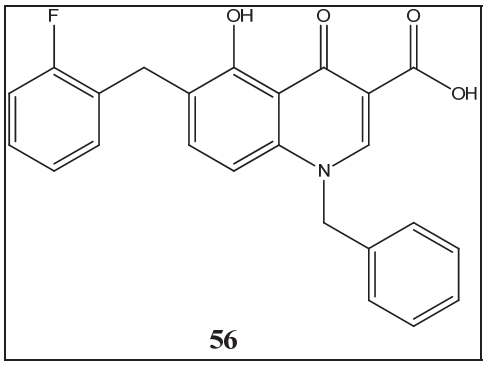

Figure 1-37. Structure of 5-hydroxylquinolone-3-carboxylic acids HIV-1 integrase inhibitors

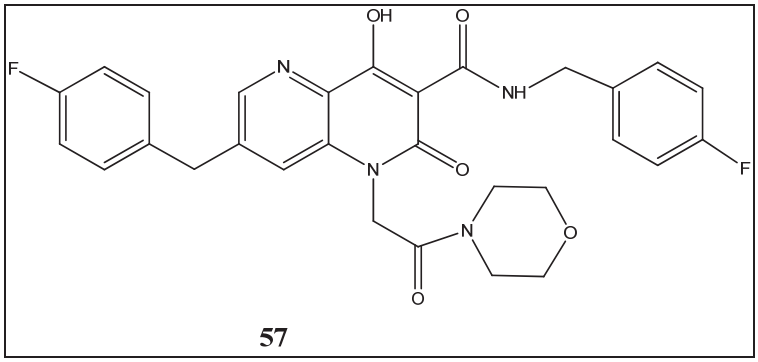

Figure 1-38. Structure of naphthyridinone HIV-1 integrase inhibitors

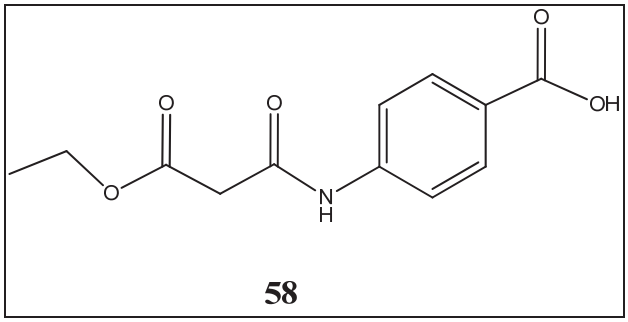

Figure 1-39. Structure of ethyl malonate amide HIV-1 integrase inhibitors

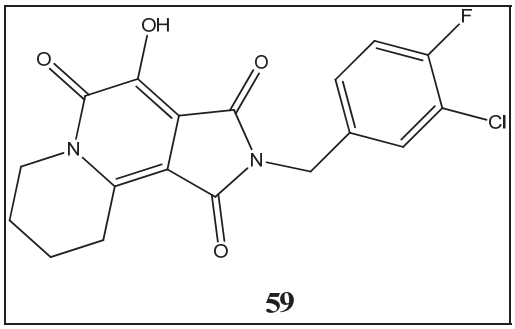

Figure 1-40. Structure of hydroxy-1H-pyrrolopyridine-trione HIV-1 integrase inhibitors

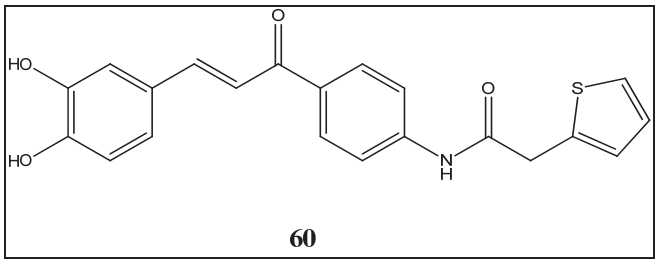

Figure 1-41. Structure of caffeoyl-anilides HIV-1 integrase inhibitors

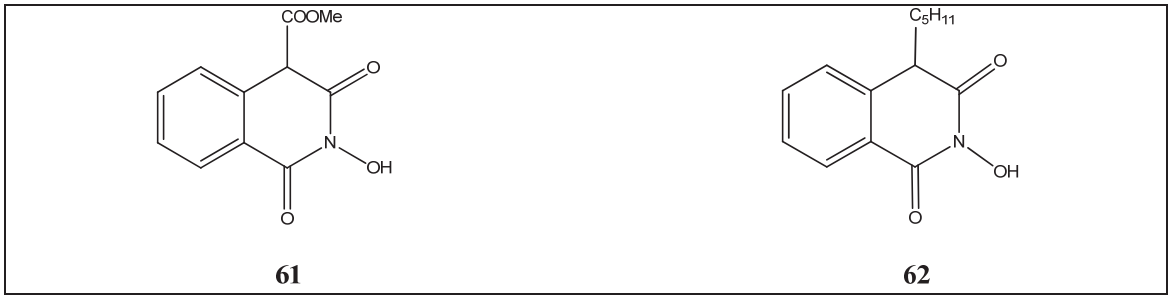

Figure 1-42. Structure of 2-hydroxyisoquinoline-1,3(2H,4H)-diones HIV-1 integrase inhibitors

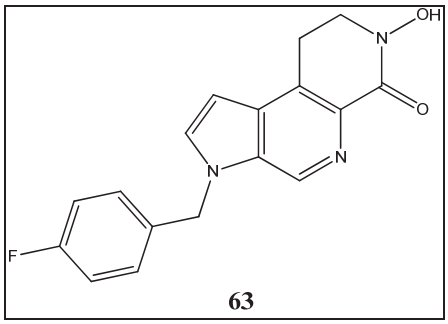

63

Figure 1-43. Structure of *N*-hydroxy-dihydronaphthyridinones HIV-1 integrase inhibitors

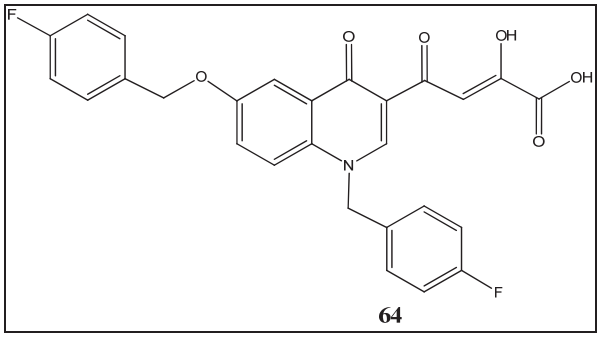

64

Figure 1-44. Structure of 6-substituted quinolonyl diketo acids HIV-1 integrase inhibitors

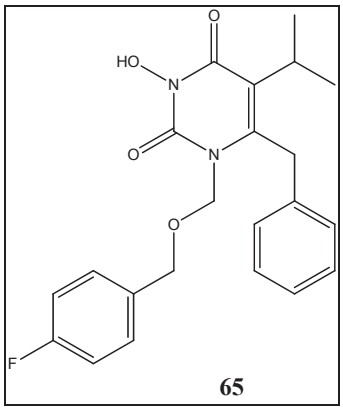

65

Figure 1-45. Structure of 3-hydroxypyrimidine-2,4-diones HIV-1 integrase inhibitors

showed lower resistance to compound **65** probably because of its anti-reverse transcriptase activity.

Substituted benzyl indole diketo acids have been designed and synthesized as HIV-1 IN inhibitors.[169] One representative compound of the series (**66**) shown in **Figure 1-46** had potent IC_{50} of 6 nM against ST step and moderate antiviral activity inhibiting HIV-1 replication with an EC_{50} of 8.5 μM.

A new series of naphthyridinone and quinolone carboxylic acid HIV-1 integrase inhibitors were synthesized to improve their microsomal stability.[170] Compound **67** (**Figure 1-47)** had an EC_{50} of 9.9 nM and microsomal stability (% remaining) of 97%.

2-Pyrrolinones were discovered from a pharmacophore model and synthesized as HIV-1 IN inhibitors.[171] Compound **68** shown in **Figure 1-48** inhibited both ST (IC_{50} = 40 μM) in assays and HIV-1 replication (EC_{50} = 0.31 μM) in TZM-bl cells.

Azaindole *N*-methyl hydroxamic acids have been reported as potent HIV-1 IN inhibitors.[172] Compound **69** shown in **Figure 1-49** demonstrated an IC_{50} of 382 nM against ST and inhibited HIV-1 replication with an EC_{50} of 29 nM in CEM-SS cells.

Pyrazolone was discovered as a novel scaffold for IN inhibition inhibiting ST with low μM concentrations.[173] The most active compound (**70**) of the series shown in **Figure 1-50** inhibited ST with an IC_{50} of 3.0 μM.

A series of bicyclic inhibitors possessing the azoles, thiazole, and imidazole as metal chelating moieties (**Figure 1-51)** were synthesized as HIV-1 IN inhibitors. The most promising compound (**71**) had an EC_{50} of 6 nM.[174]

2-Pyrrolidinyl-*N*-methyl pyrimidones (**Figure 1-52)** were explored and developed as orally bioavailable potent HIV-1 IN inhibitors.[175] Compound **72** was highly active against viral replication (CIC_{95} = 5 nM) and also showed a good pharmacokinetic profile.

2-Arylnaphthalenediols and polyhydroxylated compounds were reported as HIV-1 IN inhibitors.[176] One of the most promising compounds (**73**) shown in **Figure 1-53** had an IC_{50} of 0.85 μM against ST and an EC_{50} of 3.0 μM in MT-4 cells.

Structure-activity relationships studies on benzylindolediketo acids were developed by investigation of the hydrophobic region.[177] One of the most active compounds of the series (**74**) shown in **Figure 1-54** had an IC_{50} of 30 nM against ST and an EC_{50} of 0.43 μM against HIV-1 in MT-4 cells.

A series of 2,3-dihydroxybenzamide (**Figure 1-55)** containing compound (**75**) was reported to inhibit ST and LEDGF with IC_{50}s of 19 μM and 8 μM, respectively.[178]

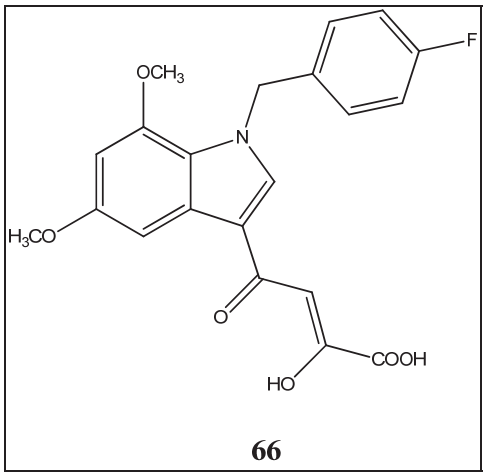

66

Figure 1-46. Structure of indole diketo acids HIV-1 integrase inhibitors

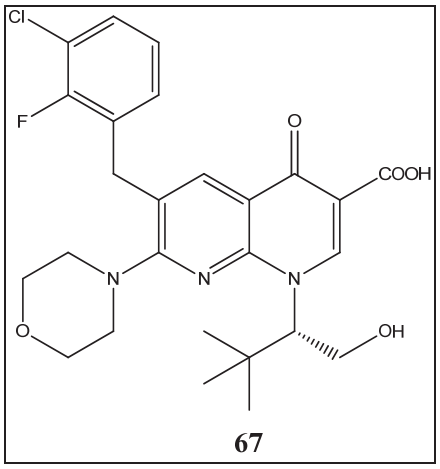

67

Figure 1-47. Structure of quinolone carboxylic acid HIV-1 integrase inhibitors

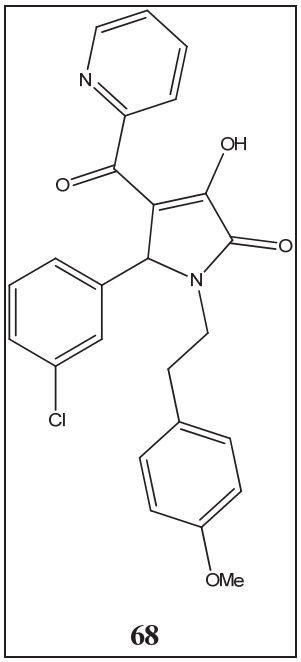

68

Figure 1-48. Structure of 2-pyrrolinones HIV-1 integrase inhibitors

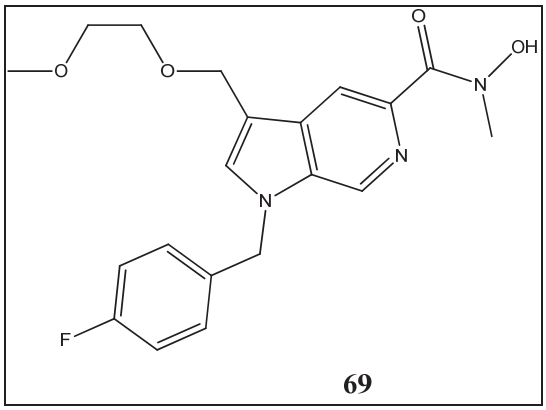

69

Figure 1-49. Structure of azaindole *N*-methyl hydroxamic acids HIV-1 integrase inhibitors

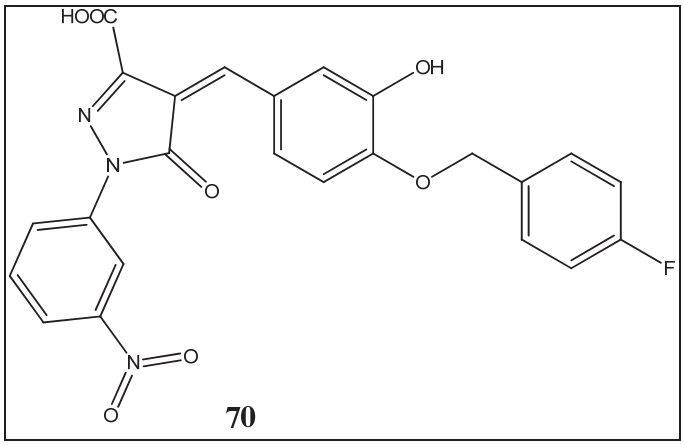

Figure 1-50. Structure of pyrazolone HIV-1 integrase inhibitors

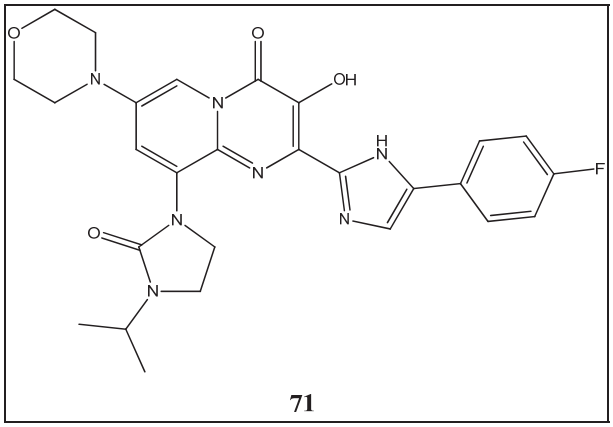

Figure 1-51. Structure of bicyclic pyrazole containing HIV-1 integrase inhibitors

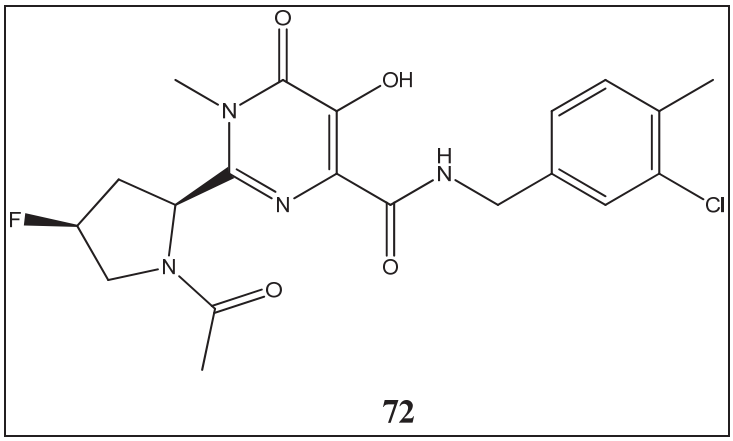

72

Figure 1-52. Structure of 2-pyrrolidinyl-*N*-methyl pyrimidones HIV-1 integrase inhibitors

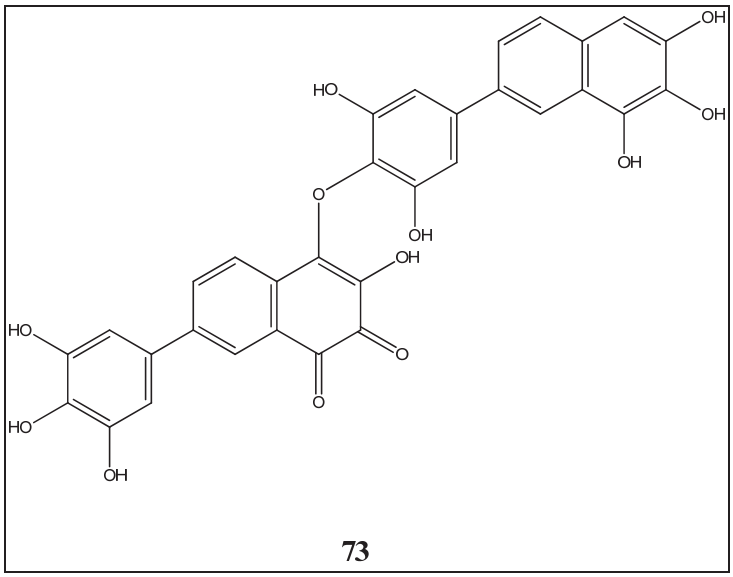

73

Figure 1-53. Structure of 2-arylnaphthalenediols HIV-1 integrase inhibitors

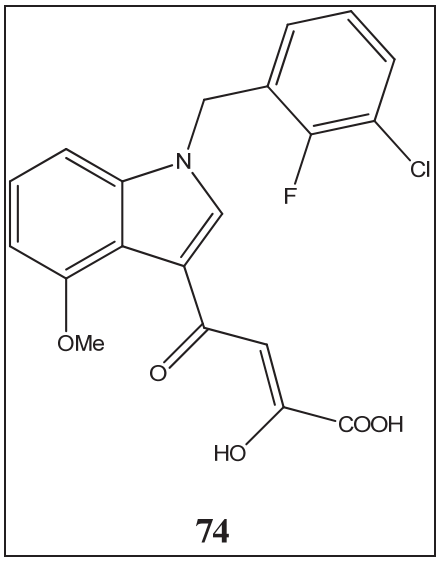

Figure 1-54. Structure of benzylindole diketo acids HIV-1 integrase inhibitors

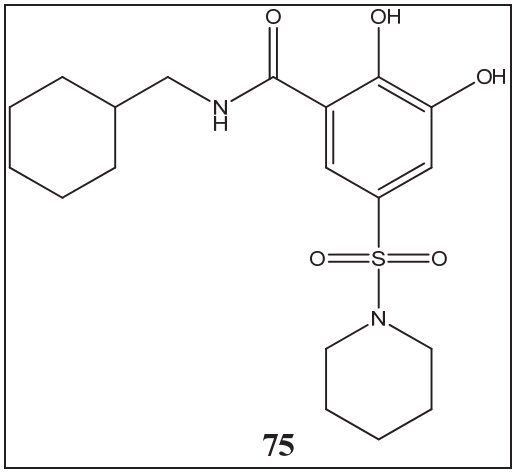

Figure 1-55. Structure of 2,3-dihydroxybenzamide HIV-1 integrase inhibitors

CHAPTER 2. RESEARCH OBJECTIVE

Synthesis of HIV-1 Integrase Inhibitors

The emergence of multi-drug resistance and failure of HAART therapy, which targets primarily the RT and PR, to eliminate HIV from patient demand inhibition of other steps essential for viral survival and replication. In this regard, HIV-1 IN, which is crucial enzyme for viral replication, has emerged as a promising target for the development of anti-retroviral drugs.

Although highly promising IN inhibitors have been developed, raltegravir is the only IN inhibitor approved by the FDA. Emergence of resistance against raltegravir and the clinically advanced drug candidate, elvitegravir necessitates the development of novel scaffolds targeting IN. In this study, covered in Chapter 3, a novel series of 3-keto salicylic acid chalcones with diverse structural features were synthesized and biologically evaluated as promising integrase inhibitors. Few analogs of the series showed good activities against ST in *in vitro* enzymatic assay and were also equally potent against HIV-1 replication in cell cultures.

In Chapter 4, the chalcone scaffold was modified to a structurally related amide to synthesize a new series of compounds. A vast majority of potent IN inhibitors, including raltegravir, have an amide functionality which gives a conformationally favorable orientation to the halo benzyl group present in these compounds. In this study, 10 new amide analogs were synthesized and evaluated as HIV-1 integrase inhibitors. A couple of amide derivatives showed good *in vitro* potencies against ST step and displayed moderate anti-viral activities in cell cultures. These compounds hold promise for further optimization to obtain more potent HIV-1 IN inhibitors. In the search of novel scaffolds for integrase inhibition, some structurally diverse compounds containing metal chelating atoms were also synthesized and tested for IN inhibitory activity.

β-Diketo acid analogs were the first representative compounds that entered clinical trials. Previously, our laboratory has reported 5(H)-phenanthridin-6-one diketo acid as a new class of HIV-1 integrase inhibitors. In Chapter 5, 10 analogs of this series having electron withdrawing groups on the phenanthrene ring were synthesized and tested as HIV-1 integrase inhibitors. Most of the analogs showed good *in vitro* ST and 3′-P activities and selected compounds when tested for their antiviral activity, showed moderate inhibition of HIV-1 replication. Modeling studies, described in Chapter 6, suggest that these compounds could be investigated against viral mutants resistant to currently available IN inhibitors.

Computational Studies on HIV-1 Integrase Inhibitors

Despite two decades of tremendous effort leading to promising IN inhibitors their binding modes, until recently, remained elusive. The absence of a complete DNA-bound

crystal structure has presented significant challenge to the structure-based design of IN inhibitors. Although X-ray structures of individual human HIV domains and their combinations have been reported, the absence of a 3D structure of HIV-1 IN and viral DNA along with the two-divalent metals in the active site make the structural information hitherto available limited and far from reality. To address this limitation, a homology model of HIV-1 integrase in complex with the viral DNA was constructed, by our collaborators at the Oak Ridge National Laboratory. The homology model was built based on the recently reported crystal structure of the foamy virus IN-DNA complex (PDB 3L2T and 3L2U).

In Chapter 6, a detailed computational study was undertaken to elucidate the binding modes of approved IN inhibitor raltegravir, elvitegravir, and our synthesized IN inhibitors. To determine the stereo-electronic features important for ligand binding, in the absence of a crystal structure of a full-length HIV-1 IN-DNA complex, a ligand-based approach was first employed. A PHASE pharmacophore model of the synthesized chalcone and amide derivatives was developed to determine their bio-active conformations which were then used for deriving 3D-QSAR CoMFA and CoMSIA models. The resulting QSAR models had limited predictive ability probably because of the narrow range of activities of compounds in the dataset. Next, with the goal of developing a statistically significant and predictive model capable of estimating potent compounds, a comprehensive 3D-QSAR CoMFA and CoMSIA study was undertaken. A data set of 103 compounds including our synthesized chalcone and structurally related amide IN inhibitors, raltegravir and elvitegravir and their analogs reported in literature were used for the 3D-QSAR study. Atom-fit alignments and MM-GBSA validated docking-based conformations were used for the 3D-QSAR modeling. This study has yielded statistically significant models that could be further optimized to predict the activities of novel related HIV-1 IN inhibitors. Binding free energies of the inhibitors were also derived using the Linear Interaction Approximation (LIA) calculations, and the energy parameters were then used for building a LIA QSAR model. The resulting energy contributions were also studied to gain insights into the binding modes of raltegravir and elvitegravir and to validate the binding conformations of our synthesized IN inhibitors. Another objective of the computational studies was to use structure-based design to rationally guide the synthesis of potential 3-ketosalicylic acid amides IN inhibitors. RACHEL, a drug optimization module was used to design compounds with an aim of having desired interaction with the enzyme. Finally, to determine the binding modes of our synthesized phenanthrene derivatives, docking studies were performed and their poses evaluated.

CHAPTER 3. SYNTHESIS AND BIOLOGICAL EVALUATION OF 3-KETO SALICYLIC ACID CHALCONES AS NOVEL HIV-1 INTEGRASE INHIBITORS*

Introduction

β-Diketo acid derivatives and bioisosteres as represented by S-1360 constitute the first integrase inhibitor class to have entered clinical trials. Naphthyridine carboxamides such as L-870,810 have also advanced to clinical trials as have novel quinolone carboxylic acids such as GS-9137 (elvitegravir) which is currently undergoing Phase III clinical trials. Inspite of over two decades of extensive research leading to promising IN inhibitors, hitherto only one IN inhibitor, raltegravir, a pyrimidinone carboxamide, has been approved for clinical use. Moreover, emergence of resistance against raltegravir due to viral mutations usually T66I, N155H, Q148H/R and E92Q, demands exploration of novel scaffolds for IN inhibition in the treatment of HIV infection.[138,139]

In this chapter, is reported the synthesis and biological evaluation of chalcone derivatives having 3-keto salicylic acid moieties as a new class of IN inhibitors. We have undertaken substantial analog synthesis and carried out systematic exploration of the structure activity relationship. It is established that potent IN inhibitors have two common structural features viz., a hydrophobic benzyl group and a chelating motif capable of binding two Mg^{2+} ions. With a 3-keto salicylic acid as chelating pharmacophoric moiety, diverse structural modifications of the hydrophobic aromatic feature were made to synthesize 52 novel chalcone derivatives.

Chemistry

In the present study, a novel series of IN inhibitors was discovered based on modification of the diketo acid pharmacophoric group as represented by structure III (**Figure 3-1**). The 2-position OH and 3-postion keto groups together mimic the keto-enol tautomer of the β-diketo group. Attachment of the carboxylic acid at the 1-position gave the 3-keto salicylic acid moiety of III, intended to interact with IN similar to the β-diketo acids. A styryl group was attached to the 3-position keto group to create chalcones (IV) (**Figure 3-1**), the type of which have not yet been investigated as HIV IN inhibitors to our knowledge. The chalcone moiety was also reduced to give an ethylene linker.

The synthesis of target chalcones was performed according to reaction (**Scheme 3-1**). 5-substituted salicylic acid (X = COOH) starting materials **76 a-e** were first acetylated with acetic anhydride and concentrated sulfuric acid. The acetylated

* Adapted with permission. Sharma, H.; Patil, S.; Sanchez, T. W.; Neamati, N.; Schinazi, R. F.; Buolamwini, J. K. Synthesis, biological evaluation and 3D-QSAR studies of 3-keto salicylic acid chalcones and related amides as novel HIV-1 integrase inhibitors. *Bioorg. Med. Chem.* **2011**, 19, 2030-2045.[179]

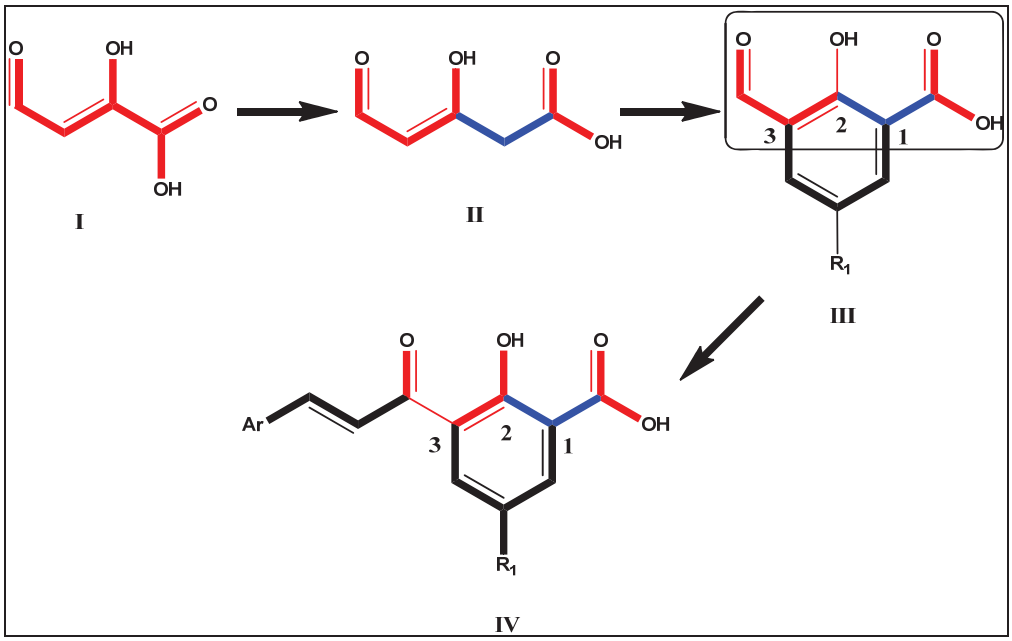

Figure 3-1. Design of 3-keto salicylic acid chalcone as HIV-1 integrase inhibitors

Scheme 3-1. Synthesis of compounds 61-108

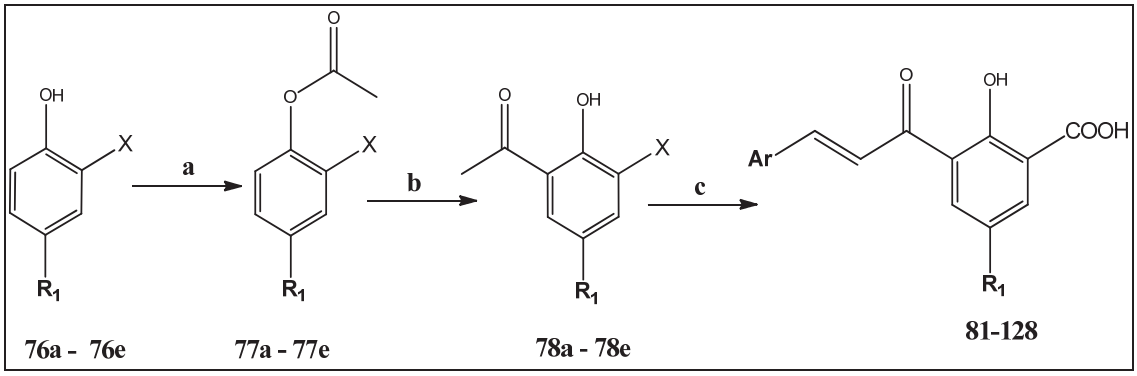

Reagents and conditions: (a) Ac_2O, H_2SO_4, 20 min; yield 75-88%(b) $AlCl_3$, 160 °C, 3 h; yield 26-34% (c) ArCHO, NaOH, EtOH, rt, 1-5 days; yields 15-74%.

intermediates **77 a-e** were then subjected to Fries rearrangement reaction using anhydrous aluminum chloride and heating at 160 °C to transfer the acetyl group from the 2-position oxygen to the 3-position to yield 3-acetyl salicylic acid intermediates **78 a-e**. The next step involved a Claisen-Schmidt condensation reaction of intermediate **78** with various aryl aldehydes at room temperature using NaOH to obtain the target chalcones **81**-**128**.[180] The synthesis of compounds **129** and **130** was achieved following **Scheme 3-2** by using appropriate aromatic aldehydes and commercially available 1-(5-bromo-2-hydroxy-3-nitro-phenyl)ethanone starting material**.** To determine the importance of the α,β-unsaturated bond (chalcone scaffold) to IN inhibitory activity, the synthesis of compound **131** and **132** was undertaken by reduction of compounds **81** and **107**, respectively, by Pd/C-catalyzed hydrogenation (**Scheme 3-3**).

Results and Discussions

Structure-Activity Relationships

After synthesis, target compounds were tested for integrase inhibitory activity to assess their potency and study the SAR. In general, the compounds behaved as typical diketo acid IN inhibitors, being selective against the ST step (**Table 3-1**) compared to 3′-P. The selected potent compounds of the series were then tested for their ability to inhibit HIV replication in cell culture. All the biological studies were performed by collaborators.

Substitution on aromatic ring A. Compound **131**, 2-hydroxy-3-(3-phenyl-propyl)-benzoic acid, in which salicylic acid is connected to an unsubstituted phenyl ring B by a propylene linker exhibited only weak inhibitory activity with IC_{50} of >100 μM for 3′-P and 91 μM for ST. Modification to an α,β-unsaturated linker along with substitution with Br at R_1 (compound **81** used as reference) demonstrated a significant increase in both activity and ST selectivity (IC_{50} 25 μM for ST vs. IC_{50} 75 μM for 3′-P). With the presence of bromine substituent at R_1 on aromatic ring A being shown to be important for activity, chlorine and fluorine substituents were also investigated. Compounds with a Br substituent were the most active followed by F which was a little better than Cl. To determine the effect of hydrophobic interactions, a methyl group was substituted for the halogens at R_1 (see compound **128**). Compound **128** was found to be 13 times less active than the corresponding Br-substituted compound **96**. Since Br and a methyl group are similar in steric terms, this implies that it is not the hydrophobic effect of the halogen, but possibly the electronegativity and/or polarizability that might be the dominant effect. The 3-keto salicylic acid pharmacophore was designed to coordinate with Mg^{2+}. To test this hypothesis, the carboxylic acid was replaced with a NO_2 functionality (**129**, **130**) and this modification diminished HIV inhibitory activity. Replacement of the carboxyl group with another polar group but with weaker coordination ability, CN (compound **127**) also resulted in reduced inhibitory activity. This probably indicates that the formal negative charge of the free ionizable acidic moiety, that would chelate better with the metal ion, is

Scheme 3-2. Synthesis of compounds 129 and 130

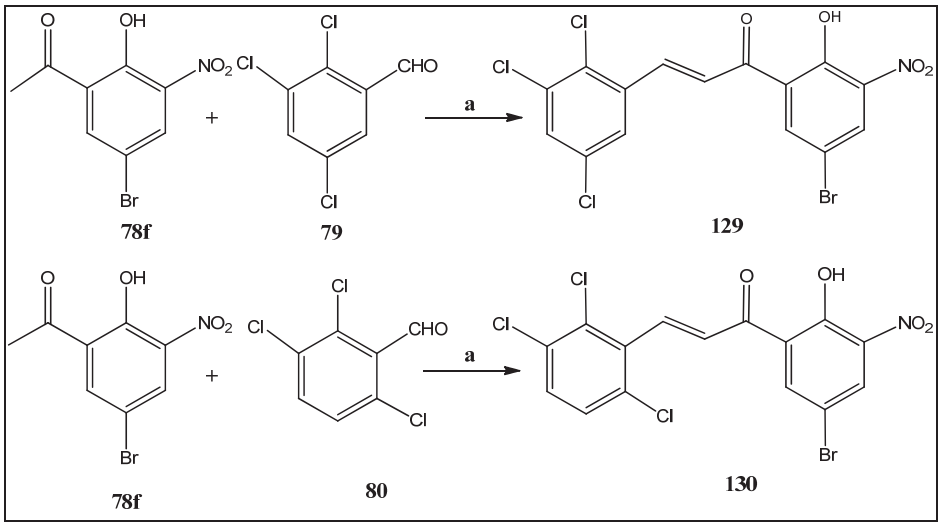

Reagents and conditions: (a) ArCHO, NaOH, EtOH, rt; yields 58-65%.

Scheme 3-3. Synthesis of compounds 131 and 132

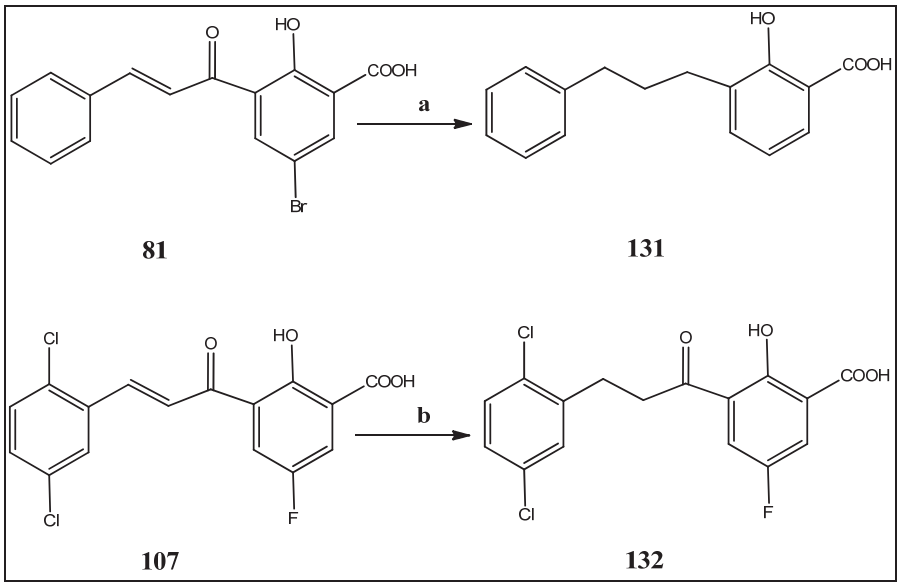

Reagents and conditions: (a) H_2, Pd/C (10 mol%), methanol 10 h (b) H_2, Pd/C (10 mol%), methanol 2 h; yields 43-72%.

Table 3-1. Structure and HIV-1 integrase inhibitory activities of chalcones synthesized

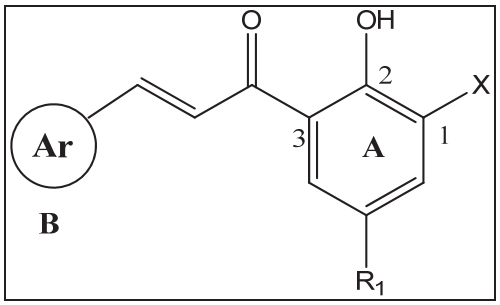

Cpd.	Ar	X	R_1	Activity IC_{50} (μM)	
				3′-P[a]	ST[b]
81	Ph	COOH	Br	75 ± 14	25 ± 5
82	2-Cl-Ph	COOH	Br	52 ± 13	14 ± 4
83	2-F-Ph	COOH	Br	74 ± 25	32 ± 3
84	3-Cl-Ph	COOH	Br	45 ± 10	9 ± 3
85	4-Cl-Ph	COOH	Br	81 ± 28	12 ± 1
86	4-Br-Ph	COOH	Br	11 ± 4	5 ± 2
87	4-I-Ph	COOH	Br	69	35
88	2,4-di-Cl-Ph	COOH	Br	28 ± 12	7 ± 4
89	2,3-di-Cl-Ph	COOH	Br	58 ± 13	19 ± 11
90	2,3-di-MeO-Ph	COOH	Br	62 ± 14	34 ± 6
91	2,3,4-tri-MeO-Ph	COOH	Br	85 ± 20	51 ± 16
92	2,5-di-Cl-Ph	COOH	Br	47 ± 14	18 ± 4
93	2,6-di-Cl-Ph	COOH	Br	52 ± 12	16 ± 8
94	3,4-di-Cl-Ph	COOH	Br	27 ± 11	14 ± 4
95	2,3,5-tri-Cl-Ph	COOH	Br	20 ± 12	13 ± 5
96	2,3,6-tri-Cl-Ph	COOH	Br	23 ± 12	<3.7
97	4-Cl-Ph	COOH	Cl	85 ± 13	53 ± 21
98	2,4-di-Cl-Ph	COOH	Cl	>100	>100
99	2,3-di-Cl-Ph	COOH	Cl	100	92 ± 14
100	2,5-di-Cl-Ph	COOH	Cl	75	25
101	2,3,5-tri-Cl-Ph	COOH	Cl	55 ± 40	17 ± 3
102	2,3,6-tri-Cl-Ph	COOH	Cl	77 ± 20	30 ± 5
103	3,4-di-Cl-Ph	COOH	Cl	87 ± 13	41 ± 9
104	4-Cl-Ph	COOH	F	36 ± 13	17 ±3
105	2,4-di-Cl-Ph	COOH	F	52 ± 13	24 ± 9
106	2,3-di-Cl-Ph	COOH	F	55 ± 18	30 ± 9
107	2,5-di-Cl-Ph	COOH	F	50	29 ± 6
108	2,3,5-tri-Cl-Ph	COOH	F	33 ± 14	15 ± 4
109	2,3,6-tri-Cl-Ph	COOH	F	82 ± 16	39 ± 6
110	3,5-di-Me-Ph	COOH	Br	>100	58

Table 3-1. (Continued)

Cpd.	Ar	X	R_1	Activity IC_{50} (μM)	
				3′-P[a]	ST[b]
111	2-Cl-3,4-di-MeO-Ph	COOH	Br	>100	76
112	6-F-3,4-di-MeO-Ph	COOH	Br	>100	76
113	2-BzO-Ph	COOH	Br	21	9
114	3-(4-Cl-PhO)-Ph	COOH	Br	25	18
115	4-(4-Cl-PhO)-Ph	COOH	Br	22	16
116	3-thienyl	COOH	Br	30 ± 12	18 ± 1
117	3-(cyclopentyloxy)-Ph	COOH	Br	100	55
118	3-(2-OEt-naphthyl)	COOH	Br	92	46
119	5-MeO-naphthyl	COOH	Br	54	54 ± 25
120	5-benzothiophene	COOH	Br	23 ± 3	11 ± 1
121	2-furan-2-yl-Ph	COOH	Br	>100	16 ± 2
122	3-Cl-4,5-methylenedioxy-Ph	COOH	Br	79	63
123	3-OCF_3-Ph	COOH	Br	>100	52
124	3-NO_2-Ph	COOH	Br	49 ± 8	32 ± 6
125	3-Br-Ph	COOH	Br	19 ± 4	18 ± 1
126	3-F-Ph	COOH	Br	71 ± 1	59 ± 2
127	2,3,6-tri-Cl-Ph	CN	Br	>100	44 ± 2
128	2,3,6-tri-Cl-Ph	COOH	CH_3	>100	50 ± 9
129	2,3,5-tri-Cl-Ph	NO_2	Br	>333	68 ± 5
130	2,3,6-tri-Cl-Ph	NO_2	Br	36 ± 4	21 ± 3
131	N/A[c]	N/A	N/A	>100	91
132	N/A	N/A	N/A	>100	57 ± 5
S-1360	N/A	N/A	N/A	11 ± 2	0.6 ± 0.1

[a] 3′-P represents 3′-procesing; [b] ST represents strand transfer; [c] N/A means not applicable.

required for potent activity, supporting the hypothesis. Of course a chelation study will have to be done to confirm this.

Substitution on aromatic ring B. Various groups were substituted on aromatic B to further explore the SAR. The presence of halogens on phenyl ring B produced noticeable improvements in potency based on the type, number and position on the aromatic ring. Fluorine substitution in the ortho and meta positions (compounds **83** and **126**) diminished activity, as did iodine substitution at the para position (compound **87**). However, substitution with Cl enhanced activity specifically for ST in all the three positions (compounds **82**, **84** and **85**). Interestingly, compounds **125** and **86** with *m*-Br and *p*-Br substituent, respectively, were potent against both catalytic steps (compound **84** showed IC_{50} of 5 μM against ST activity and 11 μM against 3′-P). The 2,3,6-trichloro-substituted compound (**96**) was the most active, with IC_{50} of about ~ 4 μM against the ST reaction. This suggests a binding site pocket with high affinity for halogenated phenyl rings. This might be the site that binds the fluorobenzyl group common in potent IN inhibitors like the clinically used drug raltegravir (**Figure 1-8**). We next turned our attention to examining the following.

(1) *The effect of a bulky aryl B groups*: benzyloxy and chloro substituted phenoxy in ortho, meta and para positions of phenyl ring B enhanced activity for both 3′-P and ST steps; whereas an *ortho*-furan substituent (compound **121**) increased the inhibitory potency against ST but decreased potency against 3′-P; the increase in activity was most pronounced for the *o*-benzyloxy substituent (compound **123**), with the 3′-P and ST IC_{50} values lowered to 21 and 9 μM, respectively, compared to corresponding values of 75 and 25 μM for the parent phenyl compound **81**.

(2) *The effects of electron donating or withdrawing groups*: introduction of electron donating groups such as methoxy, methyl and cyclopentoxy (compounds **90**, **110** and **117**) decreased integrase inhibitory activity; and, increasing the number of electron donating groups resulted in further decrease in activity (compare compounds **90** and **91**). Introduction of strong electron withdrawing groups such as trifluoromethyl and nitro also diminished activity as shown by compounds **123** and **124**, respectively.

(3) Boisosteric replacement of phenyl ring B with polycyclic and heteroaromatic rings: replacement of phenyl with thiophene or benzothiophene, compounds **116** and **120**, respectively, improved activity. Naphthalene derivatives on the other hand decreased activity (compounds **118** and **119**). It thus appears that heteroaromatic B rings may improve integrase inhibitory activity.

Reduction of the α,β-unsaturated double bond of the chalcones. To explore the importance of the α,β-unsaturated bond of the chalcones on inhibitory activity, we reduced it to a single bond. Our first attempt at this was with compound **96**, but reduction also led to a loss of the Br substituent. However, reduction (**Scheme 3-3**) of analog **107**, having a fluorine substituent, which is not as good a leaving group as Br, was successful

in achieving our objective. The reduction product, compound **132**, was less active (ST IC_{50} of 57 μM) than the unsaturated analog, showing that the reduction of the double bond in the chalcone template is detrimental to activity.

Inhibition of HIV Replication in Cell Culture

To evaluate the potential of these new IN inhibitors as antiviral agents, five potent analogs were tested for the ability to inhibit HIV-1 replication in primary human peripheral blood mononuclear cells (PBMCs) infected with the virus. The toxicity of the compounds was also tested against PBMC and human CEM lymphoblastic leukemia cells. All four compounds tested inhibited HIV replication (**Table 3-2**). The most potent compounds, **96** and **86** showed comparable EC_{50} values of 7.3 and 8.3 μM, respectively. Compound **120** (integrase ST IC_{50} = 11 μM) exhibited an EC_{50} of 10 μM, while analog **88** (integrase ST IC_{50} = 7.0 μM) displayed an EC_{50} of 13.9 μM. Thus, in general the cell-based activity correlated well with the IN inhibitory potency. Moreover, the two most potent IN inhibitory compounds of the set tested, **86** and **96**, were also found to have the highest activity against HIV replication, suggesting that IN might indeed be their antiviral target. These results demonstrate moderate anti-viral activity, which is not very different from early members of the diketo acid IN inhibitors, which served as important lead compounds such as L-706,908 which had an EC_{50} of 5.7 ± 4.7 μM for inhibition of HIV replication.[181] The compounds showed cytotoxicity, with selectivity index up to 4-fold for compound **120**. It may be noteworthy that compound **120** is the only compound among the antiviral test set that had a 5-benzothiophene for ring B; this may offer clues for improving selectivity index. These results demonstrate reasonable anti-viral activity when compared to the anti-viral activity of reported diketo acid inhibitors like L-706,908 which has an EC_{50} of 5.7 ± 4.7 μM for inhibition of HIV replication. To put data in perspective with regard to AZT's activity, in the same assay, AZT had an EC_{50} of 0.001 μM.[181]

Experimental Section

Chemistry

All the reagents and solvents were purchased from the Aldrich Chemical Company and used without further purification. Progress of reactions was monitored by TLC on silica gel GHLF-250 micron plates (Analtech, Inc.). Fisher scientific Da visil grade 1740 (170–400 mesh) silica gel was used for flash column chromatography. ^1H NMR spectra were recorded on Brucker AR, 300 or 500-MHz spectrometer: chemical shifts are expressed in δ values (ppm) and coupling constants (*J*) in Hertz (Hz). Mass spectral data were determined on a Brucker-HP Esquire-LC spectrometer (ESI-MS). Melting points were determined using a Fisher-Johns melting point apparatus and are reported uncorrected. HPLC analysis of final compounds was carried out using a reverse phase SUPELCOSIL 5 μm C-18 column of dimensions 25 cm x 4.6 cm. Area % purity

Table 3-2. Anti-HIV activities of selected chalcone derivatives

Cpd.	Anti-HIV-1 activity in PBMCs[a]		Cytotoxicity (IC_{50} μM)	
	EC_{50}(μM)[b]	EC_{90}(μM)[b]	PBMCs	CEM
86	8.7	21.0	24.4	27.5
88	13.9	26.0	22.1	23.8
96	7.3	20.3	22.7	19.0
120	10.1	24.3	39.1	20.7
AZT	0.0025	0.01	>100	56.1
L-706,908	5.7 ± 4.7[c]	N/A	N/A	N/A

[a] PBMCs represents Human Peripheral blood mononuclear cells; [b] EC_{50} and EC_{90} are the effective concentrations inhibiting 50% and 90% HIV replication, respectively; [c] in the assay on human leukemic T-cell line MOLT-4, the EC_{50} of AZT was 0.001 μM.

was detected at 254 nm. An initial isocratic method comprising 40% water (solvent A) and 60% methanol (solvent B) for 20 min at a flow rate of 1.2 mL/min was optimized to a linear gradient elution with water (A) and methanol (B) at a flow-rate of 1.7 mL/min. Gradient elution of the mobile phase was either (a) 80% A to 35% A from 0-5 min, 35% A, 65% B for 5-12 min, and 35% A to 80% A from 12-15 min or (b) 60% A to 20% A from 0-4 min, 20% A and 80% B for 4-12 min and 20% A to 60% A from 12-15 min. The purity of all, but two, compounds was found to be ≥ 95%.

General procedure for the synthesis of intermediates 76a-76e. 5-Halogenated salicylic acids (46 mmol) were stirred with acetic anhydride (20 mL), and 80 µL of conc. H_2SO_4 was then added. After a few (20) min, the reaction mixture solidified and was poured into cold water. The solid so obtained was filtered and extracted with ethyl acetate, washed with brine and dried over Na_2SO_4. The solvent was evaporated under reduced pressure to obtain a crude solid, which was recrystallized from ethyl acetate/hexane to afford white crystals (**76a-76e**).

2-acetoxy-5-bromo-benzoic acid (76a). Yield 88%; mp 155-157 °C; ^{1}H NMR (300 MHz, DMSO-d_6): δ 13.44 (br s, 1H, COOH), 8.0 (d, 1H, J = 2.4 Hz, ArH), 7.85 (dd, 1H, J_1 = 8.7 Hz, J_2 = 2.7 Hz, ArH), 7.20 (d, 1H, J = 8.7 Hz, ArH), 2.2 (s, 3H, $OCOCH_3$); MS (ESI): m/z 216.6 $[M-COCH_3]^-$.

2-acetoxy-5-fluoro-benzoic acid (76b). Yield 85%; mp 133-134 °C; ^{1}H NMR (300 MHz, DMSO-d_6): δ 13.42 (br s, 1H, COOH), 7.67 (dd, 1H, J_1 = 9.0 Hz, J_2 = 3.3 Hz, ArH), 7.51 (ddd, 1H, J_1 = 8.7 Hz, J_2 = 8.1 Hz, J_3 = 3.3 Hz, ArH), 7.26 (dd, 1H, J_1 = 4.8 Hz, J_2 = 8.7 Hz, ArH), 2.24 (s, 3H, $OCOCH_3$); MS (ESI): m/z 154.7 $[M-COCH_3]^-$.

2-acetoxy-5-chloro-benzoic acid (76c). Yield 85%; mp 150-152 °C; ^{1}H NMR (300 MHz, DMSO-d_6): δ 7.88 (d, 1H, J = 2.7 Hz, ArH), 7.72 (dd, 1H, J_1 = 9.0 Hz, J_2 = 2.7 Hz, ArH), 7.27 (d, 1H, J = 8.4 Hz, ArH), 2.24 (s, 3H, $OCOCH_3$); MS (ESI): m/z 170.7 $[M-COCH_3]^-$.

Acetic acid-4-bromo-2-cyano-phenyl ester (76d). Yield 76%; mp 60-61°C; ^{1}H NMR (300 MHz, DMSO-d_6) : δ 8.26 (d, 1H, J = 2.7 Hz, ArH), 8.0 (dd, 1H, J_1 = 8.7 Hz, J_2 = 2.4 Hz, ArH), 7.44 (d, 1H, J = 8.7 Hz, ArH), 2.29 (s, 3H, $OCOCH_3$); MS (ESI): m/z 197.5 $[M-COCH_3]^-$.

2-acetoxy-5-methyl-benzoic acid (76e). Yield 75%; mp 158-160 °C; ^{1}H NMR (300 MHz, DMSO-d_6) : δ 8.01 (d, 1H, J = 1.5 Hz, ArH), 7.50 (dd, 1H, J_1 = 8.4 Hz, J_2 = 1.8 Hz, ArH), 7.12 (d, 1H, J = 8.1 Hz, ArH), 2.43 (s, 3H, $OCOCH_3$), 2.27 (s, 3H, CH_3); MS (ESI): m/z 150.7 $[M-COCH_3]^-$.

General procedure for the synthesis of intermediates 77a-77e. The O-acetylated intermediates (38.61 mmol) and $AlCl_3$ (120 mmol) were mixed in a three-necked flask and heated to 160 °C under mechanical stirring. After 3 h, the reaction

mixture was cooled to rt and poured into ice containing 20 mL concentrated HCl. The slurry was extracted with ethyl acetate, acidified with 1M HCl, washed with brine and dried over Na_2SO_4. The solvent was evaporated to give the crude product, which was washed with dichloromethane for removal of impurities, filtered and dried to give 3-acetyl salicylic acids (**77a**-77**e**) as pale brown powders.

2-acetoxy-3-acetyl-5-bromo-benzoic acid (77a). Yield 34%; mp 182-185 °C; ^{1}H NMR (300 MHz, DMSO-d_6): δ 8.06 (d, 1H, J = 2.7 Hz, ArH), 7.97 (d, 1H, J = 2.7 Hz, ArH), 2.60 (s, 3H, $COCH_3$); MS (ESI): m/z 258.7 $[M-H]^-$.

2-acetoxy-3-acetyl-5-fluoro-benzoic acid (77b). Yield 31%; mp 135-136 °C; ^{1}H NMR (300 MHz, DMSO-d_6): δ 7.78 (dd, 1H, J_1 = 8.1 Hz, J_2 = 3.3 Hz, ArH), 7.72 (dd, 1H, J_1 = 8.7 Hz, J_2 = 3.3 Hz, ArH), 2.62 (s, 3H, $COCH_3$); MS (ESI): m/z 196.7 $[M-H]^-$.

2-acetoxy-3-acetyl-5-chloro-benzoic acid (77c). Yield 32%; mp 160-163 °C; ^{1}H NMR (300 MHz, DMSO-d_6): δ 7.95 (d, 1H, J = 3.0 Hz, ArH), 7.85 (d, 1H J = 2.7 Hz, ArH), 2.61 (s, 3H, $COCH_3$); MS (ESI): m/z 212.7 $[M-H]^-$.

3-acetyl-5-bromo-2-hydroxy-benzonitrile (77d). Yield 26%; mp 75-77 °C; ^{1}H NMR (300 MHz, DMSO-d_6): δ 13.17 (s, 1H, OH), 8.41 (d, 1H, J = 2.4 Hz, ArH), 8.32 (d, 1H, J = 2.4 Hz, ArH), 2.68 (s, 3H, $COCH_3$); MS (ESI): m/z 239.6 $[M-H]^-$.

3-acetyl-2-hydroxy-5-methyl-benzoic acid (77e). Yield 28%; mp >180 °C (dec); ^{1}H NMR (300 MHz, DMSO-d_6): δ 7.80 (s, 1H, ArH), 7.64 (s, 1H, ArH), 2.59 (s, 3H, $COCH_3$), 2.24 (s, 3H, CH_3); MS (ESI): m/z 192.7 $[M-H]^-$.

General procedure for the synthesis of chalcones (81-128). Equimolar amounts of aromatic aldehydes and intermediates **77a-77e** were dissolved in 10 mL of ethanol, and 5 mL of 25% aq NaOH was added. More solvent was added to help stirring in cases of excessive precipitation. The reaction mixture was stirred at rt for 1-5 days or until completion of reaction (6 h for compound **127**). The mixture was then poured into ice and acidified with 3M HCl to pH 4. The yellow precipitate formed was filtered and washed with water. The crude solid was purified by column chromatography (10-25% ethyl acetate/hexane) and/or recrystallized with ethanol or THF/water to yield pure chalcones.

5-bromo-2-hydroxy-3-(3-phenyl-acryloyl)-benzoic acid (81). Yellow solid, yield 58%; mp 210-212 °C; ^{1}H NMR (300 MHz, MeOH-d_4): δ 8.08 (d, 1H, J = 2.4 Hz, ArH), 8.04 (d, 1H, J = 2.7 Hz, ArH), 7.81 (dd, 2H, J_1 = 7.5 Hz, J_2 = 2.1 Hz, ArH), 7.68 (s, 2H, H-α and H-β), 7.42-7.44 (m, 3H, ArH); MS (ESI): m/z 346.6 $[M-H]^-$; HPLC: t_R 7.71 min, purity 99.10%.

5-bromo-3-[3-(2-chloro-phenyl)-acryloyl]-2-hydroxy-benzoic acid (82). Yellow solid, yield 60%; mp 211-214 °C; ^{1}H NMR (300 MHz, DMSO-d_6): δ 8.08 (d, 1H, J = 2.7 Hz, ArH), 8.03 (d, 1H, J = 2.7 Hz, ArH), 8.01 (dd, 1H, J_1 = 5.5 Hz, J_2 = 1.5 Hz, ArH), 7.94 (d, 1H, J = 15.9 Hz, H-β), 7.78 (d, 1H, J = 15.9 Hz, H-α), 7.59 (dd, 1H, J_1 = 8.4 Hz, J_2 =

1.8 Hz, ArH), 7.46 (ddd, 2H, J_1 = 7.5 Hz, J_2 = 7.2 Hz, J_3 = 1.8Hz, ArH); MS (ESI): m/z 380.6 $[M-H]^-$; HPLC: t_R 8.05 min, purity 98.82%.

5-bromo-3-[3-(2-fluoro-phenyl)-acryloyl]-2-hydroxy-benzoic acid (83). Yellow solid, yield 47%; mp 185-187 °C; ^{1}H NMR (300 MHz, DMSO-d_6): δ 8.05 (d, 1H, J = 2.1 Hz, ArH), 8.0 (s, 1H, H-β), 7.93 (t, 1H, J = 7.2 Hz, ArH), 7.74 (s, 1H, H-α), 7.73 (d, 1H, J = 2.7 Hz, ArH), 7.51 (d, 1H, J = 6.9 Hz, ArH), 7.31 (dd, 1H, J_1 = 8.7 Hz, J_2 = 7.2 Hz, ArH), 7.29 (t, 1H, J = 7.2, ArH); MS (ESI): m/z 364.7 $[M-H]^-$; HPLC: t_R 7.24 min, purity 99.39%.

5-bromo-3-[3-(3-chloro-phenyl)-acryloyl]-2-hydroxy-benzoic acid (84). Yellow solid, yield 56%; mp 234-236 °C; ^{1}H NMR (300 MHz, DMSO-d_6): δ 8.06 (d, 1H, J = 2.7 Hz, ArH), 8.01 (d, 1H, J = 2.7 Hz, ArH), 7.92 (s, 1H, ArH), 7.76 (d, 1H, J = 15.9 Hz, H-β), 7.75 (t, 1H, J = 7.8 Hz ArH), 7.63 (d, 1H, J = 15.9 Hz, H-α), 7.50 (dd, 2H, J_1 = 8.7 Hz, J_2 = 1.5 Hz, ArH); MS (ESI): m/z 380.6 $[M-H]^-$; HPLC: t_R 7.67 min, purity 99.30%.

5-bromo-3-[3-(4-chloro-phenyl)-acryloyl]-2-hydroxy-benzoic acid (85). Yellow solid, yield 62%; mp 238-241 °C; ^{1}H NMR (300 MHz, DMSO-d_6): δ 8.04 (d, 1H, J = 15.3 Hz, H-β), 7.91 (d, 1H, J = 2.4 Hz, ArH), 7.74 (d, 2H, J = 8.4 Hz, ArH), 7.71 (d, 1H, J = 3.0 Hz, ArH), 7.58 (d, 1H, J = 15.3 Hz, H-α), 7.50 (d, 2H, J = 8.4 Hz, ArH); MS (ESI): m/z 380.6 $[M-H]^-$; HPLC: t_R 8.1 min, purity 99.10%.

5-bromo-3-[3-(4-bromo-phenyl)-acryloyl]-2-hydroxy-benzoic acid (86). Yellow solid, yield 34%; mp 236-238 °C; ^{1}H NMR (300 MHz, DMSO-d_6): δ 8.06 (d, 1H, J = 2.7 Hz, ArH), 8.02 (d, 1H, J = 2.7 Hz, ArH), 7.74 (d, 2H, J = 8.7 Hz, ArH), 7.69 (s, 1H, H-β), 7.67 (d, 2H, J = 8.7 Hz, ArH), 7.65 (s, 1H, H-α); MS (ESI): m/z 424.6 $[M-H]^-$; HPLC: t_R 6.05 min, purity: 99.02%.

5-bromo-2-hydroxy-3-[3-(4-iodo-phenyl)-acryloyl]-benzoic acid (87). Yellow solid, yield 48%; mp 237-239 °C; ^{1}H NMR (300 MHz, DMSO-d_6): δ 8.06 (d, 1H, J = 2.7 Hz, ArH), 8.01 (d, 1H, J = 2.7 Hz, ArH), 7.83 (d, 1H, J = 8.4 Hz, ArH), 7.73 (d, 1H, J = 15.9 Hz, H-β), 7.69 (d, 1H, J = 8.4 Hz, ArH), 7.60 (d, 1H, J = 15.3 Hz, H-α), 7.59 (d, 2H J = 8.4 Hz, ArH); MS (ESI): m/z 472.6 $[M-H]^-$; HPLC: t_R 6.46 min, purity 94.70%.

5-bromo-3-[3-(2,4-dichloro-phenyl)-acryloyl]-2-hydroxy-benzoic acid (88). Yellow solid, yield 54%; mp 234-235 °C; ^{1}H NMR (300 MHz, DMSO-d_6): δ 8.08 (d, 1H, J = 2.7 Hz, ArH), 8.05 (d, 1H, J = 8.4 Hz, ArH), 8.05 (d, 1H, J = 2.7 Hz, ArH), 7.87 (d, 1H, J = 15.9 Hz, H-β), 7.76 (d, 1H, J = 15.9 Hz, H-α), 7.76 (d, 1H, J = 2.1 Hz, ArH), 7.52 (dd, 1H, J_1 = 8.4 Hz, J_2 = 1.5 Hz, ArH); MS (ESI): m/z 414.8 $[M-H]^-$; HPLC: t_R 10.91 min, purity 98.23%.

5-bromo-3-[3-(2,3-dichloro-phenyl)-acryloyl]-2-hydroxy-benzoic acid (89). Yellow solid, yield 50%; mp 226-228 °C; ^{1}H NMR (300 MHz, DMSO-d_6): δ 8.08 (d, 1H, J = 2.7 Hz, ArH), 8.03 (d, 1H, J = 2.4 Hz, ArH), 7.98 (d, 1H, J = 8.1 Hz, ArH), 7.91 (s, 1H, H-β), 7.77 (d, 1H, J = 15.6 Hz, H-α), 7.74 (d, 1H, J = 7.8 Hz, ArH), 7.46 (t, 1H, J = 7.8 Hz, ArH); MS (ESI): m/z 414.8 $[M-H]^-$; HPLC: t_R 6.46 min, purity: 99.08%.

5-bromo-3-[3-(2,3-dimethoxy-phenyl)-acryloyl]-2-hydroxy-benzoic acid (90). Yellow solid, yield 51%; mp 195-197 °C; ^{1}H NMR (300 MHz, DMSO-d_6): δ 8.02 (s, 1H, ArH), 7.92 (s, 1H, ArH), 7.86 (d, 1H, J = 16.2 Hz, H-β), 7.75 (d, 1H, J = 15.9 Hz, H-α), 7.40 (dd, 1H, J_1 = 5.7 Hz, J_2 = 3.0 Hz, ArH), 7.13-7.15 (m, 2H, ArH), 3.83 (s, 3H, OCH_3), 3.77 (s, 3H, OCH_3); MS (ESI): m/z 406.8 $[M-H]^-$; HPLC: t_R 7.03 min, purity: 99.7%.

5-bromo-2-hydroxy-3-[3-(2,3,4-trimethoxy-phenyl)-acryloyl]-benzoic acid (91). Yellow solid, yield 49%; mp 194-195 °C; ^{1}H NMR (300 MHz, DMSO-d_6): δ 8.05 (d, 1H, J = 1.8 Hz , ArH), 8.02 (d, 1H, J = 1.8 Hz ArH), 7.80 (d, 1H, J = 15.9 Hz, H-β), 7.63 (d, 1H, J = 8.7 Hz, ArH), 7.10 (d, 1H, J = 15.9 Hz, H-α), 6.92 (d, 1H, J = 8.7 Hz, ArH), 3.87 (s, 1H, OCH_3), 3.84 (s, 1H, OCH_3), 3.77 (s, 1H, OCH_3); MS (ESI): m/z 436.8 $[M-H]^-$; HPLC: t_R 6.88 min, purity: 99.36%.

5-bromo-3-[3-(2,5-dichloro-phenyl)-acryloyl]-2-hydroxy-benzoic acid (92). Yellow solid, yield 51%; mp 232-234 °C; ^{1}H NMR (300 MHz, DMSO-d_6): δ 8.16 (d, 1H, J = 2.4 Hz, ArH), 8.11 (d, 1H, J = 2.7 Hz, ArH), 8.0 (d, 1H, J = 2.7 Hz, ArH), 7.87 (s, 2H, H-α and H-β), 7.65 (d, 1H, J = 8.4 Hz, ArH), 7.57 (dd, 1H, J_1 = 8.4 Hz, J_2 = 2.4 Hz, ArH); MS (ESI): m/z 414.7 $[M-H]^-$; HPLC: t_R 8.03 min, purity 97.30%.

5-bromo-3-[3-(2,6-dichloro-phenyl)-acryloyl]-2-hydroxy-benzoic acid (93). Yellow solid, yield 54%; mp 235-237 °C; ^{1}H NMR (300 MHz, DMSO-d_6): δ 8.08 (d, 1H, J = 2.7 Hz, ArH), 7.96 (d, 1H, J = 2.7 Hz, ArH), 7.79 (d, 1H, J = 16.5 Hz, H-β), 7.67 (d, 1H, J = 16.5 Hz, H-α), 7.60 (d, 2H, J = 8.1 Hz, ArH), 7.41-7.46 (t, 1H, J = 8.7 Hz, ArH); MS (ESI): m/z 414.6 $[M-H]^-$; HPLC: t_R 7.96 min, purity 96.60%.

5-bromo-3-[3-(3,4-dichloro-phenyl)-acryloyl]-2-hydroxy-benzoic acid (94). Yellow solid, yield 48%; mp 218-221 °C; ^{1}H NMR (300 MHz, DMSO-d_6): δ 8.07 (d, 1H, J = 15.9 Hz, H-β), 8.0 (s, 1H, ArH), 7.93 (d, 1H, J = 2.7 Hz, ArH), 7.72 (d, 1H, J = 2.7 Hz, ArH), 7.70 (d, 2H, J = 7.5 Hz), 7.56 (d, 1H, J = 15.9 Hz, H-α); MS (ESI): m/z 414.6 $[M-H]^-$; HPLC: t_R 7.25 min, purity 97.0%.

5-bromo-2-hydroxy-3-[3-(2,3,5-trichloro-phenyl)-acryloyl]-benzoic acid (95). Yellow solid, yield 54%; mp 212-214 °C; ^{1}H NMR (300 MHz, DMSO-d_6): δ 8.10 (d, 1H, J = 2.4 Hz, ArH), 8.08 (d, 1H, J = 2.7 Hz, ArH), 8.05 (d, 1H, J = 2.7 Hz, ArH), 7.96 (d, 1H, J = 2.4 Hz, ArH), 7.84 (br s, 2H, H-α and H-β); MS (ESI): m/z 448.6 $[M-H]^-$; HPLC: t_R 7.41 min, purity 98.21%.

5-bromo-2-hydroxy-3-[3-(2,3,6-trichloro-phenyl)-acryloyl]-benzoic acid (96). Yellow solid, yield 57%; mp 220-223 °C; ^{1}H NMR (300 MHz, DMSO-d_6): δ 8.07 (d, 1H, J = 2.7 Hz, ArH), 7.97 (d, 1H, J = 2.4 Hz, ArH), 7.73 (d, 1H, J = 8.7 Hz, ArH), 7.71 (d, 1H, J = 16.2 Hz, H-β), 7.61-7.64 (m, 2H, H-α and ArH); MS (ESI): m/z 448.6 $[M-H]^-$; HPLC: t_R 7.13 min, purity 99.20%.

5-chloro-3-[3-(4-chloro-phenyl)-acryloyl]-2-hydroxy-benzoic acid (97). Yellow solid, yield 43%; mp 213-215 °C; ^{1}H NMR (300 MHz, DMSO-d_6): δ 7.95 (d, 1H, J = 2.1 Hz, ArH), 7.93 (d, 1H, J = 2.7 Hz, ArH), 7.84 (dd, 2H, J_1 = 6.9 Hz, J_2 = 1.5 Hz, ArH), 7.66

(s, 2H, H-β and H-α), 7.51 (dd, 2H, J_1 = 6.9 Hz, J_2 = 1.5 Hz, ArH); MS (ESI): m/z 336.9 $[M-H]^-$; HPLC: t_R 6.13 min, purity 99.55%.

5-chloro-3-[3-(2,4-dichloro-phenyl)-acryloyl]-2-hydroxy-benzoic acid (98). Yellow solid, yield 48%; mp 248-250 °C; ^{1}H NMR (300 MHz, MeOH-d_4): δ 8.05 (d, 1H, J = 15.9 Hz, H-β), 7.93 (d, 1H, J = 8.7 Hz, ArH), 7.84 (d, 1H, J = 2.4 Hz, ArH), 7.80 (d, 1H, J = 15.3 Hz, H-α), 7.73 (d, 1H, J = 2.1 Hz, ArH), 7.65 (d, 1H, J = 2.7 Hz, ArH), 7.52 (dd, 1H, J_1 = 8.4 Hz, J_2 = 2.1 Hz, ArH); MS (ESI): m/z 370.8 $[M-H]^-$; HPLC: t_R 6.76 min, purity 99.14%.

5-chloro-3-[3-(2,3-dichloro-phenyl)-acryloyl]-2-hydroxy-benzoic acid (99). Yellow solid, yield 41%; mp 250-252 °C; ^{1}H NMR (300 MHz, DMSO-d_6): δ 8.10 (d, 1H, J = 15.3 Hz, H-β), 7.85-7.89 (m, 3H, H-α and ArH), 7.70 (d, 1H, J = 7.2 Hz, ArH), 7.62 (s, 1H, ArH), 7.45 (t, 1H, J = 7.5 Hz, ArH); MS (ESI): m/z 370.8 $[M-H]^-$; HPLC: t_R 6.06 min, purity 96.61%.

5-chloro-3-[3-(2,5-dichloro-phenyl)-acryloyl]-2-hydroxy-benzoic acid (100). Yellow solid, yield 42%; mp 247-249 °C; ^{1}H NMR (300 MHz, DMSO-d_6): δ 8.20 (d, 1H, J = 1.2 Hz, ArH), 8.04 (s, 2H, H-β and ArH), 7.90 (s, 2H, H-α and ArH), 7.67 (d, 1H, J = 8.4 Hz, ArH), 7.61 (dd, 1H, J_1 = 8.4 Hz, J_2 = 1.5 Hz, ArH); MS (ESI): m/z 370.7 $[M-H]^-$; HPLC: t_R 8.39 min, purity 99.0%.

5-chloro-2-hydroxy-3-[3-(2,3,5-trichloro-phenyl)-acryloyl]-benzoic acid (101). Yellow solid, yield 37%; mp 235-237 °C; ^{1}H NMR (300 MHz, DMSO-d_6): δ 8.05 (d, 1H, J = 15.9 Hz, H-β), 7.91 (d, 2H, J = 1.2 Hz, ArH), 7.82 (d, 1H, J = 3.0 Hz, ArH), 7.75 (d, 1H, J = 15.6 Hz, H-α), 7.60 (d, 1H, J = 2.7 Hz, ArH); MS (ESI): m/z 404.6 $[M-H]^-$; HPLC: t_R 7.18 min, purity 98.81%.

5-chloro-2-hydroxy-3-[3-(2,3,6-trichloro-phenyl)-acryloyl]-benzoic acid (102). Yellow solid, yield 49%; mp 229-231 °C; ^{1}H NMR (300 MHz, DMSO-d_6): δ 7.99 (d, 1H, J = 16.2 Hz, H-β), 7.86 (d, 1H, J = 2.1 Hz, ArH), 7.71 (d, 1H, J = 2.7 Hz, ArH), 7.69 (d, 1H, J = 7.8 Hz, ArH), 7.65 (d, 1H, J = 8.4 Hz, ArH), 7.60 (d, 1H, J = 16.2 Hz, H-α); MS (ESI): m/z 404.6 $[M-H]^-$; HPLC: t_R 6.58 min, purity 95.66%.

5-chloro-3-[3-(3,4-dichloro-phenyl)-acryloyl]-2-hydroxy-benzoic acid (103). Yellow solid, yield 54%; mp >240 °C (dec); ^{1}H NMR (300 MHz, DMSO-d_6): δ 8.05 (d, 1H, J = 15.9 Hz, H-β), 7.99 (s, 1H, ArH), 7.80 (d, 1H, J = 3.0 Hz, ArH), 7.71 (d, 2H, J = 6.0 Hz, ArH), 7.58 (d, 1H, J = 3.0 Hz, ArH), 7.56 (d, 1H, J = 15.9 Hz, H-α); MS (ESI): m/z 370.8 $[M-H]^-$; HPLC: t_R 6.78 min, purity 99.60%.

3-[3-(4-chloro-phenyl)-acryloyl]-5-fluoro-2-hydroxy-benzoic acid (104). Yellow solid, yield 56%; mp 198-200 °C; ^{1}H NMR (300 MHz, DMSO-d_6): δ 7.91 (d, 1H, J = 15.9 Hz, H-β), 7.60 (d, 1H, J = 15.9 Hz, H-α), 7.68 (dd, 1H, J_1 = 8.4 Hz, J_2 = 3.3 Hz, ArH), 7.76 (d, 2H, J = 8.4 Hz, ArH), 7.49 (d, 2H, J = 8.7 Hz, ArH), 7.54 (dd, 1H, J_1 = 9.3 Hz, J_2 = 3.3 Hz, ArH); MS (ESI): m/z 318.8 $[M-H]^-$; HPLC: t_R 7.11 min, purity 99.11%.

3-[3-(2,4-dichloro-phenyl)-acryloyl]-5-fluoro-2-hydroxy-benzoic acid (105). Yellow solid, yield 41%; mp 260-262 °C; ^{1}H NMR (300 MHz, DMSO-d_6): δ 8.12 (d, 1H, J = 15.6 Hz, H-β), 7.93 (d, 1H, J = 8.4 Hz, ArH), 7.81 (d, 1H, J = 15.9 Hz, H-α), 7.74 (d, 1H, J = 2.1 Hz, ArH), 7.65 (dd, 1H, J_1 = 8.7 Hz, J_2 = 3.3 Hz, ArH), 7.52 (dd, 1H, J_1 = 8.4 Hz, J_2 = 2.1 Hz, ArH), 7.43 (dd, 1H, J_1 = 9.3 Hz, J_2 = 3.3 Hz, ArH); MS (ESI): m/z 352.8 [M−H]$^-$; HPLC: t_R 6.51 min, purity 99.5%.

3-[3-(2,3-dichloro-phenyl)-acryloyl]-5-fluoro-2-hydroxy-benzoic acid (106). Yellow solid, yield 47%; mp 222-224 °C; ^{1}H NMR (500 MHz, DMSO-d_6): δ 7.94 (d, 1H, J = 7.8 Hz, ArH), 7.90 (s, 2H, H-α and H-β), 7.77 (dd, 1H, J_1 = 8.5 Hz, J_2 = 3.0 Hz, ArH), 7.73 (d, 1H, J = 8.0 Hz, ArH), 7.46 (t, 1H, J = 8.0 Hz, ArH), 7.66 (dd, 1H, J_1 = 9.0 Hz, J_2 = 2.5 Hz, ArH); MS (ESI): m/z 352.8 [M−H]$^-$; HPLC: t_R 5.68 min, purity 97.20%.

3-[3-(2,5-dichloro-phenyl)-acryloyl]-5-fluoro-2-hydroxy-benzoic acid (107). Yellow solid, yield 59%; mp 238-240 °C; ^{1}H NMR (300 MHz, DMSO-d_6): δ 8.07 (d, 1H, J = 15.9 Hz, H-β), 7.93 (d, 1H, J = 2.4 Hz, ArH), 7.76 (d, 1H, J = 15.9 Hz, H-α), 7.66 (dd, 1H, J_1 = 8.4 Hz, J_2 = 3.6 Hz, ArH), 7.60 (d, 1H, J = 8.7 Hz, ArH), 7.52 (dd, 1H, J_1 =8.7 Hz, J_2 = 2.4 Hz, ArH), 7.42 (dd, 1H, J_1 = 9.3 Hz, J_2 = 3.6 Hz, ArH); MS (ESI): m/z 352.8 [M−H]$^-$; HPLC: t_R 6.02 min, purity 98.43%.

5-fluoro-2-hydroxy-3-[3-(2,3,5-trichloro-phenyl)-acryloyl]-benzoic acid (108). Yellow solid, yield 53%; mp 231-233 °C; ^{1}H NMR (300 MHz, DMSO-d_6): δ 8.02 (d, 1H, J = 2.4 Hz, ArH), 7.95 (d, 1H, J = 15.9 Hz, H-β), 7.92 (d, 1H, J = 2.4 Hz, ArH), 7.79 (d, 1H, J = 15.6 Hz, H-α), 7.74 (dd, 1H, J_1 = 8.4 Hz, J_2 = 3.3 Hz, ArH), 7.64 (dd, 1H, J_1 = 9.0 Hz, J_2 = 3.3 Hz, ArH); MS (ESI): m/z 388.6 [M−H]$^-$; HPLC: t_R 8.11 min, purity 97.86%.

5-fluoro-2-hydroxy-3-[3-(2,3,6-trichloro-phenyl)-acryloyl]-benzoic acid (109). Yellow solid, yield 46%; mp 235-237 °C; ^{1}H NMR (300 MHz, DMSO-d_6): δ 8.11 (d, 1H, J = 16.2 Hz, H-β), 7.70 (d, 1H, J = 8.7 Hz, ArH), 7.62 (d, 1H, J = 8.7 Hz, ArH), 7.58 (d, 1H, J = 16.2 Hz, H-α), 7.66 (dd, 1H, J_1 = 8.4 Hz, J_2 = 3.6 Hz, ArH), 7.44 (dd, 1H, J_1 = 9.3 Hz, J_2 = 3.6 Hz, ArH); MS (ESI): m/z 388.6 [M−H]$^-$; HPLC: t_R 7.57 min, purity 97.57%.

5-bromo-3-[3-(3,5-dimethyl-phenyl)-acryloyl]-2-hydroxy-benzoic acid (110). Yellow solid, yield 51%; mp 223-225 °C; ^{1}H NMR (300 MHz, DMSO-d_6): δ 8.06 (d, 1H, J = 2.7 Hz, ArH), 7.99 (d, 1H, J = 1.8 Hz, ArH), 7.61 (d, 1H, J = 16.5 Hz, H-β), 7.58 (d, 1H, J = 16.5 Hz, H-α), 7.40 (s, 2H, Hz, ArH), 7.10 (s, 1H, ArH), 2.32 (s, 6H, CH_3); MS (ESI): m/z 374.9 [M−H]$^-$; HPLC: t_R 6.59 min, purity 99.0%.

5-bromo-3-[3-(2-chloro-3,4-dimethoxy-phenyl)-acryloyl]-2-hydroxy-benzoic acid (111). Yellow solid, yield 21%; mp 217-220 °C; ^{1}H NMR (300 MHz, DMSO-d_6): δ 8.05 (d, 1H, J = 2.7 Hz, ArH), 8.00 (d, 1H, J = 2.7 Hz, ArH), 7.90 (d, 1H, J = 15.6 Hz, H-β), 7.81 (d, 1H, J = 8.7 Hz, ArH), 7.68 (d, 1H, J = 15.6 Hz, H-α), 7.16 (d, 1H, J = 8.7 Hz, ArH), 3.90 (s, 3H, OCH_3), 3.77 (s, 3H, OCH_3); MS (ESI): m/z 440.8 [M−H]$^-$; HPLC: t_R 6.46 min, purity 99.0%.

5-bromo-3-[3-(2-fluoro-4,5-dimethoxy-phenyl)-acryloyl]-2-hydroxy-benzoic acid (112). Yellow solid, yield 32%; mp 193-195 °C; ^{1}H NMR (300 Hz, DMSO-d_6): δ 8.03 (d, 1H, J = 2.7 Hz, ArH), 7.93 (d, 1H, J = 2.7 Hz, ArH), 7.66 (s, 2H, H-β and H-α), 7.38 (d, 1H, J = 7.2 Hz, ArH), 7.00 (d, 1H, J = 12.3 Hz, ArH), 3.84 (s, 3H, OCH_3), 3.82 (s, 3H, OCH_3); MS (ESI): m/z 424.8 $[M-H]^-$; HPLC: t_R 7.19 min, purity 97.51%.

3-[3-(2-benzyloxy-phenyl)-acryloyl]-5-bromo-2-hydroxy-benzoic acid (113). Yellow solid, yield 26%; mp > 165 °C (dec); ^{1}H NMR (300 MHz, MeOH-d_4): δ 7.92-7.95 (m, 2H, H-β and ArH), 7.72 (d, 1H, J = 7.5 Hz, ArH), 7.65 (d, 1H, J = 2.7 Hz, ArH), 7.47 (d, 2H, J = 7.2 Hz, ArH), 7.30-7.42 (m, 5H, H-α, and ArH), 7.20 (d, 1H, J = 8.1 Hz, ArH), 7.0 (t, 1H, J = 7.5 Hz, ArH), 5.22 (s, 2H, CH_2); MS (ESI): m/z 452.8 $[M-H]^-$; HPLC: t_R 7.83 min, purity 95.65%.

5-bromo-3-{3-[3-(4-chloro-phenoxy)-phenyl]-acryloyl}-2-hydroxy-benzoic acid (114). Yellow solid, yield 42%; mp 162-165 °C; ^{1}H NMR (300 MHz, DMSO-d_6): δ 7.94 (s, 2H, ArH), 7.74 (d, 1H, J = 6.9 Hz, ArH), 7.70 (d, 1H, J = 15.9 Hz, H-β), 7.40-7.46 (m, 6H, H- α and ArH), 7.20 (d, 1H, J = 7.8 Hz, ArH), 7.0 (t, 1H, J = 6.9 Hz, ArH); (ESI): m/z 472.6 $[M-H]^-$; HPLC: t_R 5.86 min, purity 96.8%.

5-bromo-3-{3-[4-(4-chloro-phenoxy)-phenyl]-acryloyl}-2-hydroxy-benzoic acid (115). Yellow solid, yield 35%; mp 219-220 °C; ^{1}H NMR (300 MHz, DMSO-d_6): δ 8.06 (d, 1H, J = 2.1 Hz, ArH), 8.02 (d, 1H, J = 2.1 Hz, ArH), 7.84 (d, 2H, J = 8.4 Hz, ArH), 7.67 (d, 1H, J = 15.9 Hz, H-β), 7.59 (d, 1H, J = 15.9 Hz, H-α), 7.48 (d, 2H, J = 8.7 Hz, ArH), 7.13 (d, 2H, J = 8.7 Hz, ArH), 7.07 (d, 2H, J = 8.7 Hz, ArH); MS (ESI): m/z 472.6 $[M-H]^-$; HPLC: t_R 7.23 min, purity 99.44%.

5-bromo-2-hydroxy-3-(3-thiophen-3-yl-acryloyl)-benzoic acid (116). Yellow solid, yield 54%; mp 207-210 °C; ^{1}H NMR (300 MHz, DMSO-d_6): δ 7.97 (s, 2H, ArH), 7.75 (d, 1H, J = 15.9 Hz, H-β), 7.65 (s, 1H, ArH), 7.61 (s, 1H, ArH), 7.58 (d, 1H, J = 15.6 Hz, H-α), 7.48 (d, 1H, J = 4.2 Hz, ArH); MS (ESI): m/z 352.6 $[M-H]^-$; HPLC: t_R 6.91 min, purity 99.71%.

5-bromo-3-[3-(3-cyclopentyloxy-4-methoxy-phenyl)-acryloyl]-2-hydroxy-benzoic acid (117). Yellow solid, yield 31%; mp 233-235 °C; ^{1}H NMR (300 MHz, MeOH-d_4): δ 7.91 (d, 1H, J = 2.7 Hz, ArH), 7.82 (d, 1H, J = 15.6 Hz, H-β), 7.67 (d, 1H, J = 3.0 Hz, ArH), 7.59 (d, 1H, J = 15.9 Hz, H-α), 7.26 (d, 1H, J = 8.7 Hz, ArH), 7.25 (s, 1H, ArH), 6.99 (d, 1H, J = 8.1 Hz, ArH), 4.86 (p, 1H, J = 5.7 Hz, cyclopentyl), 3.79 (s, 3H, CH_3) 1.87-1.92 (m, 2H, cyclopentyl), 1.66-1.72 (m, 4H, cyclopentyl), 1.57-1.60 (m, 2H, cyclopentyl); MS (ESI): m/z 460.8 $[M-H]^-$; HPLC: t_R 7.19 min, purity 97.51%.

5-bromo-3-[3-(2-ethoxy-naphthalen-1-yl)-acryloyl]-2-hydroxy-benzoic acid (118). Yellow solid, yield 23%; mp 216-218 °C; ^{1}H NMR (300 MHz, MeOH-d_4): δ 8.48 (d, 1H, J = 15.9 Hz, H-β), 8.30 (d, 1H, J = 8.4 Hz, ArH), 8.19 (d, 1H, J = 2.7 Hz, ArH), 8.17 (d, 1H, J = 15.9 Hz, H-α), 7.92 (d, 1H, J = 9.0 Hz, ArH), 7.88 (d, 1H, J = 2.7 Hz, ArH), 7.84 (d, 1H, J = 8.4 Hz, ArH), 7.55 (t, 1H, J = 7.2 Hz, ArH), 7.37-7.44 (m, 2H, ArH), 4.33 (q, 2H, J = 6.9 Hz, CH_2), 1.55 (t, 3H, J = 6.9 Hz, CH_3); MS (ESI): m/z 440.9 $[M-H]^-$;

HPLC: t_R 8.53 min, purity 95.0%.

5bromo-2-hydroxy-3-[3-(6-methoxy-naphthalen-2-yl)-acryloyl]-benzoic acid (119). Yellow solid, yield 15%; mp 239-241 °C; ^{1}H NMR (300 Hz, MeOH-d_4): δ 8.17 (d, 1H, J = 2.4 Hz, ArH), 8.01 (s, 1H, H-β), 7.86 (d, 1H, J = 7.9 Hz, ArH), 7.84 (d, 2H, J = 8.1 Hz, ArH), 7.83 (d, 1H, J = 2.4 Hz, ArH), 7.80 (s, 2H, H-α, and ArH), 7.26 (d, 1H, J = 2.4 Hz, ArH), 7.16 (dd, 1H, J_1 = 8.7 Hz, J_2 = 2.4 Hz, ArH), 3.93 (s, 3H, OCH_3); MS (ESI): m/z 426.8 $[M-H]^-$; HPLC: t_R 6.07 min, purity 98.93%.

3-(3benzo[b]thiophen-5-yl-acryloyl)-5-bromo-2-hydroxy-benzoic acid (120). Yellow solid, yield 21%; mp 235-237 °C; ^{1}H NMR (300 MHz, DMSO-d_6): δ 8.21 (s, 1H, ArH), 8.1 (d, 1H, J = 15.9 Hz, H-β), 8.0 (s, 1H, ArH), 7.92 (d, 1H, J = 2.7 Hz, ArH), 7.82 (d, 1H, J = 5.4 Hz, ArH), 7.73 (d, 1H, J = 15.9, H-α), 7.72 (d, 1H, J = 3 Hz, ArH), 7.72 (s, 1H, ArH), 7.53 (d, 1H, J = 5.1 Hz, ArH); MS (ESI): m/z 402.8 $[M-H]^-$; HPLC: t_R 5.53 min, purity 98.31%.

5-bromo-3-[3-(2-furan-2-yl-phenyl)-acryloyl]-2-hydroxy-benzoic acid (121). Yellow solid, yield 36%; mp 208-209 °C; ^{1}H NMR (300 MHz, DMSO-d_6): δ 7.92 (m, 3H, H-β and ArH), 7.87 (s, 1H, H-α), 7.81 (d, 1H, J = 2.7 Hz, ArH), 7.70 (s, 1H, ArH), 7.68 (d, 1H, 9.6 Hz, ArH), 7.48 (t, 2H, J = 7.5 Hz, ArH), 6.66 (s, 1H, ArH), 6.63 (s,1H, ArH); MS (ESI): m/z 412.8 $[M-H]^-$; HPLC: t_R 5.77 min, purity 95.02%.

5-bromo-3-[3-(6-chloro-benzo[1,3]dioxol-5-yl)-acryloyl]-2-hydroxy-benzoic acid (122). Yellow solid, yield 18%; mp 228-231 °C; ^{1}H NMR (300 MHz, DMSO-d_6): δ 8.10 (s, 1H, ArH), 8.07 (s, 1H, ArH), 7.90 (d, 1H, J = 15 Hz, H-β), 7.66 (s, 1H, ArH), 7.63 (d, 1H, J = 14.7 Hz, H-α), 7.21 (s, 1H, ArH), 6.16 (s, 2H, CH_2); MS (ESI): m/z 424.6 $[M-H]^-$; HPLC: t_R 7.82 min, purity 99.0%.

5-bromo-2-hydroxy-3-[3-(3-trifluoromethoxy-phenyl)-acryloyl]-benzoic acid (123). Yellow solid, yield 44 %; mp 217-219 °C; ^{1}H NMR (300 MHz, DMSO-d_6): δ 8.07 (d, 1H, J = 2.7 Hz, ArH), 8.03 (d, 1H, J = 2.7 Hz, ArH), 7.80-7.84 (br s, 2H, H-α and H-β), 7.72 (s, 1H, ArH), 7.70 (s, 1H, J = 4.0 Hz, ArH), 7.58 (t, 1H, J = 7.8 Hz, ArH), 7.45 (d, 1H, J = 7.5 Hz, ArH); MS (ESI): m/z 430.8 $[M-H]^-$; HPLC: t_R 6.06 min, purity 99.30%.

5-bromo-2-hydroxy-3-[3-(3-nitro-phenyl)-acryloyl]-benzoic acid (124). Yellow solid, yield 62%; mp 200-202 °C; ^{1}H NMR (500 MHz, DMSO-d_6): δ 8.62 (s, 1H, ArH), 8.26 (s, 2H, ArH), 8.07 (s, 1H, H-β), 8.02 (s, 1H, H-α), 7.81 (d, 2H, J = 7.0 Hz, ArH), 7.75 (t, 1H, J = 7.0 Hz, ArH); MS (ESI): m/z 391.8 $[M-H]^-$; HPLC: t_R 11.47 min, purity 95.59%.

5-bromo-3-[3-(3-bromo-phenyl)-acryloyl]-2-hydroxy-benzoic acid (125). Yellow solid, yield 31%; mp 235-237 °C; ^{1}H NMR (300 MHz, DMSO-d_6): δ 8.0 (d, 1H, J = 15.9 Hz, H-β), 7.92 (d, 1H, J = 2.7 Hz, ArH), 7.90 (s, 1H, ArH), 7.72 (d, 1H, J = 6.6 Hz, ArH), 7.70 (d, 1H, J = 2.4 Hz, ArH), 7.59 (d, 1H, J = 8.4 Hz, ArH), 7.55 (d, 1H, J = 15.9 Hz, H-α), 7.39 (t, 1H, J = 7.8 Hz, ArH); MS (ESI): m/z 424.6 $[M-H]^-$; HPLC: t_R 6.14 min, purity 98.81%.

5-bromo-3-[3-(3-fluoro-phenyl)-acryloyl]-2-hydroxy-benzoic acid (126). Yellow solid, yield 59%; mp 190-193 °C; ^{1}H NMR (500 MHz, DMSO-d_6): δ 8.0 (d, 1H, J = 2.0 Hz, ArH), 7.93 (s, 1H, ArH), 7.80 (d, 1H, J = 16.0 Hz, H-β), 7.60-7.77 (m, 3H, H-α and ArH), 7.48 (d, 1H, J = 6.5 Hz, ArH), 7.28 (d, 1H, J = 8.0 Hz, ArH); MS (ESI): m/z 364.7 $[M-H]^-$; HPLC: t_R 5.39 min, purity 92.5%.

5-bromo-2-hydroxy-3-[3-(2,3,6--trichloro-phenyl)-acryloyl]-benzonitrile (127). Orange solid, yield 74%; mp 139-141 °C; ^{1}H NMR (300 MHz, DMSO-d_6): δ 8.34 (d, 1H, J = 16.2 Hz, H-β), 7.69 (d, 1H, J = 3.0 Hz, ArH), 7.66 (d, 1H, J = 9.0 Hz, ArH), 7.58 (d, 1H, J = 8.7 Hz, ArH), 7.46 (d, 1H, J = 2.4 Hz, ArH), 7.43 (d, 1H, J = 16.2 Hz, H-α); MS (ESI): m/z 431.6 $[M-H]^-$; HPLC: t_R 6.37 min, purity: 95.69%.

2-hydroxy-5-methyl-3-[3-(2,3,6--trichloro-phenyl)-acryloyl]-benzoic acid (128). Yellow solid, yield 58.5%; mp 205-208 °C; ^{1}H NMR (300 MHz, DMSO-d_6): δ 7.87 (s, 1H, ArH), 7.74 (s, 1H, ArH), 7.70 (d, 1H, J = 8.7 Hz, ArH), 7.59-7.64 (m, 3H, H-α, H-β and ArH), 2.29 (s, 3H, CH_3); MS (ESI): m/z 384.8 $[M-H]^-$; HPLC: t_R 6.01 min, purity 97.84%.

General procedure for the synthesis of chalcones (129 -130). A similar procedure to the one mentioned above for the synthesis of chalcones (**81-128**) was followed (**Scheme 1-2**) with appropriate aromatic aldehydes starting materials **79**, **80** and commercially available 1-(5-bromo-2-hydroxy-3-nitro-phenyl)-ethanone, **78f** to synthesize chalcones **129** and **130**.

1-(5-bromo-2-hydroxy-3-nitro-phenyl)-3-(2,3,5-trichloro-phenyl)-propenone (129). Yellow solid, yield 65%; mp 175-178 °C; ^{1}H NMR (300 MHz, DMSO-d_6): δ 8.13 (d, 1H, J = 15.6 Hz, H-β), 7.76 (d, 1H, J = 15.9 Hz, H-α), 8.05 (d, 1H, J = 2.7 Hz, ArH), 8.0 (d, 2H, J = 2.4 Hz, ArH), 7.92 (d, 1H, J = 2.4 Hz, ArH); MS (ESI): m/z 451.8 $[M-H]^-$; HPLC: t_R 5.46 min, purity 97.30%.

1-(5-bromo-2-hydroxy-3-nitro-phenyl)-3-(2,3,6-trichloro-phenyl)-propenone (130). Yellow solid, yield 58%; mp 153-154 °C; ^{1}H NMR (500 MHz, DMSO-d_6): δ 8.32 (s, 1H, ArH), 8.24 (s, 1H, ArH), 7.77 (d, 1H, J = 16.5 Hz, H-β), 7.75 (d, 1H, J = 9.0 Hz, ArH), 7.65 (d, 1H, J = 15.0 Hz, H-α), 7.63 (d, 1H, J = 8.0 Hz, ArH); MS (ESI): m/z 451.8 $[M-H]^-$; HPLC: t_R 6.53 min, purity 98.0%.

2-hydroxyl-3-(3-phenylpropyl) benzoic acid (131). Compound **81** (0.05 g, 0.195 mmol) was dissolved in ethanol (10 mL) and Pd/C (10 mol%, 5 mg) was added. The resulting solution was stirred under hydrogen at atmospheric pressure for 10 h at rt. After the reaction was complete, the reaction mixture was filtered through celite, and evaporated to dryness. The resulting crude solid was purified by preparative TLC to give a white solid, yield 72%; mp 125-127 °C; ^{1}H NMR (300 MHz, DMSO-d_6): δ 11.66 (s,1H, OH), 7.67 (dd, 1H, J_1 = 7.8 Hz, J_2 = 1.5 Hz, ArH), 7.39 (dd, 1H, J_1 = 7.2 Hz, J_2 = 1.5 Hz, ArH), 7.16-7.30 (m, 5H, ArH), 6.85 (t, 1H, J = 7.8 Hz, ArH), 2.62 (t, 4H, J = 7.2 Hz, CH_2), 1.81-1.91 (m, 2H, CH_2); MS (ESI): m/z 254.8 $[M-H]^-$; HPLC: t_R 7.61 min, purity 98 %.

3-[3-(2,5-dichloro-phenyl)-propionyl]-5-fluoro-2-hydroxy-benzoic acid (132). Compound **107** (0.2 g, 0.563 mmol) was dissolved in methanol (10 mL) and Pd/C (10 mol %, 20 mg) was added. The resulting solution was stirred under hydrogen at atmospheric pressure for 2 h at room temperature. After the reaction was complete, the reaction mixture was filtered through celite, and evaporated to dryness. The resulting crude solid was recrystallized from ethanol to give a white solid, yield 43%; mp 163-164 °C; ^{1}H NMR (300 MHz, DMSO-d_6): δ 7.79 (d, 1H, J = 8.4 Hz, ArH), 7.74 (d, 1H, J = 9.0, ArH), 7.49 (s, 1H, ArH), 7.45 (d, 1H, J = 8.7 Hz, ArH), 7.31 (d, 1H, J = 8.1 Hz, ArH), 3.39 (t, 2H, J = 6.9 Hz, CH_2), 3.02 (t, 2H, J = 6.9 Hz, CH_2); MS (ESI): m/z 356.9 $[M-H]^-$; HPLC: t_R 8.34 min, purity 96.36%.

Biological Assays

Materials, chemicals, and enzymes. All compounds were dissolved in DMSO and the stock solutions were stored at -20 °C. γ[^{32}P]-ATP was purchased from either Amersham Biosciences or ICN. The expression systems for wild-type IN were a generous gift from Dr. Robert Craigie, Laboratory of Molecular Biology, NIDDK, NIH, Bethesda, MD. Cell lines were obtained from American Type Culture Collection (ATCC, Rockville, MD).

Preparation of oligonucleotide substrates. The oligonucleotides 21top, 5′-GTGTGGAAAATCTCTAGCAGT-3′, and 21bot, 5′-ACTGCTAGAGATTTTCCACAC-3′, were purchased from the Norris Cancer Center Microsequencing Core Facility (University of Southern California) and purified by UV shadowing on polyacrylamide gel. To analyze the extent of 3′-P and ST using 5′-end labeled substrates, 21top was 5′-end labeled using T4 polynucleotide kinase (Epicentre, Madison, WI) and γ[32P]-ATP (Amersham Biosciences or ICN). The kinase was heat-inactivated and 21-bot was added in 1.5M excess. The mixture was heated at 95 °C, allowed to cool slowly to rt, and run through a G25 mini spin column (USA Scientific) to separate double-stranded oligonucleotide from unincorporated material.

Integrase assays. To determine the extent of 3′-P and ST, wild-type IN was preincubated at a final concentration of 200 nM with the inhibitor in reaction buffer (50 mM NaCl, 1 mM HEPES, pH 7.5, 50 μM EDTA, 50 μM dithiothreitol, 10% glycerol (w/v), 7.5 mM $MnCl_2$, 0.1 mg/mL bovine serum albumin, 10 mM 2-mercaptoethanol, 10% dimethylsulfoxide, and 25 mM MOPS, pH 7.2) at 30 °C for 30 min. An aliquot (5μL) was electrophoresed on a denaturing 20% polyacrylamide gel (0.09 M Tris- borate, pH 8.3, 2 mM EDTA, 20% acrylamide, and 8M urea). Gels were dried, exposed in a phosphorImager cassette, and analyzed using a Typhoon 8610 Variable Mode Imager (Amersham Biosciences) and quantitated using ImageQuant 5.2. Percent inhibition (%I) was calculated using (**Equation 3-1**);

$$\% I = 100 * [1 - (D - C/(N - C) \quad \textbf{(Eq. 3-1)}$$

where C, N, and D are the fractions of 21-mer substrate converted to 19-mer (3′-P product) or ST products for DNA alone, DNA plus IN, and IN plus compound, respectively. The IC_{50} values were determined by plotting the logarithm of compound concentration versus percent inhibition to obtain the concentration that produced 50% inhibition.

Anti-HIV-1 activity assay. The testing of the ability of potent compounds to inhibit HIV replication in cell culture was done according to a previously reported procedure.[182] PBMC (107 cells/T25flask) were stimulated with phytohemagglutinin for 3 days and infected with a wild-type HIV-1 strain (strain LAI) at 100 50% tissue culture infective doses, as described previously.[182] The cultures were kept for 5 days in the presence of test compounds at serial 1-log dilutions. Subsequently, human PBMC were removed from the culture supernatant by centrifugation (400g, 10 min, 4 °C). This clarified supernatant was tested by a reverse transcriptase assay.

Cytotoxicity assays. The cytotoxicity of compounds was evaluated using uninfected PBMC and CEM leukemia cells according to a previous method.[183] PBMC were obtained from whole blood of healthy individuals, while CEM were obtained from the ATCC (Rockville, MD). The PBMC and CEM cells were cultured in the presence or absence of compound for 6 days. After this time period, cells were stained with Trypan blue dye, and counted for cell proliferation and viability according to the previously reported procedure.[184]

CHAPTER 4. SYNTHESIS AND BIOLOGICAL EVALUATION OF 3-KETO SALICYLAMIDE AS NOVEL HIV-1 INTEGRASE INHIBITORS*

Introduction

The benzyl carboxamide group was recognized as an important moiety with the discovery of naphthyridine carboxamides as a new class of HIV-IN inhibitors. Examples include L-870,810 and L-870,812 (**Figure 1-20**). Further efforts led to the development of the pyrimidinone carboxamide class containing the approved drug raltegravir.[51] The carboxamide moiety though not an absolute requirement is believed to give a conformationally favorable orientation to the halogenated benzyl group present in potent inhibitors to bind into the cavity formed by protein-DNA interface. In this chapter, the α,β-unsaturated moiety of our synthesized chalcone derivatives (described in Chapter 3) was modified to an amide functionality to synthesize a novel series of compounds, salicylic acid 3-carboxamides.

Chemistry

The synthesis of target compound **149** is shown in **Scheme 4-1**. Commercially available 5-bromo salicylic acid (**133a**) was first formylated with chloroform at the 2-position (*ortho*) by the Reimer-Tiemann reaction[185] to yield the aldehyde intermediate **134**. In the next step, intermediate **134** was coupled with 4-fluorobenzyl amine to afford intermediate **135** which was subsequently subjected to oxidation with $KMnO_4$ to yield compound **149**.[186]

Low yield of the formylation step (8-10%), and a potential side product (Schiffs base) in the coupling reaction prompted us to employ an alternate synthetic route (**Scheme 4-2**). Thus, for the synthesis of compounds **150**-**152**, 3-formyl salicylaldehyde (**133b**) was used as the starting material, which was brominated with *N*-bromo succinimide (NBS) in acetonitrile to afford intermediate **134** in higher (90%) yields.[187] Next, the sequence of subsequent steps was altered in that the intermediate **134** was first subjected to $KmNO_4$ oxidation to form a di-acid derivative **136**. Intermediate **136** was then coupled with equimolar amounts of the appropriate amines in the presence of HOBt and EDCI to form the desired amides **150** and **151**.[188] For the synthesis of compound **152**, the di-acid intermediate **136** was treated with excess of 4-fluorobenzyl amine (2.2 eq) under similar conditions.

For the synthesis of amide compounds **153**-**156**, shown in **Scheme 4-3**, commercially available acids (**137**–**140**) were subjected to HOBt/EDCI coupling with

* Portions of this chapter adapted with permission. Sharma, H.; Patil, S.; Sanchez, T. W.; Neamati, N.; Schinazi, R. F.; Buolamwini, J. K. Synthesis, biological evaluation and 3D-QSAR studies of 3-keto salicylic acid chalcones and related amides as novel HIV-1 integrase inhibitors. *Bioorg. Med. Chem.* **2011**, 19, 2030-2045.[179]

Scheme 4-1. Synthesis of compound 149

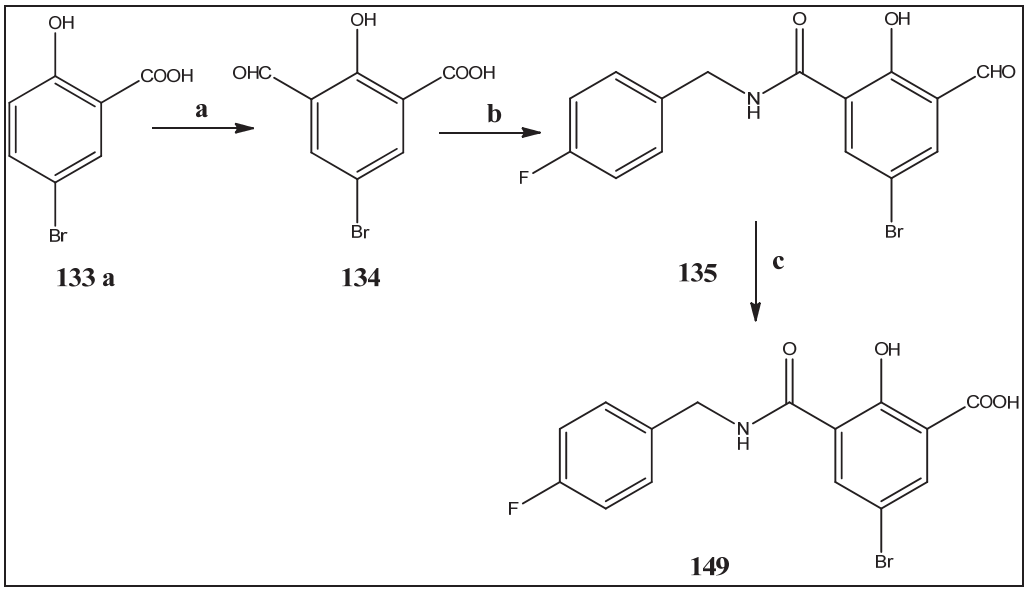

Reagents and conditions: (a) $CHCl_3$, NaOH, H_2O, reflux, 48 h; yield 13% (b) 4-F benzylamine, EDCI, HOBt, Et_3N, rt, overnight; yield 41% (c) $KMnO_4$, H_2O/Pyridine, 90 °C, overnight; yield 80%.

Scheme 4-2. Synthesis of compounds 150-152

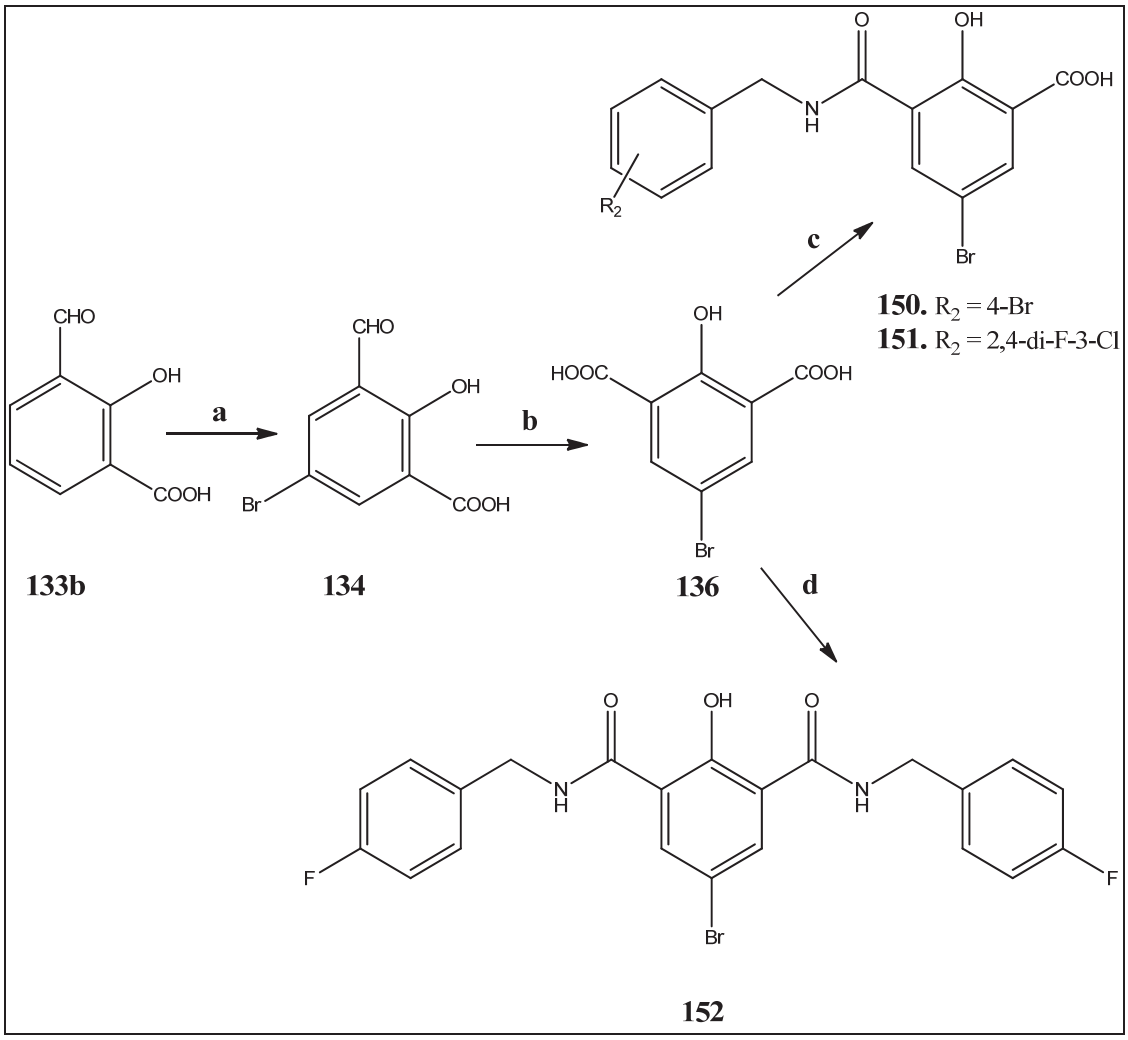

Reagent and conditions: (a) NBS, CH_3CN, rt, 3 h; yield 90% (b) $KMnO_4$, H_2O/Pyridine, 90 °C , overnight; 80% (c) amines (0.90 eq), EDCI, HOBt, Et_3N, rt, overnight; yields 34-62% (d) 4-F benzylamine (2.2 eq), EDCI, HOBt, Et_3N, rt, overnight; yield 48%.

Scheme 4-3. Synthesis of compounds 153-156

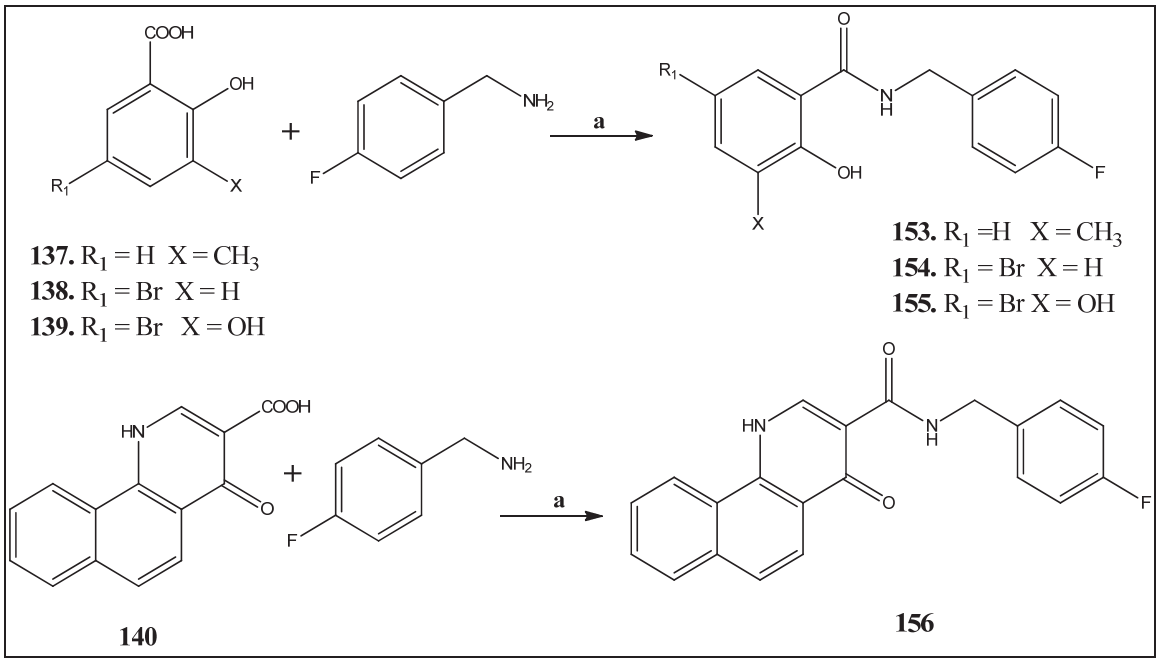

Reagent and conditions: (a) 4-F benzylamine, EDCI, HOBt, Et_3N, rt, overnight; yields 53-76%.

4-fluoro benzyl amine. The synthesis of compound **157** was performed according to **Scheme 4-4**. The commercially available 5-acetyl-2-hydroxy-3-methoxybenzoic acid (**141**) was first converted to the corresponding amide with standard HOBt/EDCI coupling. The methoxy substituent in amide intermediate (**142**) was then demethylated using BBr_3 in DCM at 0 °C.[189] The hydroxyl intermediate (**143**) was then reacted with benzaldehyde, using aq. sodium hydroxide by Aldol condensation to afford the desired final α,β-unsaturated compound **157**. The synthesis of compound **158** was achieved using **Scheme 4-5** in which the 3-acetyl-5-bromo-2-hydroxybenzoic acid intermediate (**78a**), which was synthesized in Chapter 3, was subjected to routine HOBt/EDCI amide coupling followed by an Aldol condensation. The synthesis of compound **159**, shown in **Scheme 4-6**, was achieved according to a method previously reported.[190] First, a solution of peracetic acid was synthesized by stirring a mixture of acetic anhydride and H_2O_2 at ice for 4 h. *N*-hydroxylation of the starting material, 6-hydroxy picolinic acid was achieved by peracetic acid in a mixture of trifluoroacetic acid and glacial acetic acid and heating at 80 °C for 10 h. In the next step, the *N*-hydroxyl group of intermediate **146** was protected using benzyl chloride and K_2CO_3 in methanol to obtain benzyl-protected intermediate **147**. The acid moiety in intermediate **147** was then converted to acid chloride using oxalyl chloride in the presence of a catalytic amount of DMF in toluene and heating at 80 °C for 4 h. The acid chloride formed was then subsequently reacted with 4-fluorobenzyl amine in THF by stirring at 60 °C for overnight to afford intermediate **148**. In the last step, the benzyl group was deprotected with acid to give final compound **159**.

Results and Discussions

Structure Activity Relationship (SAR)

The chalcone functionality contained in compounds synthesized in Chapter 3 was modified to a structurally related amide to synthesize a new series of HIV-IN inhibitors. Compound **149** having an acid functionality at the X position (**Table 4-1**) showed low μM ST inhibitory activity (IC_{50} value of 15 μM) suggesting that the α,β-unsaturated moiety of chalcones could be replaced with an amide functionality with retention of comparative inhibitory activity but with an increase in ST selectivity. Intermediate **135** having an aldehyde group at the X position was also tested for SAR purposes and was found to be more active than the corresponding acid containing compound **149**. The synthesis of compounds **153** and **154** was undertaken to determine the ability of two-chelating atoms in inhibiting HIV-IN activity. The discovery of elvitegravir has showed that the presence of even two coplanar chelating moieties, represented by the β-ketone and a carboxylic acid is sufficient for potent clinically relevant IN inhibition. Compound **153** (X= CH_3 R_1 = H) was found to be inactive with ST IC_{50} > 100 μM. In order to further ascertain if the loss in activity of compound **153** was due to the lack of a chelating atom at the X position, compound **154** (X= CH_3 R_1 = Br) was synthesized. Compound **154** also showed ST IC_{50} > 100 μM indicating the importance of a metal-chelating group at the X position. Next, an OH substituted compound **155** was synthesized and was found

Scheme 4-4. Synthesis of compound 157

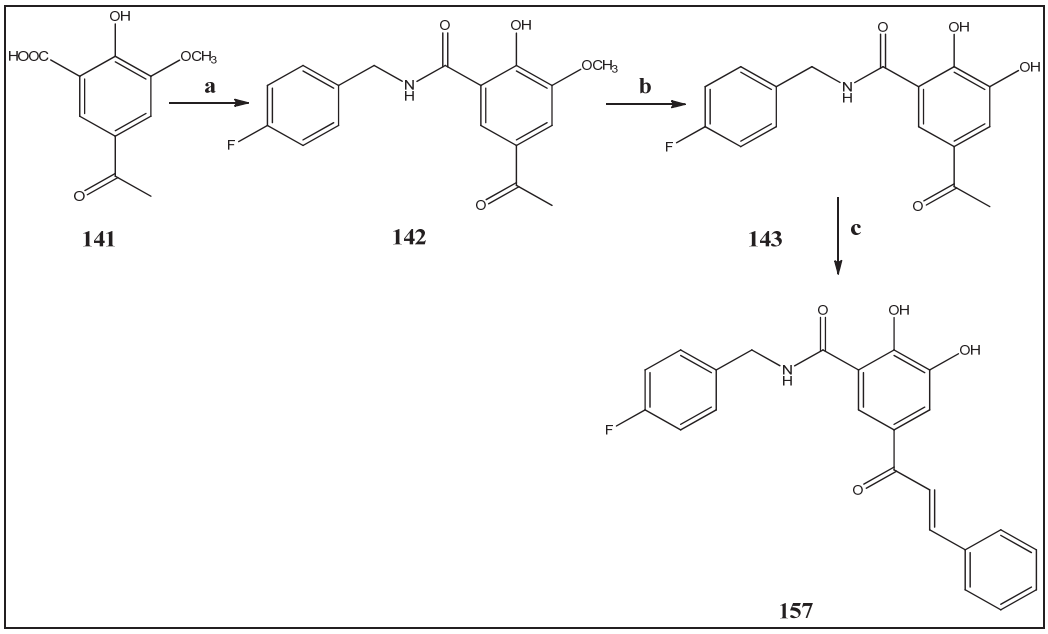

Reagent and conditions: (a) 4-F benzylamine, EDCI, HOBt, Et_3N, rt, overnight; yield 74% (b) BBr_3, DCM, 0 °C to rt, overnight; (c) C_6H_5CHO, NaOH, ethanol, rt, overnight; overall (steps b and c) yield 36%.

Scheme 4-5. Synthesis of compound 158

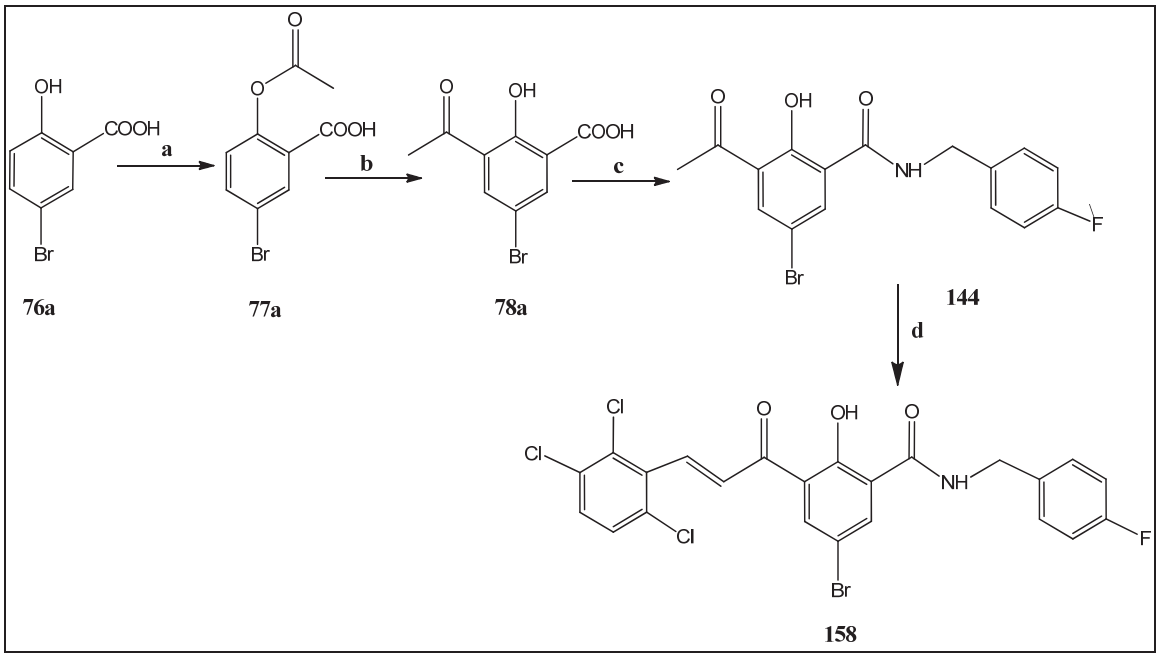

Reagent and conditions: (a) Ac_2O, H_2SO_4, 20 min; yield 88% (b) $AlCl_3$, 160 °C, 3 h; yield 34% (c) 4-F benzylamine, EDCI, HOBt, Et_3N, rt, overnight; yield 41% (d) ArCHO, NaOH, EtOH, rt, 24 h; yield 51%.

Scheme 4-6. Synthesis of compound 159

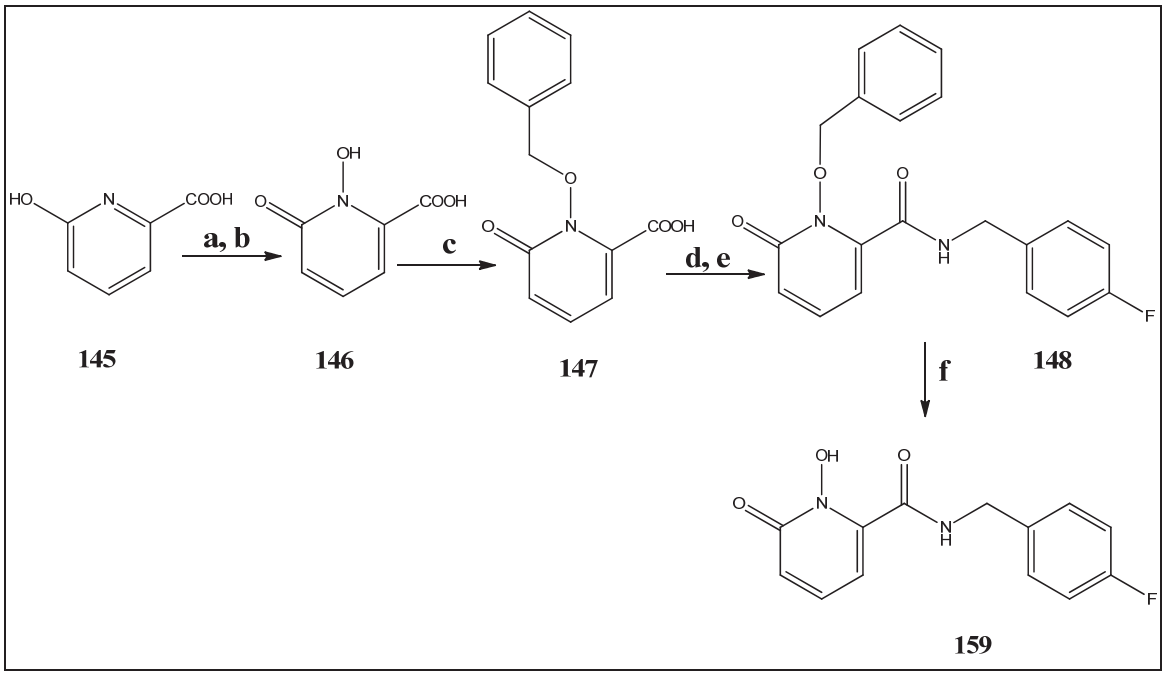

Reagent and conditions: (a) H_2O_2, Ac_2O, 4 h; (b) TFA, GAA, 80 °C, 6 h; overall (steps a and b) yield 60% (c) BnCl, K_2CO_3, MeOH, 16 h, reflux; yield 41% (d) $(COCl)_2$, toluene, DMF, 60 °C, 4 h; (e) 4-F benzylamine, Et_3N, THF, 60 °C,12 h; overall (steps d and e) yield 41% (f) HOAc /Conc. HCl, rt, 2 days; yield 67%.

Table 4-1. Structures and activities of 3-keto salicylic acid amides HIV-1 integrase inhibitors

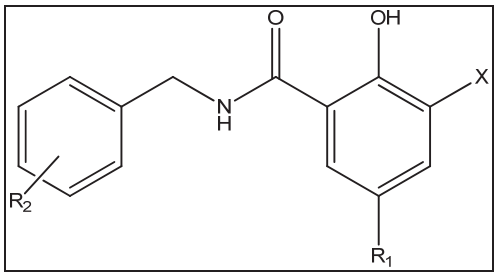

Cpd.	X	R_1	R_2	Activity IC_{50} (μM)	
				3′-P[a]	ST[b]
135	CHO	Br	4-F	>100	
144	$COCH_3$	Br	4-F	>100	8 ± 1
149	COOH	Br	4-F	>100	
150	COOH	Br	4-Br	>100	>100
					15 ± 3
151	COOH	Br	2,4-di-F-3-Cl	>100	69 ±13
152	$CONHCH_2$-4-F-Ph	Br	4-F	>100	4 ± 1
153	H	Br	4-F	>100	6 ± 2
154	CH_3	H	4-F	>100	>100
155	OH	Br	4-F	53 ± 2	>100
157	OH	COCHCH-Ph	4-F	64 ± 6	13 ± 6
158	COCHCH-2,3,6-tri-Cl-Ph	Br	4-F	>100	21 ± 6
156	N/A	N/A	N/A	>100	100
159	N/A	N/A	N/A	>333	255 ± 6

[a] 3′-P = 3′-procesing; [b] ST = strand transfer.

to be marginally better (ST IC_{50} = 13 μM) than the acid containing compound suggesting that a catechol substituent is well tolerated. This is in agreement with literature as polyhydroxylated compounds have been reported as HIV-IN inhibitors.[112] The chalcone series of IN inhibitors have demonstrated that substitution at the R_1 position resulted in notable changes in ST activities. For further development of this series of compounds structure-based design, described in Chapter 6, was attempted using the RACHEL lead optimization software (Tripos Inc). Thus, compound **157** was designed and synthesized based on the binding interactions of raltegravir. It has an extended side chain with an aromatic ring to serve as an oxadiazole mimic for obtaining π-stacking interactions with Tyr143 in the IN active site. The phenyl ring was thus connected to the core 3-keto salicylamide ring with an α,β-unsaturated linker. Unfortunately, this modification resulted in a loss of activity (ST IC_{50} = 21 μM) relative to its reference compound (13 μM). Further modifications with various linkers and heterocyclic ring system need to be explored to determine the SAR at this position. The diamide compound **152** was designed with the objective of increasing contacts with the protein. This modification resulted in improvement in ST activity with IC_{50} of 6.0 μM opening the possibilities of further modifications. Compounds **150** and **151** were synthesized to determine the effects of other halogens on the phenyl ring of their benzyl carboxamide moieties. Compound **150** with a *p*-bromo substituent at the R_2 position was four times less active than compound **149**. Moreover, compound **151** resulted in 4-folds improvement in inhibitory activity with IC_{50} of 4.0 μM in ST assay with respect to compound **149** and fifteen-folds more active than compound **150** indicating that further modifications, possibly with different halogens, could improve the ST activities of this series of compounds.

With an aim of discovering new pharmacophores for inhibiting HIV-1 IN, synthesis of compounds **156** and **159** was undertaken. Compound **159** is a 3-hydroxy-2-pyridinone which has been reported to have strong metal (Fe^{3+}) chelating[191,192] properties. This compound was inactive against IN suggesting that this system may not chelate Mg^{2+} with similar potencies.

Inhibition of HIV Replication in Cell Culture

To evaluate the potential of the amide derivatives as antiviral agents, three active analogs were tested for the ability to inhibit HIV-1 replication in primary human peripheral blood mononuclear cells (PBMCs) infected with the virus. The toxicity of the compounds was also tested against PBMC and human CEM lymphoblastic leukemia cells. In general, the compounds showed reduced anti-viral activities. Compounds **135** and **152** showed moderate activities while compound **151** was inactive in inhibiting HIV replication (**Table 4-2**). The low antiviral activities may have to do with solubility, absorption, binding to serum proteins in cell culture media and/or cellular distribution factors.

Table 4-2. Anti-HIV activity of selected amide derivatives

Cpd.	Anti-HIV-1 activity in PBMCs[a]		Cytotoxicity (IC_{50} μM)	
	EC_{50}(μM)[b]	EC_{90}(μM)[b]	PBMCs	CEM
135	30.8	52.7	44.0	40.2
151	>100	>100	26.4	26.4
152	49.6 ± 4.2	>100	18.0	14.3
AZT	0.0025	0.01	>100	56.1
L-706,908	5.7 ± 4.7[c]	N/A[d]	N/A	N/A

[a] PBMCs represents Human Peripheral blood mononuclear cells; [b] EC_{50} and EC_{90} are the effective concentrations inhibiting 50% and 90% HIV replication, respectively; [c] in the assay on human leukemic T-cell line MOLT-4, the EC_{50} of AZT was 0.001 μM; [d] N/A represents not available.

Experimental Section

Chemistry

All the reagents and solvents were purchased from the Aldrich Chemical Company and used without further purification. Progress of reactions was monitored by TLC on silica gel GHLF-250 micron plates (Analtech, Inc.). Fisher scientific Da visil grade 1740 (170-400 mesh) silica gel was used for flash column chromatography. ^{1}H NMR spectra were recorded on Brucker AR, 300 or 500-MHz spectrometer: chemical shifts are expressed in δ values (ppm) and coupling constants (*J*) in Hertz (Hz). Mass spectral data were determined on a Brucker-HP Esquire-LC spectrometer (ESI-MS). Melting points of solids were determined using a Fisher-Johns melting point apparatus and are reported uncorrected. HPLC analysis of final compounds was carried out using a reverse phase SUPELCOSIL 5 μm C-18 column of dimensions 25 cm x 4.6 cm. Area % purity was detected at 254 nm. An initial isocratic method comprising 40% water (solvent A) and 60% methanol (solvent B) for 20 min at a flow rate of 1.2 mL/min was optimized to a linear gradient elution with water (A) and methanol (B) at a flow-rate of 1.7 mL/min. Gradient elution of the mobile phase was either 80% A to 35% A from 0-5 min, 35% A and 65% B for 5-12 min and 35% A to 80% A from 12-15 min or 80% A to 20% A from 0-4 min, 20% A and 80% B for 4-17 min and 20% A to 80% A from 17-20 min.

5-bromo-3-formyl-2-hydroxy-benzoic acid (134). Method (a): NaOH (5.53 g, 0.138 mol) was added to a solution of 5-bromosalicylic acid (5 g, 23.0 mmol) in DCM (45 mL) and water (1 mL, 55.55 mmol) at rt. The reaction mixture was refluxed for 48 h, diluted with water and acidified with 6M HCl to pH 1.0. The resulting solution was extracted with ethyl acetate washed with brine and dried over Na_2SO_4. The organic layer was evaporated to yield a crude product which was purified by column chromatography (25-35% MeOHl/DCM) to give a white solid, yield 13%; mp 172-174 °C; ^{1}H NMR (300 MHz, DMSO-d_6): δ 10.27 (s, 1H, CHO), 8.12 (d, 1H, J = 2.7, ArH), 7.93 (d, 1H, J = 2.7 ArH); MS (ESI): m/z 244.7 $[M-H]^-$.

5-bromo-*N*-(4-fluoro-benzyl)-3-formyl-2-hydroxy-benzamide (135). To a solution of intermediate (0.4 g, 1.63 mmol), HOBt (0.441 g, 3.26 mmol) and Et_3N (0.45 mL, 3.26 mmol) in DCM (20 mL) was added EDCI (0.344 g, 1.8 mmol) at 0 °C. 4-fluorobenzylamine (0.20 mL, 1.8 mmol) was then added and the reaction mixture stirred overnight at rt. The reaction mixture was extracted with ethyl acetate, washed with dilute hydrochloric acid and sodium bicarbonate solution. The organic layer was further washed with brine and dried over sodium sulfate. The crude was purified by recrystalization with ethyl acetate/hexane to give a yellow solid. yield 41%; mp 135-137 °C; ^{1}H NMR (300 MHz, DMSO-d_6): δ 10.27 (s,1H, CHO), 9.90 (s, 1H, NH), 8.41 (s, 1H, ArH), 7.87 (s, 1H, ArH), 7.40 (d, 2H, J = 8.1 Hz, ArH), 7.18 (*t*, 2H, J = 8.1 Hz, ArH), 4.52 (s, 2H, CH_2); MS (ESI): m/z 351.9 $[M-H]^-$.

5-bromo-*N*-(4-fluoro-benzyl)-2-hydroxy-isopthalamic acid (149). Intermediate **135** (0.20 g, 0.568 mmol) was added to a mixture of water (2.5 mL) and pyridine (2.5 mL).

the reaction mixture was heated to 90 °C, $KMnO_4$ (0.18 g, 1.13 mmol) was added to the hot solution was and the heating continued overnight at 90 °C. After completion, the mixture was filtered through celite and evaporated to dryness. The resulting residue was purified by recrystalization from ethyl acetate/hexane. White solid; yield 80 %; mp 208-210 °C; ^{1}H NMR (300 MHz, DMSO-d_6): δ 10.20 (s, 1H, NH), 7.98 (s, 1H, ArH), 7.85 (s, 1H, ArH), 7.13-7.34 (m, 4H, ArH), 4.50 (s, 2H, CH_2); MS (ESI): m/z 367.9 $[M-H]^-$; HPLC: t_R 4.21 min, purity 97.7%.

5-bromo-3-formyl-2-hydroxy-benzoic acid (134). Method (b): 3-formyl salicylic acid hydrate starting material (1.0 g, 6.0 mmol) was dissolved in dry acetonitrile (20 mL). *N*-bromo succinimide (1.02 g, 5.73 mmol) was added and the reaction mixture stirred at rt for 3 h. The white crystals formed were filtered and washed with water. The filtrate was extracted with ethyl acetate, and washed with brine. The organic layer was dried over Na_2SO_4 and evaporated to dryness. The two fractions were combined to give intermediate as white crystals, yield 90%; mp 172-174 °C; ^{1}H NMR (300 MHz, DMSO-d_6): δ 10.27 (s, 1H, CHO), 8.12 (d, 1H, J = 2.7, ArH), 7.93 (d, 1H, J = 2.7 ArH); MS (ESI): m/z 244.7 $[M-H]^-$.

5-bromo-2-hydroxyisophthalic acid (136). Intermediate **134** (0.30 g, 1.22 mmol) was added to a mixture of water (3.5 mL) and pyridine (3.5 mL). The reaction mixture was heated to 90 °C, $KMnO_4$ (0.387g, 2.45 mmol) was added to the hot solution was and the heating continued overnight at 90 °C. After completion, the mixture was filtered through celite and evaporated to dryness. The resulting residue was washed with ethyl acetate and purified by recrystalization from ethanol. Yield 68%; mp >220 °C; ^{1}H NMR (300 MHz, DMSO-d_6): δ 10.25 (s, 1H, OH), 7.60 (s, 1H, ArH), 7.92 (s, 1H, ArH); MS (ESI): m/z 260.7 $[M-H]^-$.

General procedure for the synthesis of compounds 150 and 151. Intermediate 136 (0.50 g, 1.91 mmol), HOBt (0.517g, 3.83 mmol) and triethyl amine (0.534 mL, 3.83 mmol) were added to a mixture of DCM (10 mL) and DMF (10 mL) at 0 °C. EDCI (0.404 g, 2.10 mmol) was added to the above solution followed by 4-bromo-benzylamine (0.22 mL, 1.82 mmol) or 3-chloro-2,4-difluorobenzylamine (0.323 gm, 1.82 mmol) for compounds 150 and 151, respectively. The reaction mixture was then stirred overnight at rt. After the reaction, the reaction mixture was evaporated and poured into excess water, and extracted with ethyl acetate. The organic layer was washed with dilute hydrochloric acid and sodium bicarbonate solution and then with brine and dried over sodium sulfate. The resulting crude solid was washed with hexane and recrystalization with ethyl acetate.

5-bromo-3-((4-bromobenzyl)carbamoyl)-2-hydroxybenzoic acid (150). White solid, yield 34%; mp >220 °C dec; ^{1}H NMR (500 MHz, DMSO-d_6): δ 9.28 (s, 1H, NH), 8.07 (d, 1H, J = 2.0 Hz, ArH), 7.96 (d, 1H, J = 2.0 Hz, ArH), 7.52 (d, 1H, J = 8.0 Hz, ArH), 7.27 (d, 1H, J = 8.0 Hz, ArH), 4.47 (d, 2H, J = 6.0 Hz, CH_2); MS (ESI): m/z $[M-H]^-$; HPLC: t_R 6.41 min, purity 99.7%.

5-bromo-*N*-(3-chloro-2,4-difluorobenzyl)-2,3-dihydroxybenzamide (151). Yellow

solid, yield 62%; mp 140-142 °C; ^{1}H NMR (300 MHz, DMSO-d_6): δ 9.73 (s, 1H, NH), 8.02 (s, 1H, ArH), 7.92 (s, 1H, ArH), 7.45 (d, 1H, J = 7.8 Hz, ArH), 7.27 (d, 1H, J = 9.0 Hz, ArH), 4.56 (d, 2H, J = 5.1 Hz, CH_2); MS (ESI): m/z 419.8 $[M-H]^-$; HPLC: t_R 4.43 min, purity 97.7%.

5-bromo-*N*^{1},*N*^{3}-bis(4-fluorobenzyl)-2-hydroxyisophthalamide (152). Intermediate **136** (0.20 g, 0.766 mmol), HOBt (0.415 g, 3.06 mmol) and Et_3N (0.22 mL, 1.53 mmol) was added in a mixture of DCM (20 mL) and DMF (5 mL) at 0 °C. EDCI (0.323 g, 1.69 mmol) was added to the above solution followed by 4-fluorobenzylamine (0.20 mL, 1.69 mmol) after which the reaction mixture was kept at 0 °C for 1 h and stirred overnight at rt. The reaction mixture was then evaporated and poured into excess water, and extracted with ethyl acetate. The organic layer was washed with dilute hydrochloric acid and sodium bicarbonate solution and then with brine and dried over sodium sulfate. The crude was washed with hexane and purified by column chromatography with 5-10% of MeOH/DCM to give pure compound **152**. Yellow solid; yield 48%; mp 235-237 °C; ^{1}H NMR (300 MHz, DMSO-d_6): δ 9.23 (bs, 2H, NH), 8.09 (d, 1H, J = 2.7 Hz, ArH), 7.98 (d, 1H, J = 2.7 Hz, ArH), 7.29-7.39 (m, 4H, ArH), 4.48 (d, 1H, J = 4.2 Hz, CH_2); MS (ESI): m/z 474.8 $[M-H]^-$.

General procedure for the synthesis of compounds 153-156. Similar procedure for amide coupling described above for compound 149 was used such that appropriate commercially available acids (0.25 g, 0.98 mmol), HOBt (0.29 g, 2.1 mmol) and Et3N (0.15 mL, 0.98 mmol) were added to either DCM or THF (15 mL) at 0 °C. EDCI (0.22 g, 1.07 mmol) was added to the above solution followed by 4-fluorobenzylamine (0.12 mL, 0.98 mmol) after which the reaction mixture was kept at ice for 1 h and then allowed to come to rt and stirred overnight for 14 h. The reaction mixture was then evaporated and extracted with ethyl acetate. The organic layer was washed with dilute hydrochloric acid and sodium bicarbonate solution and then with brine and dried over sodium sulfate. The resulting crude was washed with hexane and purified by column chromatography (10-20% ethyl acetate/ hexane or recrystallized with ethyl acetate/hexane.

***N*-(4-fluoro-benzyl)-2-hydroxy-3-methyl-benzamide (153).** White solid; yield 76%; mp 165-166 °C; ^{1}H NMR (300 MHz, DMSO-d_6): δ 13.10 (s, 1H, OH), 9.43 (t, 1H, J = 6.0 Hz, NH), 7.72 (d, 1H, J = 7.2 Hz, ArH), 7.37 (d, 1H, J = 8.7 Hz, ArH), 7.35 (d, 1H, J = 8.4 Hz, ArH), 7.31 (d, 1H, J = 7.2 Hz, ArH), 7.15 (t, 2H, J = 9.0 Hz, ArH), 6.78 (t, 1H, J = 7.5 Hz, ArH), 4.48 (d, 1H, J = 6.0 Hz, CH_2), 2.15 (s, 3H, CH_3); MS (ESI): m/z 257.9 $[M-H]^-$; HPLC: t_R 8.63 min, purity 99.11%.

5-bromo-*N*-(4-fluoro-benzyl)-2-hydroxy-benzamide (154). White solid; yield 62%; mp 83-84 °C; ^{1}H NMR (300 MHz, DMSO-d_6): δ 12.47 (s,1H, OH), 9.37 (t, 1H, J = 5.7 Hz, NH), 8.07 (d, 1H, J = 2.4 Hz, ArH), 7.55 (dd, 1H, J_1 = 8.7 Hz, J_2 = 2.4 Hz, ArH), 7.36 (dd, 2H, J_1 = 8.1 Hz, J_2 =5.7 Hz, ArH), 7.15 (t, 2H, J = 9.0, ArH), 6.89 (d, 1H, J = 8.7 Hz, ArH), 4.47 (d, 2H, J = 5.7 Hz, CH_2); MS (ESI): m/z 323.8 $[M-H]^-$; HPLC: t_R 9.7 min, purity 98.66%.

5-bromo-*N*-(4-fluorobenzyl)-2,3-dihydroxybenzamide (155). Yellow solid; yield 61 %; mp 215-217 °C; ^{1}H NMR (300 MHz, DMSO-d_6): δ 9.42 (t, 1H, J = 5.4 Hz, NH), 7.56 (d, 1H, J = 2.4 Hz, ArH), 7.36 (dd, 2H, J_1 = 8.1 Hz, J_2 = 2.4 Hz, ArH), 7.16 (t, 2H, J = 8.7 Hz, ArH), 7.05 (d, 1H, J = 2.4 Hz, ArH), 4.47 (d, 2H, J = 5.4 Hz, CH_2); MS (ESI): m/z 339.8 $[M-H]^-$.

***N*-(4-fluorobenzyl)-4-oxo-1,4-dihydrobenzo[h]quinoline-3-carboxamide (156).** White solid; yield 53%; ^{1}H NMR (500 MHz, DMSO-d_6): δ 8.83 (s, 1H, NH), 8.61 (d, 1H, J = 6.5 Hz, NH), 8.30 (d, 1H, J = 9.0 Hz, ArH), 8.08 (d, 1H, J = 9.0 Hz, ArH), 7.85 (d, 1H, J = 8.5 Hz, ArH), 7.75-7.77 (m, 2H, ArH), 7.42 (dd, 3H, J_1 = 9.0 Hz, J_2 = 1.5 Hz), 7.06 (t, 3H, J = 9.0 Hz, ArH); MS (ESI): m/z 344.9 $[M-H]^-$.

5-acetyl-N-(4-fluorobenzyl)-2-hydroxy-3-methoxybenzamide (142). 5-acetyl-2-hydroxy-3-methoxybenzoic acid starting material (1.0 g, 4.76 mmol), HOBt (1.28 g, 9.51 mmol) and Et_3N (0.66 mL, 4.76 mmol) was added in a THF (20 mL) at 0 °C. EDCI (1.0 g, 5.23 mmol) was added to the above solution followed by 4-fluorobenzylamine (0.54 mL, 4.76 mmol) after which the reaction mixture was kept at 0 °C for 1 h and stirred overnight at rt. After the reaction, the reaction mixture was evaporated to a small volume and extracted with ethyl acetate. The organic layer was washed with dilute hydrochloric acid and sodium bicarbonate solution and then with brine and dried over sodium sulfate. The resulting crude was washed with hexane and recrystallized with ethyl acetate/hexane to give pure intermediate **142**. White solid, mp 165-167 °C; yield 74%; ^{1}H NMR (500 MHz, DMSO-d_6): δ 9.67(s, 1H, NH), 8.20 (d, 1H, J = 1.0 Hz, ArH), 7.55 (d, 1H, J = 1.0 Hz, ArH), 7.39 (dd, 2H, J_1 = 8.5 Hz, J_2 = 6.0 Hz, ArH), 7.17 (t, 2H, J = 8.5 Hz, ArH), 4.53 (d, 2H, J = 6.0 Hz, CH_2), 3.85 (s, 3H, 3.85, OCH_3), 2.55 (s, 3H, 2.55, $COCH_3$); MS (ESI): m/z 316.0 $[M-H]^-$.

5-cinnamoyl-*N*-(4-fluorobenzyl)-2,3-dihydroxybenzamide (157). To a solution of intermediate **142** (1.0 g, 3.15 mmol) in DCM (20 mL) was added BBr_3 (6.30 mL of 1M solution in DCM) at 0 °C. The reaction mixture was allowed to come to room temperature and stirred for 16 h. After the reaction, the mixture was quenched with ice cold water and extracted with DCM. The organic layer was evaporated and dried in vacuo to give the demethoxy intermediate **143**, which was used for the next step without further purification (MS (ESI): m/z 301.9 $[M-H]^-$). Intermediate **143** (0.80 gm, 2.64 mmol) and benzaldehyde (0.26 mL, 2.64 mmol), were dissolved in 10 mL of ethanol, and 5 mL of 25% aq NaOH was added. The reaction mixture was stirred at room temperature for 24 h. The mixture was then poured into ice and acidified with 3 M HCl to pH 4. The yellow precipitate formed was filtered and washed with water. The crude solid was purified by preparative chromatography (DCM: ethyl acetate, 8:2) to afford pure compound **157**. Brown solid; overall yield 36%; mp 170-173 °C; ^{1}H NMR (300 MHz, DMSO-d_6): δ 13.56 (s, 1H, OH), 9.73 (s, 1H, NH), 9.66 (s, 1H, OH), 8.26 (s, 1H, ArH), 7.75-7.93 (m, 4H, ArH, Hα, Hβ), 7.67 (s, 1H, ArH), 7.37-7.54 (m, 5H, ArH), 7.18 (m, 2H, ArH), 4.57 (s, 2H, CH_2); MS (ESI): m/z 390.0 $[M-H]^-$.

3-acetyl-5-bromo-*N*-(4-fluorobenzyl)-2-hydroxybenzamide (144). Intermediate **78a** (1.0 g, 3.86 mmol), which was synthesized as an intermediate in the Chapter 3, HOBt

(1.04 g, 7.72 mmol) and triethylamine (0.53 mL, 3.86 mmol) were added in DCM (20 mL) at 0 °C. EDCI (0.81 g, 4.24 mmol) was added to the above solution followed by 4-fluorobenzylamine (0.44 mL, 3.86 mmol) after which the reaction mixture was kept at ice for 1 h and stirred overnight at rt. After the reaction, the reaction mixture was evaporated to a small volume and extracted with ethyl acetate. The organic layer was washed with dilute hydrochloric acid and sodium bicarbonate solution and then with brine and dried over sodium sulfate. The resulting crude was washed with hexane and purified by column chromatography (10-20% ethyl acetate/hexane). White solid; mp 125-126 °C; yield 41%; mp 125-126 °C; ^{1}H NMR (500 MHz, DMSO-d_6): δ 9.43 (t, 1H, J = 6.0 Hz, NH), 8.26 (s, 1H, ArH), 7.98 (s, 1H, ArH), 7.38-7.42 (m, 2H, ArH), 7.16 (t, 2H, J = 8.5 Hz, ArH), 2.63 (s, 3H, $COCH_3$); MS (ESI): m/z 365.9 $[M-H]^-$.

(E)-5-bromo-*N*-(4-fluorobenzyl)-2-hydroxy-3-(3-(2,3,6-trichlorophenyl) acryloyl) benzamide (158). Intermediate **144** (0.53 g, 1.44 mmol) and 2,3,6-trichlorobenzaldehyde (0.33 g, 1.44 mmol) were dissolved in 10 mL of ethanol, and 5 mL of 25% aq NaOH was added. The reaction mixture was stirred at rt for 24 h. The mixture was then poured into ice and acidified with 3M HCl to pH 4. The yellow precipitate formed was filtered and washed with water. The crude was purified using preparative TLC to give pure compound **158**. Yellow solid; yield 51%; mp 108-110 °C; ^{1}H NMR (500 MHz, DMSO-d_6): δ 9.43 (t, 1H, J = 5.0 Hz, NH), 8.16 (s, 1H, ArH), 7.81-7.97 (m, 2H, ArH, H-β), 7.68 (d, 1H, J = 8.5 Hz, ArH), 7.59 (d, 1H, J = 8.5 Hz, ArH), 7.50 (d, 1H, J = 16.0 Hz, H-α), 7.34 (dd, 2H, J_1 = 8.0 Hz, J_2 = 5.5 Hz), 7.13 (t, 2H, J = 8.5 Hz), 4.47 (d, 2H, J = 5.0 Hz, CH_2); MS (ESI): m/z 555.8 $[M-H]^-$.

1-hydroxy-6-oxo-1,6-dihydropyridine-2-carboxylic acid (146). A mixture of acetic anhydride (4 mL) and 30% H_2O_2 (1 mL) was stirred in ice bath for 4 h to form a homogenous peracetic acid solution. The peracetic acid formed was then added drop-wise to a stirring solution of 6-hydroxypicolinic acid (0.25 gm, 1.79 mmol) in a mixture of trifluoro acetic acid (3 mL) and glacial acetic acid (3 mL). The reaction mixture was stirred at rt for 1h and then heated gradually to 80 °C and kept at 80 °C for 10 h. After the reaction, the reaction mixture was evaporated and 10% KOH solution was added to the residue and the solution stirred at 80 °C for another 6 h after which the product was precipitated with conc. HCl. The crude was purified using column chromatography (10-25% MeOH: DCM) to afford pure **146**. White solid; yield 60%; ^{1}H NMR (300 MHz, DMSO-d_6): δ 7.45 (dd, 1H, J_1 = 9.0 Hz, J_2 = 7.2 Hz, ArH), 6.73 (dd, 1H, J_1 = 9.0 Hz, J_2 = 1.8 Hz, ArH), 6.65 (dd, 1H, J_1 = 6.9 Hz, J_2 = 1.5 Hz, ArH); MS (ESI): m/z 153.7 $[M-H]^-$.

1-(benzyloxy)-6-oxo-1,6-dihydropyridine-2-carboxylic acid (147). Benzyl chloride (3.09 mmol, 0.357 mL) was added to a solution of intermediate **146** (0.40 gm, 2.58 mmol) and anhydrous K_2CO_3 (5.16 mmol) in methanol (20 mL). The reaction was then refluxed for 16 h. After the reaction, the reaction mixture was filtered and evaporated to dryness. The residue was dissolved in water and acidified with 6M HCl to a pH 2.0. The white precipitate formed was filtered, washed with cold water and dried to give a pure product. White solid; mp 178-180 °C; yield 41%; ^{1}H NMR (300 MHz, DMSO-d_6): δ 7.40-7.52 (m, 6H, ArH), 6.74 (dd, 1H, J_1 = 9.1 Hz, J_2 = 1.8 Hz, ArH), 6.56 (dd, 1H, J_1 =

6.6 Hz, J_2 = 1.5 Hz, ArH), 5.28 (s, 2H, CH_2); MS (ESI): m/z 243.8 $[M-H]^-$.

1-(benzyloxy)-*N*-(4-fluorobenzyl)-6-oxo-1,6-dihydropyridine-2-carboxamide (148). Excess oxalyl chloride was added to a suspension of intermediate **147** (0.475 gm, 1.93 mmol) in toluene (10 mL). DMF (1 drop) as catalyst was added after which the mixture became clear. The resulting solution was stirred at 60 °C for 4 h and the solvent evaporated to dryness. The resulting residue (acid chloride) was directly used for the next reaction. The crude acid chloride (0.45 g, 1.71 mmol) was dissolved in dry THF and Et_3N (0.24 mL) was added. 4-fluoro benzyl amine (0.19 mL, 1.71 mmol) was then added to the above solution and reaction mixture stirred overnight at 60 °C. After the reaction was complete, the solvent was evaporated and extracted with DCM. The organic layer was washed with 1M NaOH and 1M HCl and evaporated to get the crude product. The crude was purified using column chromatography (10-20% ethyl acetate/hexane) to get pure intermediate **148**. White solid; mp 183-185 °C; overall yield 41%; ^{1}H NMR (300 MHz, DMSO-d_6): δ 9.41 (t, 1H, J = 5.5 Hz, NH), 7.50 (dd, 1H, J_1 = 8.5 Hz, J_2 = 6.5 Hz, ArH), 7.36-7.40 (m, 5H, ArH), 7.32 (dd, 2H, J_1 = 8.0 Hz, J_2 = 6.0 Hz, ArH), 7.04 (t, 2H, J = 8.5 Hz, ArH), 6.66 (d, 1H, J = 9.0 Hz, ArH), 6.35 (d, 1H, J = 6.5 Hz, ArH), 5.23 (s, 2H, CH_2), 4.41 (d, 2H, J = 5.5 Hz, CH_2); MS (ESI): m/z 375.1 [M+23].

***N*-(4-fluorobenzyl)-1-hydroxy-6-oxo-1,6-dihydropyridine-2-carboxamide (159).** The intermediate **148** (0.27 gm, 0.766 mol) was deprotected using a 1:1 mixture of HCl and glacial acetic acid and stirring at rt for 48 h. the reaction mixture was then evaporated, dissolved in minimum amount of water, filtered and dried. The crude was crystallized with ethyl acetate. White solid; yield 67%; mp 138-140 °C; ^{1}H NMR (300 MHz, DMSO-d_6): δ 9.31(t, 1H, J = 5.5 Hz, NH), 7.36-7.42 (m, 3H, ArH), 7.16 (t, 2H, J = 9.0 Hz, 6.58 (d, 1H, J = 9.5 Hz, ArH), 6.33 (d, 1H, J = 7.0 Hz), 4.41 (d, 2H, J = 5.5 Hz); MS (ESI): m/z 285.0 [M+23].

Biological Assays

Materials, chemicals, and enzymes. All compounds were dissolved in DMSO and the stock solutions were stored at -20 °C. γ[^{32}P]-ATP was purchased from either Amersham Biosciences or ICN. The expression systems for wild-type IN were a generous gift from Dr. Robert Craigie, Laboratory of Molecular Biology, NIDDK, NIH, Bethesda, MD. Cell lines were obtained from American Type Culture Collection (ATCC, Rockville, MD).

Preparation of oligonucleotide substrates. The oligonucleotides 21top, 5′-GTGTGGAAAATCTCTAGCAGT-3′, and 21bot, 5′-ACTGCTAGAGATTTTCCACAC-3′, were purchased from the Norris Cancer Center Microsequencing Core Facility (University of Southern California) and purified by UV shadowing on polyacrylamide gel. To analyze the extent of 3′-P and ST using 5′-end labeled substrates, 21top was 5′-end labeled using T4 polynucleotide kinase (Epicentre, Madison, WI) and γ[32P]-ATP

(Amersham Biosciences or ICN). The kinase was heat-inactivated and 21-bot was added in 1.5M excess. The mixture was heated at 95 °C, allowed to cool slowly to rt, and run through a G25 mini spin column (USA Scientific) to separate double-stranded oligonucleotide from unincorporated material.

Integrase assays. To determine the extent of 3′-P and ST, wild-type IN was preincubated at a final concentration of 200 nM with the inhibitor in reaction buffer (50 mM NaCl, 1 mM HEPES, pH 7.5, 50 μM EDTA, 50 μM dithiothreitol, 10% glycerol (w/v), 7.5 mM $MnCl_2$, 0.1 mg/mL bovine serum albumin, 10 mM 2-mercaptoethanol, 10% dimethylsulfoxide, and 25 mM MOPS, pH 7.2) at 30 °C for 30 min. An aliquot (5μL) was electrophoresed on a denaturing 20% polyacrylamide gel (0.09 M Tris-borate, pH 8.3, 2 mM EDTA, 20% acrylamide, and 8M urea). Gels were dried, exposed in a PhosphorImager cassette, and analyzed using a Typhoon 8610 Variable Mode Imager (Amersham Biosciences) and quantitated using ImageQuant 5.2. Percent inhibition (%I) was calculated using (**Equation 3-1**). The IC_{50} values were determined by plotting the logarithm of compound concentration versus percent inhibition to obtain the concentration that produced 50% inhibition.

Anti-HIV-1 activity assay. The testing of the ability of potent compounds to inhibit HIV replication in cell culture was done according to a previously reported procedure.[182] PBMC (107 cells/T25flask) were stimulated with phytohemagglutinin for 3 days and infected with a wild-type HIV-1 strain (strain LAI) at 100 50% tissue culture infective doses, as described previously.[182] The cultures were kept for 5 days in the presence of test compounds at serial 1-log dilutions. Subsequently, human PBMC were removed from the culture supernatant by centrifugation (400g, 10 min, 4 °C). This clarified supernatant was tested by a reverse transcriptase assay.

Cytotoxicity assays. The cytotoxicity of compounds was evaluated using uninfected PBMC and CEM leukemia cells according to a previous method.[183] PBMC were obtained from whole blood of healthy individuals, while CEM were obtained from the ATCC (Rockville, MD). The PBMC and CEM cells were cultured in the presence or absence of compound for 6 days. After this time period, cells were stained with Trypan blue dye, and counted for cell proliferation and viability according to the previously reported procedure.[184]

CHAPTER 5. SYNTHESIS AND BIOLOGICAL STUDIES OF PHENANTHRENE DIKETO ACIDS AS HIV-1 INTEGRASE INHIBITORS

Introduction

Raltegravir is currently the only IN inhibitor approved by the FDA.[51] Unfortunately, clinical studies have reported viral mutants particularly T66I, G148H, N155H, and double mutant G148H G140S, that are resistant to both raltegravir and elvitegravir.[138,139] Thus, it is highly imperative to design new chemical classes as second generation HIV-1 IN inhibitors that not only have potent inhibitory activities, but also have the potential to circumvent the eminent failure resulting from the emergence of viral resistance to current IN inhibitors.

Previously, our laboratory has reported 5(*H*)-phenanthridin-6-one diketo acids and related compounds as a novel class of HIV-1 IN inhibitors.[152] In this chapter, I have synthesized a series of substituted phenanthrene β-diketo acids having potent *in vitro* IN inhibitory activities. Selected compounds were also tested for their abilities to inhibit HIV-1 replication in cell culture.

Chemistry

The synthesis of target phenanthrenes β-diketo acids was accomplished by first synthesizing the acetyl phenanthrene intermediates **168a-168h** using **Scheme 5-1**. On the basis of commercial availability, two different sets of starting materials were used to perform the Suzuki coupling reaction. Thus, either the acetyl boronic acid derivatives (**160a-160d**) were reacted with the aldehyde containing halogen partners (**161a-161d**) to synthesize intermediates **164a-164d** or alternatively, the formyl boronic acid derivatives (**162e-162h**) were coupled with iodo acetyl starting materials (**163e-163h**) to synthesize intermediates **164e-164h**. For the coupling reaction, our first attempt with Pd $(PPh_3)_4$ in toluene did not yield the desired product. The reaction was then successfully optimized by using a polymer bound Pd $(PPh_3)_4$ with triethyl amine as a base in a dioxane-ethanol solvent under inert atmosphere.[193,194] Conditions varied from ice-cold (0 °C) to reflux and the reaction was stirred from 6 h to 48 h depending upon the starting materials used. The aldehyde intermediates were converted to the corresponding alkynes by Seyferth-Gilbert homologation under which, a mixture of intermediates **164a-164h**, dimethyl-(1-diazo-2-oxopropyl) phosphonate, and K_2CO_3 was stirred in methanol at 0 °C for 17 h.[195] The alkyne intermediates **165a-165h** were then subjected to a 6-endo dig cyclization with $PtCl_2$ by refluxing in toluene for 24 h under inert conditions to yield desired phenanthrenes **168a-168h**.[196] An alternative efficient microwave synthesis reported by Kim *et al.*[197] was also used to synthesize the acetyl phenanthrene derivatives **168i** and **168j** (**Scheme 5-2**). This one-pot synthesis of 9′-acetyl phenanthrenes was accomplished by a step-wise Suzuki-Miyaura coupling reaction followed by an intramolecular Aldol condensation. Therefore, **166a** and **166b** phenyl propanone starting materials were coupled with (2-formyl-4-methoxyphenyl) boronic acid (**167**) using Pd $(PPh_3)_4$ with

Scheme 5-1. Synthesis of intermediates 168a-168h

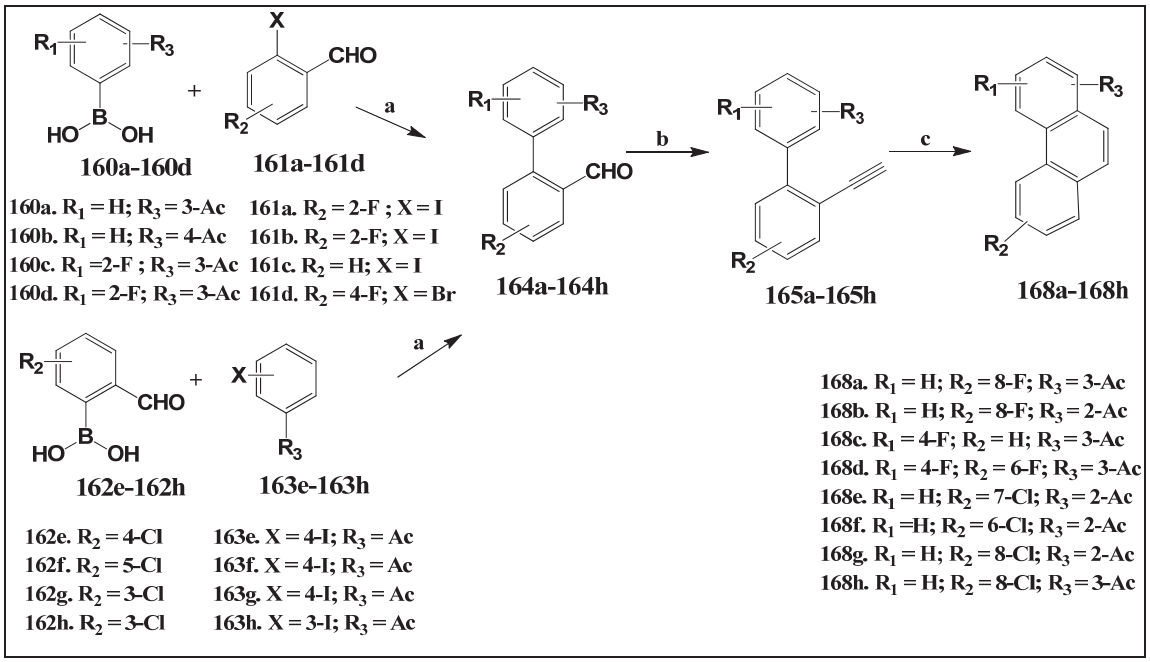

Reagent and conditions: (a) Polymer bound Pd $(PPh_3)_4$ (1mol%), Et_3N, dioxane, EtOH ice/reflux , 6 h-2 days; yields 34-78% (b) dimethyl-(1-diazo-2-oxopropyl) phosphonate, K_2CO_3, MeOH, ice, 17 h; yields 35-64% (c) $PtCl_2$, toluene, reflux, 24 h; yields 43-60%.

Scheme 5-2. Synthesis of intermediates 168i-168j

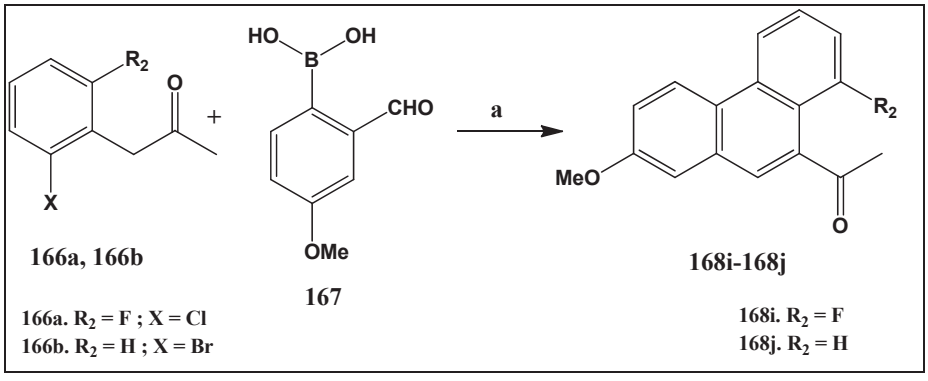

Reagent and conditions: (a) Microwave: 10 min, 150 °C, Pd $(PPh_3)_4$ (4 mol%), S-Phos (6 mol%), Cs_2CO_3, toluene-EtOH (2:1); yields 48-51%.

cesium carbonate as a base and S-Phos as catalyst. The reaction was performed in toluene/ethanol (2:1) mixture and irradiated at 60-80 W power and 150 °C for 10 min. All the acetyl phenanthrene intermediates **168i-168j** were then subjected to oxalylation reaction. Our initial attempt with diethyl oxalate did not yield the desired product. Literature reports[198] suggest terbutyl methyl oxalate as an oxalylating agent for halogen-substituted acetophenones. The use of terbutyl methyl oxalate (**170**), which was prepared according to literature[199] by the reaction of methyl chlorooxo acetate, t-butanol and pyridine in anhydrous ether, successfully resulted in the formation (**Scheme 5-3**) of the corresponding diketo esters **171i-171j**. The ester derivatives were taken to the next step directly without further purification and hydrolyzed with aq. NaOH to their corresponding desired diketo acid final products **172-181**.

Biological Results and Discussion

The synthesized target compounds (**Table 5-1**) were then tested for their ability to inhibit strand transfer (ST) and 3′-processing (3′-P). The structure activity relationship around these halogen-substituted phenanthrene derivatives suggests that the β-diketo acid functionality is well tolerated at R_1 and R_2 positions. For e.g., compare analogs **176**, **177**, and **179** all of which have potent and similar ST IC_{50}s of 1.4, 1.3, and 1.2 μM, respectively. However, comparison of compounds **179** vs. **178** and **172** vs. **173** indicates that the β-diketo acid functionality is slightly more favorable at R_2 position. In particular, compound **159** was about four times more active than compound **178** against ST reaction. Our laboratory has previously reported unsubstituted phenanthrene derivative **182** with diketo acid at the R_2 position had ST IC_{50} value of 2.7 μM.[152] With respect to compound **182**, while substitution of chlorine moiety at R_6 position (compound **179**) improved activity, a fluoro substituent at this position (compound **172**) resulted in a slight loss of potency; also implying that the Cl substituent did better than the fluoro counterpart (compare compounds **179** and **172**) at this position. That fluorine may not be an optimal substituent at R_6 position is also evident when one considers that compound **181** (ST IC_{50} of 3 μM) was two-folds more active than compound **180** (ST IC_{50} of 6 μM). Chlorine was also found to improve activity at R_4 and R_5 positions. Compounds **177** and **176** were about four times more potent than their unsubstituted counterparts (2,4-dioxo-4-(phenanthren-2-yl) butanoic acid, ST IC_{50} of 4.8 μM), synthesized previously.[152] Chlorine substitution at R_5 in compound **176** also improved selectivity (nine-folds) for the ST step. Compound **177** showed potent activities against both 3′-P and ST reactions with IC_{50}s of 5.0 μM and 1.3 μM, respectively. The reason for the dramatic loss of potency for both ST and 3′-P with compound **174** is not very apparent. It might be due to ineffective metal chelation by the β-diketo acid functionality considering, the electron withdrawing effect of the adjacent fluorine substituent. The improvement of activity of compound **175** (ST IC_{50} of 8.0 μM) implies a favorable effect of the fluorine substituent at the R_5 position. This may be one of the reasons why compound **176**, having a more hydrophobic Cl at the R_5 position, has improved activity over compound **175**; also implying that hydrophobic interaction at this position may be an important contributor to activity. Compound **181**, with an electron donating methoxy group at the R_1 position, and the diketo acid moiety at R_7 showed an IC_{50} of 3 μM against ST. This is a significant loss

Scheme 5-3. Synthesis of compounds 172-181

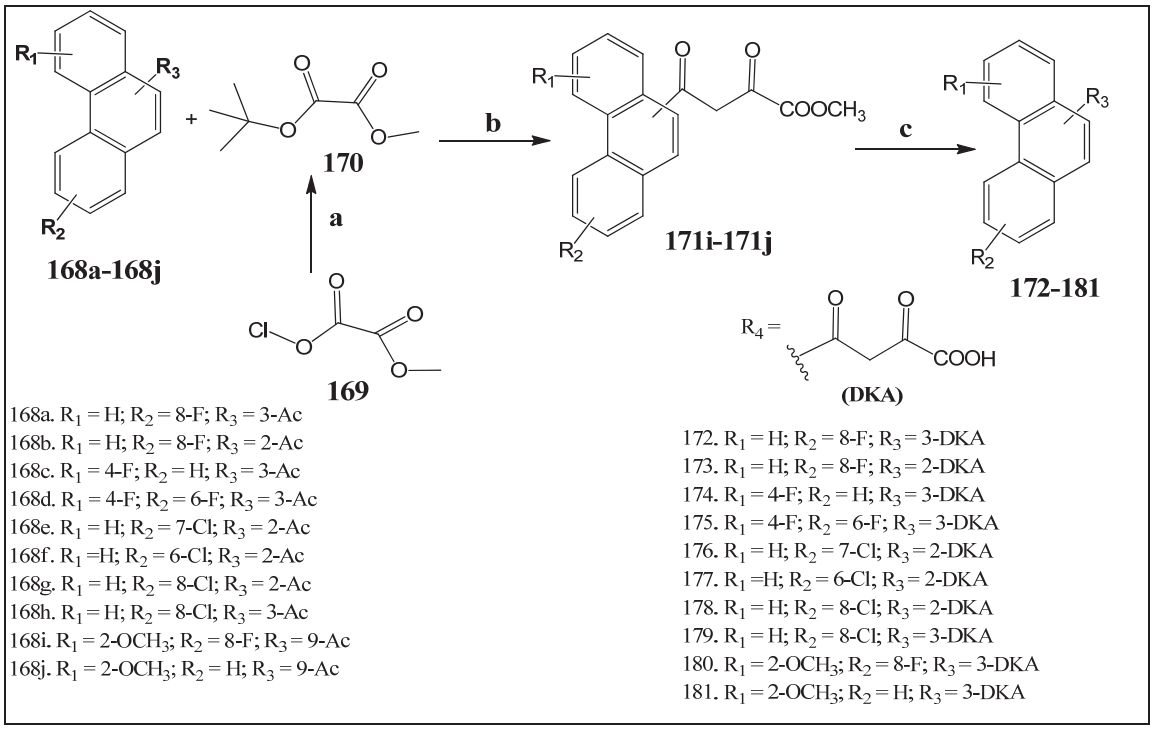

168a. R_1 = H; R_2 = 8-F; R_3 = 3-Ac
168b. R_1 = H; R_2 = 8-F; R_3 = 2-Ac
168c. R_1 = 4-F; R_2 = H; R_3 = 3-Ac
168d. R_1 = 4-F; R_2 = 6-F; R_3 = 3-Ac
168e. R_1 = H; R_2 = 7-Cl; R_3 = 2-Ac
168f. R_1 =H; R_2 = 6-Cl; R_3 = 2-Ac
168g. R_1 = H; R_2 = 8-Cl; R_3 = 2-Ac
168h. R_1 = H; R_2 = 8-Cl; R_3 = 3-Ac
168i. R_1 = 2-OCH_3; R_2 = 8-F; R_3 = 9-Ac
168j. R_1 = 2-OCH_3; R_2 = H; R_3 = 9-Ac

172. R_1 = H; R_2 = 8-F; R_3 = 3-DKA
173. R_1 = H; R_2 = 8-F; R_3 = 2-DKA
174. R_1 = 4-F; R_2 = H; R_3 = 3-DKA
175. R_1 = 4-F; R_2 = 6-F; R_3 = 3-DKA
176. R_1 = H; R_2 = 7-Cl; R_3 = 2-DKA
177. R_1 =H; R_2 = 6-Cl; R_3 = 2-DKA
178. R_1 = H; R_2 = 8-Cl; R_3 = 2-DKA
179. R_1 = H; R_2 = 8-Cl; R_3 = 3-DKA
180. R_1 = 2-OCH_3; R_2 = 8-F; R_3 = 3-DKA
181. R_1 = 2-OCH_3; R_2 = H; R_3 = 3-DKA

Reagent and conditions: (a) t-butanol, pyridine, ether, rt, 2 h; (b) NaOMe, MeOH, 60 °C, 4 h; (c) aq. NaOH, MeOH-THF(1:1), 6 h; overall (steps b and c) yield 78-93%.

Table 5-1. Structure and HIV-1 IN inhibitory activities of phenanthrene β-diketo acids

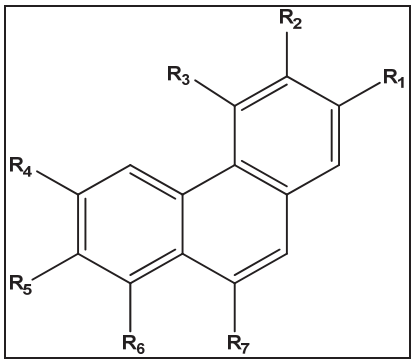

Cpd.	R_1	R_2	R_3	R_4	R_5	R_6	R_7	Activity (IC_{50} μM)	
								3′-P[a]	ST[b]
172	H	DKA[c]	H	H	H	F	H	11 ± 2	3 ± 2
173	DKA	H	H	H	H	F	H	35 ± 13	4 ± 1
174	H	DKA	F	H	H	H	H	83 ± 15	63 ± 16
175	H	DKA	F	H	F	H	H	63 ± 12	8 ± 2
176	DKA	H	H	H	Cl	H	H	12 ± 3	1.4
177	DKA	H	H	Cl	H	H	H	5 ± 3	1.3 ± 0.1
178	DKA	H	H	H	H	Cl	H	19 ± 2	4 ± 1
179	H	DKA	H	H	H	Cl	H	11 ± 4	1.2 ± 0.3
180	OCH_3	H	H	H	H	F	DKA	44 ± 10	6 ± 2
181	OCH_3	H	H	H	H	H	DKA	32 ± 12	3 ± 2
182[d]	H	DKA	H	H	H	H	H	25 ± 7	2.7 ± 2

[a] 3′-P = 3′-procesing; [b] ST = Strand Transfer; [c] DKA = diketo acid; [d] compound previously reported.[152]

of activity when compared to its parent unsubstituted diketo acid analog, 2,4-dioxo-4-(phenanthren-9-yl)butanoic acid (ST IC_{50} of 0.38 μM) that our laboratory has earlier reported.[152] This suggests that the R_1 position is sensitive to modifications and could be further exploited to determine the structure activity relationship around this novel class of IN inhibitors.

Next, to determine their potential as anti-HIV agents, two potent analogs (compounds **176** and **177**) were tested for their ability to inhibit HIV-1 replication in primary human peripheral blood mononuclear cells (PBMC). Both compounds showed moderate inhibition of HIV replication with IC_{50}s of 20.7 and 27.5 μM, respectively, (**Table 5-2**). The reduced antiviral potency might be because of poor solubility, binding to serum proteins and/or cellular distribution factors. The cytotoxicity assays showed that the selected compounds, **176** and **177**, have toxicities when tested against PBMC, human CEM lymphoblastic leukemia cells and African green monkey Vero cells. However, a phenanthrene analog (**183**) which our lab has previously reported possessed potent anti-HIV activity (EC_{50} of 8.0 μM) and had selectivity index of 10 for inhibition of HIV replication in cell culture. This indicates that this series could be further developed with optimization efforts directed at reducing their cell-based toxicities and simultaneously enhancing their anti-viral activities.

Experimental Section

Chemistry

All the reagents and solvents were purchased from the Aldrich Chemical Company and used without further purification. Progress of reactions was monitored by TLC on silica gel GHLF-250 micron plates (Analtech, Inc.). Fisher scientific Da visil grade 1740 (170–400 mesh) silica gel was used for flash column chromatography. ^1H NMR spectra were recorded on Brucker AR, 300 or 500-MHz spectrometer: chemical shifts are expressed in δ values (ppm) and coupling constants (*J*) in Hertz (Hz). Mass spectral data were determined on a Brucker-HP Esquire-LC spectrometer (ESI-MS). Infra red (IR) spectra of alkyne derivatives were recorded on a Perkin Elmer Spectrum 100 FT-IR spectrometer. HPLC analysis of final compounds was carried out using a reverse phase SUPELCOSIL 5 μm C-18 column of dimensions 25 cm x 4.6 cm. Area % purity was detected at 254 nm. A linear gradient elution with water (A) and methanol (B) at a flow-rate of 1.5 mL/min was used. Gradient elution of the mobile phase was 80% A to 20% A from 0-3 min, 20% A and 80% B for 3-17 min and 20% A to 80% A from 17-20 min. Melting points of solids were determined using a Fisher-Johns melting point apparatus and are reported uncorrected.

General procedure for the synthesis of intermediates 164a-164h. Acetyl phenyl boronic acid derivatives (3.78 g, 20.77 mmol) were reacted with halogen containing aldehyde partners (4 g, 16 mmol) or alternatively, aldehyde phenyl

Table 5-2. Anti-HIV activities of selected phenanthrene compounds

Comp.	R_1	R_4	R_5	EC_{50} (μM)	Cytotoxicity (IC_{50} μM)		
					PBMC[a]	CEM[b]	VERO[c]
176	DKA	H	Cl	20.9 ± 15.8	14.1	12.1	7.2
177	DKA	Cl	H	27.5 ± 10.2	4.0	13.1	4.5

[a] Human Peripheral blood mononuclear cells; [b] CEM lymphoblastic leukemia cells; [c] African green monkey Vero cells.

boronic acid starting materials (3.9 g, 21.13 mmol) were reacted with halogen substituted acetophenones (4.0 g, 16.25 mmol) for the Suzuki coupling reaction. Thus, aryl halide and polymer bound Pd $(PPh_3)_4$ (0.25 g, 1.35 mol%) were added to a dioxane-ethanol (30 mL, 4:1) mixture. This was followed by the addition of triethylamine (1.17 mL, 32 mmol) and the boronic acid derivative. The resultant solution was degassed several times with argon and stirred in ice or refluxed for 6-48 h depending upon the starting materials used. After the reaction, the mixture was filtered through celite and evaporated to dryness. The crude material was purified by column chromatography (10-20% ethyl acetate/ hexane) to obtain pure intermediates **164a-164h**.

3'-acetyl-3-fluoro-[1,1'-biphenyl]-2-carbaldehyde (164a). Yellow solid; mp 73-75 °C; yield 42%; ^{1}H NMR (300 MHz, DMSO-d_6): δ 9.94 (s, 1H, CHO), 8.04 (d, 1H, J = 7.2 Hz, ArH), 7.95 (s, 1H, ArH), 7.77 (dd, 1H, J_1 = 9.0 Hz, J_2 = 3.0 Hz, ArH), 7.65 (d, 2H, J = 7.2 Hz, ArH), 7.45 (t, 1H, J = 7.8 Hz, ArH), 7.35 (d, 1H, J = 7.8 Hz, ArH), 2.62 (s, 3H, $COCH_3$); MS (ESI): m/z 265.0 $[M+Na]^+$.

4'-acetyl-3-fluoro-[1,1'-biphenyl]-2-carbaldehyde (164b). Yellow solid; mp 106-108 °C; yield 63%; ^{1}H NMR (300 MHz, DMSO-d_6): δ 9.94 (s, 1H, CHO), 8.05 (d, 2H, J = 8.4 Hz, ArH), 7.74-7.82 (m, 1H, ArH), 7.55 (d, 2H, J = 8.1 Hz, ArH), 7.46 (t, 1H, J = 8.4 Hz, ArH), 7.35 (d, 1H, J = 7.5 Hz, ArH), 2.64 (s, 3H, $COCH_3$); MS (ESI): m/z 265.0 $[M+Na]^+$.

3'-acetyl-2'-fluoro-[1,1'-biphenyl]-2-carbaldehyde (164c). White solid; mp 74-76 °C; yield 45%; ^{1}H NMR (300 MHz, DMSO-d_6): δ 9.89 (d, 1H, J = 2.1 Hz, CHO), 8.0 (d, 1H, J = 7.8 Hz, ArH), 7.87-7.93 (m, 1H, ArH), 7.79-7.84 (m, 1H, ArH), 7.66-7.72 (m, 2H, ArH), 7.52 (d, 1H, J = 7.5 Hz, ArH), 7.42-7.48 (m, 1H, ArH), 2.58 (d, 3H, J = 4.2 Hz, $COCH_3$); MS (ESI): m/z 265.0 $[M+Na]^+$.

3'-acetyl-2',5-difluoro-[1,1'-biphenyl]-2-carbaldehyde (164d). Light yellow solid; mp 48-50 °C; yield 34 %; ^{1}H NMR (300 MHz, DMSO-d_6): δ 9.82 (d, 1H, J = 2.4 Hz, CHO), 8.09 (dd, 1H, J_1 = 8.4 Hz, J_2 = 6.0 Hz, ArH), 7.92 (dt, 1H, J_1 = 7.5 Hz, J_2 = 1.8 Hz, ArH), 7.73 (dt, 1H, J_1 = 7.8 Hz, J_2 = 1.8 Hz, ArH), 7.55 (dt, 1H, J_1 = 8.7 Hz, J_2 = 2.7 Hz, ArH), 7.43-7.50 (m, 2H, ArH), 2.60 (d, 3H, J = 4.2 Hz, $COCH_3$); MS (ESI): m/z 283.0 $[M+Na]^+$.

4'-acetyl-4-chloro-[1,1'-biphenyl]-2-carbaldehyde (164e). White solid; mp 138-140 °C; yield 71%; ^{1}H NMR (300 MHz, DMSO-d_6): δ 9.83 (s, 1H, CHO), 8.08 (d, 2H, J = 8.1 Hz, ArH), 7.92 (d, 1H, J = 2.1 Hz, ArH), 7.85 (dd, 1H, J_1 = 8.4 Hz, J_2 = 2.4 Hz, ArH), 7.62 (d, 2H, J = 8.4 Hz, ArH), 7.60 (d, 1H, J = 8.4 Hz, ArH), 2.64 (s, 3H, $COCH_3$); m/z 281.0 $[M+Na]^+$.

4'-acetyl-5-chloro-[1,1'-biphenyl]-2-carbaldehyde (164f). White solid; mp 100-102 °C; yield 71%; ^{1}H NMR (300 MHz, DMSO-d_6): δ 9.83 (s, 1H, CHO), 8.07 (d, 2H, J = 8.4 Hz, ArH), 7.97 (d, 1H, J = 8.4 Hz, ArH), 7.71 (d, 1H, J = 8.4 Hz, ArH), 7.66 (d, 2H, J = 7.5 Hz, ArH), 7.63 (s, 1H, ArH), 2.65 (s, 3H, $COCH_3$); MS (ESI): m/z 281.0 $[M+Na]^+$.

4'-acetyl-3-chloro-[1,1'-biphenyl]-2-carbaldehyde (164g). Light yellow solid; mp 95-97 °C; yield 78%; ^{1}H NMR (300 MHz, DMSO-d_6): δ 10.13 (s, 1H, CHO), 8.02 (dd, 2H, J_1 = 8.11 Hz, J_2 = 1.5 Hz, ArH), 7.66-7.73 (m, 2H, ArH), 7.50 (dd, 2H, J_1 = 8.1 Hz, J_2 = 1.2 Hz, ArH), 7.43-7.46 (m, 1H, ArH), 2.63 (d, 3H, J = 1.5 Hz, $COCH_3$); MS (ESI): m/z 281.0 $[M+Na]^+$.

3'-acetyl-3-chloro-[1,1'-biphenyl]-2-carbaldehyde (164h). White solid; mp 86-88 °C; yield 58%; ^{1}H NMR (300 MHz, DMSO-d_6): δ 10.15 (s, 1H, CHO), 7.99-8.02 (m, 1H, ArH), 7.91 (s, 1H, ArH), 7.58-7.73 (m, 4H, ArH), 7.47 (dd, 1H, J_1 = 6.6 Hz, J_2 = 1.8 Hz, ArH), 2.61 (s, 1H, $COCH_3$); MS (ESI): m/z 281.0 $[M+Na]^+$.

General procedure for the synthesis of intermediates 165a-165h. Dimethyl-(1-diazo-2-oxopropyl) phosphonate (4.46 g, 23.21 mmol) was added drop wise to a mixture of K_2CO_3 (4.0 g, 28.94 mmol) in methanol (30 mL) at 0 °C. The solution was stirred for 10 min during which the color turned yellow. Aldehyde intermediates **164a-164h** (3.0 g, 11.62 mmol) were then added to the above solution and the reaction stirred in ice for 17 h. After completion of reaction, the reaction mixture was evaporated. Saturated $NaHCO_3$ solution was added to the residue and extracted with ethyl acetate. The ethyl acetate layer was evaporated to dryness and the crude was purified by column chromatography (5-15% ethyl acetate/hexane) to afford pure intermediates **165a-165h**.

1-(2'-ethynyl-3'-fluoro-[1,1'-biphenyl]-3-yl)ethanone (165a). Brown flakes; mp 56-58 °C; yield 59%; IR neat 3288 cm^{-1} (alkyne C-H), 2107 cm^{-1} (alkyne C-C); ^{1}H NMR (300 MHz, DMSO-d_6): δ 8.15 (s, 1H, ArH), 8.06 (d, 1H, J = 7.5 Hz, ArH), 7.83 (d, 1H, J = 7.2 Hz, ArH), 7.52-7.65 (m, 2H, ArH), 7.36 (t, 2H, J = 7.8 Hz, ArH), 4.48 (s, 1H, alkyne CH), 2.62 (s, 3H, $COCH_3$); MS (ESI): m/z 261.0 $[M+Na]^+$.

1-(2'-ethynyl-3'-fluoro-[1,1'-biphenyl]-4-yl)ethanone (165b). Off-white solid; mp 100-102 °C; yield 63 %; IR neat 3282 cm^{-1} (alkyne C-H), 2116 cm^{-1} (alkyne C-C); ^{1}H NMR (300 MHz, DMSO-d_6): δ 8.05 (d, 2H, J = 8.1 Hz, ArH), 7.72 (d, 2H, J = 8.4 Hz, ArH), 7.56 (dd, 1H, J_1 = 7.8 Hz, J_2 = 7.5 Hz, ArH), 7.39 (t, 1H, J = 8.7 Hz, ArH), 7.34 (d, 1H, J = 7.5 Hz, ArH), 4.5 (s, 1H, alkyne CH), 2.64 (s, 3H, $COCH_3$); MS (ESI): m/z 261.0 $[M+Na]^+$.

1-(2'-ethynyl-2-fluoro-[1,1'-biphenyl]-3-yl)ethanone (165c). Violet liquid; yield 57%; ^{1}H NMR (300 MHz, DMSO-d_6): δ 7.84 (t, 1H, J = 7.5 Hz, ArH), 7.64 (d, 2H, J = 6.9 Hz, ArH), 7.37-7.56 (m, 4H, ArH), 4.11 (s, 1H, alkyne CH), 2.60 (d, 1H, J = 4.2 Hz, $COCH_3$); MS (ESI): m/z 261.0 $[M+Na]^+$.

1-(2'-ethynyl-2,5'-difluoro-[1,1'-biphenyl]-3-yl)ethanone (165d). Violet solid; mp 51-53 °C; yield 35%; IR neat 3312 cm^{-1} (alkyne C-H); ^{1}H NMR (300 MHz, DMSO-d_6): δ 7.83-7.90 (m, 1H, ArH), 7.66-7.73 (m, 2H, ArH), 7.32-7.44 (m, 3H, ArH), 4.10 (s, 1H, alkyne CH), 2.64 (dd, 3H, J_1 = 1.8 Hz, J_2 = 1.5 Hz, $COCH_3$); MS (ESI): m/z 279.0 $[M+Na]^+$.

1-(4'-chloro-2'-ethynyl-[1,1'-biphenyl]-4-yl)ethanone (165e). White solid; mp 138-140 °C; yield 61%; IR neat 3230 cm^{-1} (alkyne C-H), 2097 cm^{-1} (alkyne C-C); ^1H NMR (300 MHz, DMSO-d_6): δ 8.04 (d, 2H, J = 7.8 Hz, ArH), 7.71 (s, 1H, ArH), 7.70 (d, 2H, J = 8.1 Hz, ArH), 7.61 (d, 1H, J = 8.1 Hz, ArH), 7.50 (d, 1H, J = 8.4 Hz, ArH), 4.25 (s, 1H, alkyne CH), 2.63 (s, 3H, $COCH_3$); m/z 277.0 $[M+Na]^+$.

1-(5'-chloro-2'-ethynyl-[1,1'-biphenyl]-4-yl)ethanone (165f). White solid; mp 102-104 °C; yield 64%; IR neat 3224 cm^{-1} (alkyne C-H), 2106 cm^{-1} (alkyne C-C); ^1H NMR (300 MHz, DMSO-d_6): δ 8.02 (d, 2H, J = 8.1 Hz, ArH), 7.71 (d, 2H, J = 7.8 Hz, ArH), 7.65 (d, 1H, J = 8.1 Hz, ArH), 7.54 (d, 1H, J = 1.5 Hz, ArH), 7.49-7.52 (m, 1H, ArH), 4.26 (s, 1H, alkyne CH), 2.64 (s, 3H, $COCH_3$); MS (ESI): m/z 277.0 $[M+Na]^+$.

1-(3'-chloro-2'-ethynyl-[1,1'-biphenyl]-4-yl)ethanone (165g). Light yellow solid; mp 123-125 °C; yield 50%; IR neat 3266 cm^{-1} (alkyne C-H), 2109 cm^{-1} (alkyne C-C); ^1H NMR (300 MHz, DMSO-d_6): δ 8.05 (dd, 2H, J_1 = 8.1 Hz, J_2 = 1.5 Hz, ArH), 7.70 (dd, 2H, J_1 = 8.1 Hz, J_2 = 1.5 Hz, ArH), 7.63 (d, 1H, J = 8.7 Hz, ArH), 7.52 (dt, 1H, J_1 = 7.8 Hz, J_2 = 1.8 Hz, ArH), 7.42 (d, 1H, J = 7.8 Hz, ArH), 4.96 (s, 1H, alkyne CH), 2.63 (d, 3H, J = 1.8 Hz, $COCH_3$); MS (ESI): m/z 277.0 $[M+Na]^+$.

1-(3'-chloro-2'-ethynyl-[1,1'-biphenyl]-3-yl)ethanone (165h). White solid; mp 97-99 °C; yield 46%; IR neat 3293 cm^{-1} (alkyne C-H), 2104 cm^{-1} (alkyne C-C); ^1H NMR (300 MHz, DMSO-d_6): δ 8.13 (s, 1H, ArH), 8.00 (d, 1H, J = 7.2 Hz, ArH), 7.81 (d, 1H, J = 7.2 Hz, ArH), 7.61-7.65 (m, 2H, ArH), 7.53 (t, 1H, J = 7.8 Hz, ArH), 7.45 (d, 1H, J = 7.8 Hz, ArH), 4.53 (s, 1H, alkyne CH); MS (ESI): m/z 277.0 $[M+Na]^+$.

General procedure for the synthesis of intermediates 168a-168h. A solution of alkyne intermediates **165a-165h** (1.0 g, 4.19 mmol) and $PtCl_2$ (0.55 g, 5 mol%) in toluene (20 mL) was stirred at 80 °C in argon for 24 h. After the reaction, the solution was filtered through celite and evaporated to dryness. The crudes were then purified by column chromatography (5-15% ethyl acetate/hexane) to give pure intermediates **168a-168h**.

1-(8-fluorophenanthren-3-yl)ethanone (168a). White solid; mp 80-82 °C; yield 60%; ^1H NMR (300 MHz, DMSO-d_6): δ 9.36 (s, 1H, ArH), 8.83 (d, 1H, J = 7.8 Hz, ArH), 8.09-8.16 (m, 3H, ArH), 7.99 (d, 1H, J = 9.0 Hz, ArH), 7.77 (d, 1H, J = 7.8 Hz, ArH), 7.55 (d, 1H, J = 7.8 Hz, ArH), 2.81 (s, 3H, $COCH_3$); MS (ESI): m/z 261.0 $[M+Na]^+$.

1-(8-fluorophenanthren-2-yl)ethanone (168b). Light yellow solid; mp 128-130 °C; yield 51%; ^1H NMR (300 MHz, DMSO-d_6): δ 8.95 (d, 1H, J = 8.7 Hz, ArH), 8.75 (d, 1H, J = 8.4 Hz, ArH), 8.73 (s, 1H, ArH), 8.21 (dd, 1H, J_1 = 8.7 Hz, J_2 = 1.5 Hz, ArH), 8.12 (d, 1H, J = 9.0 Hz, ArH), 8.07 (d, 1H, J = 9.0 Hz, ArH), 7.72-7.79 (m, 1H, ArH), 7.58 (t, 1H, J = 7.8 Hz, ArH), 2.75 (s, 3H, $COCH_3$); MS (ESI): m/z 261.0 $[M+Na]^+$.

1-(4-fluorophenanthren-3-yl)ethanone (168c). Off-white solid; mp 80-82 °C; yield 57%; ^1H NMR (300 MHz, DMSO-d_6): δ 9.03 (d, 1H, J = 7.8 Hz, ArH), 8.11 (d, 1H, J =

7.5 Hz, ArH), 8.07 (d, 1H, J = 9.0 Hz, ArH), 7.92-8.01 (m, 3H, ArH), 7.74-7.84 (m, 2H, ArH), 2.78 (d, 3H, J = 4.5 Hz, $COCH_3$); MS (ESI): m/z 261.0 $[M+Na]^+$.

1-(4,6-difluorophenanthren-3-yl)ethanone (168d). White solid; mp 128-130 °C; yield 53%; ^{1}H NMR (300 MHz, DMSO-d_6): 8.60 (d, 1H, J = 12.6 Hz, ArH), 8.18 (t, 1H, J = 7.8 Hz, ArH), 8.06 (d, 1H, J = 8.7 Hz, ArH), 7.87-8.01 (m, 3H, ArH), 7.66 (t, 1H, J = 8.4 Hz, ArH), 2.76 (d, 3H, J = 4.5 Hz, $COCH_3$); MS (ESI): m/z 279.0 $[M+Na]^+$.

1-(7-chlorophenanthren-2-yl)ethanone (168e). Light yellow solid; mp 122-124 °C; yield 43%;^{1}H NMR (300 MHz, DMSO-d_6): δ 8.92 (dd, 2H, J_1 = 8.7 Hz, J_2 = 2.1 Hz, ArH), 8.69 (s, 1H, ArH), 8.20 (d, 1H, J = 9.3 Hz, ArH), 8.18 (s, 1H, ArH), 8.08 (d, 1H, J = 9.0 Hz, ArH), 7.93 (d, 1H, J = 9.0 Hz, ArH), 7.76 (dd, 1H, J_1 = 8.7 Hz, J_2 = 2.1 Hz, ArH), 2.74 (s, 3H, $COCH_3$); MS (ESI): m/z 277.0 $[M+Na]^+$.

1-(6-chlorophenanthren-2-yl)ethanone (168f). Yellow solid; mp 103-105 °C; yield 53%;^{1}H NMR (300 MHz, DMSO-d_6): δ 8.99 (d, 1H, J = 8.7 Hz, ArH), 8.96 (s, 1H, ArH), 8.68 (d, 1H, J = 1.5 Hz, ArH), 8.17 (dd, 1H, J_1 = 8.7 Hz, J_2 = 1.8 Hz, ArH), 8.08 (d, 1H, J = 8.4 Hz, ArH), 8.04 (d, 1H, J = 9.0 Hz, ArH), 7.96 (d, 1H, J = 9.0 Hz, ArH), 7.75 (dd, 1H, J_1 = 8.4 Hz, J_2 = 1.8 Hz, ArH), 2.75 (s, 3H, $COCH_3$); MS (ESI): m/z 277.0 $[M+Na]^+$.

1-(8-chlorophenanthren-2-yl)ethanone (168g). White solid; mp 108-110 °C; yield 54%; ^{1}H NMR (300 MHz, DMSO-d_6): δ 8.98 (d, 1H, J = 8.7 Hz, ArH), 8.75 (s, 1H, ArH), 8.24 (d, 1H, J = 8.1 Hz, ArH), 8.04 (d, 1H, J = 6.9 Hz, ArH), 7.91 (d, 1H, J = 7.5 Hz, ArH), 7.70 (d, 1H, J = 6.9 Hz, ArH), 7.52 (t, 1H, J = 7.8 Hz, ArH), 7.41 (d, 1H, J = 7.5 Hz, ArH), 2.63 (s, 3H, $COCH_3$); MS (ESI): m/z 277.0 $[M+Na]^+$.

1-(8-chlorophenanthren-1-yl)ethanone and **1-(8-chlorophenanthren-3-yl)ethanone isomer (168h).** White solid; mp 110-112 °C yield 60%; ^{1}H NMR (300 MHz, DMSO-d_6): δ 9.13 (d, 1H, J = 8.4 Hz, ArH), 8.94 (d, 1H, J = 8.4 Hz, ArH), 8.58 (d, 1H, J = 9.6 Hz, ArH), 8.16-8.23 (m, 3H, ArH), 8.13 (s, 1H, ArH), 7.99 (d, 1H, J = 7.8 Hz, ArH), 7.87 (d, 2H, J = 8.1 Hz, ArH), 7.82 (d, 1H, J = 7.8 Hz, ArH), 7.75 (t, 2H, J = 7.5 Hz, ArH), 7.62-7.70 (m, 1H, ArH), 7.40-7.60 (m, 2H, ArH), 2.78 (s, 3H, $COCH_3$), 2.63 (s, 3H, $COCH_3$); MS (ESI): m/z 277.0 $[M+Na]^+$.

General procedure for the synthesis of intermediates 168i and 168j. To a thick-well borosilicate glass vial (10 mL) was added phenyl propanone starting materials (0.20 g, 0.94 mmol), 4-methoxy-2-formyl boronic acid (0.20 g, 1.12 mmol), Pd $(PPh_3)_4$ (0.043 g, 4mol %), Cs_2CO_3 (0.91 g, 2.82 mmol) and S-Phos (0.022 g, 6 mol%) sequentially in a toluene: ethanol (4 mL:2 mL) mixture. The reaction vial was then sealed and placed in a microwave reactor and irradiated with 60-80 W power at 150 °C for 10 min. The reaction mixture was then cooled to room temperature and diluted with excess ethyl acetate. The resulting solution was filtered through celite and concentrated in vacuo. The crude solid was purified by column chromatography (10-15% ethyl acetate/hexane).

1-(8-fluoro-2-methoxyphenanthren-9-yl)ethanone (168i). Yellow solid; mp

110-112 °C; yield 48%; ^{1}H NMR (300 MHz, DMSO-d_6): δ 8.76 (dd, 1H, J_1 = 9.0 Hz, J_2 = 2.4 Hz, ArH), 8.65 (dd, 1H, J_1 = 8.4 Hz, J_2 = 2.7 Hz, ArH), 7.88 (d, 1H, J = 2.7 Hz, ArH), 7.68-7.74 (m, 1H, ArH), 7.56 (bs, 1H, ArH), 7.39-7.48 (2H, m, ArH), 3.94 (d, 3H, J = 2.7 Hz, OCH_3), 2.61(t, 3H, J = 2.4 Hz, $COCH_3$); MS (ESI): m/z 291.0 $[M+Na]^+$.

1-(2-methoxyphenanthren-9-yl)ethanone (168j). Yellow solid; mp 97-99 °C; yield 51%; ^{1}H NMR (300 MHz, DMSO-d_6): δ 8.78 (d, 1H, J = 7.5 Hz, ArH), 8.76 (d, 1H, J = 8.4 Hz, ArH), 8.58 (d, 1H, J = 8.7 Hz, ArH), 8.50 (s, 1H, ArH), 7.64 (s, 1H, ArH), 7.59-7.72 (m, 2H, ArH), 7.43 (d, 1H, J = 8.7 Hz, ArH), 3.95 (s, 3H, OCH_3), 2.80 (s, 3H, $COCH_3$); MS (ESI): m/z 273.0 $[M+Na]^+$.

Synthesis of reagent *tert*-butyl methyl oxalate (170). Methyl oxalyl chloride (4.08 mmol, 0.376 mL) was added drop wise to a mixture of anhydrous pyridine (4.08 mmol, 194 µL), *tert*-butanol (2.04 mmol, 0.194 µL) and anhydrous ether (5 mL), and the resulting solution stirred at room temperature for 2 h. After the reaction, water was added to the mixture followed by a saturated solution of $NaHCO_3$. The reaction mixture was thereafter extracted with ethyl acetate and organic layer was concentration to obtain *tert*-butyl methyl oxalate (**170**) which was used without further purification. White liquid; MS (ESI): m/z 183.0 $[M+Na]^+$.

General procedure for the synthesis of final diketo acid compounds 172-181. To a stirred solution of freshly prepared NaOMe (145 mg Na metal in 2 mL methanol) in anhydrous THF(15 mL) at rt was added drop wise a mixture of tert-butyl methyl oxalate (1 mL) and acetyl phenanthrene intermediates (**168a-168j**) (0.4 g, 1.57 mmol) in DME (15 mL). The resulting red colored mixture was stirred at room temperature for 4 h. After the reaction, the mixture was poured into cold water and acidified with dilute HCl. Solid ester intermediates were precipitated in quantitative yields and were dried in vacuo and taken to the next step without further purification. Aqueous NaOH (5.87 mL, 1M) was added to the solution of ester intermediates **171i-171j** (0.50 g, 1.47 mmol) in a MeOH-THF (1:1, 20 mL) mixture. The resulting solution was stirred at rt for 6 h. After the reaction the mixture was poured into cold water and acidified with dilute HCl. The solid precipitated was dried in vacuo. The crude was recrystallized with ethanol to give pure final products **172-181**.

4-(8-fluorophenanthren-3-yl)-2,4-dioxobutanoic acid (172). Yellow solid; yield 89%; mp 138-140 °C; ^{1}H NMR (500 MHz, DMSO-d_6): δ 9.43 (s, 1H, ArH), 8.91 (d, 1H, J = 8.0 Hz, ArH), 8.27 (d, 1H, J = 9.0 Hz, ArH), 8.10-8.30 (m, 3H, ArH, enolic CH), 8.05 (d, 1H, J = 9.0 Hz, ArH), 7.75-7.80 (m, 1H, ArH), 7.56 (t, 1H, J = 9.0 Hz, ArH); MS (ESI): m/z 308.8 $[M-H]^-$.

4-(8-fluorophenanthren-2-yl)-2,4-dioxobutanoic acid (173). Yellow solid; yield 92%; mp 205-206 °C; ^{1}H NMR (300 MHz, DMSO-d_6): δ 9.0 (d, 1H, J = 8.7 Hz, ArH), 8.89 (s, 1H, ArH), 8.76 (d, 1H, J = 8.4 Hz, ArH), 8.30 (d, 1H, J = 8.7 Hz, ArH), 8.18 (d, 1H, J = 8.7 Hz, ArH), 8.10 (d, 1H, J = 9.0 Hz, ArH), 7.57-7.78 (m, 2H, ArH), 7.35 (s, 1H, enolic CH); MS (ESI): m/z 308.8 $[M-H]^-$.

4-(4-fluorophenanthren-3-yl)-2,4-dioxobutanoic acid (174). Dark yellow solid; yield 87%; mp 226-227 °C; ^{1}H NMR (300 MHz, DMSO-d_6): δ 10.03 (d, 1H, J = 7.2 Hz, ArH), 8.12-8.20 (m, 3H, ArH), 7.99-8.07 (m, 2H, ArH), 7.74-7.80 (m, 2H, ArH), 7.10 (s, 1H, enolic CH); m/z 288.7 $[M-HF]^-$; HPLC: t_R 4.11 min, purity 97.5%.

4-(4,6-difluorophenanthren-3-yl)-2,4-dioxobutanoic acid (175). Yellow solid; yield 81%; mp >250 °C dec; ^{1}H NMR (300 MHz, DMSO-d_6): δ 9.63 (d, 1H, J = 13.8 Hz, ArH), 8.09-8.17 (m, 3H, ArH), 7.97 (d, 1H, J = 7.8 Hz, ArH), 7.89 (d, 1H, J = 8.7 Hz, ArH), 7.62 (t, 1H, J = 8.4 Hz, ArH), 7.05 (s, 1H, enolic CH); m/z 306.8 $[M-HF]^-$; HPLC: t_R 4.11 min, purity 98.4%.

4-(7-chlorophenanthren-2-yl)-2,4-dioxobutanoic acid (176). Yellow solid; yield 93%; mp 220-222 °C; ^{1}H NMR (300 MHz, DMSO-d_6): δ 8.96 (d, 1H, J = 9.0 Hz, ArH), 8.92 (d, 1H, J = 9.0 Hz, ArH), 8.84 (d, 1H, J = 1.7 Hz, ArH), 8.27 (dd, 1H, J_1 = 8.7 Hz, J_2 = 1.8 Hz, ArH), 8.18 (d, 1H, J = 2.1 Hz, ArH), 8.15 (d, 1H, J = 9.0 Hz, ArH), 7.95 (d, 1H, J = 9.0 Hz, ArH), 7.75 (dd, 1H, J_1 = 9.0 Hz, J_2 = 2.1 Hz, ArH), 7.32 (s, 1H, enolic CH); m/z 325.0 $[M-H]^-$.

3-(6-chlorophenanthren-2-yl)-3-oxopropanoic acid (177). Yellow solid; yield 78%; mp 213-215 °C; ^{1}H NMR (300 MHz, DMSO-d_6): δ 9.02 (d, 1H, J = 9.0 Hz, ArH), 8.97 (s, 1H, ArH), 8.82 (s, 1H, ArH), 8.24 (d, 1H, J = 8.7 Hz, ArH), 8.08 (d, 2H, J = 8.4 Hz, ArH), 7.97 (d, 1H, J = 9.0 Hz, ArH), 7.77 (d, 1H, J = 8.7 Hz, ArH), 7.28 (s, 1H, enolic CH); m/z 325.0 $[M-H]^-$.

4-(8-chlorophenanthren-2-yl)-2,4-dioxobutanoic acid (178). Yellow solid; yield 86%; mp 204-206 °C; ^{1}H NMR (300 MHz, DMSO-d_6): δ 9.0 (d, 1H, J = 8.1 Hz, ArH), 8.92 (d, 1H, J = 7.8 Hz, ArH), 8.87 (s,1H, ArH), 8.28 (d, 1H, J = 8.7 Hz, ArH), 8.23 (d, 2H, J = 1.2 Hz, ArH), 7.90 (d, 1H, J = 6.3 Hz, ArH), 7.74 (t, 1H, J = 7.5 Hz, ArH), 7.31 (s, 1H, enolic CH); m/z 325.0 $[M-H]^-$.

4-(8-chlorophenanthren-3-yl)-2,4-dioxobutanoic acid (179). Yellow solid; yield 83%; mp >235 °C dec; ^{1}H NMR (300 MHz, DMSO-d_6): δ 9.34 (s, 1H, ArH), 9.02 (d, 1H, J = 8.1 Hz, ArH), 8.00-8.26 (m, 5H, ArH, enolic CH), 7.85 (d, 1H, J = 7.5 Hz, ArH), 7.74 (t, 1H, J = 7.8 Hz, ArH); m/z 325.0 $[M-H]^-$.

4-(8-fluoro-2-methoxyphenanthren-9-yl)-2,4-dioxobutanoic acid (180). Yellow solid; yield 91%; mp 211-213 °C; ^{1}H NMR (300 MHz, DMSO-d_6): δ 8.80 (d, 1H, J = 9.0 Hz, ArH), 8.70 (d, 1H, J = 8.1 Hz, ArH), 8.02 (s, 1H, ArH), 7.75 (t, 1H, J = 8.1 Hz), 7.66 (d, 1H, J = 2.1 Hz, ArH), 7.43-7.51 (m, 2H, ArH), 6.58 (s, 1H, enolic CH), 3.95 (s, 3H, OCH_3); MS (ESI): m/z 338.9 $[M-H]^-$.

4-(2-methoxyphenanthren-9-yl)-2,4-dioxobutanoic acid (181). Orange solid; yield 88%; mp 198-200 °C; ^{1}H NMR (300 MHz, DMSO-d_6): δ 8.82 (d, 1H, J = 9.0 Hz, ArH), 8.79 (d, 1H, J = 9.3 Hz, ArH), 8.50 (d, 1H, J = 8.1 Hz, ArH), 8.41 (s, 1H, ArH), 7.74 (s, 1H, ArH), 7.72 (t, 1H, J = 8.1 Hz, ArH), 7.64 (t, 1H, J = 8.1 Hz, ArH), 7.45 (dd, 1H, J_1 = 9.0 Hz, J_2 = 2.7 Hz, ArH), 6.98 (s, 1H, enolic CH), 3.94 (s, 3H, ArH); MS (ESI): m/z

320.9 $[M-H]^-$.

Biological Assays

Materials, chemicals, and enzymes. All compounds were dissolved in DMSO and the stock solutions were stored at -20 °C. γ[^{32}P]-ATP was purchased from either Amersham Biosciences or ICN. The expression systems for wild-type IN were a generous gift from Dr. Robert Craigie, Laboratory of Molecular Biology, NIDDK, NIH, Bethesda, MD. Cell lines were obtained from American Type Culture Collection (ATCC, Rockville, MD).

Preparation of oligonucleotide substrates. The oligonucleotides 21top, 5′-GTGTGGAAAATCTCTAGCAGT-3′, and 21bot, 5′-ACTGCTAGAGATTTTCCACAC-3′, were purchased from the Norris Cancer Center Microsequencing Core Facility (University of Southern California) and purified by UV shadowing on polyacrylamide gel. To analyze the extent of 3′-P and ST using 5′-end labeled substrates, 21top was 5′-end labeled using T4 polynucleotide kinase (Epicentre, Madison, WI) and γ[32P]-ATP (Amersham Biosciences or ICN). The kinase was heat-inactivated and 21-bot was added in 1.5M excess. The mixture was heated at 95 °C, allowed to cool slowly to rt, and run through a G25 mini spin column (USA Scientific) to separate double-stranded oligonucleotide from unincorporated material.

Integrase assays. To determine the extent of 3′-P and ST, wild-type IN was preincubated at a final concentration of 200 nM with the inhibitor in reaction buffer (50 mM NaCl, 1 mM HEPES, pH 7.5, 50 μM EDTA, 50 μM dithiothreitol, 10% glycerol (w/v), 7.5 mM $MnCl_2$, 0.1 mg/mL bovine serum albumin, 10 mM 2-mercaptoethanol, 10% dimethylsulfoxide, and 25 mM MOPS, pH 7.2) at 30 °C for 30 min. An aliquot (5μL) was electrophoresed on a denaturing 20% polyacrylamide gel (0.09 M Tris-borate, pH 8.3, 2 mM EDTA, 20% acrylamide, and 8M urea). Gels were dried, exposed in a PhosphorImager cassette, and analyzed using a Typhoon 8610 Variable Mode Imager (Amersham Biosciences) and quantitated using ImageQuant 5.2. Percent inhibition (%I) was calculated using (**Equation 3-1**). The IC_{50} values were determined by plotting the logarithm of compound concentration versus percent inhibition to obtain the concentration that produced 50% inhibition.

Anti-HIV-1 activity assay. The testing of the ability of potent compounds to inhibit HIV replication in cell culture was done according to a previously reported procedure.[182] PBMC (107 cells/T25flask) were stimulated with phytohemagglutinin for 3 days and infected with a wild-type HIV-1 strain (strain LAI) at 100 50% tissue culture infective doses, as described previously.[182] The cultures were kept for 5 days in the presence of test compounds at serial 1-log dilutions. Subsequently, human PBMC were

removed from the culture supernatant by centrifugation (400g, 10 min, 4 °C). This clarified supernatant was tested by a reverse transcriptase assay.

Cytotoxicity assays. The cytotoxicity of compounds was evaluated using uninfected PBMC and CEM leukemia cells according to a previous method.[183] PBMC were obtained from whole blood of healthy individuals, while CEM were obtained from the ATCC (Rockville, MD). The PBMC and CEM cells were cultured in the presence or absence of compound for 6 days. After this time period, cells were stained with Trypan blue dye, and counted for cell proliferation and viability according to the previously reported procedure.[184]

CHAPTER 6. COMPUTATIONAL STUDIES ON HIV-1 INTEGRASE INHIBITORS*

Introduction

The absence of a complete DNA-bound HIV IN crystal structure has presented a significant challenge for the structure-based design of potent IN inhibitors. Although X-ray structures of individual human HIV domains and their combinations (core domain and N terminal domain; core domain and C terminal domain; and core domain with an inhibitor (5-CITEP)) have been reported,[62-76] most of these structures have an unresolved flexible loop. Moreover, there are differences in conformations of the active site residues in the two structures that show a completely resolved flexible loop (chain B of 1BIS and chain C of 1BL3).[66,67] The absence of a 3D structure of IN and viral DNA along with the two-divalent metals bound in the active site makes the structural information hitherto available limited and may be far from reality.

In the first part of this chapter, three dimensional structure-activity relationship (3D-QSAR) studies were conducted to gain insights into the binding of chalcone IN inhibitors (described in Chapter 3) at the IN active site. CoMFA and CoMSIA 3D-QSAR models were derived to study the influence of stereoelectronic, hydrophobic and hydrogen bonding interactions on activity; and to establish predictive tools for design of novel inhibitors. In the absence of the complete HIV-DNA crystal structure, ligand-based pharmacophore alignments were used to develop the 3D-QSAR models. The resulting models showed moderate statistical significance and limited predictive ability.

With an aim to develop improved QSAR models, in the next part of this chapter, a homology model of full length IN-DNA-Raltegravir complex developed by our collaborator at the Oak Ridge National Laboratory, was used to perform the docking-based QSAR studies. The models developed demonstrated significant improvement in terms of statistical significance and predictive ability over the previous ligand-based models. Prospective compounds predicted by the models were synthesized and tested for HIV-1 IN inhibitory activities.

The third part of this chapter describes docking studies and exploration of binding modes of the substituted phenanthrene β-diketo acids synthesized in Chapter 5. These studies have provided insights into designing further modifications to improve their HIV-1 IN inhibitory activities.

In last part of this chapter, I have attempted structure-based design to modify our synthesized amide derivatives as well as performed *in silico* screening to discover new

* Portions of this chapter adapted with permission. Sharma, H.; Patil, S.; Sanchez, T. W.; Neamati, N.; Schinazi, R. F.; Buolamwini, J. K. Synthesis, biological evaluation and 3D-QSAR studies of 3-keto salicylic acid chalcones and related amides as novel HIV-1 integrase inhibitors. *Bioorg. Med. Chem.* **2011**, 19, 2030-2045.[179]

hits for inhibition of HIV-1 IN. The 3D-database searches have resulted in the discovery of a hit, displaying ST inhibitory activity of 9 μM, that could be developed as a novel class of HIV-1 IN inhibitor.

Ligand-Based Modeling Studies

Generation of a Pharmacophore Model Using the PHASE Program

Knowledge of the structure of target protein inhibitor interations is limited as no crystal structure of human integrase-ligand-DNA complex is available. Therefore, to explore the bioactive conformation of these novel IN inhibitors, the PHASE[200] (v3.0) pharmacophore mapping program implemented in Maestro modeling program package (v8.5; Shrodinger Inc.) was used. The 3D structures of molecules were constructed in and imported from the SYBYL modeling program (v8.3, Tripos). Conformers of each molecule were generated using the OPLS_2005 force field in the macromodel conformational analysis program of PHASE. A set of pharmacophoric sites based on features defined in PHASE were assigned to the molecules. These included H-bond acceptor (A), H-bond donor (D), hydrophobic group (H), negatively charged group (N) and aromatic ring (R). The three most potent compounds of the chalcone series, compound **86**, **88** and **96** were selected as actives for use in identifying a common pharmacophore hypothesis using a tree-based partitioning technique of PHASE. The resulting pharmacophores were then scored and ranked. The top twenty pharmacophore hypotheses were analyzed and validated by partial least square (PLS) regression-based PHASE 3D-QSAR. Random external test sets were generated automatically to determine the predictive ability of the models. The hypothesis that afforded the best PLS statistics (**Table 6-1**) and the highest predicted ability consisted of six features viz., two H-bond acceptors, two hydrophobic groups, a negative group and one aromatic ring (**Figure 6-1**). Two H-bond acceptor features mapped onto the oxygen of the hydroxyl and the 3-keto moiety and negative feature mapped onto the carboxylate group of the salicylic acid pharmacophore. The two hydrophobic features mapped to the halogen substituent of ring A and the *para* substituted halogen in aryl ring B. The aromatic pharmacophoric feature mapped onto aromatic ring A. Residuals of the training and the test set are listed in **Tables 6-2** and **6-3**, respectively. The prediction curve for the test set is shown in **Figure 6-2**. As can be seen, the hypothesis gave a good predictive model with a predictive r^2 of 0.57 for an external test set of ten compounds. It was also able to distinguish active and inactive compounds, with the latter group not aligning well to the features (**Figure 6-3** and **Figure 6-4**).

Ligand-Based 3D-QSAR Analysis

CoMFA and CoMSIA 3D-QSAR models. Statistical analysis by PLS[201,202] was done using CoMFA and CoMSIA descriptors as independent variables and biological

Table 6-1. Residuals of training set by PHASE 3D-QSAR

Cpd.	Actual ST pIC_{50}	Predicted ST pIC_{50}	Residuals
81	4.60	4.85	-0.25
82	4.85	4.59	0.26
83	4.49	4.53	-0.04
85	4.92	4.84	0.08
86	5.30	4.94	0.36
87	4.45	4.85	-0.40
88	5.15	5.02	0.13
89	4.72	4.66	0.06
90	4.46	4.59	-0.13
91	4.29	4.29	0.00
92	4.74	4.87	-0.13
93	4.79	4.83	-0.04
95	4.88	4.82	0.06
96	5.40	5.40	0.00
97	4.27	4.49	-0.22
98	4.00	4.21	-0.21
99	4.03	4.48	-0.45
103	4.39	4.44	-0.05
104	4.76	4.63	0.13
105	4.62	4.33	0.29
106	4.52	4.44	0.08
107	4.54	4.63	-0.09
108	4.82	4.59	0.23
110	4.23	4.42	-0.19
111	4.12	3.94	0.18
112	4.12	4.15	-0.03
113	5.04	4.99	0.05
114	4.74	4.79	-0.05
115	4.79	4.79	0.00
116	4.74	4.85	-0.11
117	4.26	4.32	-0.06
118	4.33	4.16	0.17
119	4.26	4.28	-0.02
120	4.96	4.86	0.10
124	4.49	4.46	0.03
125	4.74	4.60	0.14
126	4.23	4.32	-0.09
127	4.40	4.24	0.16
128	4.30	4.37	-0.07
129	4.16	4.10	0.06
130	4.68	4.80	-0.12
149	4.82	4.83	-0.01
153	4.00	4.26	-0.26

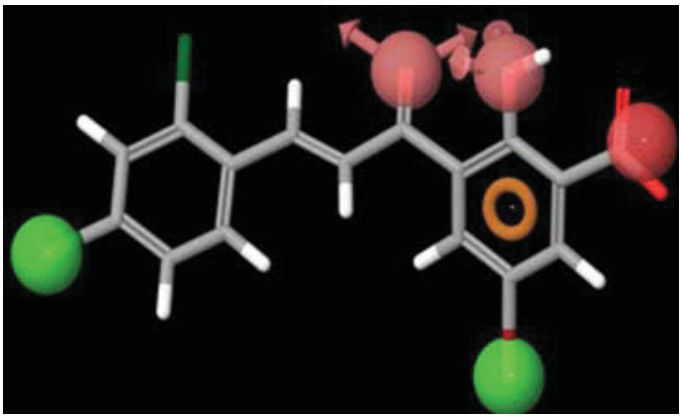

Figure 6-1. The best pharmacophore hypothesis (AAHHNR) mapped on compound 88

Table 6-2. PLS statistics of PHASE 3D-QSAR model

PLS statistics	Results
q^2	0.57
r^2	0.74
SD	0.17
F	28.30
PLS factors	4.00
Pearson r	0.75

Table 6-3. Residuals of test set by PHASE 3D-QSAR

Cpd.	Actual ST pIC_{50}	Predicted ST pIC_{50}	Residuals
84	5.04	4.86	0.18
94	4.85	4.78	0.07
100	4.60	4.71	-0.11
101	4.77	4.63	0.14
102	4.52	4.25	0.27
109	4.41	4.28	0.13
121	4.80	4.91	-0.11
122	4.20	4.51	-0.31
123	4.28	4.46	-0.18
154	4.00	4.35	-0.35

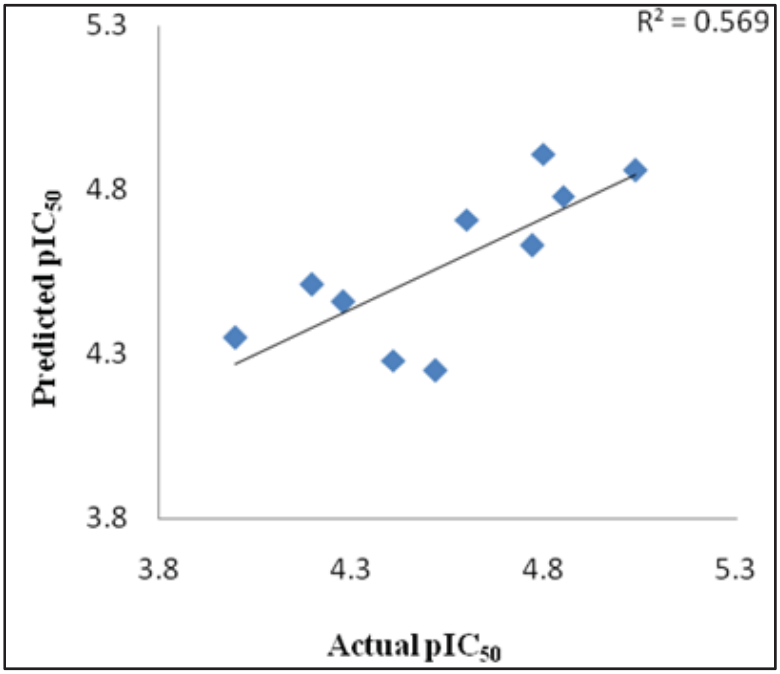

Figure 6-2. PHASE 3D-QSAR predictions of the test set

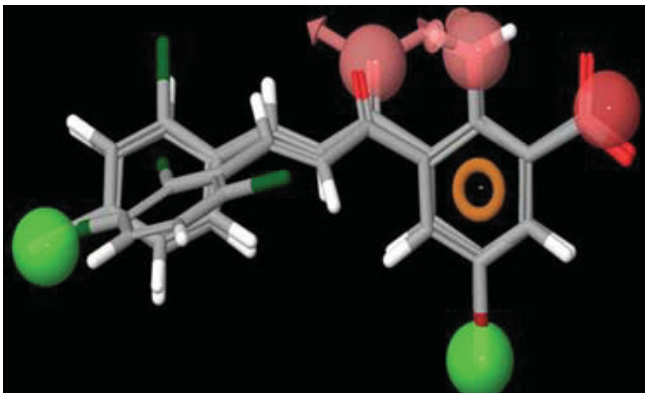

Figure 6-3. Alignment of active compounds by PHASE

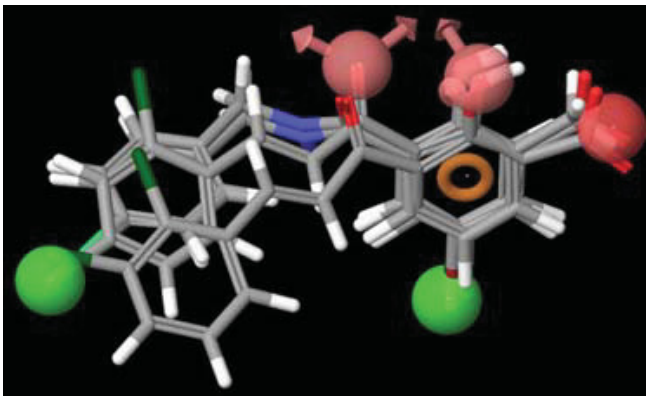

Figure 6-4. Alignment of inactive compounds by PHASE

activity in the form of pIC_{50} values as dependent variable. The molecular alignment used for CoMFA and CoMSIA 3D-QSAR modeling was derived from PHASE pharmacophore mapping (Schrödinger, Inc.). PHASE derived pharmacaphore hypotheses have been successfully used to derive "bioactive conformations" for 3D-QSAR modeling in previous work from our laboratory[203] and elsewhere (Telvekar *et al*.).[204] Thus, "bioactive conformations" of all the molecules from PHASE conformational analysis were superimposed using the MATCH alignment tool in SYBYL (**Figure 6-5**). Fifty three (53) synthesized target compounds were used for the 3D-QSAR analyses. The Leave-One-Out (LOO) method of cross validation was used for initial assessment of the predictive abilities of the models with the training sets. The optimal number of components used in the final QSAR models was that which gave the smallest standard error of prediction. Reliability of the models was tested by prediction of 10 compounds selected as an external test set using factor analysis. The PLS analysis results from both the CoMFA and CoMSIA models are summarized in **Table 6-4**. Cross-validated q^2 values of 0.43 and 0.54 were obtained for CoMFA and CoMSIA, respectively. Results of rigorous statistical testing using group cross-validation (20 groups), bootstrapping and randomization of activity data demonstrated the robustness of the QSAR models. Both CoMSIA and CoMFA identified six outliers, which were excluded on the basis of their extreme residual values (**Table 6-5**). Out of these, five outliers were common to both CoMFA and CoMSIA. These were compounds **87**, **98**, **99**, **126** and **128**. The reasons for compound **126** being an outlier are not apparent. With compound **87** (iodo substituted) and compound **128** ($X = CH_3$), their outlier status may stem from structural uniqueness, whereas the outlier status of compounds **98** and **99** (least active analogs, X = Cl) may drive from different binding modes. The CoMFA and CoMSIA predictions for the training and the test sets are shown in **Figures 6-6** and **6-7**, respectively. The CoMFA and CoMSIA residual values for the training set are given in **Table 6-5** and the corresponding values for the test set in **Table 6-6**. In concordance with the higher q^2 value, the CoMSIA model performed better than CoMFA model, and predicted all test set compounds within 0.56 log unit of the actual pIC_{50} values.

CoMFA and CoMSIA contour maps. Steric CoMFA maps (**Figure 6-8**) show green contours around the *ortho* and *para* positions on aryl ring B indicating that bulky groups are favored at these positions. This is validated by the fact that a benzyl group substitution at the *ortho*-position resulted in higher activity (compound **113**). Compounds **115** and **120**, which have a bulky chloro phenoxy and thiophene groups around the green contour at the *para*-position also displayed better inhibitory activities. A large yellow contour surrounds a small green contour at the *meta* position on aryl ring B suggesting that only a limited bulk is favorable for activity. This is apparent by the loss of inhibitory activity observed with compound **117**, the bulky cyclopentyl ring of which occupies the sterically disfavored yellow contour region. There is also a green contour evident at the R_1 position on the aromatic ring A. This may be the reason why among the three halogens at that position, bromine, which is the bulkiest, afforded the highest activity. At the aryl ring B, CoMFA electrostatic map reveals a red contour at the 3′-position suggesting that electronegative groups could increase activity at this position. This is most exemplified by the 3′-Cl substitution in compound **84** which had an IC_{50}

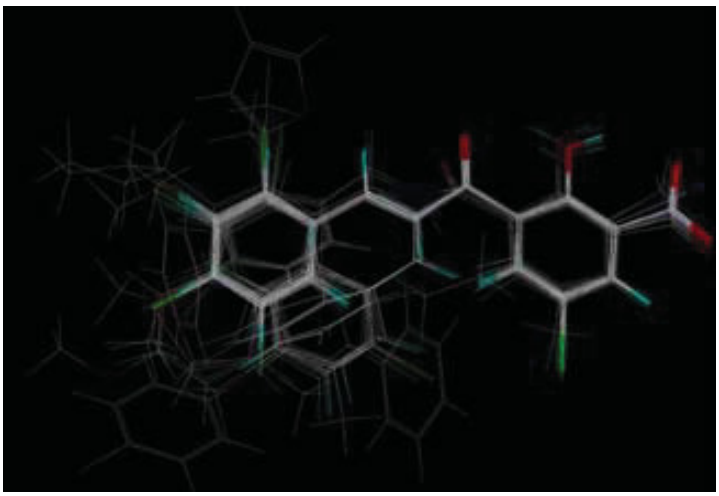

Figure 6-5. Alignment of dataset for 3D-QSAR

Table 6-4. PLS statistics of CoMFA and CoMSIA 3D-QSAR

PLS statistics	CoMFA	CoMSIA
q^2	0.43	0.54
r^2	0.94	0.94
S	0.09	0.09
F	78.32	78.69
PLS components	6.0	6.00
Field contribution		
Steric	0.474	0.100
Electrostatic	0.526	0.428
Hydrophobic		0.283
Donor		0.146
Acceptor		0.044
Bootstrapping r^2 (20 runs)	0.96 ± 0.01	0.96 ± 0.01
Randomization r^2 (20 runs)	0.33	0.39
Cross-validation q^2 (20 runs)	0.44	0.50

Table 6-5. Residuals of training set of CoMFA and CoMSIA models

Cpd.	Actual ST pIC_{50}	CoMFA Res.	CoMSIA Res.
81	4.60	-0.13	-0.12
82	4.85	0.12	0.12
83	4.49	-0.18	-0.19
84	5.04	0.05	0.03
85	4.92	-0.15	-0.08
86	5.30	0.16	0.11
87	4.45	-0.62	-0.96
88	5.15	0.21	0.19
89	4.72	0.10	-0.07
90	4.46	0.06	-0.04
91	4.29	0.05	-0.003
92	4.74	0.01	0.04
93	4.79	-0.03	-0.03
94	4.85	-0.13	-0.03
95	4.88	0.07	0.11
96	5.40	-0.05	-0.05
97	4.27	-0.02	0.09
98	4.00	-0.62	-0.89
99	4.03	-0.79	-0.74
100	4.60	0.02	0.005
101	4.77	0.01	0.11
102	4.52	0.03	0.06
104	4.76	-0.009	0.04
105	4.62	-0.02	-0.13
106	4.52	-0.03	-0.12
107	4.54	0.06	0.04
109	4.41	-0.001	-0.04
110	4.23	-0.05	-0.05
111	4.12	-0.02	-0.02
114	4.74	-0.07	-0.01
115	4.79	-0.07	0.56
117	4.26	-0.03	0.00
118	4.33	0.07	0.09
119	4.26	0.002	-0.03
120	4.96	0.10	0.04
122	4.20	0.01	-0.07
123	4.28	-0.84	-0.09
126	4.23	-0.41	-0.31
127	4.35	-0.05	-0.01
128	4.30	-1.03	-1.03
129	4.16	-0.01	0.11
153	4.00	-0.047	-0.05
154	4.00	0.07	0.04

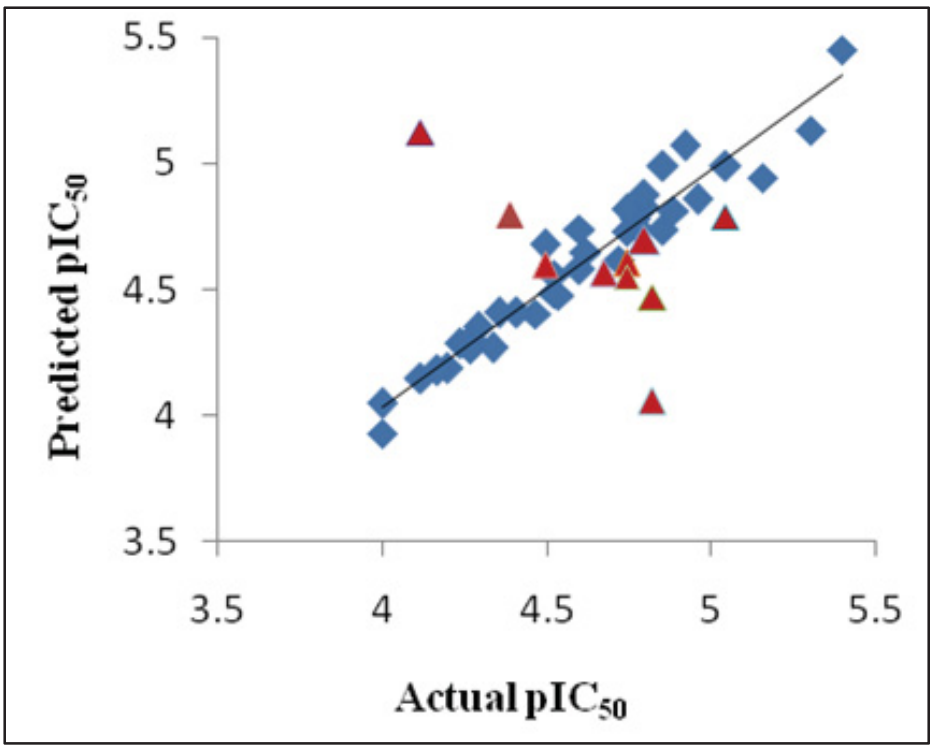

Figure 6-6. Predictions of ST activities of the training and the test set compounds by CoMFA

Training and the test sets are represented by blue diamonds and red triangles, respectively.

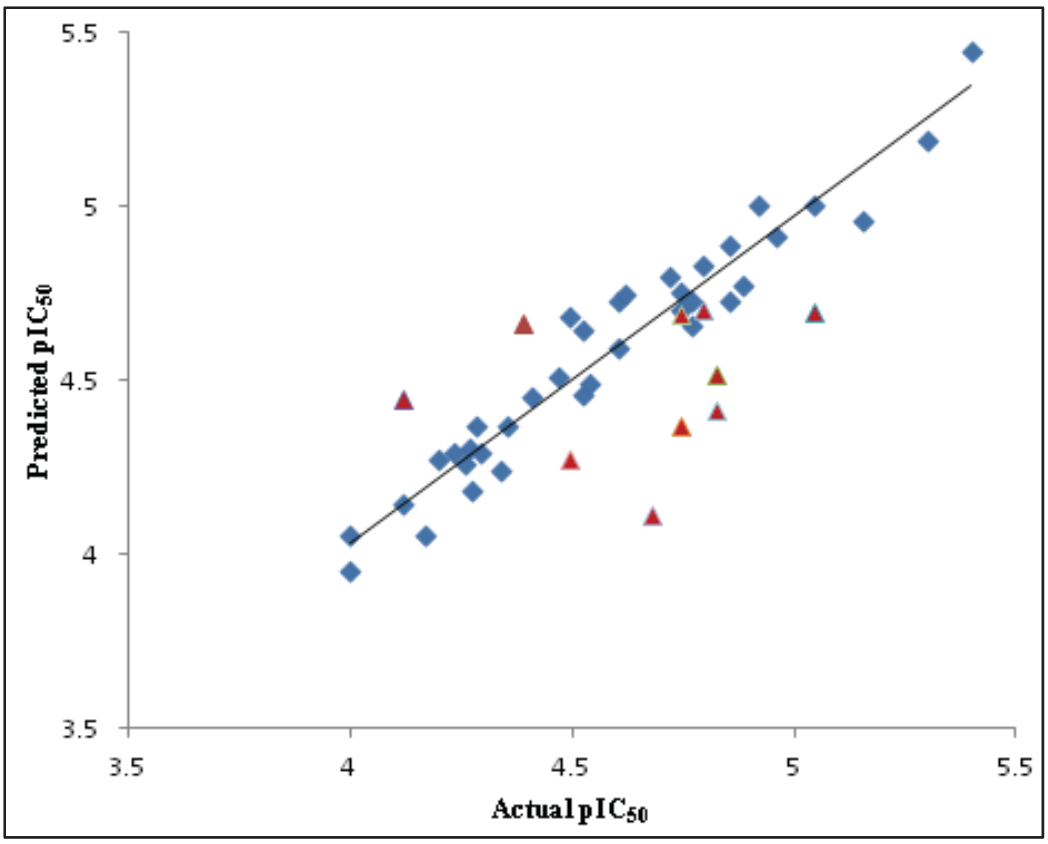

Figure 6-7. Predictions of ST activities of the training and the test set compounds by CoMSIA

Training and the test sets are represented by blue diamonds and red triangles, respectively.

Table 6-6. Residuals of the test set predictions given by CoMSIA and CoMSIA models

Cpd.	Actual ST pIC_{50}	CoMFA Res.	CoMSIA Res.
103	4.39	-0.41	-0.28
108	4.82	0.35	0.30
112	4.12	-1.00	-0.32
113	5.04	0.25	0.35
116	4.74	0.14	0.37
121	4.79	0.09	0.09
124	4.49	-0.10	0.22
125	4.74	0.19	0.05
130	4.67	0.11	0.56
149	4.82	0.76	0.40

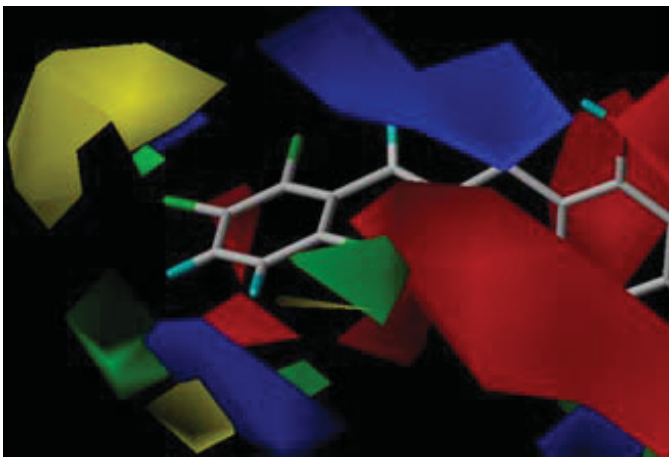

Figure 6-8. CoMFA steric and electrostatic contour plots of ligand-based model

Green and yellow contours illustrate regions where steric bulk has favorable and unfavorable effects on activity, respectively. Blue and red isopleths indicate regions where an increase of positive and negative charge is required for activity.

value of 9 μM. However, for compound **126,** a decrease in activity was observed. Red contours are also present at the 5′- and the 6′-positions. The dichloro-substituted compounds **92** and **93** having Cl at the 5′- and 6′-positions showed improved activities. There are also distant blue contours around aryl ring B, which predicts that electropositive groups should increase activity at these positions. Electronegative oxygen atom of the methoxy substituents in compounds **91**, **111** and **112** points towards the blue contours and thus may explain the loss of activity observed by the presence of methoxy groups in these compounds. The red contours around the salicylic acid moiety in aryl ring A suggest that a negative charge is important for activity in this region, possibly for chelation with the active site Mg^{2+} ions. This is in agreement with the proposed mechanism of action of these compounds as HIV-1 integrase inhibitors. There is a red contour around the 4′-position and both blue and red contours at the 5′-position (R_1). This suggests that polarizability effect might be important at R_1 and could explain the increased activity conferred by bromine substitution over other halogens and the similar-sized hydrophobic methyl group at this position.

The CoMSIA steric contour map shown in **Figure 6-9** reveals a large green contour around aryl ring B. Like in the CoMFA, the electrostatic contours of CoMSIA also show red contours at the 3′ and the 4′-positions on ring B, and at the 5′-position (R_1) on ring A. There is a blue contour located at the position of the hydrogen atom of the hydroxyl group of the salicylic acid moiety. The hydrophobic, H-bond donor and acceptor contours are shown in **Figure 6-10**. There is a white contour located near the R_1 substituent position which suggests hydrophophilic groups increase activity at this region. This might be the reason why compound **128** which has a hydrophobic methyl group was less active than the fluorine (compound **109**) and chlorine substituted analogs (compound **102**) at the R_1 position. Furthermore, compound **128** resulted in 13 times reduction of activity when compared to bromine at this position. The improved activity observed with bromine at R_1 position may result because of its polarization effect. White contours are also evident at the 2′ and the 5′-positions on ring B indicating that hydrophilic groups are favored for activity. This was confirmed with the loss of potency of compounds **90** and **110** which have hydrophobic methoxy and methyl groups at these regions. There is another white region observed over the 3-keto oxygen again signifying the presence of hydrophilic groups at this position. There is a yellow contour close to the 4′-positions on ring B. A hydrophobic group at the 4′-position is expected to increase activity, as bromine substituent does in compound **86** and chlorine substituent in compound **85**. The 3′-keto functionality perfectly fit the magenta contour within their vicinity indicating that they may act as H-bond acceptors. The cyan contour which appears to have merged into the magenta contour might result from the hydrogen of the hydroxyl moiety. It indicates its role as H-bond donor and may involve in H-bonding interactions with the acceptor residues (acidic catalytic triad) of the receptor active site. The good congruence of CoMFA and CoMSIA contour maps with the observed biological activity suggests these models could aid the design of more active compounds.

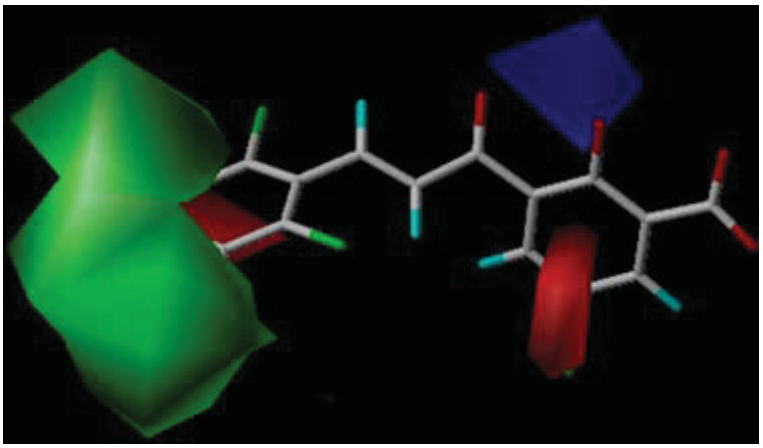

Figure 6-9. CoMSIA steric and electrostatic contour plots of ligand-based model

Green contour illustrates region where steric bulk has favorable effect on activity. Blue and red isopleths indicate regions where an increase of positive and negative charge is required for activity.

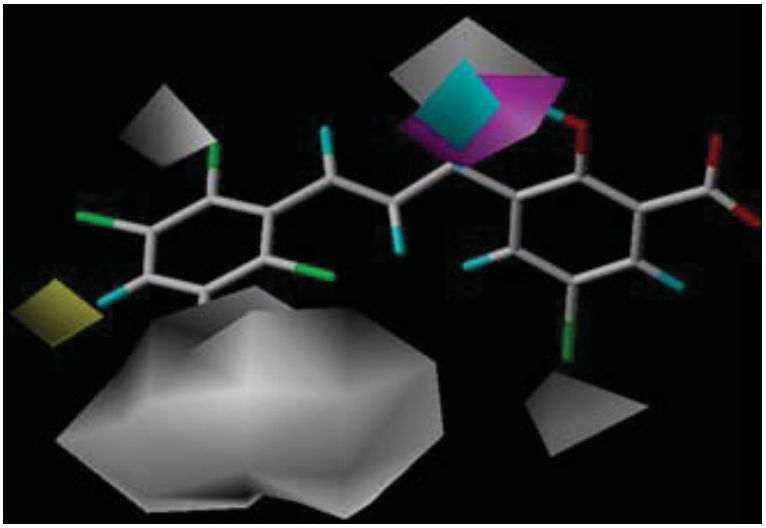

Figure 6-10. CoMSIA hydrophobic, H-bond donor and H-bond acceptor contour plots of ligand-based model

White contours indicate regions where hydrophilic groups increase activity, whereas yellow contours indicate regions where hydrophobic groups increase activity, cyan indicates region where H-donors increase activity and magenta contour indicate region where H-bond acceptor groups increase activity.

Homology Model-Guided Computational Studies on HIV-1 IN Inhibitors

Later, in order to improve the statistical significance and predictive power of our developed 3D-QSAR models, a structure-based approach was followed. Furthermore, a different strategy was used to obtain new composite 3D-QSAR models by incorporating important physico-chemical parameters from potent IN inhibitory compounds to guide our lead optimization efforts on a novel series of 3-keto salicylic acid IN inhibitors synthesized in Chapter 4. The approved raltegravir,[51] which belongs to the class of *N*-methyl-4-hydroxypyrimidinone carboxamides,[134,135] diketotriazole S-1360[125] and naphthyridine carboxamide L-870,812[127] all have three metal-chelating groups in a coplanar conformation mimicking the β-diketo acid motif. Promising IN inhibitors were thus designed as bioisosteres of the diketo acid functionality. However, the advent of mono-keto quinolone HIV-1 IN inhibitors[143,205] showed that the presence of even two coplanar chelating moieties, represented by the β-ketone and a carboxylic acid in elvitegravir is sufficient for potent clinically relevant IN inhibition. Although it is established that potent IN inhibitors have two common structural features viz., a hydrophobic benzyl group and a chelating motif capable of binding two Mg^{2+} ions, a detailed understanding of the structural features essential for HIV-IN inhibitory activity still evades researchers. Therefore, it is important to develop quantitative structure-activity relationships (QSARs) that combine the most advanced first and second-generation inhibitors to arrive at a comprehensive and more unified model for IN inhibition. Although QSAR studies on IN inhibitors have been reported,[206-210] there is none combining the two classes viz., the *N*-methyl-4-hydroxypyrimidinone-carboxamide and 4-quinolone-3-carboxylic acid as represented by the approved raltegravir, the clinically advanced elvitegravir and their analogs.

The absence of a 3D structure of IN and viral DNA along with the two-divalent metals bound in the active site makes the structural information hitherto available limited and may be far from reality. As shown in the **Figure 6-11**, the inhibitor binding site is located at the interface between catalytic core domain (CCD) and C-terminal domain (CTD), and involving contacts with the 3′ terminus of the viral DNA. Therefore, the correct binding mode of drug molecules could not have been predicted based on previous partial IN structures. It has been shown that the full-length IN-DNA-inhibitor complex model would be required to gain a better understanding of how the inhibitors act against IN.

Thus to achieve our objective, we first developed a new homology model of HIV-1 IN in complex with DNA and inhibitors, based on the recently published crystal structure of the foamy virus IN-DNA complex (PDB 3L2T and 3L2U)[93] for use in structure-based 3D-QSAR studies. Although homology models using the foamy virus IN-DNA complex as template were reported by Tang[211] and Krishnan *et al.*,[95] they were not without shortcomings. The model developed by Tang *et al.* consisted of only the CCD-DNA complex and may not be a true representation considering the absence of CTD and NTD, both of which have been implicated in viral DNA binding. Although, the model reported by Krishnan *et al.* involved all the three domains and the viral DNA, no direct contacts of raltegravir with mutant residues Gln148 and Asn155 that are involved

Figure 6-11. PFV IN active site

Protein is shown in cartoon representation (green); inhibitor RLT is shown in licorice representation; DNA is shown in ribbon representation (purple); two magnesium ions are shown as mauve spheres; the residues within 6 Å of RLT are shown as orange lines. Only one protein chain is shown for clarity.

in viral resistance, are observed. Thus, first a homolog model of a full-length HIV-1 IN-DNA- inhibitor complex was constructed by our collaborator at the Oak Ridge National Laboratory. The sequence alignment of HIV-1 and foamy IN, which are about 20% identical, is shown in **Figure 6-12**. The homology model was then used for docking simulations to explore binding interactions of inhibitors with the DNA-bound HIV IN. A data set of 103 compounds including our synthesized IN inhibitors described in Chapters 3 and 4 together with raltegravir and elvitegravir and their analogs reported in the literature[134,135,143,205] were used for docking and 3D-QSAR studies. Because determining the bioactive conformation is critical to developing a successful QSAR model, alignments obtained from docking on the homology model were used for the study and compared with the usual atom-by atom alignments. 3D-QSAR coefficient contour maps were superimposed over the IN active site to visualize and advance our understanding of the ligand-receptor interactions.

Homology Model: Analysis of Binding Sites

Interactions of the substituted benzyl group. Binding mode and interactions of raltegravir are shown in **Figure 6-13** and **Figure 6-14**; and those of elvitegravir in **Figure 6-15** and **Figure 6-16**, respectively. The docking indicated that the *para*-fluoro benzyl ring of raltegravir is nicely inserted into the cavity (**Figure 6-13**) that is formed by displacement of the 3′-adenosine the when viral DNA associates with integrase in a pre-integration complex. This unpairing of the terminal 3′-adenosine of the donor DNA duplex is essential to unmask the scissile phosphodiester bond for 3′-P and subsequent ST reactions. Thus, the interactions of viral DNA with the IN and subsequent unpairing of its 3′-adenosine result in a cavity being formed at the DNA-protein interface. The 3-chloro-2-fluorobenzyl ring of elvitegravir also occupied the same cavity (**Figure 6-15**) formed by the DNA-protein interface as the *para*-fluoro benzyl ring of raltegravir, but is oriented slightly upwards at about 45° angle within the cavity relative to raltegravir. The phenyl rings of both raltegravir and elvitegravir are involved in π-π interaction with the cytosine base of the viral DNA (see **Figure 6-14** and **Figure 6-16**). While, the phenyl ring of raltegravir interacts with the adenine and guanine bases, it is the methoxy and *meta*-chlorine substituents in elvitegravir that make contacts with the adenine and guanine bases of the viral DNA, respectively. Furthermore, the *para*-fluorine substituent in raltegravir and the *ortho*-fluorine substituent in elvitegravir engaged in electrostatic interactions with the 4-amino group of the cytosine of the donor DNA. The phenyl rings of both compounds interact with Glu152. Gln148 appears within 4Å radius of raltegravir and elvitegravir, in our homology models. Thus, our homology models suggest physical contacts between raltegravir and elvitegravir with Gln148, which is in agreement with the observation that mutation of this residue results in resistance to these drugs. We should note that in the crystal structure of foamy virus IN–DNA in complex with raltegravir or elvitegravir, there appeared to be no physical contact between both drugs and the equivalent residue Ser217.[93] The *p*-fluoro phenyl ring of raltegravir also makes extensive vdW with the side chain methylenes, and electrostatic contacts with the amino group of Gln146. In contrast, while the vdW contact with Gln146 is maintained, there is no

Figure 6-12. Amino acid sequence alignment of PFV and HIV-1 IN

Residues are colored according to the clustal color scheme.

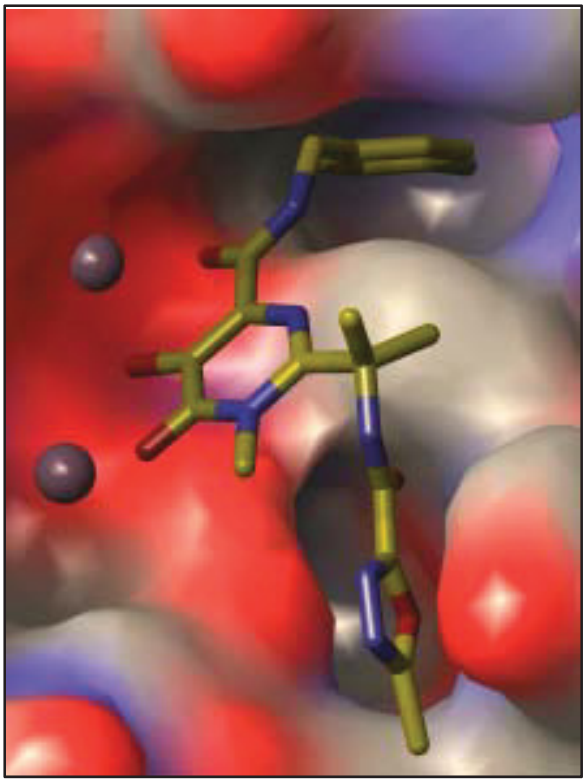

Figure 6-13. Binding mode of raltegravir within the active site of IN-DNA homology model

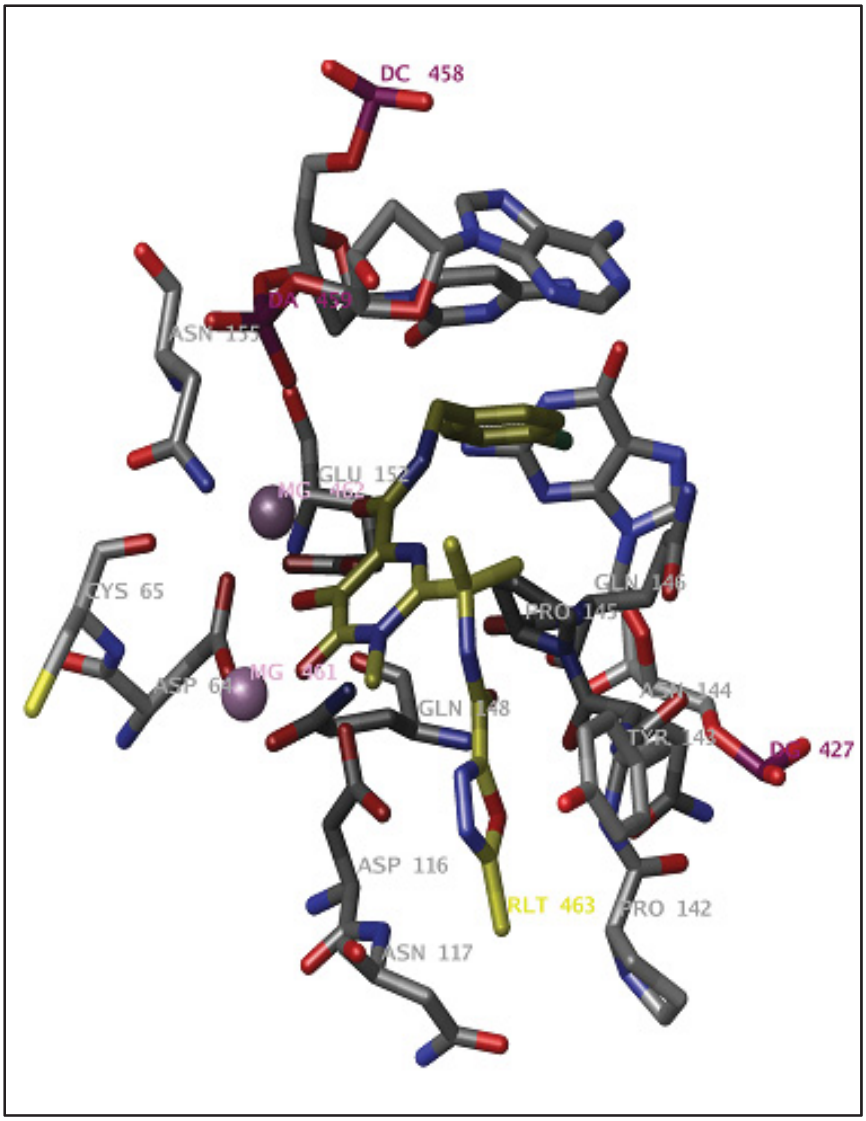

Figure 6-14. Binding interactions of raltegravir

Mg^{2+} ions are represented by purple spheres. Active site residues is represented by tubes and colored by element. Raltegravir is represented in tubes and highlighted with yellow carbons. Other atoms in ligand are colored as follows: O, red; N, blue; F, bright green. Hydrogens are omitted for clarity.

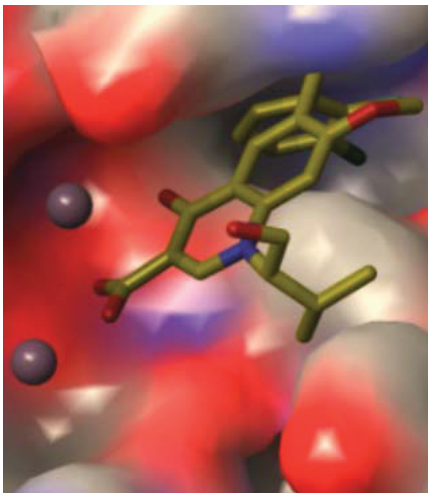

Figure 6-15. Binding mode of elvitegravir within the active site of IN-DNA homology model

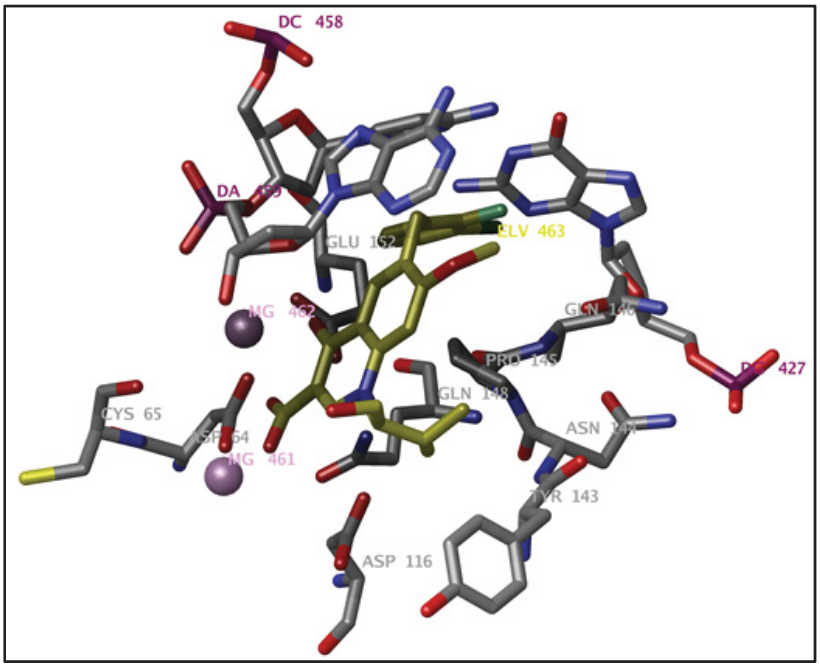

Figure 6-16. Binding interactions of elvitegravir

Mg^{2+} ions are represented by purple spheres. Active site residues are represented by tubes and colored by element. Elvitegravir is represented in tubes and highlighted with yellow carbons. Other atoms in the ligand are colored as follows: O, red; N, blue; F, bright green; Cl, dark green. Hydrogens are omitted for clarity.

apparent electrostatic interaction with this residue in the case of elvitegravir, which on the other hand appears to be directed more towards Gln152.

Interactions of metal-chelating motif. The three-metal chelating groups in raltegravir are involved in coordination with the two metal atoms (Mg^{2+}) in the IN active site. The pyrimidinone oxo and the acidic hydroxyl oxygen coordinate in a bi-dentate manner with the Mg^{2+} between Asp116 and Asp64. Likewise, the keto oxygen of the carboxamide moiety and the acidic hydroxyl oxygen are chelated with the second Mg^{2+} between Asp64 and Glu152. This hydroxyl moiety may also engage in H-bonding interaction with Gln148, Asp64 and Asp116. The binding pose of elvitegravir shows that it's two chelating pharmacophore namely, the 4-keto group and the carboxylate coordinates the two Mg^{2+} ions in the integrase active site.

Interactions of side chain. The *gem*-dimethyl oxadiazole carboxamide moiety in raltegravir is inserted into the cleft formed by Asp116, Asn117 and loop residues Pro142, Tyr143, Asn144 and Pro145. One of the methyl groups of the *gem*-dimethyl moiety interacts with Pro145. The oxadiazole ring is involved in π-stacking interaction with the phenyl ring of Tyr143. The methyl on the oxadiazole is engaged in vdW interactions with the side chain methylene of Asn117. Site 3 binding region in elvitegravir has a hydroxyalkyl chain which in our model is also directed towards this cleft. One of the two methyl groups of the isopropyl substituents makes hydrophobic contacts with Tyr143, while the other makes contact with Pro145. The binding interactions revealed by the model are in accordance with those seen with the foamy virus crystal structure complex with these inhibitors, and confirm the importance of this side chain in the binding of raltegravir and elvitegravir. Tyr143 is a conserved residue among all the classes of polynucleotidyl transferases[212] and is proposed to be important for viral DNA binding. Another key residue to target is Asn117 which is implicated in binding of the host DNA[213] and may thus be important for potent strand transfer (ST) inhibitory activity. Our homology model has also revealed Arg263 and Lys264 as important residues close to the active site that are involved in viral DNA binding.

Docking Studies

For prediction of bioactive conformation and binding modes of our synthesized chalcone and amide compounds, we conducted docking simulations using the GLIDE (v5.7) program from Schrödinger Inc. (Portland, Oregon, USA).[214] Both standard-precision (SP) and extra-precision (XP) modes of GLIDE were evaluated using a flexible ligand and rigid receptor routine. Twenty docking poses were obtained for each molecule, the docking being terminated if two consecutive solutions were within a rmsd of 5 Å. Overlay of the X-ray derived conformation of raltegravir (**Figure 6-17**) over the docked (SP) conformation resulted in a lower rmsd of 0.60 between all heavy atoms as compared with an rmsd of 0.64 obtained with GLIDE XP. The SP option was therefore selected for subsequent docking studies, moreover, in addition to slightly better in reproducing the

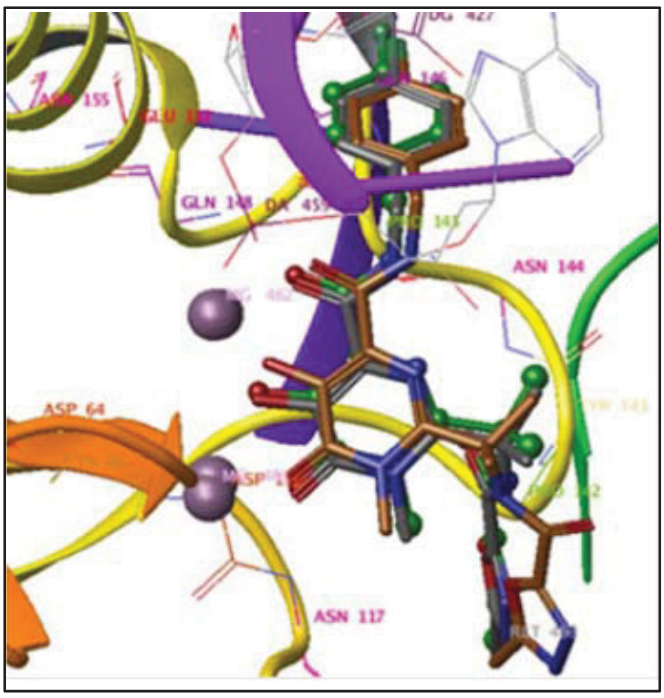

Figure 6-17. Overlay of the crystal structure, homology model, and docked conformations of raltegravir

Crystal structure derived conformation of raltegravir is colored green and represented by ball and stick; the homology model derived conformation is colored in element and represented by tubes; and the GLIDE docking (SP) derived pose is colored by orange carbons and shown in tubes. The homology model is shown in ribbons and Mg^{2+} is shown by purple sphere. Hydrogens are omitted for clarity.

crystal structure conformation it is computationally less expensive. To test the ranking accuracy of GLIDE (SP), the docked poses of raltegravir and elvitegravir were analyzed, and it was found that the poses of elvitegravir have better G-scores and E-model energies and were ranked higher than those of raltegravir. This reflected the enzyme inhibitory activities of the two compounds, with elvitegravir being more potent than raltegravir. The best pose of the two most active compounds (**86** and **96**) selected on the basis of glide score are shown in **Figure 6-18**. The topmost pose of compound **86** showed that its *para*-bromobenzyl group is inserted into the cavity formed by the DNA-protein interface (**Figure 6-18**). The phenyl ring interacts with the cytosine and adenine bases of the viral DNA and also makes favorable vdW contacts with Gln146 and Pro145 (**Figure 6-19**). Furthermore, the *para*-bromo substituent interacted with amino group of Gln146. The 3-keto and the carboxylate group chelated the two divalent (Mg^{2+}) ions in accordance with the proposed mechanism of action of ST inhibitors. The hydroxyl group also weakly coordinated with Mg^{2+} and makes H-bonding contact with the carboxylate of Asp116. The docking pose of compound **96** revealed that the 2,3,6-trichloro-substituted phenyl ring does not dock into the cavity formed by the DNA-protein interface, but was placed rather on the opposite (180°) side exposed to solvent. In this orientation, the trichlorophenyl group interacted with Pro142, the methylene of Ser119 and the methine of Gly118 (**Figure 6-20**). The salicylic acid motif coordinates with the two Mg^{2+} ions, and the hydroxyl group H-bonds to the carboxylate of Asp116. The bromine substituent on the salicylic acid appears to weakly interact with Tyr143 and Pro145. The docking poses thus suggest the presence of multiple binding modes for the chalcones. Their smaller size gives them the flexibility to adopt different poses within the IN active site as opposed to the relatively bulky elvitegravir and raltegravir which preferentially docked in their respective 'bioactive conformations'.

The amide derivative (compound **149**) docked into the IN active site as shown in **Figure 6-21** and **Figure 6-22**. Similar to the *p*-fluorobenzyl group in raltegravir, the *p*-fluorobenzyl group of compound **149** also fitted well into the cavity formed at the IN-DNA interface, and make contacts with Pro145 and Glu152. The phenyl ring π-stacks with the pyrimidinone ring of cytosine, as well as interact with the adenine base of the viral DNA. The F atom makes vdW contacts with side chain methylenes of Gln146 and may be involved in H-bonding with the amino group of the cytosine. The 3-keto salicylic acid motif coordinates with the two metals in the IN active site. Furthermore, the 2-hydroxyl group forms H-bond with Glu152. Notably, no interactions with Tyr143 and Asn117 were observed. These compounds could be optimized to interact extensively with these residues to improve their inhibitory activities. The models developed could thus serve as a surrogate platform for structure-based design of potent IN inhibitors.

With a further objective of using the docked conformations to build a docking-based QSAR model all 103 IN inhibitors of the dataset were docked on the IN active site and 20 poses for each compound were generated. These include 3-keto salicylic acid chalcones (**Table 3-1**) and amide derivatives (**Table 4-1**), synthesized in previous chapters. The data set also included reported *N*-methyl-4-hydroxypyrimidinone carboxamides (**Tables 6-7** to **6-12**) and 4-quinolone-3-carboxylic acid and analogs (**Tables 6-13** and **6-14**). Top-most (based on the glide score) pose of 85 compounds

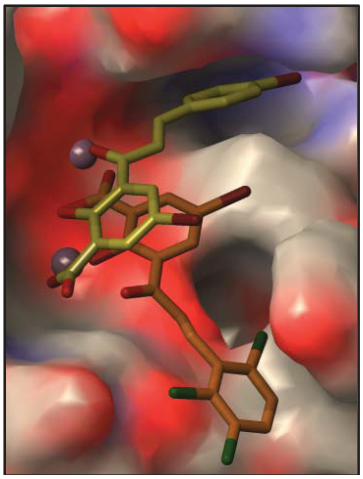

Figure 6-18. Comparison of the docked poses of compounds 86 and 96

Compound **86** is colored by yellow carbons and compound **96** colored by orange carbons. Mg^{2+} ions are shown by purple spheres.

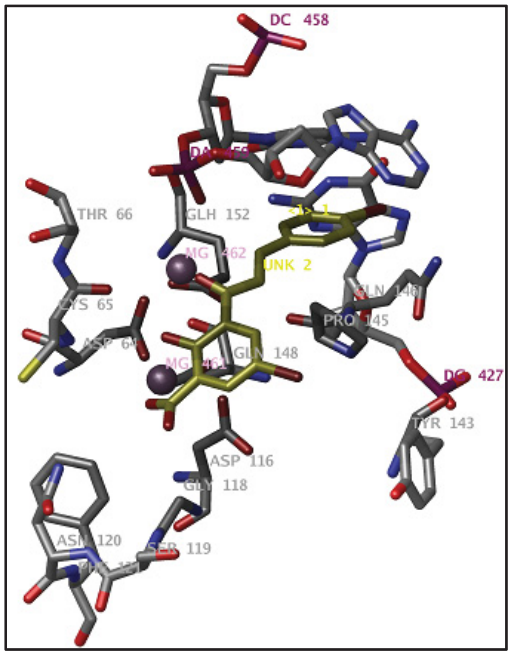

Figure 6-19. Binding interactions of compound 86 in the IN active site

Compound **86** is colored by yellow carbons. Other atoms in the ligand are colored as follows: O, red; Br, dark red. Amino acid residues are colored in element; Mg^{2+} ions are shown by purple spheres.

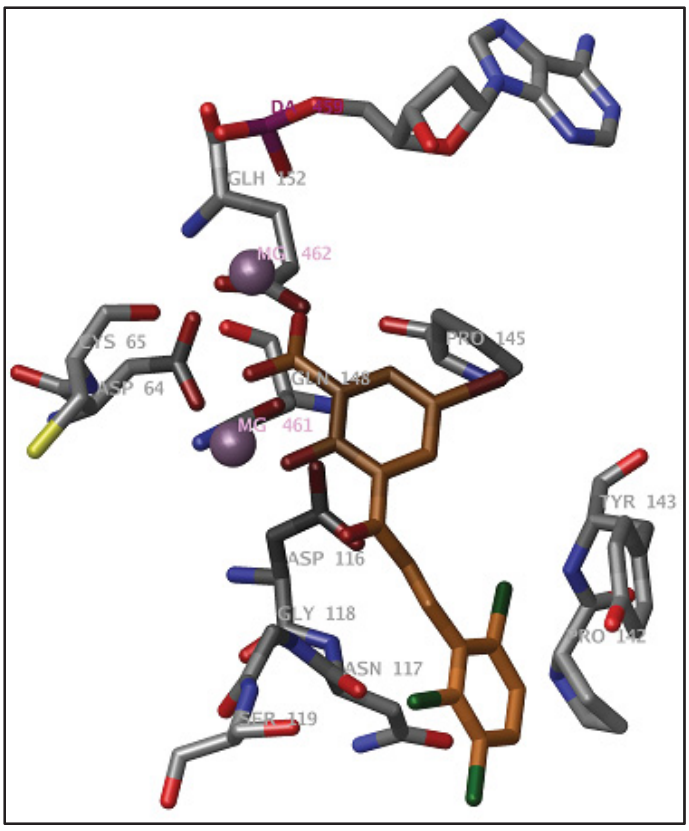

Figure 6-20. Binding interactions of chalcone derivative 96 in the IN active site

Compound **96** is colored by orange carbons. Other atoms in ligand are colored as follows: O, red; Br, dark red; Cl, dark green. Amino acid residues are colored in element; and Mg^{2+} ions are shown by purple spheres.

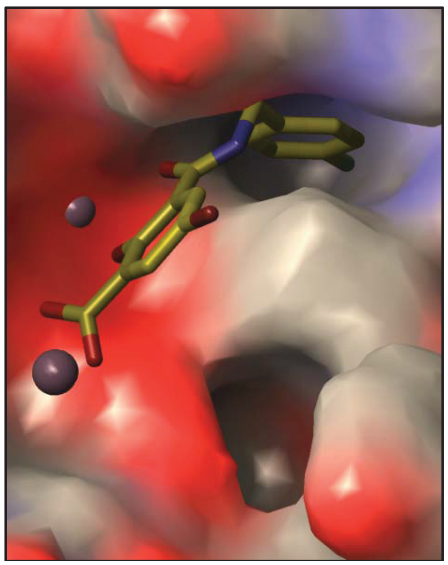

Figure 6-21. Binding mode of amide derivative 149 in the IN active site

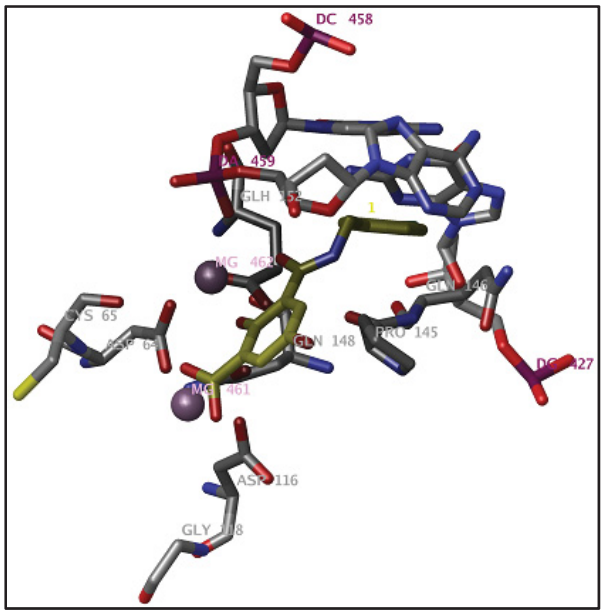

Figure 6-22. Binding interactions of compound 149 within IN-DNA homology model

Compound **149** is colored by yellow carbons. Other atoms in the ligand are colored as follows: O, red; Br, dark red; F, bright green. Mg^{2+} ions are represented by purple spheres. IN-DNA complex is colored by element and represented in tubes. Hydrogens are omitted for clarity.

Table 6-7. Structure and HIV-1 IN inhibitory activities of *N*-methyl-4-hydroxypyrimidinone-carboxamides (scaffold 1) used in 3D-QSAR study

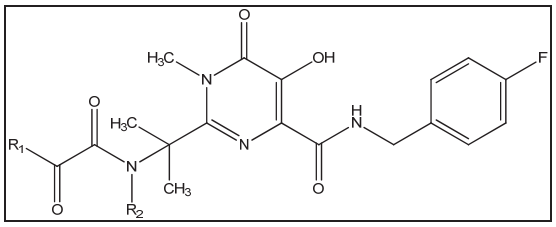

Cpd.	R_1	R_2	ST[a] IC_{50} (μM)
183	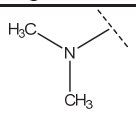	H	0.010
184	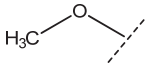	H	0.015
185	OH	H	0.004
186	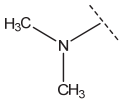	CH_3	0.015
187	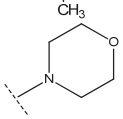	H	0.020
188	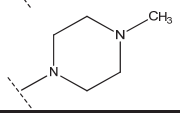	H	0.026

[a] ST represents strand transfer.

(Table adapted with permission from: Summa, V.; Petrocchi, A.; Bonelli, F.; Crescenzi, B.; Donghi, M.; Ferrara, M.; Fiore, F.; Gardelli, C.; Gonzalez Paz, O.; Hazuda, D. J.; Jones, P.; Kinzel, O.; Laufer, R.; Monteagudo, E.; Muraglia, E.; Nizi, E.; Orvieto, F.; Pace, P.; Pescatore, G.; Scarpelli, R.; Stillmock, K.; Witmer, M. V.; Rowley, M. Discovery of raltegravir, a potent, selective orally bioavailable HIV-integrase inhibitor for the treatment of HIV-AIDS infection. *J. Med. Chem.* **2008,** 51, 5843-5855.)[134]

Table 6-8. Structure and HIV-1 IN inhibitory activities of *N*-methyl-4-hydroxypyrimidinone-carboxamides (scaffold 2) used in 3D-QSAR study

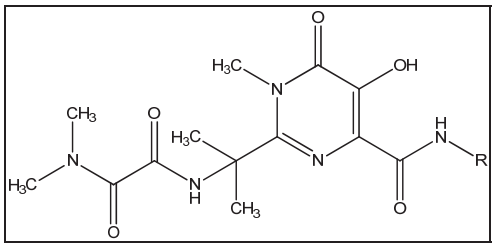

Cpd.	R	ST[a] IC_{50} (μM)
189	Me	>5.0
190	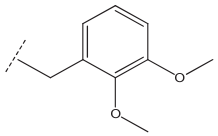	0.021
191	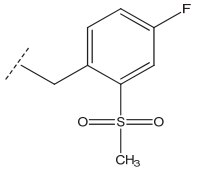	0.004
192	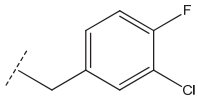	0.009

[a] ST represents strand transfer.

(Table adapted with permission from: Summa, V.; Petrocchi, A.; Bonelli, F.; Crescenzi, B.; Donghi, M.; Ferrara, M.; Fiore, F.; Gardelli, C.; Gonzalez Paz, O.; Hazuda, D. J.; Jones, P.; Kinzel, O.; Laufer, R.; Monteagudo, E.; Muraglia, E.; Nizi, E.; Orvieto, F.; Pace, P.; Pescatore, G.; Scarpelli, R.; Stillmock, K.; Witmer, M. V.; Rowley, M. Discovery of raltegravir, a potent, selective orally bioavailable HIV-integrase inhibitor for the treatment of HIV-AIDS infection. *J. Med. Chem.* **2008,** 51, 5843-5855.)[134]

Table 6-9. Structure and HIV-1 IN inhibitory activities of *N*-methyl-4-hydroxypyrimidinone-carboxamides (scaffold 3) used in 3D-QSAR study

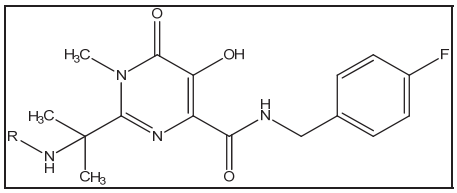

Cpd.	R	ST[a] IC_{50} (μM)
193[b]	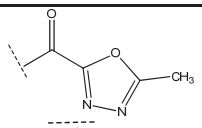	0.015
194	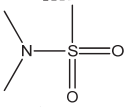	0.012
195	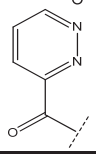	0.015

[a] ST represents strand transfer; [b] structure of raltegravir.

(Table adapted with permission from: Summa, V.; Petrocchi, A.; Bonelli, F.; Crescenzi, B.; Donghi, M.; Ferrara, M.; Fiore, F.; Gardelli, C.; Gonzalez Paz, O.; Hazuda, D. J.; Jones, P.; Kinzel, O.; Laufer, R.; Monteagudo, E.; Muraglia, E.; Nizi, E.; Orvieto, F.; Pace, P.; Pescatore, G.; Scarpelli, R.; Stillmock, K.; Witmer, M. V.; Rowley, M. Discovery of raltegravir, a potent, selective orally bioavailable HIV-integrase inhibitor for the treatment of HIV-AIDS infection. *J. Med. Chem.* **2008,** 51, 5843-5855.)[134]

Table 6-10. Structure and HIV-1 IN inhibitory activities of *N*-methyl-4-hydroxypyrimidinone-carboxamides (scaffold 4) used in 3D-QSAR study

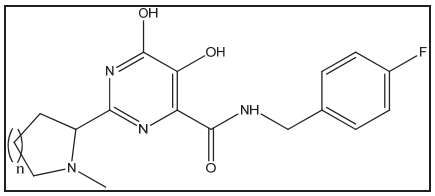

Cpd.	n	ST[a] IC_{50} (μM)
196	1	0.12
197	2	0.22

[a] ST represents strand transfer.

(Table adapted with permission from: Gardelli, C.; Nizi, E.; Muraglia, E.; Crescenzi, B.; Ferrara, M.; Orvieto, F.; Pace, P.; Pescatore, G.; Poma, M.; Ferreira Mdel, R.; Scarpelli, R.; Homnick, C. F.; Ikemoto, N.; Alfieri, A.; Verdirame, M.; Bonelli, F.; Paz, O. G.; Taliani, M.; Monteagudo, E.; Pesci, S.; Laufer, R.; Felock, P.; Stillmock, K. A.; Hazuda, D.; Rowley, M.; Summa, V. Discovery and synthesis of HIV integrase inhibitors: development of potent and orally bioavailable N-methyl pyrimidones. *J. Med. Chem.* **2007,** 50, 4953-4975.)[135]

Table 6-11. Structure and HIV-1 IN inhibitory activities of *N*-methyl-4-hydroxypyrimidinone-carboxamides (scaffold 5) used in 3D-QSAR study

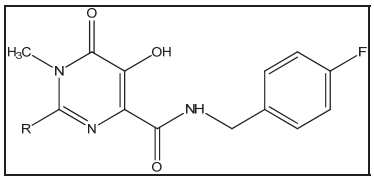

Cpd.	R	ST[a] IC_{50} (μM)
198	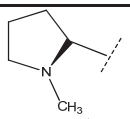	0.062
199	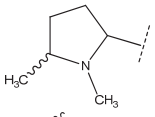	0.69
200	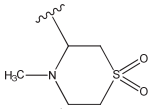	0.14
201	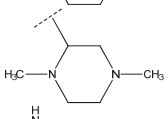	0.10
202	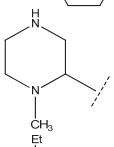	0.20
203	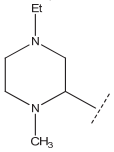	0.25
204	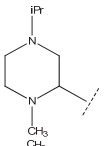	0.13
205	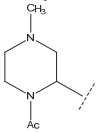	4.00

[a] ST represents strand transfer.

(Table adapted with permission from: Gardelli, C.; Nizi, E.; Muraglia, E.; Crescenzi, B.; Ferrara, M.; Orvieto, F.; Pace, P.; Pescatore, G.; Poma, M.; Ferreira Mdel, R.; Scarpelli, R.; Homnick, C. F.; Ikemoto, N.; Alfieri, A.; Verdirame, M.; Bonelli, F.; Paz, O. G.; Taliani, M.; Monteagudo, E.; Pesci, S.; Laufer, R.; Felock, P.; Stillmock, K. A.; Hazuda, D.; Rowley, M.; Summa, V. Discovery and synthesis of HIV integrase inhibitors: development of potent and orally bioavailable N-methyl pyrimidones. *J. Med. Chem.* **2007,** 50, 4953-4975.)[135]

Table 6-12. Structure and HIV-1 IN inhibitory activities of *N*-methyl-4-hydroxypyrimidinone-carboxamides (scaffold 6) used in 3D-QSAR study

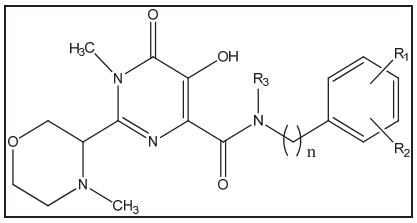

Cpd.	R_1	R_2	R_3	n	ST[a] IC_{50} (μM)
206	H	H	Me	1	>5
207	2-F	H	H	1	0.175
208	3-Cl	H	H	1	0.062
209	3-Br	H	H	1	0.019
210	3-OMe	H	H	1	0.140

[a] ST represents strand transfer.

(Table adapted with permission from: Gardelli, C.; Nizi, E.; Muraglia, E.; Crescenzi, B.; Ferrara, M.; Orvieto, F.; Pace, P.; Pescatore, G.; Poma, M.; Ferreira Mdel, R.; Scarpelli, R.; Homnick, C. F.; Ikemoto, N.; Alfieri, A.; Verdirame, M.; Bonelli, F.; Paz, O. G.; Taliani, M.; Monteagudo, E.; Pesci, S.; Laufer, R.; Felock, P.; Stillmock, K. A.; Hazuda, D.; Rowley, M.; Summa, V. Discovery and synthesis of HIV integrase inhibitors: development of potent and orally bioavailable N-methyl pyrimidones. *J. Med. Chem.* **2007,** 50, 4953-4975.)[135]

Table 6-13. Structure and HIV-1 IN inhibitory activities of 4-quinolone-3-carboxylic acid-carboxamides (scaffold 1) used in 3D-QSAR study

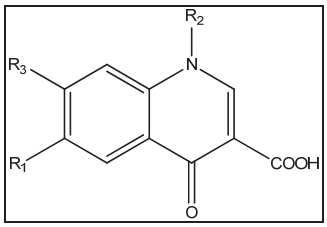

Cpd.	R_1	R_2	R_3	ST[a] IC_{50} (μM)
211	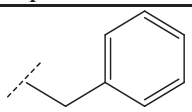	H	H	1.6 ± 0.300
212	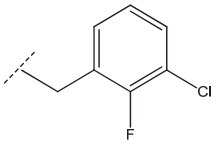	H	H	0.043 ± 0.008
213	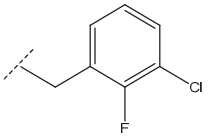	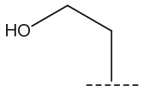	H	0.024 ± 0.011
214	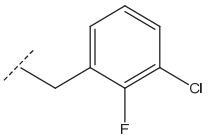	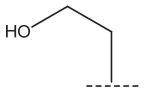	OCH_3	0.009 ± 0.002
215	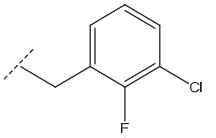	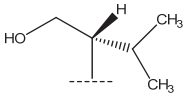	H	0.008 ± 0.001
216[b]	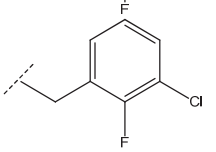	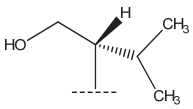	OCH_3	0.007 ± 0.002

[a] ST represents strand transfer; [b] structure of elvitegravir.

(Table adapted with permission from: Sato, M.; Motomura, T.; Aramaki, H.; Matsuda, T.; Yamashita, M.; Ito, Y.; Kawakami, H.; Matsuzaki, Y.; Watanabe, W.; Yamataka, K.; Ikeda, S.; Kodama, E.; Matsuoka, M.; Shinkai, H. Novel HIV-1 integrase inhibitors derived from quinolone antibiotics. *J. Med. Chem.* **2006,** 49, 1506-1508.)[143]

Table 6-14. Structure and HIV-1 IN inhibitory activities of 4-quinolone-3-carboxylic acid-carboxamides (scaffold 2) used in 3D-QSAR study

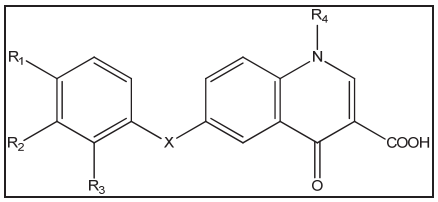

Cpd.	X	R_1	R_2	R_3	R_4	ST[a] IC_{50} (μM)
217	O	F	Cl	H	$(CH_2)_2OH$	>100
218	S	H	H	H	$(CH_2)_2OH$	18.5 ± 3.7
219	CH_2	Cl	H	Cl	$(CH_2)_2OH$	0.2 ± 0.0
220	CH_2	Cl	H	Cl	$(CH_2)_3OH$	1.3 ± 0.1
221	CH_2	Cl	H	Cl	$(CH_2)_4OH$	0.6 ± 0.3
222	CH_2	Cl	H	Cl	$(CH_2)_2N(CH_3)_2$	24.1 ± 5.9
223	CH_2	Cl	H	Cl	$(CH_2)_2OCH_3$	16.5 ± 0.7
224	CO	Cl	H	Cl	$(CH_2)_2OH$	>100
225	CO	Cl	H	Cl	$(CH_2)_3OH$	>100
226	CO	Cl	H	Cl	$(CH_2)_4OH$	>100
227	CHCH	H	H	H	$(CH_2)_2OH$	>100
228	CONH	H	H	H	$(CH_2)_2OH$	>100
229	NHCO	H	H	H	$(CH_2)_2OH$	>100
230	NH	H	Cl	F	$(CH_2)_2OH$	>100
231	NH	H	Cl	F	CH_2CH_3	>100

[a] ST represents strand transfer.

(Table adapted with permission from: Pasquini, S.; Mugnaini, C.; Tintori, C.; Botta, M.; Trejos, A.; Arvela, R. K.; Larhed, M.; Witvrouw, M.; Michiels, M.; Christ, F.; Debyser, Z.; Corelli, F. Investigations on the 4-quinolone-3-carboxylic acid motif. 1. Synthesis and structure-activity relationship of a class of human immunodeficiency virus type 1 integrase inhibitors. *J. Med. Chem.* **2008,** 51, 5125-5129.)[205]

found to have identical binding modes. The other poses for the remaining compounds were then studied and 13 more compounds were identified to share similar binding modes. Markedly different poses were obtained for compounds **191**, **214**, **217**, **220**, and **223**. These compounds may have different binding mode or require an induced fit. Although it is well established that the GLIDE docking is successful in giving the best ligand poses, it fails to rank-order compounds on the basis of their binding affinities. We observed that Glide score showed no correlation ($r^2 = 0.05$) with the ST inhibitory activities for the 98 similar binding compounds. Thus to further validate their "bioactive conformations" a post-docking MM-GBSA rescoring was performed.

MM-GBSA Results

The docked poses of the pruned dataset were subjected to Molecular Mechanics/Generalized Born Surface Area (MM-GBSA)[215] free energy calculations with PRIME (v) of the Schrödinger package. The calculated ΔG_{bind} along with vdW contributions to binding free energy are listed in **Table 6-15**. Analysis of the MM-GBSA calculations revealed an improved correlation, with $r^2 = 0.34$, between the binding free energies (ΔG_{bind}) and the ST inhibitory activities (**Figure 6-23**). A low, albeit better, correlation might be a result of a large and diverse set of chemical structures included in the analysis and a poor estimation of electrostatic binding energies. However, the vdW contribution to the MM-GBSA binding free energy correlated best with the activities with an r^2 value of 0.57 (**Figure 6-24**), which went up to 0.62 with the removal of one outlier (compound **113**). A better correlation with the vdW energy term is significant since hydrophobic interactions are one of the most important contributors to IN inhibitory activity, and all potent IN inhibitors have a common hydrophobic halogenated benzyl ring system as a pharmacophoric feature. Another important contribution to the IN inhibitory activity comes from the electrostatic interactions, notably the coordination of the metal-chelating heteroatoms in an IN inhibitor with Mg^{2+} in the IN active site. The electrostatic contributions to the binding free energy are however not well predicted (data not shown). Previous studies[216, 217] have shown that electrostatic energies are difficult to estimate particularly when the dataset have both charged and neutral molecules as is the case with the present study. Moreover, the negatively charged residues, Asp64, Asp116, Glu152 and the two Mg^{2+} ions are involved in important interactions with inhibitors in the IN active site. This system warrants further studies to determine the effects of protein charge states, electrostatic interactions cut-offs, parameterization of Mg^{2+} and the effect of solute dielectric constant in the calculation of polar solvation energies. Although prime MM-GBSA did not predict accurate binding affinities, it was successful in discriminating the data set into active and inactive compounds and validated the docking derived 'bioactive conformations' for 3D-QSAR studies.

Table 6-15. Results of free energy calculations by Prime MM-GBSA

Cpd.	ST[a] pIC_{50}	ΔE_{vdW}[b]	ΔG_{bind}[c]	Cpd.	ST[a] pIC_{50}	ΔE_{vdW}[b]	ΔG_{bind}[c]
81	4.60	-37.70	-6.33	**130**	4.67	-29.98	-13.63
82	4.85	-35.39	-19.30	**149**	4.82	-36.94	-6.32
83	4.49	-39.00	-11.52	**153**	4.00	-34.56	-3.41
84	5.04	-25.46	-11.41	**154**	4.00	-33.07	-0.85
85	4.92	-26.84	-1.60	**155**	4.88	-34.30	-14.90
86	5.30	-28.39	-4.79	**183**	8.00	-49.16	-25.99
87	4.45	-28.98	3.77	**184**	7.82	-47.31	-23.00
88	5.13	-28.63	-24.25	**185**	8.39	-46.12	-33.17
89	4.72	-39.03	-20.05	**186**	7.82	-49.23	-26.32
90	4.46	-28.17	-10.75	**187**	7.69	-53.89	-14.50
91	4.29	-31.13	-14.47	**188**	7.58	-49.50	-18.62
92	4.74	-35.34	-15.91	**189**	5.30	-39.23	-11.15
93	4.79	-34.29	-19.40	**190**	7.67	-45.10	-17.67
94	4.85	-26.66	-16.78	**192**	8.04	-50.90	-28.62
95	4.88	-28.61	-23.72	**193**	7.82	-53.16	-36.04
96	5.43	-30.41	-25.26	**194**	7.92	-48.03	-17.85
97	4.27	-25.25	-12.55	**195**	7.82	-54.68	-15.89
98	4.00	-28.93	0.27	**196**	6.92	-38.24	-13.52
99	4.03	-38.10	-20.39	**197**	6.65	-36.54	-11.69
100	4.60	-34.37	-15.78	**198**	7.00	-41.86	-15.60
101	4.76	-27.73	-23.46	**199**	6.16	-42.60	-22.80
102	4.52	-29.64	-24.89	**200**	6.85	-41.47	-17.45
103	4.38	-25.87	-16.25	**201**	7.00	-42.29	-18.98
104	4.76	-23.73	-8.31	**202**	6.69	-42.38	-19.51
105	4.61	-25.95	-17.72	**203**	6.60	-43.74	-26.00
106	4.52	-30.02	-19.88	**204**	6.88	-45.00	-27.90
107	4.53	-27.90	-16.80	**205**	5.39	-44.73	-17.11
108	4.82	-25.39	-14.12	**206**	5.30	-41.10	-17.03
109	4.40	-27.36	-20.57	**207**	6.75	-42.57	-18.06
110	4.23	-29.06	-0.58	**208**	7.20	-43.18	-20.70
111	4.11	-32.14	0.30	**209**	7.72	-38.83	-19.28
112	4.11	-28.81	-17.90	**210**	6.85	-43.05	-14.69
113	5.04	-55.14	-8.66	**211**	5.79	-36.08	-13.24
114	4.74	-42.70	-8.18	**212**	7.36	-37.86	-18.06
115	4.79	-43.87	-15.13	**213**	7.61	-41.43	-14.66
116	4.74	-25.41	-10.32	**215**	8.08	-46.00	-23.88
117	4.25	-32.82	-12.33	**216**	8.14	-46.90	-26.64
118	4.33	-28.20	-2.46	**218**	4.74	-42.09	-19.74
119	4.25	-35.18	7.00	**219**	6.69	-29.96	-33.75
120	4.95	-27.33	-12.42	**221**	6.22	-32.79	-21.98
121	4.79	-32.29	-20.32	**222**	4.61	-29.89	-9.10
122	4.20	-28.55	-19.60	**224**	4.00	-29.53	-12.84
123	4.28	-26.55	-9.40	**225**	4.00	-38.45	1.80

Table 6-15. (Continued)

Cpd.	ST[a] pIC_{50}	ΔE_{vdW}[b]	ΔG_{bind}[c]	Cpd.	ST[a] pIC_{50}	ΔE_{vdW}[b]	ΔG_{bind}[c]
124	4.49	-25.68	-9.55	**226**	4.00	-29.02	-4.09
125	4.74	-25.25	-9.30	**227**	4.00	-29.57	-5.34
126	4.22	-36.65	-6.59	**228**	4.00	-30.55	-4.21
127	4.35	-28.73	-4.40	**229**	4.00	-29.68	-10.79
128	4.30	-28.85	-22.05	**230**	4.00	-31.40	-14.31
129	4.16	-27.15	-3.69	**231**	4.00	-24.93	-4.49

[a] ST represents strand transfer; [b] represents van der Waals energy; [c] represents binding free energy.

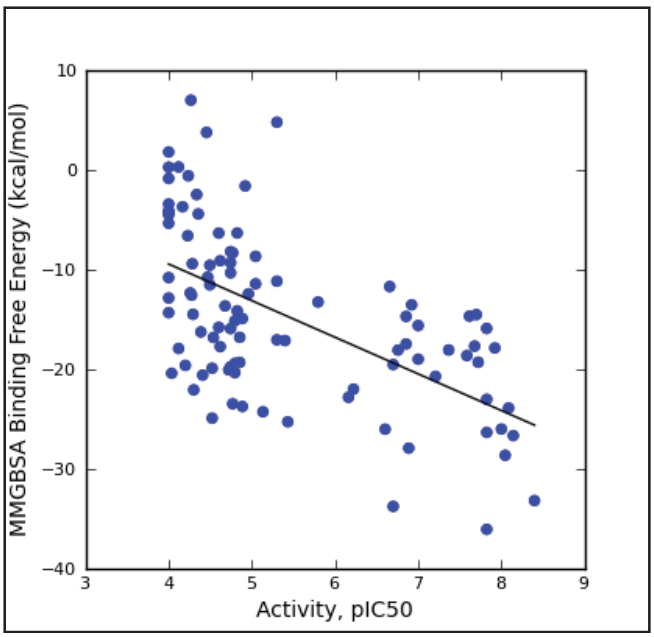

Figure 6-23. Correlation between the MM-GBSA ΔG_{bind} and the ST inhibitory activities (pIC_{50}s)

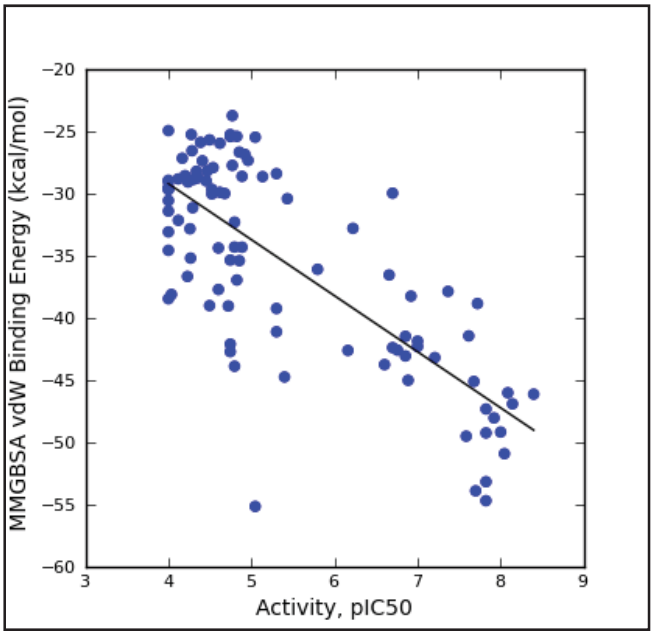

Figure 6-24. Correlation between the MM-GBSA ΔG_{vdW} energies and the ST inhibitory activities (pIC_{50}s)

Homology Model-Guided 3D-QSAR Studies

Molecular data set. A total of 103 compounds were used for the 3D-QSAR studies. Although the data set represented several different compound classes, they all share a somewhat similar structural core. These compounds have common mechanism of action (chelation of the divalent metal and inhibition of ST) and cover a wide range of IC_{50} values spanning over 5 log units, thus constitute a suitable set of compounds for QSAR studies. The dataset was also evenly distributed with regard to activity, comprising potent IN inhibitors having IC_{50}s of 7-8 nM, moderately active 3-keto salicylic acid derivatives with IC_{50}s of 4-5 μM and inactive compounds with IC_{50}s of 100 μM. To evaluate the predictive ability of models, the dataset was divided into a training set of 90 compounds and an external validation test set of 13 compounds. The test set was selected randomly using factor analysis in the SYBYL package (vX1.1, Tripos Associates Inc. St. Louis, MO) and contained compounds representing all the four different potency categories.

Conformation and alignment of the data set. For 3D-QSAR studies we compared two atom-fit alignment rules (models 1 and 2), with the docking alignment (model 3). Determination of the "bioactive conformation" is of utmost importance for the development of a successful 3D-QSAR model of the CoMFA and CoMSIA type. To this end, the developed raltegravir-IN-DNA homology model was used to extract the conformation of raltegravir (compound **193**). This conformation of raltegravir obtained from our homology model perfectly superimposed over its reported X-ray conformation in the PDB 3L2T complex. This conformation of raltegravir was used as a template for alignment and as a conformational template to build the remaining *N*-methyl-4-hydroxypyrimidinone carboxamides. Similarly, the homology model derived conformation of elvitegravir (compound **216**) was used to build the remaining 4-quinolone-3-carboxylic acid analogs. The topmost pose of the amide derivative **149** obtained from the docking simulations was used as a template to build the other amide derivatives. As discussed in the docking studies, chalcones appear to have multiple binding modes. The highest-ranked poses of the two most active compounds **86** and **96** were each used as a bioactive conformation template to build the remaining chalcones of the series. To take into account the conformations of the two most active chalcone derivatives, two different alignments rules, alignment I (model 1) and alignment II (model 2), were generated. It was primarily aimed to assess their effect on the overall unified 3D-QSAR model for IN inhibition. However, the conformations of the *N*-methyl-4-hydroxypyrimidinone carboxamides, 4-quinolone-3-carboxylic acids and 3-keto salicylic acid amides remained identical in both alignments.

Alignment I. For alignment I, the atom-fit alignment function in SYBYL was used for a pair-wise alignment of elvitegravir, chalcone and amide derivatives with raltegravir as a template. The conformations of these compounds were judiciously aligned over raltegravir template taking into consideration their interactions with the IN active site, and with atomic coordinates adjusted to provide the maximum overlap of the

molecules in the dataset. All the compounds were then partially energy minimized by the Simplex procedure to relieve excessive strain. The bound X-ray and homology model-derived conformations revealed partial overlap of the pyrimidinone and quinolone moieties of raltegravir and elvitegravir, respectively. The carboxylate of elvitegravir and the 6-oxo group of raltegravir chelate the same Mg^{2+} ion (between Asp116 and Asp64). Therefore, for alignment, the pyridone ring of elvitegravir was superimposed over the pyrimidinone ring of raltegravir such that the 3′-carbon of the quinolone system was superimposed over the 6′-carbon of the pyrimidinone ring of raltegravir. In this orientation, the C′-5 carbon of the quinolone ring in elvitegravir superimposed over the carbonyl carbon of the carboxamide moiety in raltegravir. This alignment rule resulted in a good overlap of the six-membered rings and matched the crucial metal-chelating pharmacophoric groups. Other pharmacophoric features as represented by their halogenated phenyl rings, which inserted into a cavity as shown in the homology models aligned well. The docked conformation of the topmost poses of the amide analog **149** and chalcone derivative **86**, revealed that their salicylic acid groups mimicked the pyrimidinone ring of raltegravir. The docking also suggested that the 3-keto oxygen of reference compounds **149** and **86**, and the carbonyl oxygen of the carboxamide of raltegravir interacted with the same Mg^{2+} ion (between Asp64 and Glu152). Likewise, the carboxylate groups of compounds **149** and **86** and the pyrimidinone oxo of raltegravir coordinated with the Mg^{2+} between Asp64 and Asp116. Thus, for alignment of the amide and chalcone derivatives, the salicylic acid rings of compounds **149** and **86** were aligned over the pyrimidinone ring of raltegravir such that 1′-carbon atoms of compounds **149** and **86** were superimposed over the 6′-carbon of the pyrimidinone ring of raltegravir. Furthermore, the carbonyl carbons of compounds **149** and **86** were superimposed over the carbonyl carbon of the carboxamide moiety of raltegravir. This alignment rightly positioned their halogenated phenyl rings into the hydrophobic cavity as depicted in the docking studies. The superimposition of the data set using alignment I is shown in **Figure 6-25**.

Alignment II. The pyridone ring of elvitegravir and the salicylic acid group of compound **149** were superimposed (atom-fit) over the pyrimidinone ring of raltegravir similar to alignment I. However, the docked pose of compound **96** was used as the bioactive conformation for the chalcone derivatives. As discussed in the docking section, the halogenated phenyl ring of compound **96** was placed in the opposite (180°) direction. In this orientation, the carboxylate of compound **96** is directed towards the carbonyl oxygen of the benzyl carboxamide moiety of raltegravir and both functionalities interact with the Mg^{2+} between Asp64 and Glu152. Thus for this alignment, the salicylic acid group and the carboxylate carbon of compound **96** were respectively superimposed over the pyrimidinone ring and the carbonyl carbon of the carboxamide moiety of raltegravir. The superimposition of the dataset using alignment II is shown in **Figure 6-26**.

Alignment III. Theoretically, overlaying the poses of the compounds docked at the IN active site should provide a better bioactive conformational alignment than the atom-fitting alignments I and II. Thus, to derive a truly docking based 3D-QSAR, all the 103 compounds were docked and their binding poses analyzed. The poses of 98 compounds that bound similarly were validated by MM-GBSA rescoring which gave better

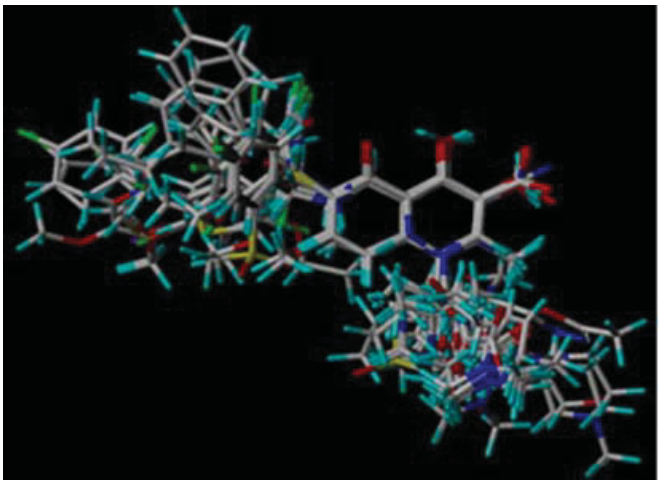

Figure 6-25. Superimposition of the data set by alignment I

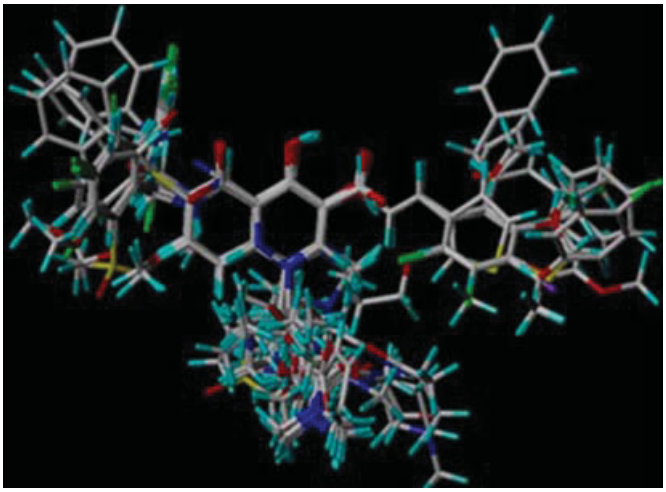

Figure 6-26. Superimposition of the data set by alignment II

correlations (ΔG_{bind} $r^2 = 0.34$; ΔE_{vdW} $r^2 = 0.57$) with ST inhibitory activities. These conformations were then overlayed, to produce an alignment III, which was in effect a combination of alignments I and II. Alignment III is depicted in **Figure 6-27** was used to build a docking-based 3D-QSAR, model 3.

PLS Results

PLS analysis using the leave-one-out (LOO) cross-validation method was used to determine predictive ability (using the cross-validated coefficient q^2) and the number of components to use in the final regression models. The optimal number of components used (5 for both models 1 and 2) was determined by the number of components that yielded the smallest standard error of prediction. Atom-fit alignments I and II were used to develop two 3D-QSAR models; model 1 and model 2, respectively. Alignment I may be more plausible since placement of the hydrophobic phenyl rings of the chalcones into the cavity should have more contact of the inhibitors with IN than alignment II in which part of the phenyl ring of the inhibitor is solvent-exposed. However, significant q^2 and r^2 values were obtained for CoMFA and CoMSIA 3D-QSARs of both models 1 and 2 (**Table 6-16**). In terms of PLS statistics, the CoMFA of both models performed better than their CoMSIA counterparts. The CoMFA 3D-QSAR model 1 performed slightly better than the CoMFA model 2, with q^2 and r^2 values of 0.82 and 0.94, respectively, compared to q^2 of 0.79 and r^2 of 0.93 for CoMFA model 2. Similar q^2 values around 0.71 were obtained for both CoMSIA models 1 and 2. On the basis of its extreme residual value, compound **189** was identified as an outlier in model 1. It was the only compound in the series which did not have a hydrophobic *p*-fluoro benzyl ring and thus its structural uniqueness might be a factor for it being an outlier.

To test the robustness of the predictive capabilities of the models, they were used to predict the activity of an external test set of 13 compounds which were excluded from the training set. The residuals of the training and test set predictions for model 1 are listed in **Tables 6-17** and **6-18**, respectively. The corresponding residual values for model 2 are given in **Tables 6-19** and **6-20**. For model 1, the CoMFA prediction curves for the training and the test set are shown in **Figure 6-28** and the corresponding CoMSIA predictions in **Figure 6-29**. The corresponding CoMFA and CoMSIA predictions for model 2 are shown in **Figure 6-30** and **Figure 6-31**, respectively. As is evident, the present study gave high correlations between actual and predicted values for the external test set. CoMFA and CoMSIA gave comparable predictive r^2 values of 0.93 and 0.83 for model 1 and corresponding predictions of 0.90 and 0.82 for model 2. In addition, more stringent group cross-validation (20 times) was applied to further test the reliability of models. As shown in **Table 6-16**, r^2_{cv} values of 0.82 was obtained for CoMFA and 0.71 for CoMSIA of model 1. The corresponding values for model 2 were 0.78 and 0.69 for CoMFA and CoMSIA, respectively. These results demonstrate that both models are stable and statistically robust. Moreover, low CoMFA and CoMSIA scrambling average q^2 values of 0.17 and 0.18, respectively for model 1 and 0.31 and 0.25 for model 2 also validate the models' statistical significance, showing they were not obtained by chance correlation. The result of bootstrapping further corroborates the robustness of the derived

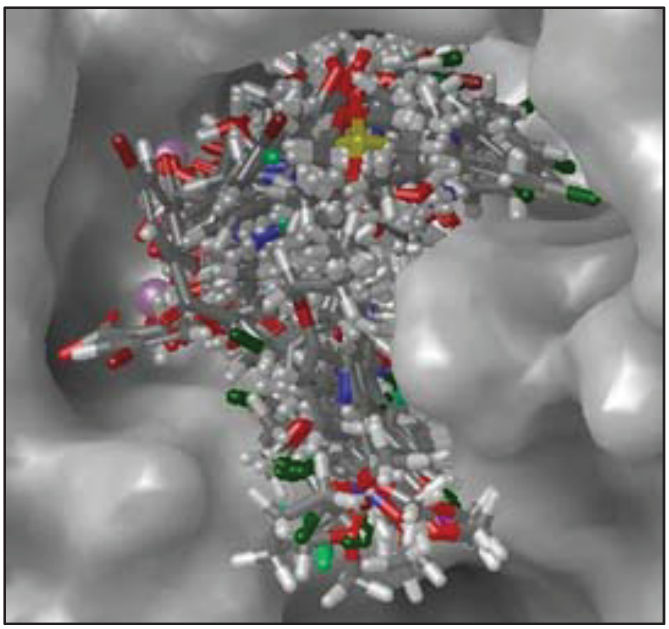

Figure 6-27. Docked conformations of the data set compounds used as alignment III

Table 6-16. PLS statistics of 3D-QSAR models

PLS Statistics	Model 1		Model 2		Model 3	
	CoMFA	CoMSIA	CoMFA	CoMSIA	CoMFA	CoMSIA
q^2	0.82	0.71	0.79	0.71	0.61	0.60
r^2	0.94	0.93	0.93	0.94	0.93	0.94
S	0.34	0.36	0.38	0.35	0.36	0.33
F	284.69	240.51	222.65	261.51	221.03	263.92
PLS Component	5	5	5	5	3	3
Field Contribution						
Steric	0.526	0.105	0.528	0.107	0.453	0.122
Electrostatic	0.474	0.288	0.472	0.292	0.547	0.242
Hydrophobic		0.242		0.223		0.193
H-Donor		0.224		0.214		0.232
H-Acceptor		0.141		0.164		0.211
Bootstrapping r^2 (20 runs)	0.94 ± 0.012	0.95 ± 0.016	0.90 ± 0.01	0.95 ± 0.01	0.95 ± 0.011	0.96 ± .009
Cross-validation q^2 (20 runs)	0.82	0.71	0.78	0.69	0.60	0.59

Table 6-17. Residuals of predictions of the training set by CoMFA and CoMSIA of model 1

Cpd.	Actual ST[a] pIC_{50}	Residuals		Cpd.	Actual ST[a] IC_{50}	Residuals	
		CoMFA	CoMSIA			CoMFA	CoMSIA
81	4.60	0.20	0.48	**149**	4.82	0.44	0.42
82	4.85	0.17	0.27	**153**	4.00	-0.43	-0.34
83	4.49	-0.07	-0.39	**154**	4.00	-0.35	-0.28
85	4.92	0.22	0.26	**155**	4.88	0.51	0.12
86	5.30	0.74	0.21	**183**	8.00	-0.26	-0.21
87	4.45	0.09	-0.26	**185**	8.39	0.54	-0.07
88	5.13	0.64	0.18	**186**	7.82	-0.03	0.40
89	4.72	0.12	0.15	**187**	7.69	-0.37	-0.60
90	4.46	0.23	0.11	**188**	7.58	-0.39	-0.12
92	4.74	0.09	0.20	**189***	5.30	-2.64	-3.16
93	4.79	0.18	0.38	**190**	7.67	-0.40	0.35
94	4.85	0.24	0.26	**191**	8.39	0.26	-0.25
95	4.88	0.29	0.32	**193**	7.82	-0.05	-0.19
97	4.27	-0.36	-0.34	**195**	7.82	-0.25	0.01
98	4.00	-0.35	-0.19	**196**	6.92	-0.01	0.27
99	4.03	-0.55	-0.59	**197**	6.65	0.19	0.25
100	4.60	-0.06	0.02	**201**	7.00	0.54	0.66
101	4.76	0.13	0.11	**202**	6.69	0.04	0.01
102	4.52	-0.04	0.01	**203**	6.60	0.04	-0.01
103	4.38	-0.23	-0.26	**204**	6.88	0.32	0.31
105	4.61	-0.09	-0.12	**205**	5.39	-0.79	-0.82
106	4.52	-0.09	-0.12	**206**	5.30	-1.08	-0.66
107	4.53	-0.14	-0.08	**207**	6.75	0.14	0.15
108	4.82	0.19	0.18	**208**	7.20	0.14	0.00
109	4.40	-0.23	-0.16	**209**	7.72	0.62	0.46
110	4.23	-0.41	-0.20	**210**	6.85	0.06	-0.01
111	4.11	-0.17	-0.31	**212**	7.36	0.78	-0.05
112	4.11	-0.18	-0.15	**213**	7.61	-0.22	-0.30
113	5.04	0.13	0.44	**214**	8.04	0.01	0.28
114	4.74	0.15	0.26	**215**	8.08	0.20	0.92
115	4.79	-0.01	0.03	**216**	8.14	0.20	0.30
116	4.74	0.07	0.30	**217**	4.00	-1.41	-1.61
117	4.25	0.01	-0.03	**218**	4.74	-0.43	-1.08
119	4.25	-0.25	-0.23	**219**	6.69	1.17	0.82
120	4.95	0.26	0.10	**220**	5.88	0.47	0.25
121	4.79	0.08	0.42	**222**	4.61	-0.73	-0.39
122	4.20	-0.35	-0.03	**223**	4.79	-0.45	-0.35
123	4.28	-0.10	-0.17	**224**	4.00	0.01	-0.23
124	4.49	-0.06	0.00	**225**	4.00	0.16	0.13
125	4.74	0.14	0.00	**226**	4.00	-0.04	0.49
126	4.22	-0.40	-0.52	**227**	4.00	-0.16	-0.47

Table 6-17. (Continued)

Cpd.	Actual ST[a] pIC_{50}	Residuals		Cpd.	Actual ST[a] pIC_{50}	Residuals	
		CoMFA	CoMSIA			CoMFA	CoMSIA
127	4.35	-0.16	-0.03	**228**	4.00	0.39	0.60
128	4.30	-0.39	-0.16	**229**	4.00	-0.19	0.18
129	4.16	-0.38	-0.61	**230**	4.00	0.01	-0.50
130	4.67	0.13	0.11	**231**	4.00	-0.05	-0.32

[a] ST represents strand transfer; * represents outlier.

Table 6-18. Residuals of predictions of the test set by CoMFA and CoMSIA of model 1

Cpd.	Actual ST[a] pIC_{50}	Residuals	
		CoMFA	CoMSIA
84	5.04	0.62	0.21
91	4.29	0.05	0.08
96	5.43	0.84	1.11
204	4.76	0.05	0.14
118	4.33	-0.03	-0.15
184	7.82	-0.57	-0.51
192	8.04	-0.16	-0.18
194	7.92	-0.42	0.22
198	7.00	-0.26	0.09
199	6.16	-0.38	0.31
200	6.85	-0.61	-0.39
211	5.79	-0.52	-1.68
221	6.22	0.76	0.66

[a] ST represents strand transfer.

Table 6-19. Residuals of predictions of the training set by CoMFA and CoMSIA of model 2

Cpd.	Actual ST[a] pIC_{50}	Residuals		Cpd.	Actual ST[a] pIC_{50}	Residuals	
		CoMFA	CoMSIA			CoMFA	CoMSIA
81	4.60	0.40	0.53	**149**	4.82	0.10	0.07
82	4.85	0.27	0.30	**153**	4.00	-0.57	-0.62
83	4.49	-0.24	-0.53	**154**	4.00	-0.44	-0.46
85	4.92	0.36	0.29	**155**	4.88	0.29	-0.30
86	5.30	0.57	0.17	**183**	8.00	-0.29	0.09
87	4.45	-0.25	-0.06	**185**	8.39	0.49	-0.18
88	5.13	-0.03	0.17	**186**	7.82	-0.03	-0.02
89	4.72	0.15	0.22	**187**	7.69	-0.24	-0.12
90	4.46	0.11	-0.06	**188**	7.58	-0.04	0.32
92	4.74	0.18	0.19	**189**	5.30	0.28	-0.38
93	4.79	0.14	0.25	**190**	7.67	-0.81	0.50
94	4.85	0.26	0.21	**191**	8.39	0.13	-0.32
95	4.88	0.32	0.32	**193**	7.82	-0.21	-0.57
97	4.27	-0.29	-0.30	**195**	7.82	-0.31	-0.19
98	4.00	0.00	-0.02	**196**	6.92	-0.35	-0.38
99	4.03	-0.54	-0.46	**197**	6.65	0.61	0.15
100	4.60	0.05	0.08	**201**	7.00	0.84	0.91
101	4.76	0.20	0.21	**202**	6.69	-0.05	0.22
102	4.52	-0.15	0.01	**203**	6.60	0.18	0.30
103	4.38	-0.21	-0.20	**204**	6.88	0.43	0.59
105	4.61	0.01	0.08	**205**	5.39	-0.78	-0.59
106	4.52	-0.09	0.04	**206**	5.30	-1.05	-0.62
107	4.53	-0.04	0.03	**207**	6.75	0.24	0.20
108	4.82	0.23	0.30	**208**	7.20	0.35	0.13
109	4.40	-0.27	0.10	**209**	7.72	0.90	0.90
110	4.23	-0.27	0.27	**210**	6.85	0.04	0.07
111	4.11	-0.22	0.17	**212**	7.36	0.76	0.26
112	4.11	-0.19	0.19	**213**	7.61	-0.05	0.12
113	5.04	0.03	-0.24	**214**	8.04	-0.21	-0.02
114	4.74	0.17	-0.14	**215**	8.08	0.13	-0.74
115	4.79	0.01	-0.13	**216**	8.14	0.15	-0.04
116	4.74	0.10	-0.06	**217**	4.00	-0.05	0.66
117	4.25	0.04	0.07	**218**	4.74	-0.44	0.60
119	4.25	-0.14	0.19	**219**	6.69	1.11	-0.97
120	4.95	0.42	-0.12	**220**	5.88	0.57	-0.26
121	4.79	0.13	0.03	**222**	4.61	-0.49	0.49
122	4.20	-0.32	0.27	**223**	4.79	-0.39	0.14
123	4.28	0.01	0.24	**224**	4.00	-0.11	0.08
124	4.49	0.08	0.05	**225**	4.00	-0.05	-0.08
125	4.74	0.26	-0.13	**226**	4.00	-0.14	-0.39
126	4.22	-0.26	0.38	**227**	4.00	-0.32	0.50

Table 6-19. (Continued)

Cpd.	Actual ST[a] pIC_{50}	Residuals		Cpd.	Actual ST[a] pIC_{50}	Residuals	
		CoMFA	CoMSIA			CoMFA	CoMSIA
127	4.35	-0.24	0.04	**228**	4.00	0.36	-0.49
128	4.30	-0.47	0.23	**229**	4.00	-0.19	-0.31
129	4.16	-0.37	0.17	**230**	4.00	-0.15	0.14
130	4.67	0.06	0.35	**231**	4.00	-0.15	0.15

[a] ST represents strand transfer.

Table 6-20. Residuals of predictions of the test set by CoMFA and CoMSIA of model 2

Cpd.	Actual ST[a] pIC_{50}	Residuals	
		CoMFA	CoMSIA
84	5.04	-0.11	0.11
91	4.29	-0.07	-0.01
96	5.43	0.70	1.06
104	4.76	0.19	0.23
118	4.33	-0.73	-0.38
184	7.82	-0.71	-0.79
192	8.04	-0.20	0.10
194	7.92	0.18	0.24
198	7.00	-0.15	0.15
199	6.16	-0.22	0.00
200	6.85	-0.43	-0.38
211	5.79	0.21	-1.57
221	6.22	0.81	0.67

[a] ST represents strand transfer.

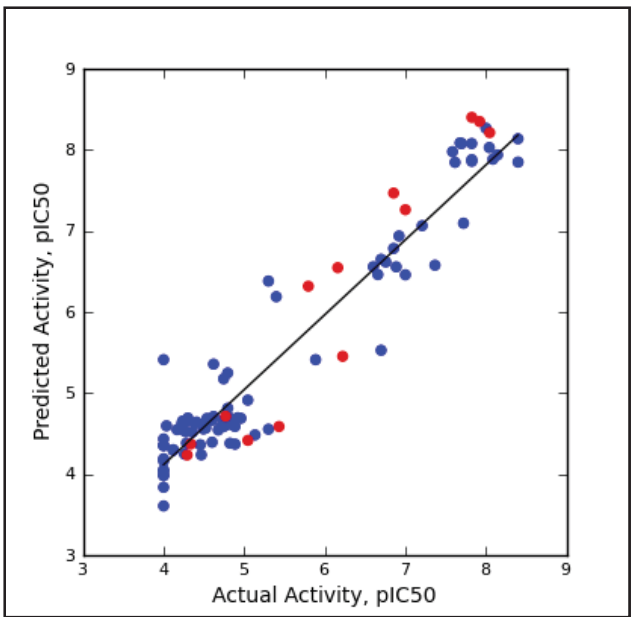

Figure 6-28. Predictions of the training and the test set by CoMFA of model 1

Training and the test sets are represented by blue and red spheres, respectively.

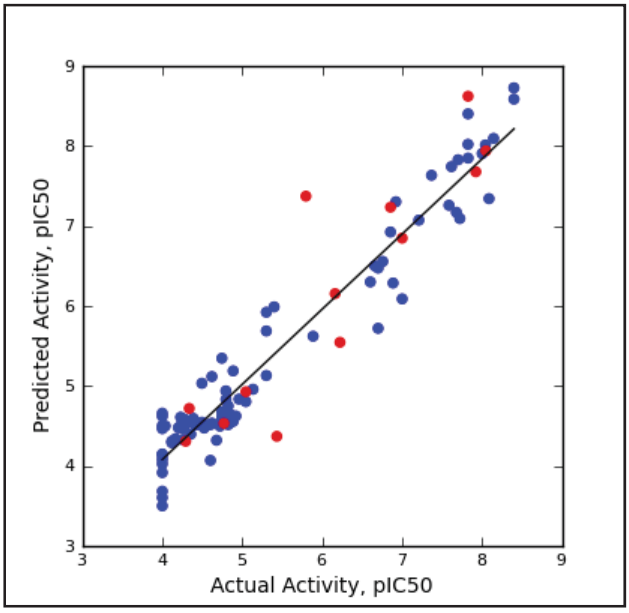

Figure 6-29. Predictions of the training and the test set by CoMSIA of model 1

Training and the test sets are represented by blue and red spheres, respectively.

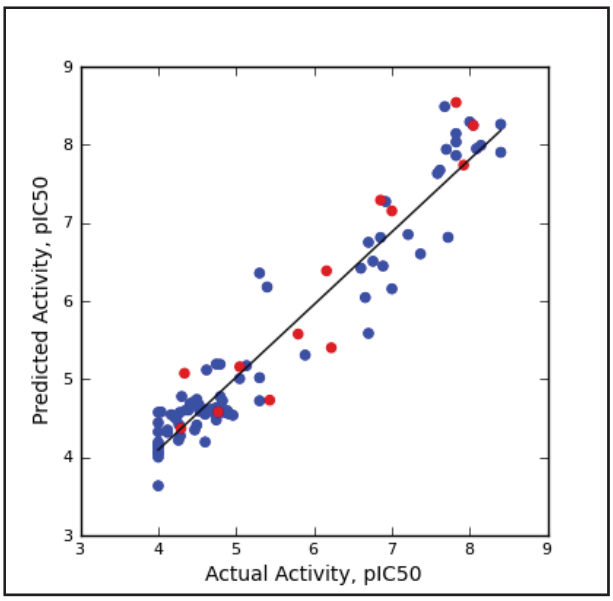

Figure 6-30. Predictions of the training and the test set by CoMFA of model 2

Training and the test sets are represented by blue and red spheres, respectively.

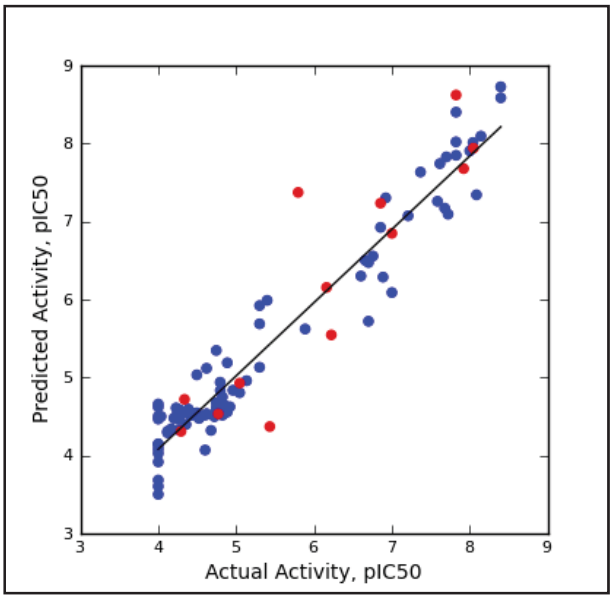

Figure 6-31. Predictions of the training and the test set by CoMSIA of model 2

Training and the test sets are represented by blue and red spheres, respectively.

models. PLS results of model 3, which was developed using the docking derived alignment, III are also shown in **Table 6-16**. For estimating predictivity, the same 13 compounds were used as an external test set. The models, which could be developed with only 3 components, gave q^2 and r^2 values of 0.61 and 0.93 for CoMFA and the corresponding values of 0.60 and 0.94 for CoMSIA. Both the CoMFA and the CoMSIA models gave low standard error of estimate (SEE) and large F values of 0.36, 221.03 and 0.33, 263.92, respectively. Cross-validation and boot-strapping results indicated that both CoMFA and CoMSIA models were statistically robust. The CoMFA model performed significantly better in estimating the test set compounds with a predictive r^2 value of 0.82 as compared with a predictive r^2 value of 0.62 obtained with the CoMSIA model. The residuals of the training and the test set predictions of model 3 are summarized in **Table 6-21** and **Table 6-22**, respectively. Plots of CoMFA and CoMSIA predictions for the training and the test set are shown in **Figures 6-32** and **6-33**. Comparison of the QSAR models suggests that the atom-based alignment models 1 and 2, gave higher q^2 values when compared with the docking-based alignment model 3. However, models 1 and 2 were derived using 5 components and the higher q^2 values might result from over-fitting of the data points because of the higher number of components used. Thus to check for any over-fitting, models 1 and 2 were revisited using 3 components. Re-derived model 1 gave q^2 and r^2 values of 0.67, 0.85 for CoMFA and 0.60 and 0.84 for CoMSIA, respectively. However, the model gave higher SEE and smaller F values (0.54, 173.69 for CoMFA and 0.57, 151.09 for CoMSIA) compared to the docking-based model 3. CoMFA and CoMSIA 3D-QSARs of model 2 when derived with 3 components gave lower q^2 and r^2 values ($q^2 = 0.58$, $r^2 = 0.75$ for CoMFA; and $q^2 = 0.55$, $r^2 = 0.76$ for CoMSIA). Moreover, these models also resulted in higher SEE and smaller F values when compared to model 3. Thus, in terms of robustness and ability to generalize, the docking-derived 3D-QSAR models are better than the ligand-based alignments I and II. Also, compared to our previous pharmacophore-based CoMFA and CoMSIA 3D-QSAR modeling of the salicylic acid derive IN inhibitors, this structure-based and composite 3D-QSAR approach has generated better models, with best q^2 and predictive r^2 values of 0.82 and 0.93, respectively, compared to best q^2 and predictive r^2 values of 0.54 and 0.57, respectively. Taken together, the results suggest that the docking-based composite QSAR models are better predictive tools than our previous QSAR models for lead optimization of the 3-keto salicylic acid series.

Contour Maps

Model 1: CoMFA contour maps. The PLS coefficients derived CoMFA steric and electrostatic contours mapped around raltegravir are displayed in **Figure 6-34** and **Figure 6-35**, respectively. The IN-DNA binding site is represented as Connolly surface which was generated by the MOLCAD program in the SYBYL modeling package. There are green and yellow contours in the region close to the *gem*-dimethyl side chain. This is the region where substantial modifications were made that eventually led to the optimized *gem*-dimethyl oxadiazole carboxamide moiety. This side chain is positioned such that the oxadiazole ring occupies a pocket, which is indicated by a green contour in the cleft

Table 6-21. Residuals of predictions of the training set by CoMFA and CoMSIA of model 3

Cpd.	Actual ST[a] pIC_{50}	Residuals		Cpd.	Actual ST[a] pIC_{50}	Residuals	
		CoMFA	CoMSIA			CoMFA	CoMSIA
81	4.60	0.19	0.15	**149**	4.82	0.26	-0.16
82	4.85	0.12	0.08	**153**	4.00	-0.45	0.11
83	4.49	0.06	0.02	**154**	4.00	0.06	0.17
85	4.92	0.37	0.66	**155**	4.88	0.08	-0.20
86	5.30	0.72	0.67	**183**	8.00	-0.41	0.61
87	4.45	-0.14	-0.21	**185**	8.39	-0.03	-0.03
88	5.13	0.46	0.44	**186**	7.82	-0.53	0.25
89	4.72	-0.01	0.03	**187**	7.69	0.45	-0.19
90	4.46	-0.003	-0.04	**188**	7.58	-0.20	-0.01
92	4.74	0.41	0.30	**189**	5.30	-0.05	-1.31
93	4.79	0.10	-0.05	**190**	7.67	0.52	-0.22
94	4.85	0.06	0.16	**191***	8.39	N/I	N/I
95	4.88	0.25	0.43	**193**	7.82	0.40	0.12
97	4.27	-0.19	-0.46	**195**	7.82	0.006	-0.22
98	4.00	-0.20	-0.46	**196**	6.92	0.01	-0.02
99	4.03	-0.65	-0.68	**197**	6.65	0.54	0.43
100	4.60	0.36	0.14	**201**	7.00	-0.08	0.21
101	4.76	0.22	0.29	**202**	6.69	0.25	0.03
102	4.52	0.23	0.04	**203**	6.60	-0.22	-0.04
103	4.38	-0.19	-0.34	**204**	6.88	-0.16	0.13
105	4.61	0.14	-0.15	**205**	5.39	-0.03	0.14
106	4.52	-0.28	-0.14	**206**	5.30	-0.45	0.002
107	4.53	0.17	0.13	**207**	6.75	-0.10	-0.02
108	4.82	-0.28	-0.01	**208**	7.20	0.06	-0.43
109	4.40	0.52	-0.07	**209**	7.72	0.69	0.44
110	4.23	-0.60	0.00	**210**	6.85	-0.06	0.10
111	4.11	-0.18	0.02	**212**	7.36	0.79	0.34
112	4.11	-0.52	-0.21	**213**	7.61	0.58	0.39
113	5.04	0.19	0.20	**214***	8.04	N/I	N/I
114	4.74	0.14	0.20	**215**	8.08	0.25	0.06
115	4.79	0.20	0.40	**216**	8.14	-0.22	-0.02
116	4.74	0.31	0.04	**217***	4.00	N/I	N/I
117	4.25	-0.26	-0.09	**218**	4.74	-1.42	-0.60
119	4.25	0.26	-0.12	**219**	6.69	-0.02	0.49
120	4.95	0.04	0.15	**220***	5.88	N/I	N/I
121	4.79	0.11	-0.03	**222**	4.61	-0.55	-0.50
122	4.20	0.40	-0.26	**223***	4.79	N/I	N/I
123	4.28	-0.13	-0.33	**224**	4.00	-0.32	0.40
124	4.49	0.07	-0.12	**225**	4.00	-0.14	-0.78
125	4.74	0.05	0.07	**226**	4.00	-0.49	0.15
126	4.22	0.02	-0.10	**227**	4.00	-0.003	-0.01

Table 6-21. (Continued)

Cpd.	Actual ST[a] pIC_{50}	Residuals		Cpd.	Actual ST[a] pIC_{50}	Residuals	
		CoMFA	CoMSIA			CoMFA	CoMSIA
127	4.35	0.01	-0.05	**228**	4.00	-0.02	-0.51
128	4.30	-0.10	-0.16	**229**	4.00	-0.26	-0.02
129	4.16	-0.13	0.20	**230**	4.00	0.20	-0.29
130	4.67	-0.20	0.13	**231**	4.00	-0.29	0.13

[*] Compounds excluded from the dataset because of the lack of common binding mode, N/I represents not included in the data set, [a] ST represents strand transfer.

Table 6-22. Residuals of predictions of the test set by CoMFA and CoMSIA of model 3

Cpd.	Actual ST[a] pIC_{50}	Residuals	
		CoMFA	CoMSIA
84	5.04	0.52	0.46
91	4.29	-0.29	-0.11
96	5.43	1.06	0.96
104	4.76	0.42	0.02
118	4.33	-0.01	-0.03
184	7.82	0.58	1.69
192	8.04	-0.66	0.48
194	7.92	1.06	1.99
198	7.00	0.70	0.28
199	6.16	-0.89	-0.18
200	6.85	0.37	-0.75
211	5.79	0.25	-0.77
221	6.22	0.46	0.50

[a] ST represents strand transfer.

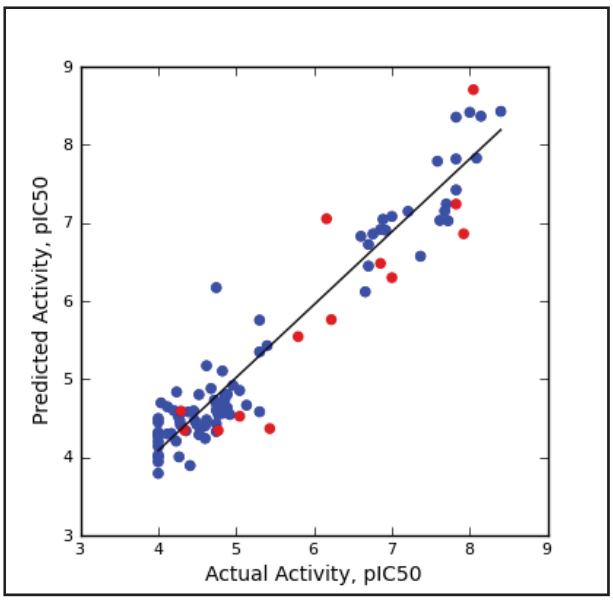

Figure 6-32. Predictions of the training and the test set by CoMFA of model 3

Training and the test sets are represented by blue and red spheres, respectively.

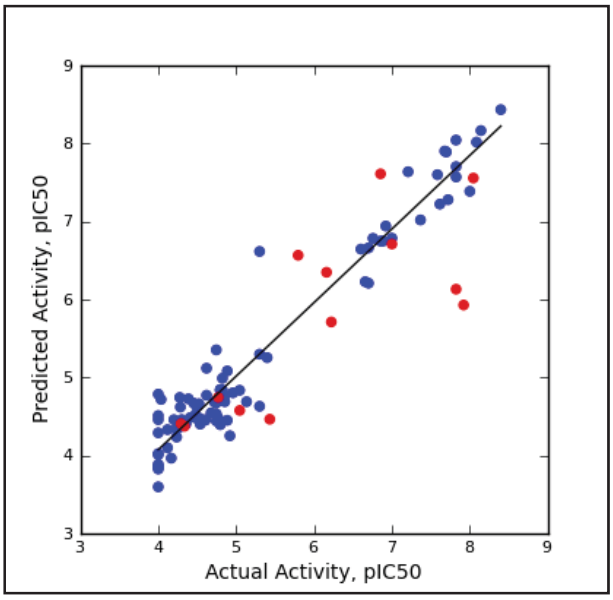

Figure 6-33. Predictions of the training and the test set by CoMSIA of model 3

Training and the test sets are represented by blue and red spheres, respectively.

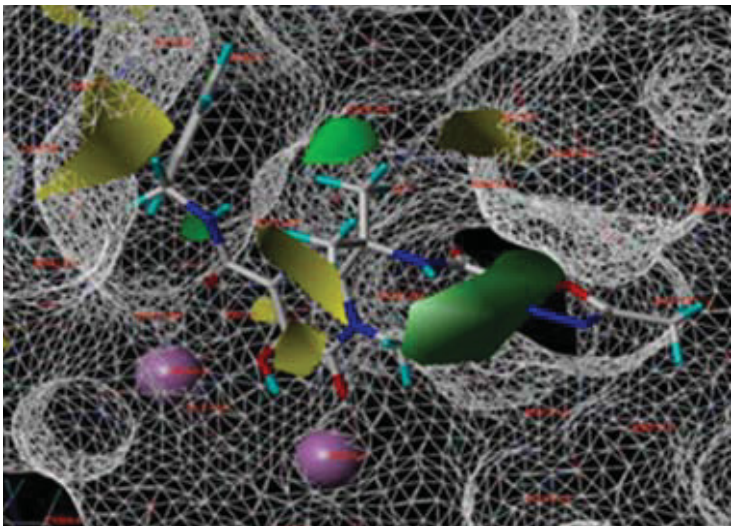

Figure 6-34. CoMFA steric contour maps of model 1 superimposed on raltegravir

Green and yellow contours illustrate regions where steric bulk has favorable and unfavorable effects on activity respectively.

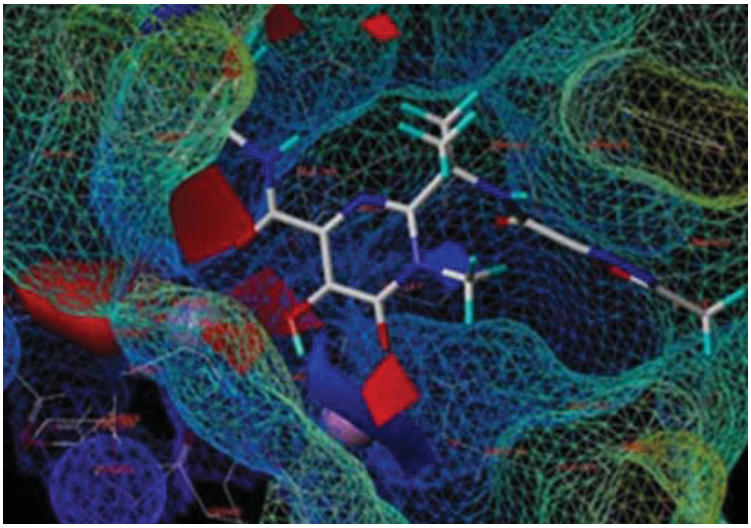

Figure 6-35. CoMFA electrostatic contour maps of model 1 superimposed on raltegravir

Blue and red isopleths indicate regions where an increase of positive and negative charge is required for activity.

formed by residues Asn117, Pro142, Tyr143, Asn144 and Pro145. The *N*-hydroxyalkyl side chain of the quinolone ring of elvitegravir also occupies the green contour and thus shows nearly 6 times improved activity relative to the unsubstituted analog (**212** vs **215**). The two yellow contours above the pyrimidinone ring indicate that steric bulk is unfavorable in this region. The *N*-acetyl substituted piperidine ring of compound **205** fits into a yellow contour, which might explain the decrease in activity of this compound and other structural analogs of 4-quinolone-3-carboxylic acids with a bulky phenyl ring, such as compounds **228** and **229**. Moreover, their hydroxyethyl side chains also point towards the steric disfavored yellow contour region, further supporting a decrease in activity of these analogs. There are several yellow regions around the hydrophobic phenyl ring, suggests that steric bulk is not favored at these positions possibly because of clashing with the donor DNA. This might be one of the reasons fluorine whose size is similar to hydrogen's is the most optimal substituent on this ring. The electrostatic map of CoMFA shows a blue contour close to the pyrimidinone ring, implying that groups that have electropositive character are favored for activity. This is supported by the presence of electron-deficient nitrogen-containing ring systems in many different classes of IN inhibitors including the pyrimidinone ring of raltegravir and the quinolone ring of elvitegravir, as well as the acidic phenolic hydrogen in this region. There are three red contours close to the metal-chelating pharmacophore of raltegravir indicating that the presence of electron rich groups is favored for activity. There is also a red contour at the *ortho*-position on the fluorobenzyl group. This is explained by the contour superimposed on elvitegravir which reveals the *ortho*-fluoro substituent occupying these red contours. A distal red contour which is close to the *meta*-postion on the benzyl group of elvitegravir again suggests that negative charge is favorable in this region. This is reflected by the presence of an electronegative chlorine substituent at this position in elvitegravir and related analogs.

Because the developed QSAR models are developed for potential use in optimizing our lead amide derivatives to more potent IN inhibitors, CoMFA contours were also mapped over compound **149**. The bromine substituent at the *para*-position of the salicylic acid group could be substituted with bulky groups for improvement of activity as a green contour resides at this region. The CoMFA contours help explain the loss in activity of compounds **117**, **118** and **119**, which have cyclopentyl and substituted polycyclic naphthalene rings placed in steric bulk disfavored yellow-contoured regions.

Model 1: CoMSIA contour maps. CoMSIA steric and electrostatic contours mapped onto raltegravir are similar to those of the CoMFA model in having two yellow contours which result from the steric clash with the amide backbone of Tyr143 and the solvent accessible surface. Like in the CoMFA map, there is a green contour which is occupied by the carboxamide moiety of the oxadiazole side chain. However, in compound **206**, the side chain is oriented towards the yellow contours and explains the loss in activity. Another steric bulk-favored green region is occupied by the *p*-fluorobenzyl group, which has a positive influence on potency. This is confirmed by the significant loss of activity of compound **189** which lack of a phenyl at this position. The green contour is flanked by a large yellow contour suggesting that bulk tolerance

within the cavity is quite limited. This could be the reason behind the reduced potency of compounds **112** and **117** in the chalcone series whose methoxy and bulky cyclopentyl groups fit into the disfavored yellow region. Similarly for compounds **118** and **119**, loss in activity might result from the naphthyl rings placed in the bulk disallowed yellow region. The phenyl ring in compounds **217**, **224**, and **227**-**229** fits into the disfavored yellow region, and that might account the significant loss in activity of these analogs.

The CoMSIA electrostatic map shows two red contours close together near the oxadiazole ring which is involved in π-stacking interactions with the phenyl ring of the Tyr143. Similar to the CoMFA electrostatic contour map, there is a blue contour over the hydroxyl group of raltegravir. This possibly reflects the ionizable acidic OH group of raltegravir. Lastly, there are two small red contours around the oxygen of the methoxy and the hydroxyl groups in elvitegravir, correctly predicting the requirement of electron rich groups at this location.

CoMSIA hydrophobic contours superimposed on raltegravir (**Figure 6-36**) show the presence of two large yellow regions indicating that hydrophobic groups at these positions are favored for activity. While one of the yellow contours is occupied by the phenyl ring in raltegravir, the phenyl ring of elvitegravir is oriented towards the second yellow contour. There is also a small yellow region at the *para*-position on the phenyl ring. Indeed, the presence of hydrophobic halogens like bromine in compound **86** or chlorine in compound **88** suggest the presence of hydrophobic interactions at this position. There is a hydrophilic region that the ribose and the phosphate regions of the viral DNA. This voluminous white contour encloses the the carboxamide moiety and extends up to the central hydroxyl substituent in the pyrimidinone ring of raltegravir. The reduced potency of compound **206** may be explained by having the hydrophobic methyl group of its *N*-methyl carboxamide moiety located in the white region, which is counter to the preference of a hydrophilic moiety. A yellow contour fits over the methyl and a white contour fits over the carbonyl group of the oxadiazole carboxamide side chain in raltegravir in agreement with their hydrophobic and hydrophilic character, respectively. The H-bond donor-acceptor contour plots mapped onto raltegravir are shown in **Figure 6-37**. The magenta contour signifies that acceptor groups on the inhibitor are favored at that location, whereas the red contour encompasses a region where H-bond acceptors are disfavored, probably because of the presence of the carbonyl oxygen of the amide backbone of Tyr143 in the receptor. Another magenta contour is merged within the purple contour suggesting an H-bond acceptor is favored but a donor is disfavored which relate to groups that interact with the backbone NH of Pro145. It is close to the 8′-position of the quinolone ring in elvitegravir indicating that acceptor groups are well tolerated at this position. There is another red contour above the phenyl ring at the *ortho* and *meta*-positions in raltegravir implying that H-bond acceptors are disfavored at these positions. One of the purple regions is merged with and complements the magenta contour at the 8′-position of the quinolone ring. The other purple region appears to complement the presence of the amino group of Gln148 in the receptor site, signifying that the presence of H-bond donor at this region is detrimental to activity. Cyan contours indicate regions where H-bond donor groups increase activity. One of the cyan contours fits the NH group of the pyrimidinone carboxamide functionality in raltegravir while the

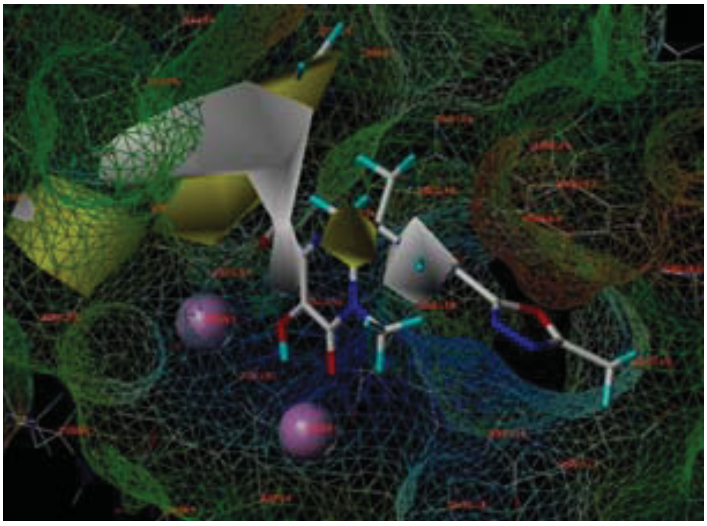

Figure 6-36. CoMSIA hydrophobic contour maps of model 1 superimposed on raltegravir

Yellow and white contours enclose areas favorable for hydrophobic and hydrophilic groups respectively.

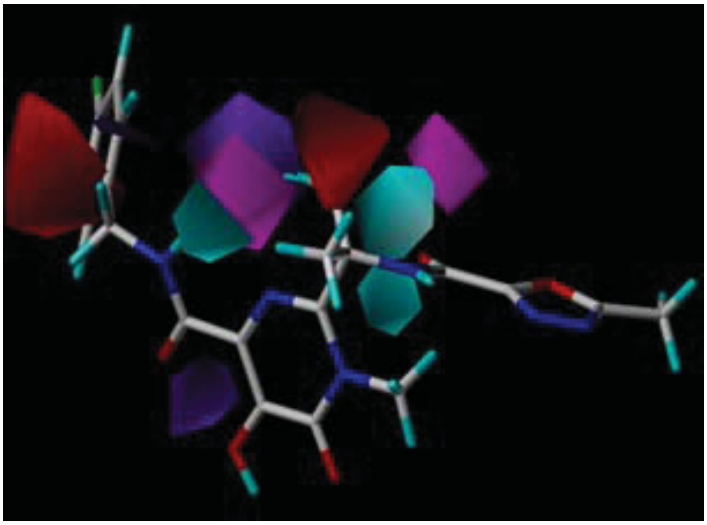

Figure 6-37. CoMSIA H-bond contours of model 1

Purple contours indicate regions where H-bond donor decreases activity whereas cyan contour illustrates regions where H-bond donor increases activity. Magenta isopleths indicate areas where H-bond acceptor increases affinity while red isopleths indicate areas where H-bond acceptor decreases affinity.

other is located in the region close to the hydroxyl of the alkyl hydroxyl group of elvitegravir.

Model 2 contour maps. The CoMFA steric (**Figure 6-38**) and electrostatic (**Figure 6-39**) contours on raltegravir arising from model 2 have similarities to the contours obtained in model 1. One green contour again fits into the oxadiazole ring suggesting that bulk is favored. Nearby yellow regions similar to those in the CoMFA contour of model 1 indicate sterically disallowed regions. Likewise, there are several red and one blue contours around the metal-chelating pharmacophore. Similar to the CoMFA model 1, the contours also explain the loss of inhibitory activity of compounds **189**, **206**, **217**, **224** and **225**, and **227**-**229**. In addition, the CoMFA contour map further reveals green regions around the two *meta*-positions on the phenyl ring, suggesting that bulky groups could be added at these positions. One of the green contours is occupied by the methyl of the methoxy group in elvitegravir, corroborating the increase in activity seen with the presence of methoxy substituents in compounds **213** vs. **214** and **215** vs. **216**. The CoMSIA steric and electrostatic contours projected onto raltegravir reveal SAR information similar to CoMSIA isopleths of model 1. However, there is a distant yellow contour which fits around the phenyl ring of the chalcone derivatives. In alignment II, the phenyl rings of the chalcones were oriented in the opposite (180°) direction to those in alignment I, and not within the cavity formed by the displacement of 3′-adenosine of the viral DNA. The hydrophobic contour of CoMSIA projected on raltegravir (**Figure 6-40**) shows two white regions around the metal-chelating pharmacophore and another similar white region below the NH of the carboxamide moiety in raltegravir and oxygen of the methoxy substituent in elvitegravir. Again as in model 1, a yellow contour close to the *gem*-dimethyl substituent is observed, suggesting a hydrophobic favored region. The H-bond donor and acceptor contours (**Figure 6-41**) show a large cyan isopleth located on the hydroxyl group of the hydroxalkyl side chain in elvitegravir. This appears to complement the red polyhedra observed in the corresponding contour maps of model 1. There are small cyan and magenta contours close to the pyrimidinone ring of raltegravir showing the positive role of a H-bond donor. There are two purple contours around the benzyl groups of raltegravir and elvitegravir implying that H-bond donors are not tolerated on the phenyl ring. One of the purple contours fits over the *meta*-chloro substituent of elvitegravir suggesting the preference for a H-bond acceptor at this position.

Model 3 contour maps. Contours resulting from docking-based alignment III are mostly similar to the contours that resulted from models 1 and 2. Since details of these contours have been described above, only the contours that differ markedly are further discussed. CoMFA and CoMSIA steric and electrostatic contours are shown in **Figure 6-42** and **Figure 6-43**, respectively. A large green contour observed in the CoMFA map is directed towards the *gem*-dimethyl substituent indicating the importance of this sterically favored group. Large yellow contours near the oxadiazole ring are evident in both CoMFA and CoMSIA maps, and may have resulted due to the lack of space beyond the oxadiazole shown by the surface protrusion on the right upper side of the oxadiaxole

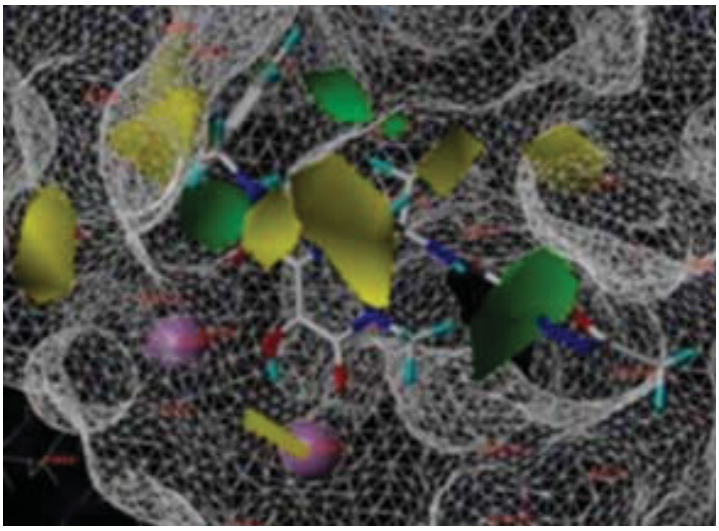

Figure 6-38. CoMFA steric contours of model 2

Green and yellow contours illustrate regions where steric bulk has favorable and unfavorable effects on activity respectively.

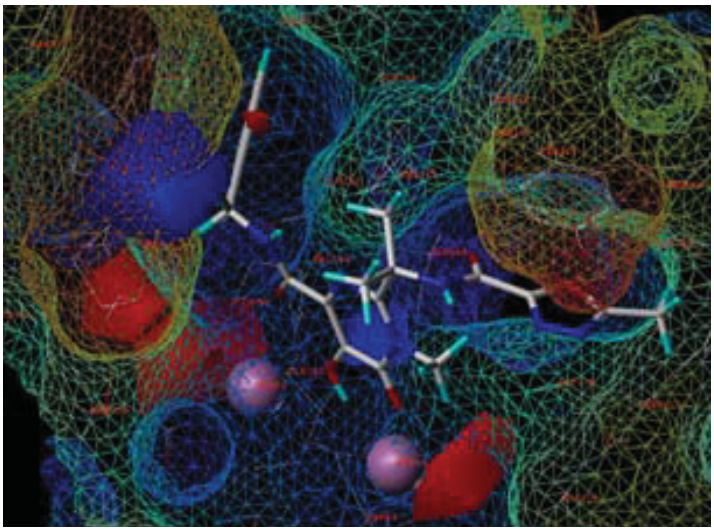

Figure 6-39. CoMFA electrostatic contours of model 2

Blue and red isopleths indicate regions where an increase of positive and negative charge is required for activity.

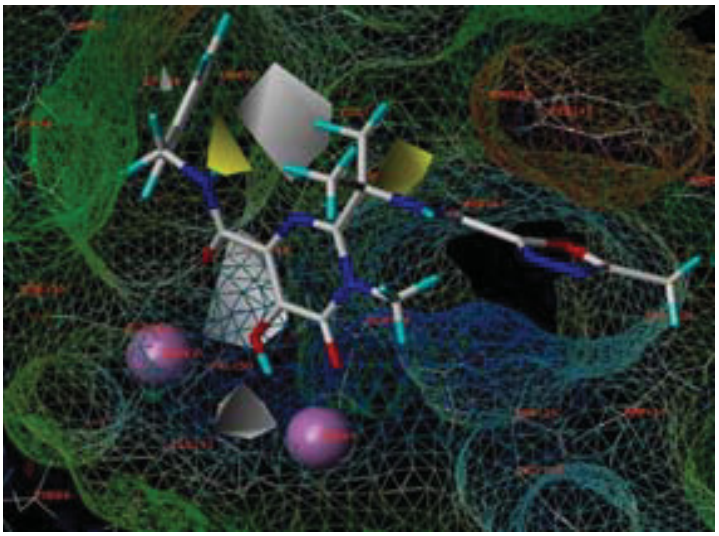

Figure 6-40. CoMSIA hydrophobic contours of model 2

Yellow and white contours enclose areas favorable for hydrophobic and hydrophilic groups respectively.

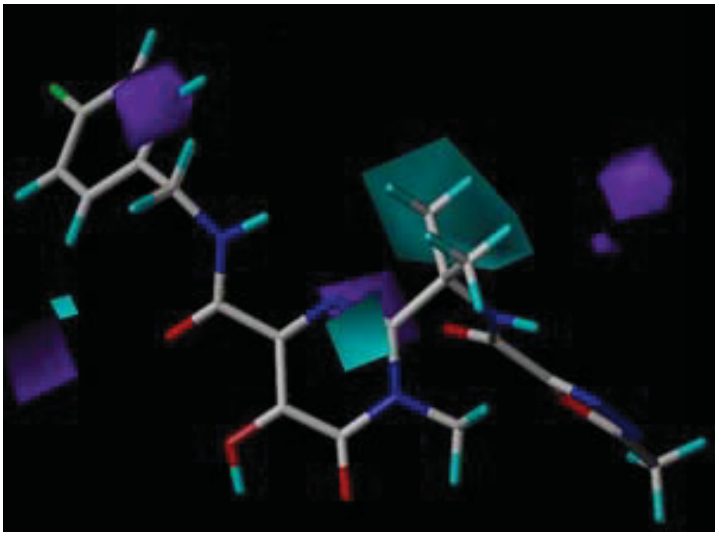

Figure 6-41. CoMSIA H-bonding contours of model 2

Purple contours indicate regions where H-bond donor decreases activity whereas cyan contour illustrates regions where H-bond donor increases activity.

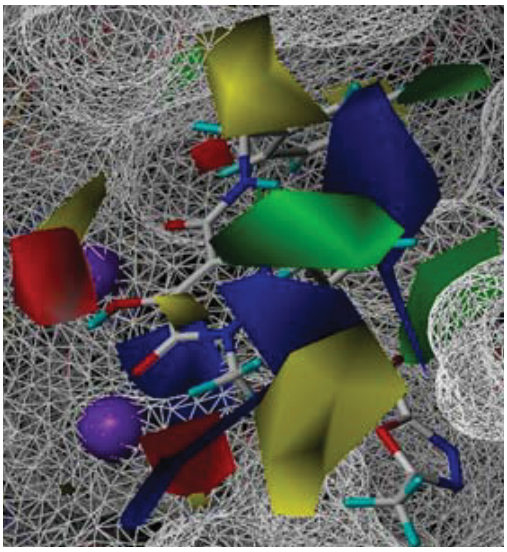

Figure 6-42. CoMFA steric and electrostatic contours of model 3

Green and yellow contours illustrate regions where steric bulk has favorable and unfavorable effects on activity respectively; blue and red isopleths indicate regions where an increase of positive and negative charge is required for activity.

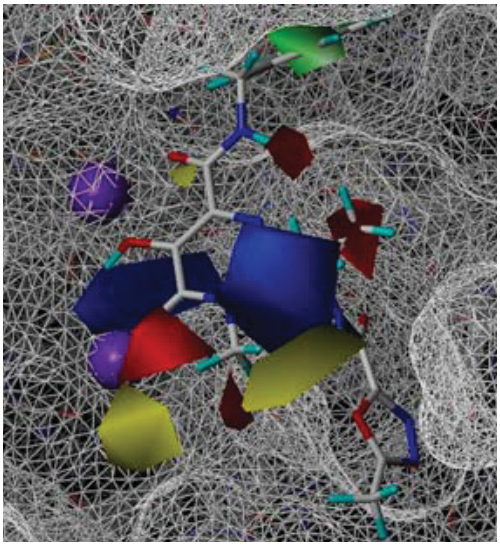

Figure 6-43. CoMSIA steric and electrostatic contours of model 3

Green and yellow contours illustrate regions where steric bulk has favorable and unfavorable effects on activity respectively; blue and red isopleths indicate regions where an increase of positive and negative charge is required for activity.

ring of raltegravir. Similarly, a green common contour is mapped onto the phenyl ring suggesting that bulk is favored inside the cavity. In the CoMFA map, a yellow contour is observed close to the benzyl moiety implying the possibility of steric clash with the surrounding DNA. Electrostatic contours show several red contours close to the metal-chelating oxygen atoms implying that electronegative groups increase activity. A blue contour common in both CoMFA and CoMSIA maps is also present near the metal-chelating pharmacophore. These contours which suggest electropositive or H-donor groups are favored for activity resulted from the acidic phenolic OH residues. A large blue contour (near the green region) observed in CoMFA is indicative of positive groups interacting with the surrounding deoxyribose phosphate backbone in the DNA. Both the CoMSIA hydrophobic, H-bond donor and H-bond acceptor contours are shown in **Figure 6-44**. There are yellow contours that map onto the hydrophobic phenyl ring and *gem*-dimethyl substituent suggesting that hydrophobic groups are favored at these positions. There are white hydrophilic regions which map on the carboxamide moiety and on the oxadiazole ring. The H-bonding contours show two purple contours close to *o*-position on the phenyl ring and a red contour close to the *m*-position indicating that H-bond donors and acceptors are disfavored at these positions, respectively. There is a purple contour close to the metal-chelating atoms implying that H-bond donors are disfavored. An overlapping magenta and red contours suggest H-bond acceptor is favored, while beside it H-bond donor is disfavored. An overlapping cyan and magenta contours occur around the NH of the benzyl carboxamide moiety indicating that NH can act as both a H-bond donor and acceptor at this position. Thus, the contour maps of model 3 reinforced the SAR features explained by contour maps of 3D-QSAR models 1 and 2. This is not surprising since the docking-based alignment II, was in a way a composite of alignments I and II.

The two best 3D-QSAR models, 1 and 3, were finally used to predict the amide derivatives that, were prospectively synthesized in Chapter 4. Thus, compounds in the correct ionization states were assigned MOPAC atomic charges and predicted for their ST activities. Comparison of the predicted vs. experimental activities is shown in **Table 6-23**. Both CoMFA and CoMSIA of the docking-based QSAR model 3 performed better than their model 1 counterparts; as all the predicted compounds were found to be within 1 log unit of the pIC_{50} values. Furthermore, the CoMFA, of model 3 predicted three out of total five compounds used for validation within 0.50 log units. With reference to related amide, compound **149**, used in the training set, the CoMFA of model 3 predicted two compounds (**152**, **157)** to be more active than the reference compound **149**. Upon biological testing it was revealed that these two compounds were reasonably predicted. Thus, the final performance of the CoMFA of QSAR model 3, which performed the best, may be considered acceptable. As the data set used in building the QSAR models included only four salicylic acid-3-carboxamides, further studies using greater number of salicylic acid-3-carboxamides derivatives in the training set may improve the predictive ability of the 3D-QSAR models for the design of related novel 3-keto salicylic acid IN inhibitors.

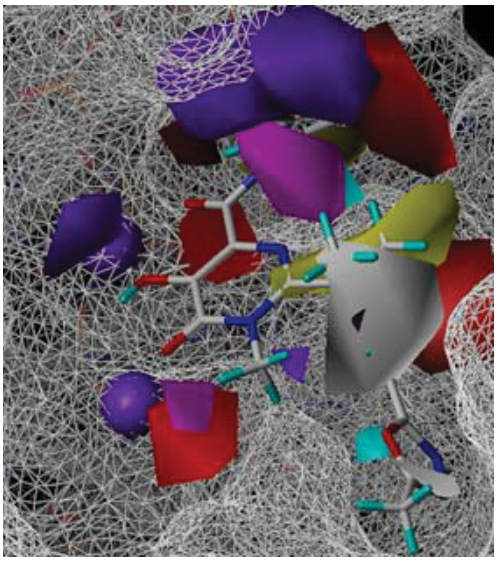

Figure 6-44. CoMSIA hydrophobic and H-bonding contours of model 3

Yellow and white contours enclose areas favorable for hydrophobic and hydrophilic groups respectively; purple contours indicate regions where H-bond donor decreases activity whereas cyan contour illustrates regions where H-bond donor increases activity. Magenta isopleths indicate areas where H-bond acceptor increases affinity while red isopleths indicate areas where H-bond acceptor decreases affinity.

Table 6-23. Comparison of the predicted activities of the 3D-QSAR models guided synthesized compounds

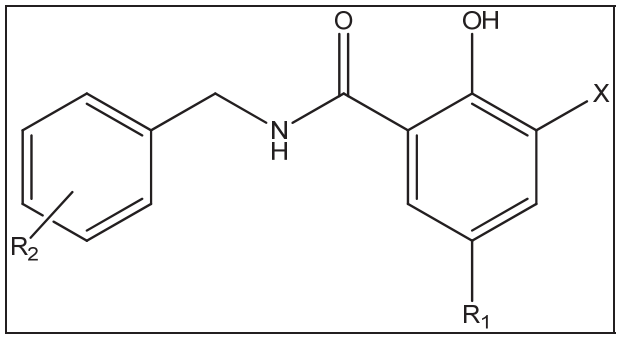

Cpd.	X	R_1	R_2	Actual pIC_{50}	Model 1 predicted pIC_{50}		Model 3 predicted pIC_{50}	
					CoMFA (Res.)[b]	CoMSIA (Res.)[b]	CoMFA(Res.)[b]	CoMSIA(Res.)[b]
149[a]	COOH	Br	4-F	4.82	4.38 (0.44)	4.40 (0.42)	4.56 (0.26)	4.98 (-0.16)
150	COOH	Br	4-Br	4.16	4.45 (-0.29)	4.39 (-0.23)	4.65 (-0.49)	5.11 (-0.95)
151	COOH	Br	2,4-di-F-3-Cl	5.39	4.44 (0.95)	4.43 (0.96)	4.56 (0.83)	5.14 (-0.25)
152	CONHCH2-4-F-Ph	Br	4-F	5.22	4.61 (0.61)	4.34 (0.88)	5.18 (0.04)	5.59 (-0.37)
157	OH	COCHCH-Ph	4-F	4.67	5.96 (-1.29)	6.03 (-1.36)	5.12 (-0.45)	5.53 (-0.86)
158	COCHCH-2,3,6-tri-Cl-Ph	Br	4-F	4.00	4.44 (-0.44)	4.16 (-0.16)	4.71 (-0.71)	4.51 (-0.51)

[a] Reference compound used as training set in 3D-QSAR models 1 and 3; [b] Represents residual values.

Linear Interaction Energy Activity Model

To compare the three dimensional (3D) molecular interaction field-based (CoMFA) and molecular similarity indices based (CoMSIA) QSAR models with the linear interaction approximation[218] derived energy parameters, a LIA QSAR model of the IN inhibitors was developed. LIA estimates the free energy of binding by deriving electrostatics, vdW, and cavity energy terms using a molecular mechanics force field and is based on the surface generalized born continuum model of solvation.[219] The objective of building the LIA QSAR model is to correlate the changes in the free energy of binding of the IN inhibitors in our dataset with their experimental IC_{50} values; and therefore to provide a direct estimation of the potencies based on their binding free energies. Although, unlike the CoMFA and CoMSIA models, the LIA calculations are not highly dependent on the molecular alignments in calculating the binding free energies, their accurate estimation is subject to giving a correct binding pose.

Thus, 98 integrase inhibitors of the dataset which shared similar binding modes, as revealed by the docking studies, were used for building the LIA QSAR model. Same test set of 13 compounds, docking-based CoMFA and CoMSIA 3D-QSAR models, was used for prediction. Correlation coefficient r^2 of 0.59 was obtained for the training set with an rmsd of 0.88. Group cross-validation (leave-4-out) q^2 of 0.54 indicates that model can reasonably predict compounds not included in the training set. The model was then used to predict the activities for the test set compounds. A plot of training and test set predictions is shown in **Figure 6-45**. Correlation coefficient r^2 of 0.79 between the actual and predicted activities of the test set indicates that the LIA model has good predictive ability. This model could estimate the binding affinities of novel HIV-1 IN inhibitors and aid the virtual screening of IN inhibitors for lead discovery and development.

The vdW, electrostatic and cavity energy terms obtained from the LIA calculations (**Table 6-24**) showed correlation of 0.44, 0.09, and 0.44, with the ST IC_{50}s, in that order. Liaison did not estimate electrostatics accurately probably because of similar reasons mentioned in the MM-GBSA results. Regression coefficients α, β, and γ, for the vdW, electrostatic and cavity energy terms were found to be 0.087, -0.01, and 0.11, respectively. This indicates that the cavity and the vdW energy terms contribute significantly to activity. The larger value for the cavity term implies that binding of IN inhibitors is greatly influenced by placement of the ligand into a binding pocket. This is in agreement with one of the most important binding requirements of potent IN inhibitors. The crystal structures of the foamy virus IN-DNA complex in the presence of IN inhibitors, raltegravir and elvitegravir, have revealed that their halogenated benzyl ring is bound in a cavity formed by the IN-DNA interface after the displacement of 3′ adenosine of the viral DNA. This feature has also been correctly depicted by our homology models of HIV-1 IN-DNA-inhibitor complex that were discussed previously. Analysis of the energy terms for raltegravir (compound **193**) and elvitegravir (compound **216**) explains their similar binding orientation in the IN active site. There is a greater desolvation penalty for raltegravir as opposed to a smaller penalty for elvitegravir. Although the halogenated benzyl groups of both dock into the cavity, the amide linkage gives the benzyl moiety in raltegravir more flexibility to get more deeply buried into the

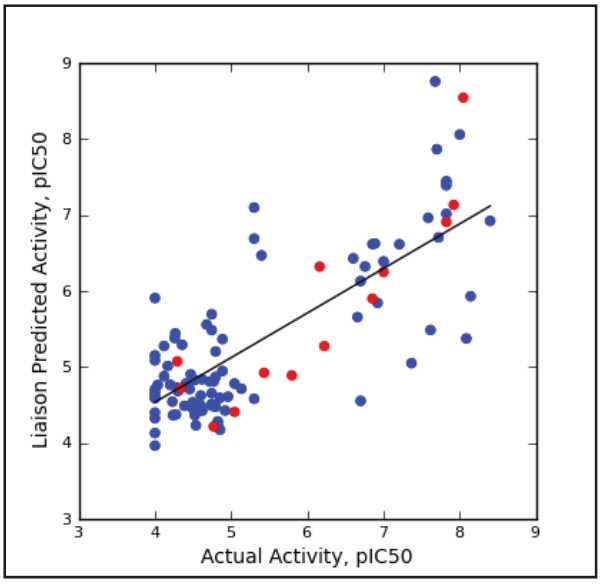

Figure 6-45. Plot of actual and predicted ST inhibitory activities (pIC_{50}s) by the LIA model

Training and the test sets are represented by blue and red spheres, respectively.

Table 6-24. Average van der Waals (U_{vdW}), electrostatic (U_{ele}) and cavity energy (U_{cav}) terms obtained from the LIA calculations

Cpd.	U_{vdW}[a]	U_{cav}[b]	U_{ele}[c]	Cpd.	U_{vdW}[a]	U_{cav}[b]	U_{ele}[c]
81	-3.64	2.58	-168.58	**130**	-27.66	2.50	-70.53
82	-3.17	3.22	-134.91	**149**	-13.87	4.41	-38.58
83	-3.91	2.59	-170.39	**153**	-36.41	4.65	-7.63
84	0.68	3.31	-188.99	**154**	-30.57	1.76	-14.81
85	-26.95	4.09	49.82	**155**	-21.30	3.23	-95.56
86	-24.27	3.66	7.71	**183**	-46.92	8.80	-82.23
87	-27.07	3.49	17.18	**184**	-38.81	6.94	-59.44
88	-2.52	3.45	-189.98	**185**	-32.81	6.60	-114.88
89	-10.07	3.88	-131.13	**186**	-39.26	7.60	-58.80
90	-2.58	3.58	-206.55	**187**	-48.65	10.16	-34.48
91	-4.31	3.88	-205.05	**188**	-36.04	7.92	-77.39
92	-7.48	3.92	-137.5	**189**	-34.42	8.61	-96.62
93	-6.45	2.86	-140.39	**190**	-53.72	10.67	-72.47
94	-1.17	3.19	-192.54	**192**	-51.16	9.62	-84.71
95	-2.99	3.09	-212.50	**193**	-42.67	8.66	-60.23
96	-3.00	2.56	-211.46	**194**	--38.97	8.33	-64.80
97	0.50	2.85	-189.28	**195**	-50.27	8.64	8.57
98	-28.18	3.10	32.94	**196**	-20.29	6.17	-120.44
99	-9.72	3.73	-131.34	**197**	-18.37	5.82	-122.33
100	-7.40	3.83	-136.34	**198**	-33.37	6.07	-50.90
101	-2.05	2.76	-210.58	**199**	-32.74	6.44	-59.14
102	-2.28	2.80	-210.01	**200**	-28.04	6.73	-54.86
103	-0.52	2.79	-192.11	**201**	-32.52	6.53	-66.60
104	2.10	2.60	-190.17	**202**	-30.96	5.92	-61.17
105	-0.25	2.82	-188.10	**203**	-34.24	6.37	-57.75
106	-6.46	2.70	-131.34	**204**	-35.59	7.18	-56.45
107	-3.92	2.76	-139.22	**205**	-33.56	7.26	-57.56
108	-0.47	2.77	-173.17	**206**	-37.09	6.55	-56.89
109	-0.67	2.42	-223.33	**207**	-32.49	5.31	-73.44
110	-20.29	4.07	-0.53	**208**	-35.37	6.67	-62.96
111	-30.44	3.94	-4.52	**209**	-35.15	6.55	-74.77
112	-2.11	3.69	-206.71	**210**	-34.90	7.01	-63.40
113	-43.47	4.33	156.91	**211**	-19.66	2.74	-70.65
114	-43.65	3.93	65.95	**212**	-19.93	2.87	-82.47
115	-39.13	4.61	114.87	**213**	-31.61	2.90	-26.08
116	-0.30	3.28	-191.02	**215**	-30.97	3.30	-16.52
117	-5.54	4.27	-220.24	**216**	-28.31	3.68	-88.37
118	-21.15	4.48	-22.96	**218**	-24.35	3.40	-81.58
119	-33.45	4.25	9.11	**219**	-10.23	3.51	-109.24
120	-1.57	3.48	-187.59	**221**	-22.61	3.30	-77.11
121	-10.34	3.51	-171.10	**222**	-19.66	3.80	-54.20
122	-3.24	3.46	-188.87	**224**	-10.92	3.45	-113.49

Table 6-24. (Continued)

Cpd.	U_{vdW}[a]	U_{cav}[b]	U_{ele}[c]	Cpd.	U_{vdW}[a]	U_{ele}[b]	U_{cav}[c]
123	-2.36	2.27	-205.83	**225**	-34.58	3.40	42.80
124	0.47	3.17	-193.39	**226**	-3.04	3.74	-152.21
125	0.04	3.43	-190.18	**227**	-7.43	4.22	-68.26
126	-3.29	2.70	-175.25	**228**	-7.51	5.05	-93.39
127	-20.81	2.68	-100.44	**229**	-6.26	5.70	-122.54
128	-1.68	2.55	-203.84	**230**	-7.09	5.36	-74.82
129	-30.26	2.37	2.51	**231**	-6.47	4.87	-140.74

[a] Represents van der Waals energy; [b] represents cavity energy term; [c] represents electrostatic energy.

cavity (see **Figure 6-13**); than that in elvitegravir (see **Figure 6-15**). This loss of desolvation energy is then immediately followed by more favorable electrostatic and vdW interactions with IN and viral DNA, contributing to potent inhibitory activities. The electrostatic energy, although not correlated well for the entire data, could be compared among raltegravir and elvitegravir given that their crystal structure conformations were used in the LIA calculations. Electrostatic terms were observed to be more favorable for elvitegravir probably because of the free negatively charged carboxylate that can participate in stronger electrostatic interactions with the two Mg^{2+} ions in the integrase active site. The vdW energy term is more favorable for raltegravir which could be due to more hydrophobic contacts with residues in the IN active site. Notably, raltegravir has an extended *gem*-dimethyl oxadiazole side chain which is involved in vdW contacts with side chain methylene of Asn117, π-stacking interactions with Tyr143 and vdW contacts with Pro142. These interactions on the other hand are not observed with the hydroxyl alkyl chain in elvitegravir. Evaluation of the energy terms for the two most active chalcone derivatives also gives support to their binding modes. As discussed in the docking section, these compounds may have two binding poses (**Figure 6-18**), one that docks their phenyl ring into the cavity (compound **86**) and the other (compound **96**) whose most frequent conformations have their phenyl ring placed away from the cavity, exposed to solvent. The LIA cavity energy term for compound **76** is less than that of compound **86**, suggesting a binding mode in which their 2,3,6-trichloro-substituted phenyl ring is placed outside the cavity and interacts with the methylene of Ser119 and the methine of Gly118. The more favorable vdW energy term for compound **86** also implies that its halo-phenyl ring docks into the cavity and makes more favorable vdW contacts.

RACHEL-Guided Design of Compound 137

Receptor-based design was attempted to synthesize amide compound **157**. Analysis of binding interactions of raltegravir (**Figure 6-14**) revealed vdW interactions between the methyl on the oxadiazole ring and the side chain methylenes of Asn117. Moreover, the oxadiazole ring in raltegravir establishes a π-stacking interaction with the phenyl ring of Tyr143. Tyr 143 is a conserved residue among the family of retroviruses and literature reports have shown that mutation of this residue (Y143 R/C) decreases viral susceptibility to raltegravir.[220] The binding interactions of elvitegravir (**Figure 6-15**) also revealed vdW interactions between its isopropyl moiety and the Tyr143 residue. Conformation of the most active compound (**96**) in the chalcone series also showed that its halogenated-phenyl ring interacted (**Figure 6-20**) with Tyr 143, Gly118, and Ser119. In contrast, no interactions with Tyr143 or Asn117 were observed in our synthesized 3-keto salicylic acid amides IN inhibitors. Based on these observations and the sterically favorable requirement, suggested by the 3D-QSAR contours, prompted me to append a bulky group with an aim of having π -stacking interactions with Tyr143. Thus, to determine the importance of this site in the inhibition of IN, the amide derivative **149**, was used as a lead to design a compound that could mimic the interactions of the oxadiazole ring of raltegravir. Towards this end, RACHEL, a lead optimization program[221] in the Sybyl molecular modeling package was used. Compound **149** bound to

the IN active site (**Figure 6-46**) suggesting that the bromine at the R_1 position could be substituted and used as a site for modification. Tyr143 was defined as the target site in the receptor for directing the fragments to grow and make contacts with this residue. Automated combinatorial optimization was then performed and the compounds were conformationally searched and iteratively processed within the IN active site. Only those compounds that dock well in the receptor site were retained as hits. To optimize the size of the resulting hits, a molecular weight filter (50-200 Da) was applied in the searching process. After the analysis, a set of 50 hits were obtained, which were then evaluated. On the basis of drug-likeness and synthetic feasibility only 1 hit (**232**) was considered for further evaluation. Compound **232** had a hydrophobic aryl akyl moiety substituted at the R_1 position. The binding interactions of compound **232** (**Figure 6-47**) revealed that the phenyl ring of the added fragment is involved in the desired *pi*-stacking interaction with Tyr143, and also made vdW contacts with Asn117. Superimposition of the conformations of raltegravir by shape complementary (**Figure 6-48**) supported the synthesis and biological testing of the derived compound.

Docking Studies of Synthesized Phenanthrene HIV-1 IN Inhibitors

To determine the binding modes of phenanthrene derivatives, synthesized in Chapter 5, docking studies were also conducted on a homology model of a complete HIV-1-DNA-complex. Docking studies predominantly revealed two distinct binding modes for the phenanthrene derivatives. The docked conformations of compound **177** are shown in **Figure 6-49** and interactions in **Figure 6-50** and **Figure 6-51**, respectively. In both orientations, the β-diketo acid chelating pharmacophore interacted with the two Mg^{2+} ions in the IN active site, thus contributing to IN inhibition in accordance with the proposed mechanism of action of ST inhibitors. The phenanthrene ring in one binding mode interacted with residues Glu92, Ser119, Asn120, and Phe121, in a novel binding region in the IN active site. In the other mode, the phenanthrene ring made contacts with Pro142, Tyr143, and Asn117, and Gly118. It is important to note that because of steric bulk, the phenanthrene ring does not dock into the cavity into which the characteristic halobenzyl moieties of advanced IN inhibitors, including raltegravir and elvitegravir, are inserted.[93] The interactions of the halobenzyl groups with DNA bases and IN residues that forms this cavity is one of the most important features contributing to potent IN strand transfer activities. Structure-based design suggests significant potential for improvement of potencies of this series of IN ST inhibitors as a halobenzyl moiety could be appended to occupy this vacant cavity. More importantly, docking studies showed no significant interactions with Gln148 and Asn155 which are key residues that cause viral resistance. Since, compound **174** resulted in a significant loss of activity (ST IC_{50} of 63 μM) its binding pose was also evaluated. It was observed that compound **174** predominantly docked in a different binding mode (**Figure 6-52**). In this orientation, while the phenanthrene ring interacted with Thr66, His67, and Leu68, only the acid and the enolic oxygen of the β-diketo acid motif chelate the two Mg^{2+} ions. The loss of potency may be attributed to a disruption of chelation by an adjacent electron withdrawing fluorine substituent. Structurally similar derivative **175** had similar binding pose (**Figure 6-53**) as **174**. However, the improved activity of compound **175** might

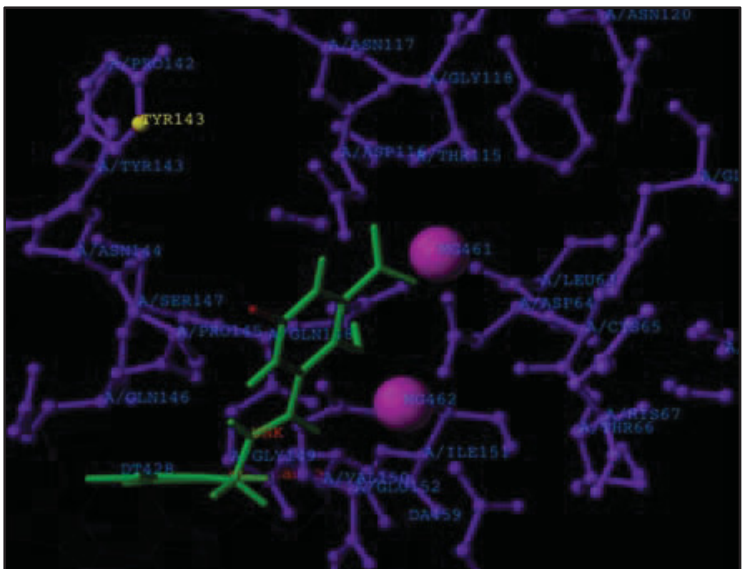

Figure 6-46. RACHEL-based design using compound 149 as lead

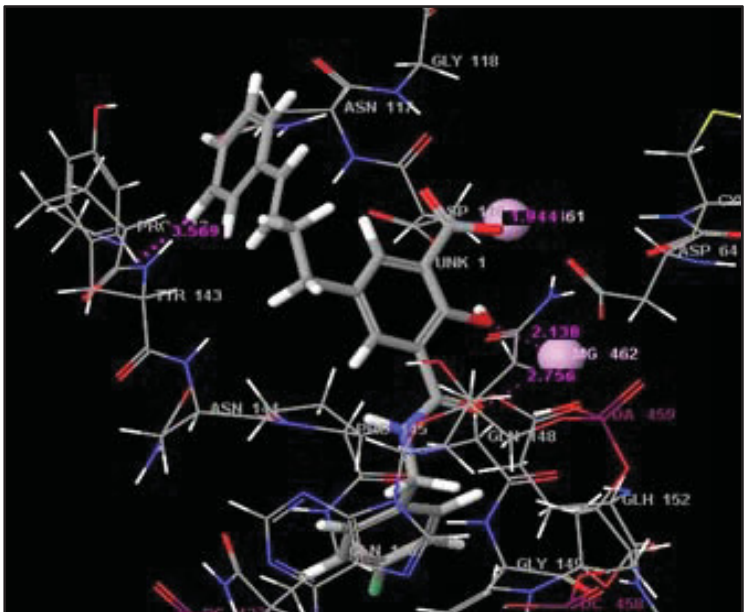

Figure 6-47. Binding interactions of RACHEL derived compound 232

Mg^{2+} ions are represented by magenta spheres. Active site residues are represented by wires. Compound **212** is represented in tubes and shown with grey carbons. Other atoms in the ligand are colored as follows: O, red; N, blue; F, bright green. H, white.

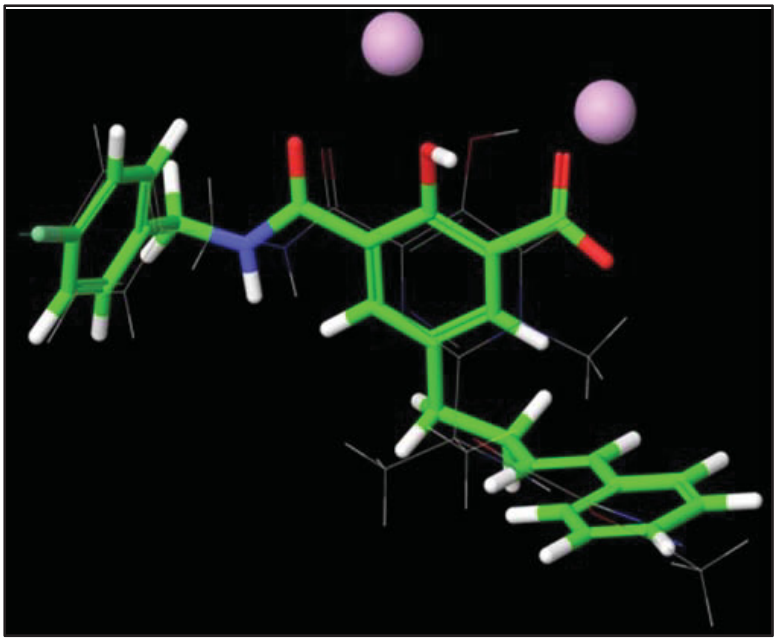

Figure 6-48. Superimposition of compound 232 over Raltegravir

Mg^{2+} ions are shown by magenta spheres. Raltegravir is shown in wires and colored by element. Compound **232** is shown in tubes and highlighted with green carbons. Other atoms in ligands are colored as follows: O, red; N, blue; F, bright green. H, white.

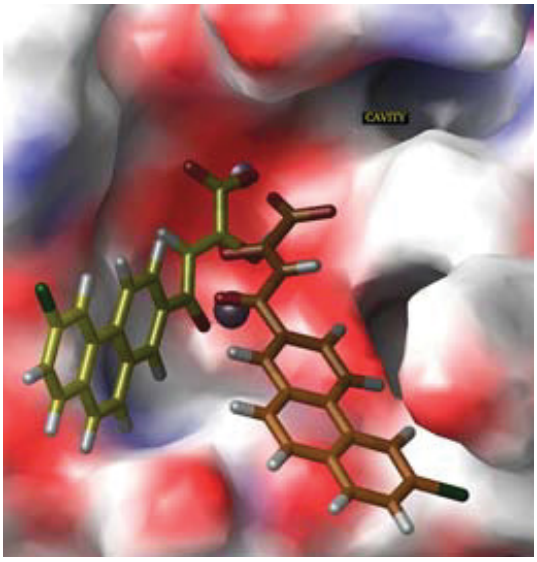

Figure 6-49. Binding modes of compound 177 in IN active site

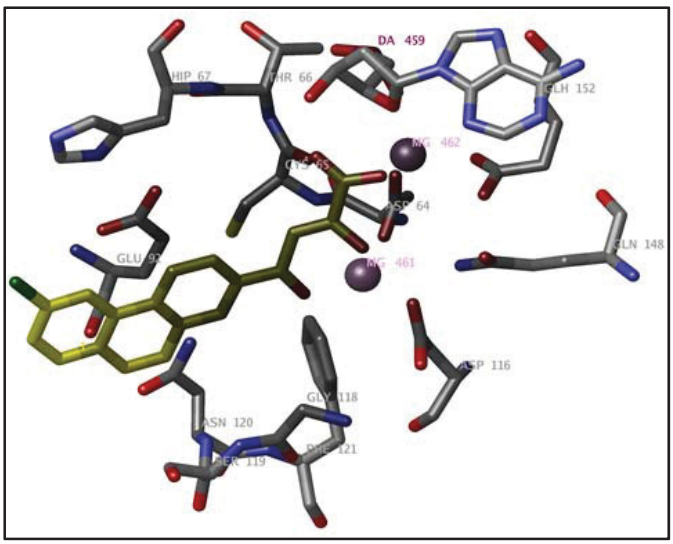

Figure 6-50. Interactions of compound 177 in one binding mode

Mg^{2+} ions are represented by purple spheres. Active site residues are represented by tubes and colored by element. Compound **177** is represented in tubes and highlighted with yellow carbons. Other atoms in the ligand are colored as follows: O, red; Cl, dark green.

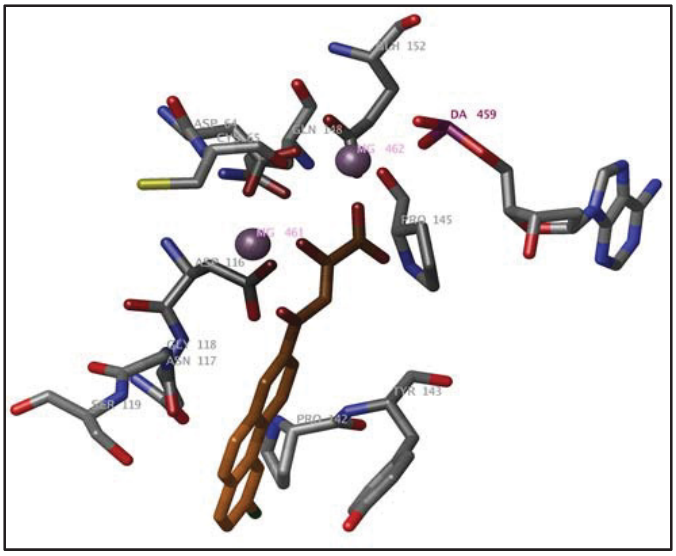

Figure 6-51. Second binding mode of compound 177

Mg^{2+} ions are represented by purple spheres. Active site residues are represented by tubes and colored by element. Compound **177** is represented in tubes and highlighted with yellow carbons. Other atoms in the ligand are colored as follows: O, red; Cl, dark green.

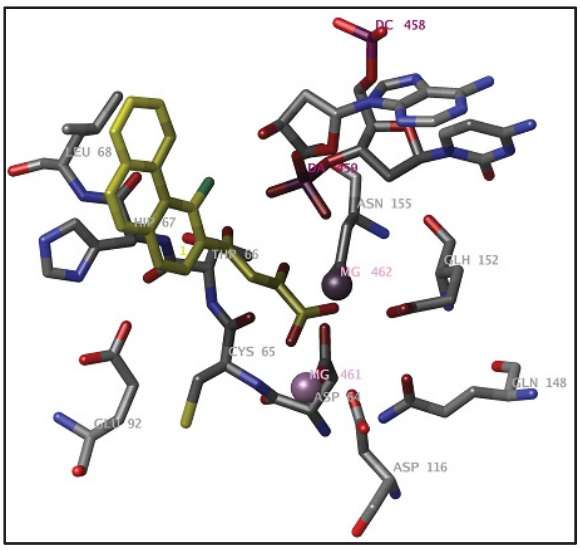

Figure 6-52. Binding interactions of compound 174 in the IN active site

Mg^{2+} ions are represented by purple spheres. Active site residues are represented by tubes and colored by element. Compound **174** is represented in tubes and highlighted with yellow carbons. Other atoms in the ligand are colored as follows: O, red; F, bright green.

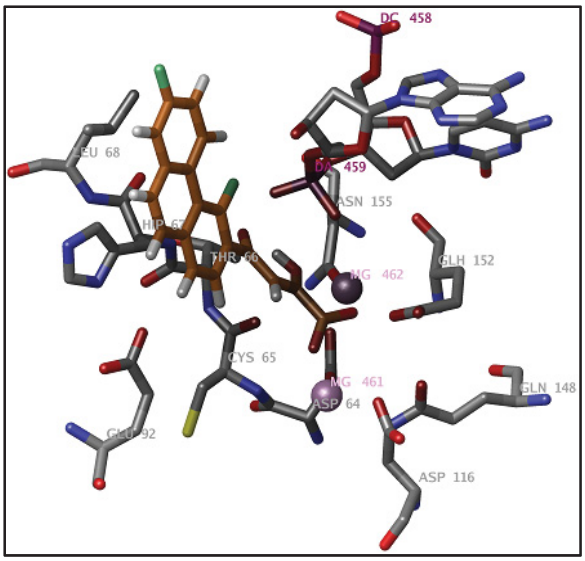

Figure 6-53. Binding interactions of compound 175 in the IN active site

Mg^{2+} ions are represented by purple spheres. Active site residues are represented by tubes and colored by element. Compound 175 is represented in tubes and highlighted with yellow carbons. Other atoms in the ligand are colored as follows: O, red; F, bright green.

result from favorable hydrophobic contact that the R_5 position fluoro makes with the alkyl side chains of Leu68.

Experimental

Docking Simulations

For prediction of bioactive conformation and binding modes of the synthesized chalcone and amide compounds; as well as for the QSAR study and the *in-silico* screening, we conducted docking simulations using the GLIDE (v5.7) program from Schrödinger Inc. (Portland, Oregon, USA). The protein and preparation wizard of Maestro (v9.2) interface in the Schrödinger modeling package was used to prepare the protein, applying the OPLS-2005 force-field. Compounds were constructed using the 3D-sketcher module in Maestro. The carboxylic acid moiety was constructed as a carboxylate for docking. The inhibitors were energy minimized using the MacroModel (v9.9) molecular mechanics program, and prepared for docking using the LigPrep (v2.5) facility in Maestro. Twenty docking poses were obtained for each molecule, the docking being terminated if two consecutive solutions were within a rmsd of 5 Å.

MM-GBSA Analysis

Computational methods to predict the binding free energy of a ligand to its receptor target include rigorous techniques like free energy perturbation (FEP)[222] and thermodynamic integration (TI)[223] methods. These methods are more accurate in predicting binding affinities in certain protein-ligand systems than the use of common scoring functions, but are computationally intensive and highly time consuming. At the next level of approximation, is a semiempirical linear interaction energy (LIE) method. Emperical scoring functions used by various docking programs are designed to include various approximations in order to determine the binding pose and estimate the binding affinities of a large number of molecules in short periods of time. Docking procedures treat proteins as rigid, do not consider protein and ligand desolvation, and ignore the entropic terms in energy calculations. Although docking algorithms have been highly successful in reproducing correct binding poses, the approximate scoring functions often fail to rank order compounds on the basis of their binding affinities. Recent advances in drug discovery have used a combination of molecular mechanics and continuum salvation methods to determine and predict the relative binding free energies with better accuracy; these include Molecular Mechanics/Poisson-Boltzmann Surface Area (MM-PBSA)[224] and Molecular Mechanics/Poisson-Generalized Born Surface Area (MM-GBSA). The MM-GBSA method evaluates binding free energies by minimization and MD of the protein-ligand complexes. **Equation 6-1**, **Equation 6-2**, and **Equation 6-3** calculates free energy of binding (ΔG_{bind}) between a ligand and its receptor as;

$$\Delta G_{bind} = \Delta H - T\Delta S = \Delta E_{MM} + \Delta G_{sol} - T\Delta S \qquad \textbf{(Eq. 6-1)}$$

$$\Delta E_{MM} = \Delta E_{internal} + \Delta E_{electrostatic} + \Delta E_{vdW} \quad \textbf{(Eq. 6-2)}$$

$$\Delta G_{sol} = \Delta G_{PB/GB} + \Delta G_{SA} \quad \textbf{(Eq. 6-3)}$$

where ΔE_{MM} is the difference between the molecular mechanics energies of protein-ligand complex and the sum of the molecular mechanics energies of the free ligand and the unliganded protein. ΔG_{sol} is the corresponding difference in the solvation energies and $-T\Delta S$ is the corresponding differences in conformational entropy upon binding. $\Delta E_{internal,}$ $\Delta E_{electrostatic}$ and ΔE_{vdw} are internal (bond length, angle, torsion), electrostatic and van der Waals (vdW) energies, respectively. $\Delta G_{PB/GB}$ and ΔG_{SA} are the electrostatic (polar) and non electrostatic (nonpolar) solvation energies, respectively.

The docking-derived conformations of 98 compounds, which have common binding modes and were used to build 3D-QSAR model 3, were first subjected to energy minimization by the local optimization module in the Prime package (v3.0 from Schrödinger Inc.) and binding free energies were calculated using the OPLS-2005 force field and the GBSA continuum model. All residues were kept frozen in the Prime calculations. The entropy penalty upon ligand binding was ignored in estimating the binding free energies which is calculated in prime-MM-GBSA using **Equation 6-4**;

$$\Delta G_{bind} = \Delta E_{MM} + \Delta G_{GB} + \Delta G_{SA} \quad \textbf{(Eq. 6-4)}$$

3D-QSAR Studies

3D-QSAR methods like comparative molecular field analysis (CoMFA)[225] and comparative molecular similarity analysis (CoMSIA)[226] are widely used to guide the synthesis of novel compounds by identifying the physiochemical properties that are important for activity, as well as an activity prediction tool. 3D structure building and CoMFA and CoMSIA studies were performed using the SYBYL program (version X1.1) on a Dell computer workstation with the Red Hat Linux operating system. All the molecules were assigned MOPAC partial atomic charges. The CoMFA descriptors, steric (Lennard-Jones 6-12 potential) and electrostatic (Coulombic potential) field energies, were calculated using Tripos force field with a distance-dependent dielectric constant, using the SYBYL default parameters: 2 Å grid points spacing, an sp^3 carbon probe atom with +1 charge, vdW radius of 1.52 Å, and energy cut-off of 30 kcal/mol. The five similarity indices in CoMSIA, namely, steric, electrostatic, hydrophobic, H-bond donor and H-bond acceptor descriptors, were calculated using a C^{1+} probe atom with a radius of 1.0 Å placed at regular grid spacing of 2 Å. A Gaussian-type distance dependence was used between grid point *q* and each atom *i* of the molecule. The default value of 0.3 was used as the attenuation factor (R). Column filtering was set to 2.0 kcal/mol. CoMSIA steric indices are related to the third power of the atomic radii, electrostatic descriptors are derived from atomic partial charges, hydrophobic fields are derived from atom-based parameters, and H-bond donor and acceptor indices are based on experimental results (SYBYL program).

Partial Least Squares Analysis

Partial least square (PLS) regression analysis is widely used to correlate important structural features with biological activity, and derives a mathematical relationship between dependent and independent variables, particularly when the number of descriptors outnumber the number of compounds.[227] For the present study, CoMFA and CoMSIA descriptors were used as independent variables and ST pIC_{50} (biological activity) values were used as dependent variable. The predictive value of the models was evaluated by leave-one-out (LOO) cross-validation. The cross-validated coefficient, q^2, was calculated using **Equation 6-5**

$$q^2 = 1 - \frac{\sum (Y_{predicted} - Y_{actual})^2}{\sum (Y_{actual} - Y_{mean})^2} \qquad \textbf{(Eq. 6-5)}$$

where $Y_{predicted}$, Y_{actual}, and Y_{mean} are predicted, actual and mean values of the target property (pIC_{50}), respectively. $\sum(Y_{predicted} - Y_{actual})^2$ is the predictive sum of squares (PRESS). Conventional correlation coefficient r^2 and its standard error, s, were also computed for the final PLS models. CoMFA and CoMSIA coefficient maps were generated by interpolation of the pair wise products between the PLS coefficients and the standard deviations of the corresponding CoMFA or CoMSIA descriptor values. External validation of the developed models was performed by determining the predictive r^2 of the test set compounds using **Equation 6-6**

$$r^2 = (SD - PRESS) / SD \qquad \textbf{(Eq. 6-6)}$$

where SD is the sum of the squared deviations between the biological activity of the molecules in the test set and the mean biological activity of the training set.

Linear Interaction Approximation (LIA) Calculations

LIA parameters were also used to develop a QSAR model for the IN inhibitors in the dataset. The docked conformations of 98 compounds having similar binding modes were separately subjected to binding affinity calculations in the Liaison module (v 5.7) from Schrödinger Inc. For the LIA calculations active-site residues surrounding the ligand were considered flexible. The LIA method uses a Surface Generalized Born (SGB) continuum solvation model to determine the binding free energy as a linear function of hydrophobic, electrostatic and cavity energy terms, which are calculated using the molecular mechanics force field, using **Equation 6-7**

$$\Delta G = \alpha \left(\langle U^{b}_{vdW} \rangle - \langle U^{f}_{vdW} \rangle \right) + \beta \left(\langle U^{b}_{elec} \rangle - \langle U^{f}_{elec} \rangle \right) + \gamma \left(\langle U^{b}_{cav} \rangle - \langle U^{f}_{cav} \rangle \right) \qquad \textbf{(Eq. 6-7)}$$

where $\langle\ \rangle$ represents the ensemble average; ^{b} means the ligand in the bound form while ^{f} means the ligand in the free form. α, β, and γ are the coefficients. The vdW, electrostatic and cavity energy terms are represented by $U_{vdW,}$ $U_{ele,}$ and $U_{cav.}$ Energy minimization

sampling using a conjugated gradient technique was used for minimization, with an rmsd of 0.01 for convergence and a maximum of 1000 steps.

CHAPTER 7. CONCLUSIONS

In summary, I have synthesized and evaluated the HIV-1 integrase inhibitory activities of a series of chalcones and related amides harboring a 3-keto salicylic acid moiety as a β-diketo acid bioisostere. Consistent with the DKA class of IN inhibitors, these series of compounds were also generally selective against the IN strand transfer step. Most of the potent compounds of the series also inhibited HIV replication in cell culture with moderate antiviral activities, which supports further development of the series. Following are the three modifications, I believe could be attempted to improve the activities to submicro and nanomolar levels.

(1) The 3-keto salicylic acid ring may be modified in that the 3-keto group could be incorporated into a ring system (**Figure 7-1**) to design bicyclic compounds. As discussed in the introduction chapter, one of the key features in the development of potent IN inhibitors is the requirement of coplanar chelating moieties. The 3-keto oxygen had an angle relative to the core salicylic acid ring. Incorporating it into a ring system may make the chelating moieties more coplanar and result in a conformation that may chelate more effectively with the two Mg^{2+} in the IN active site.

(2) All advanced IN inhibitors have a heterocyclic structural core. Future efforts could be directed at incorporating a heteroatom, preferentially nitrogen into the ring system (**Figure 7-2**).

(3) Position R_1 (see **Figure 7-1**) could be thoroughly investigated. This is the site where the gem-dimethyl oxadiazole carboxamide group of raltegravir and the isopropyl hydroxyl substituent in elvitegravir reside. Structure-based design could be used to improve the HIV-1 integrase inhibitory activity of this series of compounds. Targeting Tyr143 and Pro145 by putting other groups at the R_1 position may improve IN inhibitory activity. A series of compounds, with amines replacing the bromine at the R_1 position, have been designed and docked in the IN active site. Docking results (**Figure 7-3**) revealed that the amino substituents are positioned into a new region making contacts with Arg263 and Lys264. These amino acids appear to interact with viral DNA and could be targeted to explore their effect on IN inhibition.

I have also synthesized electronegative groups containing phenanthrene β-diketo acids as HIV-1 integrase inhibitors. Docking studies suggest that the compounds have different binding modes than raltegravir and, do not significantly interact with residues involved in viral resistance (Asn 155, Gln 148). Thus, this series of compounds could be investigated to circumvent viral resistance associated with current clinically used integrase inhibitors. However, efforts are needed to prevent their cellular toxicities and to improve their anti-viral activities. The phenanthrene could be modified to a structurally related stilbenes that may prevent their intercalation with DNA and thus, may reduce their toxicities. Docking studies have also revealed that the cavity occupied by the halobenzyl group in raltegravir and elvitegravir is vacant (see **Figure 6-46**). Further optimization could be attempted to append a halo benzyl moiety that could occupy the

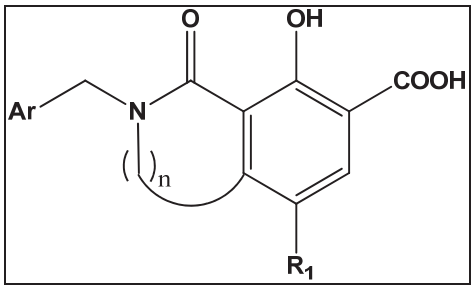

Figure 7-1. Optimization of 3-keto salicylic acid to a related bicyclic compound

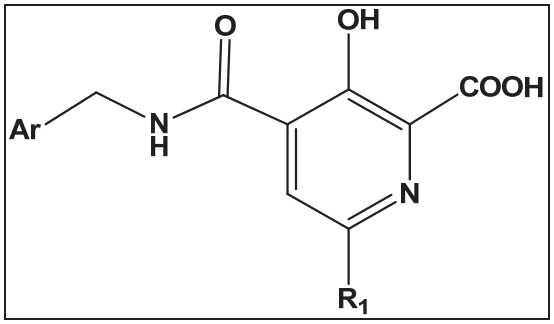

Figure 7-2. Optimization of 3-keto salicylic acid to a 4-carboxamide-3-hydroxy picolinic acid

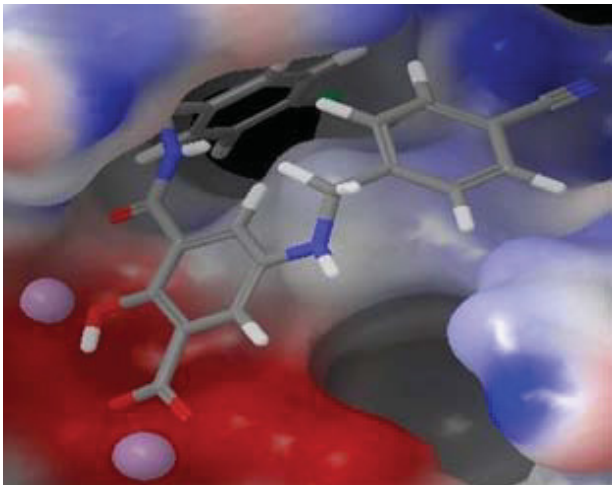

Figure 7-3. Design of new 3-carboxamide salicylic acid IN inhibitors

vacant cavity.

In computational studies, I have explored the binding modes of potent HIV IN inhibitors by docking and 3D-QSAR studies using a homology model of HIV IN-DNA complex. The binding mode of raltegravir and elvitegravir are in accordance with the foamy virus structure revealing interactions important for inhibitor-IN binding. The *para*-fluorobenzyl group in raltegravir and the halogen-substituted benzyl ring of elvitegravir insert into the cavity formed by displacement of the 3′-end of the viral DNA and engage in strong electrostatic and vdW interactions with the DNA-IN interface. The metal-chelating pharmacophore of raltegravir and elvitegravir interacted with the two metal ions (Mg^{2+}) in the IN active site. The models showed the binding contributions of the *gem*-dimethyloxadiazole carboxamide moiety in raltegravir and the *N*-alkyl hydroxyl side chain in elvitegravir and identified Tyr143 as key residues interacting with IN inhibitors.

To improve our knowledge of the stereoelectronic, hydrophobicity and hydrogen bonding requirements for IN inhibition, extensive 3D-QSAR studies were conducted using both the PHASE derived ligand-based and the homology model-guided structure-based molecular alignments. Homology model guided composite 3D-QSAR study, performed by combining four different classes of IN inhibitors, yielded significantly improved statistical results than the ligand-based 3D-QSAR study; which was conducted on synthesized chalcone and amide derivatives. Thus, integration of different scaffolds proved advantageous in arriving at a single 3D-QSAR model capable of accommodating diverse IN inhibitors without any bias for a particular functionality. The QSAR model developed using the docking-based and MM-GBSA validated alignments performed the best. Both CoMFA and CoMSIA of the docking-based model showed good predictive ability when evaluated on prospectively synthesized compounds. The CoMFA of docking-based model 3 has performed the best, and could be further developed by incorporating more of the synthesized amide derivatives in the training set and then predicting novel related IN inhibitors.

LIST OF REFERENCES

1. Curran, J. W. AIDS--two years later. *N. Engl. J. Med.* **1983**, 309, 609-611.

2. AIDS (Acquired Immuno-Deficiency Syndrome). http://cyberschoolbus.un.org/special/health/disease/aidshiv.htm United Nations Publications; Accessed October 20, **2011**.

3. Kaposi's sarcoma and pneumocystis pneumonia among heterosexual men- New York City and California. *Morb. Mortal. Wkly. Rep.* **1981**, 30, 305-308.

4. Pneumocystis pneumonia- Los Angeles. *Morb. Mort. Wkly. Rep.* **1981**, 30, 250-252.

5. Gallo, R. C. Historical essay. The early years of HIV/AIDS. *Science* **2002**, 298, 1728-1730.

6. Montagnier, L. Historical essay. A history of HIV discovery. *Science* **2002**, 298, 1727-1728.

7. Barre-Sinoussi, F.; Chermann, J. C.; Rey, F.; Nugeyre, M. T.; Chamaret, S.; Gruest, J.; Dauguet, C.; Axler-Blin, C.; Vezinet-Brun, F.; Rouzioux, C.; Rozenbaum, W.; Montagnier, L. Isolation of a T-lymphotropic retrovirus from a patient at risk for acquired immune deficiency syndrome (AIDS). *Science* **1983**, 220, 868-871.

8. Gallo, R. C.; Sarin, P. S.; Gelmann, E. P.; Robert-Guroff, M.; Richardson, E.; Kalyanaraman, V. S.; Mann, D.; Sidhu, G. D.; Stahl, R. E.; Zolla-Pazner, S.; Leibowitch, J.; Popovic, M. Isolation of human T-cell leukemia virus in acquired immune deficiency syndrome (AIDS). *Science* **1983**, 220, 865-867.

9. Stanecki. K. A. The AIDS pandemic in the 21st century. XIV International Conference on AIDS, Barcelona **2002**, 1-19.

10. Fauci, A. S. The AIDS epidemic-considerations for the 21st century. *N. Engl. J. Med.* **1999**, 341, 1046-1050.

11. Nabel, G. J. Challenges and opportunities for development of an AIDS vaccine. *Nature* **2001**, 410, 1002-1007.

12. Fauci, A. S. HIV and AIDS: 20 years of science. *Nat. Med.* **2003**, 9, 839-843.

13. Fauci, A. S. The human immunodeficiency virus: infectivity and mechanisms of pathogenesis. *Science* **1988**, 239, 617-622.

14. Fauci, A. S. Host factors and the pathogenesis of HIV-induced disease. *Nature* **1996**, 384, 529-534.

15. Greene, W. C.; Peterlin, B. M. Charting HIV's remarkable voyage through the cell: basic science as a passport to future therapy. *Nat. Med.* **2002**, 8, 673-680.

16. Rowland-Jones, S. L. Timeline: AIDS pathogenesis: what have two decades of HIV research taught us? *Nat. Rev. Immunol.* **2003**, 3, 343-348.

17. Pomerantz, R. J.; Horn, D. L. Twenty years of therapy for HIV-1 infection. *Nat. Med.* **2003**, 9, 867-873.

18. McLeod, G. X.; Hammer, S. M. Zidovudine: five years later. *Ann. Intern. Med.* **1992**, 117, 487-501.

19. Mitsuya, H.; Weinhold, K. J.; Furman, P. A.; St Clair, M. H.; Lehrman, S. N.; Gallo, R. C.; Bolognesi, D.; Barry, D. W.; Broder, S. 3'-Azido-3'-deoxythymidine (BW A509U): an antiviral agent that inhibits the infectivity and cytopathic effect of human T-lymphotropic virus type III/lymphadenopathy-associated virus in vitro. *Proc. Natl. Acad. Sci. U S A* **1985**, 82, 7096-7100.

20. Ezzell, C. AIDS drug gets green light. *Nature* **1987**, 329, 751.

21. Mehellou, Y.; De Clercq, E. Twenty-six years of anti-HIV drug discovery: where do we stand and where do we go? *J. Med. Chem.* **2010,** 53, 521-538.

22. Carr, A.; Miller, J.; Law, M.; Cooper, D. A. A syndrome of lipoatrophy, lactic acidaemia and liver dysfunction associated with HIV nucleoside analogue therapy: contribution to protease inhibitor-related lipodystrophy syndrome. *AIDS* **2000**, 14, F25-32.

23. Carr, A.; Samaras, K.; Thorisdottir, A.; Kaufmann, G. R.; Chisholm, D. J.; Cooper, D. A. Diagnosis, prediction, and natural course of HIV-1 protease-inhibitor-associated lipodystrophy, hyperlipidaemia, and diabetes mellitus: a cohort study. *Lancet* **1999,** 353, 2093-2099.

24. Safrin, S.; Grunfeld, C. Fat distribution and metabolic changes in patients with HIV infection. *AIDS* **1999,** 13, 2493-2505.

25. Carr, A.; Samaras, K.; Burton, S.; Law, M.; Freund, J.; Chisholm, D. J.; Cooper, D. A. A syndrome of peripheral lipodystrophy, hyperlipidaemia and insulin resistance in patients receiving HIV protease inhibitors. *AIDS* **1998,** 12, F51-58.

26. Carr, A. Toxicity of antiretroviral therapy and implications for drug development. *Nat. Rev. Drug Discov.* **2003**, 2, 624-634.

27. Calmy, A.; Hirschel, B.; Cooper, D. A.; Carr, A. A new era of antiretroviral drug toxicity. *Antivir. Ther.* **2009**, 14, 165-179.

28. Bangsberg, D. R.; Acosta, E. P.; Gupta, R.; Guzman, D.; Riley, E. D.; Harrigan, P. R.; Parkin, N.; Deeks, S. G. Adherence-resistance relationships for protease and non-nucleoside reverse transcriptase inhibitors explained by virological fitness. *AIDS* **2006**, 20, 223-231.

29. Bangsberg, D. R.; Perry, S.; Charlebois, E. D.; Clark, R. A.; Roberston, M.; Zolopa, A. R.; Moss, A. Non-adherence to highly active antiretroviral therapy predicts progression to AIDS. *AIDS* **2001**, 15, 1181-1183.

30 Bangsberg, D. R.; Hecht, F. M.; Charlebois, E. D.; Zolopa, A. R.; Holodniy, M.; Sheiner, L.; Bamberger, J. D.; Chesney, M. A.; Moss, A. Adherence to protease inhibitors, HIV-1 viral load, and development of drug resistance in an indigent population. *AIDS* **2000**, 14, 357-366.

31. Moyle, G.; Gatell, J.; Perno, C. F.; Ratanasuwan, W.; Schechter, M.; Tsoukas, C. Potential for new antiretrovirals to address unmet needs in the management of HIV-1 infection. *AIDS Patient Care STDS* **2008**, 22, 459-471.

32. Martinez-Picado, J.; DePasquale, M. P.; Kartsonis, N.; Hanna, G. J.; Wong, J.; Finzi, D.; Rosenberg, E.; Gunthard, H. F.; Sutton, L.; Savara, A.; Petropoulos, C. J.; Hellmann, N.; Walker, B. D.; Richman, D. D.; Siliciano, R.; D'Aquila, R. T. Antiretroviral resistance during successful therapy of HIV type 1 infection. *Proc. Natl. Acad. Sci. U S A* **2000**, 97, 10948-10953.

33. Little, S. J.; Holte, S.; Routy, J. P.; Daar, E. S.; Markowitz, M.; Collier, A. C.; Koup, R. A.; Mellors, J. W.; Connick, E.; Conway, B.; Kilby, M.; Wang, L.; Whitcomb, J. M.; Hellmann, N. S.; Richman, D. D. Antiretroviral-drug resistance among patients recently infected with HIV. *N. Engl. J. Med.* **2002**, 347, 385-394.

34. Johnson, V. A.; Brun-Vezinet, F.; Clotet, B.; Gunthard, H. F.; Kuritzkes, D. R.; Pillay, D.; Schapiro, J. M.; Richman, D. D. Update of the drug resistance mutations in HIV-1: December 2010. *Top HIV Med.* **2010**, 18, 156-163.

35. Clavel, F.; Hance, A. J. HIV drug resistance. *N. Engl. J. Med.* **2004**, 350, 1023-1035.

36. Emini, E. A.; Graham, D. J.; Gotlib, L.; Condra, J. H.; Byrnes, V. W.; Schleif, W. A. HIV and multidrug resistance. *Nature* **1993**, 364, 679.

37. Nowotny, M. Retroviral integrase superfamily: the structural perspective. *E.M.B.O. Rep*. **2009**, 10, 144-151.

38. Rambaut, A.; Posada, D.; Crandall, K. A.; Holmes, E. C. The causes and consequences of HIV evolution. *Nat. Rev. Genet.* **2004**, 5, 52-61.

39. Frankel, A. D.; Young, J. A. HIV-1: fifteen proteins and an RNA. *Annu. Rev. Biochem*. **1998**, 67, 1-25.

40. Jochmans, D. Novel HIV-1 reverse transcriptase inhibitors. *Virus Res.* **2008**, 134, 171-185.

41. Hao, Z.; Cooney, D. A.; Farquhar, D.; Perno, C. F.; Zhang, K.; Masood, R.; Wilson, Y.; Hartman, N. R.; Balzarini, J.; Johns, D. G. Potent DNA chain termination activity and selective inhibition of human immunodeficiency virus reverse transcriptase by 2',3'-dideoxyuridine-5'-triphosphate. *Mol. Pharmacol.* **1990**, 37, 157-163.

42. Fung, H. B.; Stone, E. A.; Piacenti, F. J. Tenofovir disoproxil fumarate: a nucleotide reverse transcriptase inhibitor for the treatment of HIV infection. *Clin. Ther.* **2002**, 24, 1515-1548.

43. de Bethune, M. P. Non-nucleoside reverse transcriptase inhibitors (NNRTIs), their discovery, development, and use in the treatment of HIV-1 infection: a review of the last 20 years (1989-2009). *Antiviral Res.* **2010**, 85, 75-90.

44. Prajapati, D. G.; Ramajayam, R.; Yadav, M. R.; Giridhar, R. The search for potent, small molecule NNRTIs: A review. *Bioorg. Med. Chem.* **2009**, 17, 5744-5762.

45. Hughes, P. J.; Cretton-Scott, E.; Teague, A.; Wensel, T. M. Protease inhibitors for patients with HIV-1 infection: a comparative overview. *P.& T.* **2011**, 36, 332-345.

46. Naggie, S.; Hicks, C. Protease inhibitor-based antiretroviral therapy in treatment-naive HIV-1-infected patients: the evidence behind the options. *J. Antimicrob. Chemother.* **2010**, 65, 1094-1099.

47. Kuritzkes, D. R. HIV-1 entry inhibitors: an overview. *Curr. Opin. HIV AIDS* **2009,** 4, 82-87.

48. Tilton, J. C.; Doms, R. W. Entry inhibitors in the treatment of HIV-1 infection. *Antiviral Res.* **2010,** 85, 91-100.

49. Hazuda, D. J.; Felock, P.; Witmer, M.; Wolfe, A.; Stillmock, K.; Grobler, J. A.; Espeseth, A.; Gabryelski, L.; Schleif, W.; Blau, C.; Miller, M. D. Inhibitors of strand transfer that prevent integration and inhibit HIV-1 replication in cells. *Science* **2000,** 287, 646-650.

50. Marchand, C.; Zhang, X.; Pais, G. C.; Cowansage, K.; Neamati, N.; Burke, T. R., Jr.; Pommier, Y. Structural determinants for HIV-1 integrase inhibition by beta-diketo acids. *J. Biol. Chem.* **2002,** 277, 12596-12603.

51. U.S. Food and Drug Administration. http://www.accessdata.fda.gov/scripts/cder/drugsatfda/index.cfm?fuseaction=Search.Label_ApprovalHistory#apphist; Accessed October 26, **2011**.

52. Palella, F. J. Jr.; Delaney, K. M.; Moorman, A. C.; Loveless, M. O.; Fuhrer, J.; Satten, G. A.; Aschman, D. J.; Holmberg, S. D. N. Declining morbidity and mortality among patients with advanced human immunodeficiency virus infection. HIV outpatient study investigators. *Eng. J. Med*. **1998**, 338, 853-860.

53. De Clercq, E. Toward improved anti-HIV chemotherapy: therapeutic strategies for intervention with HIV infections. *J. Med. Chem.* **1995**, 38, 2491-2517.

54. Marcello, A. Latency: the hidden HIV-1 challenge. *Retrovirology* **2006,** 3, 7.

55. Geeraert, L.; Kraus, G.; Pomerantz, R. J. Hide-and-seek: the challenge of viral persistence in HIV-1 infection. *Annu. Rev. Med.* **2008,** 59, 487-501.

56. Jones, K. S.; Coleman, J.; Merkel, G. W.; Laue, T. M.; Skalka, A. M. Retroviral integrase functions as a multimer and can turn over catalytically. *J. Biol. Chem.* **1992,** 267, 16037-16040.

57. Ren, G.; Gao, K.; Bushman, F. D.; Yeager, M. Single-particle image reconstruction of a tetramer of HIV integrase bound to DNA. *J. Mol. Biol.* **2007,** 366, 286-294.

58. Kotova, S.; Li, M.; Dimitriadis, E. K.; Craigie, R. Nucleoprotein intermediates In HIV-1 DNA integration visualized by atomic force microscopy. *J. Mol. Biol.* **2010,** 399, 491-500.

59. Faure, A.; Calmels, C.; Desjobert, C.; Castroviejo, M.; Caumont-Sarcos, A.; Tarrago-Litvak, L.; Litvak, S.; Parissi, V. HIV-1 integrase crosslinked oligomers are active in vitro. *Nucleic Acids Res.* **2005,** 33, 977-986.

60. Cherepanov, P.; Maertens, G.; Proost, P.; Devreese, B.; Van Beeumen, J.; Engelborghs, Y.; De Clercq, E.; Debyser, Z. HIV-1 integrase forms stable tetramers and associates with LEDGF/p75 protein in human cells. *J. Biol. Chem.* **2003,** 278, 372-381.

61. Bujacz, G.; Alexandratos, J.; Qing, Z. L.; Clement-Mella, C.; Wlodawer, A. The catalytic domain of human immunodeficiency virus integrase: ordered active site in the F185H mutant. *FEBS Lett.* **1996,** 398, 175-178.

62. Cai, M.; Zheng, R.; Caffrey, M.; Craigie, R.; Clore, G. M.; Gronenborn, A. M. Solution structure of the N-terminal zinc binding domain of HIV-1 integrase. *Nat. Struct. Biol.* **1997**, 4, 567-577.

63. Dyda, F.; Hickman, A. B.; Jenkins, T. M.; Engelman, A.; Craigie, R.; Davies, D. R. Crystal structure of the catalytic domain of HIV-1 integrase: similarity to other polynucleotidyl transferases. *Science* **1994,** 266, 1981-1986.

64. Cai, M.; Huang, Y.; Caffrey, M.; Zheng, R.; Craigie, R.; Clore, G. M.; Gronenborn, A. M. Solution structure of the His12 --> Cys mutant of the N-terminal zinc binding domain of HIV-1 integrase complexed to cadmium. *Protein Sci.* **1998,** 7, 2669-2674.

65. Zheng, R.; Jenkins, T. M.; Craigie, R. Zinc folds the N-terminal domain of HIV-1 integrase, promotes multimerization, and enhances catalytic activity. *Proc. Natl. Acad. Sci. U S A* **1996**, 93, 13659-13664.

66. Maignan, S.; Guilloteau, J. P.; Zhou-Liu, Q.; Clement-Mella, C.; Mikol, V. Crystal structures of the catalytic domain of HIV-1 integrase free and complexed with its metal cofactor: high level of similarity of the active site with other viral integrases. *J. Mol. Biol.* **1998,** 282, 359-368.

67. Goldgur, Y.; Dyda, F.; Hickman, A. B.; Jenkins, T. M.; Craigie, R.; Davies, D. R. Three new structures of the core domain of HIV-1 integrase: an active site that binds magnesium. *Proc. Natl. Acad. Sci. U S A* **1998,** 95, 9150-9154.

68. Greenwald, J.; Le, V.; Butler, S. L.; Bushman, F. D.; Choe, S. The mobility of an HIV-1 integrase active site loop is correlated with catalytic activity. *Biochemistry* **1999,** 38, 8892-8898.

69. Goldgur, Y.; Craigie, R.; Cohen, G. H.; Fujiwara, T.; Yoshinaga, T.; Fujishita, T.; Sugimoto, H.; Endo, T.; Murai, H.; Davies, D. R. Structure of the HIV-1 integrase catalytic domain complexed with an inhibitor: a platform for antiviral drug design. *Proc. Natl. Acad. Sci. U S A* **1999,** 96, 13040-13043.

70. Chen, J. C.; Krucinski, J.; Miercke, L. J.; Finer-Moore, J. S.; Tang, A. H.; Leavitt, A. D.; Stroud, R. M. Crystal structure of the HIV-1 integrase catalytic core and C-terminal domains: a model for viral DNA binding. *Proc. Natl. Acad. Sci. U S A* **2000,** 97, 8233-8238.

71. Molteni, V.; Greenwald, J.; Rhodes, D.; Hwang, Y.; Kwiatkowski, W.; Bushman, F. D.; Siegel, J. S.; Choe, S. Identification of a small-molecule binding site at the dimer interface of the HIV integrase catalytic domain. *Acta Crystallogr. D. Biol. Crystallogr.* **2001,** 57, 536-544.

72. Lodi, P. J.; Ernst, J. A.; Kuszewski, J.; Hickman, A. B.; Engelman, A.; Craigie, R.; Clore, G. M.; Gronenborn, A. M. Solution structure of the DNA binding domain of HIV-1 integrase. *Biochemistry* **1995,** 34, 9826-9833.

73. Eijkelenboom, A. P.; Sprangers, R.; Hard, K.; Puras Lutzke, R. A.; Plasterk, R. H.; Boelens, R.; Kaptein, R. Refined solution structure of the C-terminal DNA-binding domain of human immunovirus-1 integrase. *Proteins* **1999,** 36, 556-564.

74. Wang, J. Y.; Ling, H.; Yang, W.; Craigie, R. Structure of a two-domain fragment of HIV-1 integrase: implications for domain organization in the intact protein. *E.M.B.O. J.* **2001,** 20, 7333-7343.

75. Chen, J. C.; Krucinski, J.; Miercke, L. J.; Finer-Moore, J. S.; Tang, A. H.; Leavitt, A. D.; Stroud, R. M. Crystal structure of the HIV-1 integrase catalytic core and C-terminal domains: a model for viral DNA binding. *Proc. Natl. Acad. Sci. U S A* **2000,** 97, 8233-8238.

76. Cherepanov, P.; Ambrosio, A. L.; Rahman, S.; Ellenberger, T.; Engelman, A. Structural basis for the recognition between HIV-1 integrase and transcriptional coactivator p75. *Proc. Natl. Acad. Sci. U S A* **2005,** 102, 17308-17313.

77. Christ, F.; Voet, A.; Marchand, A.; Nicolet, S.; Desimmie, B. A.; Marchand, D.; Bardiot, D.; Van der Veken, N. J.; Van Remoortel, B.; Strelkov, S. V.; De Maeyer, M.; Chaltin, P.; Debyser, Z. Rational design of small-molecule inhibitors of the LEDGF/p75-integrase interaction and HIV replication. *Nat. Chem. Biol.* **2010,** 6, 442-448.

78. Wielens, J.; Headey, S. J.; Jeevarajah, D.; Rhodes, D. I.; Deadman, J.; Chalmers, D. K.; Scanlon, M. J.; Parker, M. W. Crystal structure of the HIV-1 integrase core domain in complex with sucrose reveals details of an allosteric inhibitory binding site. *FEBS Lett.* **2010,** 584, 1455-1462.

79. Rhodes, D. I.; Peat, T. S.; Vandegraaff, N.; Jeevarajah, D.; Le, G.; Jones, E. D.; Smith, J. A.; Coates, J. A.; Winfield, L. J.; Thienthong, N.; Newman, J.; Lucent, D.; Ryan, J. H.; Savage, G. P.; Francis, C. L.; Deadman, J. J. Structural basis for a new mechanism of inhibition of HIV-1 integrase identified by fragment screening and structure-based design. *Antivir. Chem. Chemother.* **2011,** 21, 155-168.

80. Jaskolski, M.; Alexandratos, J. N.; Bujacz, G.; Wlodawer, A. Piecing together the structure of retroviral integrase, an important target in AIDS therapy. *FEBS J.* **2009,** 276, 2926-2946

81. Sotriffer, C. A.; Ni, H.; McCammon, J. A. HIV-1 integrase inhibitor interactions at the active site: prediction of binding modes unaffected by crystal packing. *J. Am. Chem. Soc.* **2000**, 122, 6136-6137.

82. Sotriffer, C. A.; Ni, H.; McCammon, J. A. Active site binding modes of HIV-1 integrase inhibitors. *J. Med. Chem.* **2000,** 43, 4109-4117.

83. Dolan, J.; Chen, A.; Weber, I. T.; Harrison, R. W.; Leis, J. Defining the DNA substrate binding sites on HIV-1 integrase. *J. Mol. Biol.* **2009,** 385, 568-579.

84. Johnson, A. A.; Marchand, C.; Patil, S. S.; Costi, R.; Di Santo, R.; Burke, T. R., Jr.; Pommier, Y. Probing HIV-1 integrase inhibitor binding sites with position-specific integrase-DNA cross-linking assays. *Mol. Pharmacol.* **2007,** 71, 893-901.

85. Agapkina, J.; Smolov, M.; Barbe, S.; Zubin, E.; Zatsepin, T.; Deprez, E.; Le Bret, M.; Mouscadet, J. F.; Gottikh, M. Probing of HIV-1 integrase/DNA interactions using novel analogs of viral DNA. *J. Biol. Chem.* **2006,** 281, 11530-11540.

86. Lu, R.; Limon, A.; Ghory, H. Z.; Engelman, A. Genetic analyses of DNA-binding mutants in the catalytic core domain of human immunodeficiency virus type 1 integrase. *J. Virol.* **2005,** 79, 2493-2505.

87. Adesokan, A. A.; Roberts, V. A.; Lee, K. W.; Lins, R. D.; Briggs, J. M. Prediction of HIV-1 integrase/viral DNA interactions in the catalytic domain by fast molecular docking. *J. Med. Chem.* **2004,** 47, 821-828.

88. Dirac, A. M.; Kjems, J. Mapping DNA-binding sites of HIV-1 integrase by protein footprinting. *Eur. J. Biochem.* **2001,** 268, 743-751.

89. Brin, E.; Leis, J. HIV-1 integrase interaction with U3 and U5 terminal sequences in vitro defined using substrates with random sequences. *J. Biol. Chem.* **2002,** 277, 18357-18364.

90. Faure, A.; Calmels, C.; Desjobert, C.; Castroviejo, M.; Caumont-Sarcos, A.; Tarrago-Litvak, L.; Litvak, S.; Parissi, V. HIV-1 integrase crosslinked oligomers are active in vitro. *Nucleic Acids Res.* **2005,** 33, 977-986.

91. Esposito, D.; Craigie, R. Sequence specificity of viral end DNA binding by HIV-1 integrase reveals critical regions for protein-DNA interaction. *E.M.B.O. J.* **1998,** 17, 5832-5843.

92. Hare, S.; Vos, A. M.; Clayton, R. F.; Thuring, J. W.; Cummings, M. D.; Cherepanov, P. Molecular mechanisms of retroviral integrase inhibition and the evolution of viral resistance. *Proc. Natl. Acad. Sci. U S A* **2010,** 107, 20057-20062.

93. Hare, S.; Gupta, S. S.; Valkov, E.; Engelman, A.; Cherepanov, P. Retroviral intasome assembly and inhibition of DNA strand transfer. *Nature* **2010,** 464, 232-236.

94. Maertens, G. N.; Hare, S.; Cherepanov, P. The mechanism of retroviral integration from X-ray structures of its key intermediates. *Nature* **2010,** 468, 326-329.

95. Krishnan, L.; Li, X.; Naraharisetty, H. L.; Hare, S.; Cherepanov, P.; Engelman, A. Structure-based modeling of the functional HIV-1 intasome and its inhibition. *Proc. Natl. Acad. Sci. U S A* **2010,** 107, 15910-15915.

96. Pommier, Y.; Johnson, A. A.; Marchand, C. Integrase inhibitors to treat HIV/AIDS. *Nat. Rev. Drug Discov.* **2005,** 4, 236-248.

97. Savarino, A. In-Silico docking of HIV-1 integrase inhibitors reveals a novel drug type acting on an enzyme/DNA reaction intermediate. *Retrovirology* **2007**, 4, 21.

98. Grobler, J. A.; Stillmock, K.; Hu, B.; Witmer, M.; Felock, P.; Espeseth, A. S.; Wolfe, A.; Egbertson, M.; Bourgeois, M.; Melamed, J.; Wai, J. S.; Young, S.; Vacca, J.; Hazuda, D. J. Diketo acid inhibitor mechanism and HIV-1 integrase: implications for metal binding in the active site of phosphotransferase enzymes. *Proc. Natl. Acad. Sci. U S A* **2002,** 99, 6661-6666.

99. Marchand, C.; Johnson, A. A.; Karki, R. G.; Pais, G. C.; Zhang, X.; Cowansage, K.; Patel, T. A.; Nicklaus, M. C.; Burke, T. R., Jr.; Pommier, Y. Metal-dependent inhibition of HIV-1 integrase by beta-diketo acids and resistance of the soluble double-mutant (F185K/C280S). *Mol. Pharmacol.* **2003,** 64, 600-609.

100. Cherepanov, P.; Maertens, G. N.; Hare, S. Structural insights into the retroviral DNA integration apparatus. *Curr. Opin. Struct. Biol.* **2011,** 21, 249-256.

101. Sioud, M.; Drlica, K. Prevention of human immunodeficiency virus type 1 integrase expression in escherichia coli by a ribozyme. *Proc. Natl. Acad. Sci. U S A* **1991,** 88, 7303-7307.

102. Raillard, S. A.; Joyce, G. F. Targeting sites within HIV-1 cDNA with a DNA-cleaving ribozyme. *Biochemistry* **1996,** 35, 11693-11701.

103. Bouziane, M.; Cherny, D. I.; Mouscadet, J. F.; Auclair, C. Alternate strand DNA triple helix-mediated inhibition of HIV-1 U5 long terminal repeat integration in vitro. *J. Biol. Chem.* **1996,** 271, 10359-10364.

104. Mazumder, A.; Cooney, D.; Agbaria, R.; Gupta, M.; Pommier, Y. Inhibition of human immunodeficiency virus type 1 integrase by 3'-azido-3'-deoxythymidylate. *Proc. Natl. Acad. Sci. U S A* **1994,** 91, 5771-5775.

105. Rando, R. F.; Ojwang, J.; Elbaggari, A.; Reyes, G. R.; Tinder, R.; McGrath, M. S.; Hogan, M. E. Suppression of human immunodeficiency virus type 1 activity in vitro by oligonucleotides which form intramolecular tetrads. *J .Biol. Chem.* **1995,** 270, 1754-1760.

106. Middleton, T.; Lim, H. B.; Montgomery, D.; Rockway, T.; Tang, H.; Cheng, X.; Lu, L.; Mo, H.; Kohlbrenner, W. E.; Molla, A.; Kati, W. M. Inhibition of human immunodeficiency virus type I integrase by naphthamidines and 2-aminobenzimidazoles. *Antiviral Res.* **2004,** 64, 35-45.

107. Neamati, N.; Mazumder, A.; Sunder, S.; Owen, J. M.; Tandon, M.; Lown, J. W.; Pommier, Y. Highly potent synthetic polyamides, bisdistamycins, and lexitropsins as inhibitors of human immunodeficiency virus type 1 integrase. *Mol. Pharmacol.* **1998,** 54, 280-290.

108. Du, L.; Zhao, Y. X.; Yang, L. M.; Zheng, Y. T.; Tang, Y.; Shen, X.; Jiang, H. L. Symmetrical 1-pyrrolidineacetamide showing anti-HIV activity through a new binding site on HIV-1 integrase. *Acta. Pharmacol. Sin.* **2008,** 29, 1261-1267.

109. Puras Lutzke, R. A.; Eppens, N. A.; Weber, P. A.; Houghten, R. A.; Plasterk, R. H. Identification of a hexapeptide inhibitor of the human immunodeficiency virus integrase protein by using a combinatorial chemical library. *Proc. Natl. Acad. Sci. U S A* **1995,** 92, 11456-11460.

110. Sourgen, F.; Maroun, R. G.; Frere, V.; Bouziane, M.; Auclair, C.; Troalen, F.; Fermandjian, S. A synthetic peptide from the human immunodeficiency virus type-1 integrase exhibits coiled-coil properties and interferes with the in vitro integration activity of the enzyme. Correlated biochemical and spectroscopic results. *Eur. J. Biochem.* **1996,** 240, 765-773.

111. Lee-Huang, S.; Huang, P. L.; Bourinbaiar, A. S.; Chen, H. C.; Kung, H. F. Inhibition of the integrase of human immunodeficiency virus (HIV) type 1 by anti-HIV plant proteins MAP30 and GAP31. *Proc. Natl. Acad. Sci. U S A* **1995,** 92, 8818-8822.

112. Fesen, M. R.; Pommier, Y.; Leteurtre, F.; Hiroguchi, S.; Yung, J.; Kohn, K. W. Inhibition of HIV-1 integrase by flavones, caffeic acid phenethyl ester (CAPE) and related compounds. *Biochem. Pharmacol.* **1994,** 48, 595-608.

113. Mazumder, A.; Gazit, A.; Levitzki, A.; Nicklaus, M.; Yung, J.; Kohlhagen, G.; Pommier, Y. Effects of tyrphostins, protein kinase inhibitors, on human immunodeficiency virus type 1 integrase. *Biochemistry* **1995,** 34, 15111-15122.

114. Zheng, . Eich, E.; Pertz, H.; Kaloga, M.; Schulz, J.; Fesen, M. R.; Mazumder, A.; Pommier, Y. (-)-Arctigenin as a lead structure for inhibitors of human immunodeficiency virus type-1 integrase. *J. Med. Chem.* **1996**, 39, 86-95.

115. Farnet, C. M.; Wang, B.; Lipford, J. R.; Bushman, F. D. Differential inhibition of HIV-1 preintegration complexes and purified integrase protein by small molecules. *Proc. Natl. Acad. Sci. U S A* **1996,** 93, 9742-9747.

116. Mazumder, A.; Raghavan, K.; Weinstein, J.; Kohn, K. W.; Pommier, Y. Inhibition of human immunodeficiency virus type-1 integrase by curcumin. *Biochem. Pharmacol.* **1995,** 49, 1165-1170.

117. Robinson, W. E., Jr.; Cordeiro, M.; Abdel-Malek, S.; Jia, Q.; Chow, S. A.; Reinecke, M. G.; Mitchell, W. M. Dicaffeoylquinic acid inhibitors of human immunodeficiency virus integrase: inhibition of the core catalytic domain of human immunodeficiency virus integrase. *Mol. Pharmacol.* **1996,** 50, 846-855.

118. Robinson, W. E., Jr.; Reinecke, M. G.; Abdel-Malek, S.; Jia, Q.; Chow, S. A. Inhibitors of HIV-1 replication [corrected; erratum to be published] that inhibit HIV integrase. *Proc. Natl. Acad. Sci. U S A* **1996,** 93, 6326-6331.

119. Fesen, M. R.; Kohn, K. W.; Leteurtre, F.; Pommier, Y. Inhibitors of humanimmunodeficiency virus integrase. *Proc. Natl. Acad. Sci. U S A* **1993**, 90, 2399-2403.

120. Mazumder, A.; Wang, S.; Neamati, N.; Nicklaus, M.; Sunder, S.; Chen, J.; Milne, G. W.; Rice, W. G.; Burke, T. R., Jr.; Pommier, Y. Antiretroviral agents as inhibitors of both human immunodeficiency virus type 1 integrase and protease. *J. Med. Chem.* **1996,** 39, 2472-2481.

121. Mekouar, K.; Mouscadet, J. F.; Desmaele, D.; Subra, F.; Leh, H.; Savoure, D.; Auclair, C.; d'Angelo, J. Styrylquinoline derivatives: a new class of potent HIV-1 integrase inhibitors that block HIV-1 replication in CEM cells. *J. Med. Chem.* **1998,** 41, 2846-2857.

122. Mousnier, A.; Leh, H.; Mouscadet, J. F.; Dargemont, C. Nuclear import of HIV-1 integrase is inhibited in vitro by styrylquinoline derivatives. *Mol. Pharmacol.* **2004**, 66, 783-788.

123. Pannecouque, C.; Pluymers, W.; Van Maele, B.; Tetz, V.; Cherepanov, P.; De Clercq, E.; Witvrouw, M.; Debyser, Z. New class of HIV integrase inhibitors that block viral replication in cell culture. *Curr. Biol.* **2002,** 12, 1169-1177.

124. Espeseth, A. S.; Felock, P.; Wolfe, A.; Witmer, M.; Grobler, J.; Anthony, N.; Egbertson, M.; Melamed, J. Y.; Young, S.; Hamill, T.; Cole, J. L.; Hazuda, D. J. HIV-1 integrase inhibitors that compete with the target DNA substrate define a unique strand transfer conformation for integrase. *Proc. Natl. Acad. Sci .U S A* **2000,** 97, 11244-11249.

125 Billich, A. S-1360 Shionogi-GlaxoSmithKline. *Curr. Opin. Investig. Drugs* **2003,** 4, 206-209.

126. Zhang, X.; Pais, G. C.; Svarovskaia, E. S.; Marchand, C.; Johnson, A. A.; Karki, R. G.; Nicklaus, M. C.; Pathak, V. K.; Pommier, Y.; Burke, T. R. Azido-containing aryl beta-diketo acid HIV-1 integrase inhibitors. *Bioorg. Med. Chem. Lett.* **2003,** 13, 1215-1219.

127. Hazuda, D. J.; Young, S. D.; Guare, J. P.; Anthony, N. J.; Gomez, R. P.; Wai, J. S.; Vacca, J. P.; Handt, L.; Motzel, S. L.; Klein, H. J.; Dornadula, G.; Danovich, R. M.; Witmer, M. V.; Wilson, K. A.; Tussey, L.; Schleif, W. A.; Gabryelski, L. S.; Jin, L.; Miller, M. D.; Casimiro, D. R.; Emini, E. A.; Shiver, J. W. Integrase inhibitors and cellular immunity suppress retroviral replication in rhesus macaques. *Science* **2004,** 305, 528-532.

128. McColl, D. J.; Chen, X. Strand transfer inhibitors of HIV-1 integrase: bringing IN a new era of antiretroviral therapy. *Antiviral Res.* **2010,** 85, 101-118.

129. Hazuda, D. J.; Anthony, N. J.; Gomez, R. P.; Jolly, S. M.; Wai, J. S.; Zhuang, L.; Fisher, T. E.; Embrey, M.; Guare, J. P., Jr.; Egbertson, M. S.; Vacca, J. P.; Huff, J. R.; Felock, P. J.; Witmer, M. V.; Stillmock, K. A.; Danovich, R.; Grobler, J.; Miller, M. D.; Espeseth, A. S.; Jin, L.; Chen, I. W.; Lin, J. H.; Kassahun, K.; Ellis, J. D.; Wong, B. K.; Xu, W.; Pearson, P. G.; Schleif, W. A.; Cortese, R.; Emini, E.; Summa, V.; Holloway, M. K.; Young, S. D. A naphthyridine carboxamide provides evidence for discordant resistance between mechanistically identical inhibitors of HIV-1 integrase. *Proc. Natl. Acad. Sci. U S A* **2004,** 101, 11233-11238.

130. Garvey, E. P.; Johns, B. A.; Gartland, M. J.; Foster, S. A.; Miller, W. H.; Ferris, R. G.; Hazen, R. J.; Underwood, M. R.; Boros, E. E.; Thompson, J. B.; Weatherhead, J. G.; Koble, C. S.; Allen, S. H.; Schaller, L. T.; Sherrill, R. G.; Yoshinaga, T.; Kobayashi, M.; Wakasa-Morimoto, C.; Miki, S.; Nakahara, K.; Noshi, T.; Sato, A.; Fujiwara, T. The naphthyridinone GSK364735 is a novel, potent human immunodeficiency virus type 1 integrase inhibitor and antiretroviral. *Antimicrob. Agents Chemother.* **2008,** 52, 901-908.

131. Wai, J. S.; Kim, B.; Fisher, T. E.; Zhuang, L.; Embrey, M. W.; Williams, P. D.; Staas, D. D.; Culberson, C.; Lyle, T. A.; Vacca, J. P.; Hazuda, D. J.; Felock, P. J.; Schleif, W. A.; Gabryelski, L. J.; Jin, L.; Chen, I. W.; Ellis, J. D.; Mallai, R.; Young, S. D. Dihydroxypyridopyrazine-1,6-dione HIV-1 integrase inhibitors. *Bioorg. Med. Chem. Lett.* **2007,** 17, 5595-5599.

132. Langford, H. M.; Williams, P. D.; Homnick, C. F.; Vacca, J. P.; Felock, P. J.; Stillmock, K. A.; Witmer, M. V.; Hazuda, D. J.; Gabryelski, L. J.; Schleif, W. A. Design and synthesis of substituted 4-oxo-4,5,6,7-tetrahydropyrazolo[1,5-a]pyrazine-2-carboxamides, novel HIV-1 integrase inhibitors. *Bioorg. Med. Chem. Lett.* **2008,** 18, 721-725.

133. Fisher, T. E.; Kim, B.; Staas, D. D.; Lyle, T. A.; Young, S. D.; Vacca, J. P.; Zrada, M. M.; Hazuda, D. J.; Felock, P. J.; Schleif, W. A.; Gabryelski, L. J.; Anari, M. R.; Kochansky, C. J.; Wai, J. S. 8-Hydroxy-3,4-dihydropyrrolo[1,2-a]pyrazine-1(2H)-one HIV-1 integrase inhibitors. *Bioorg. Med. Chem. Lett.* **2007,** 17, 6511-6515.

134. Summa, V.; Petrocchi, A.; Bonelli, F.; Crescenzi, B.; Donghi, M.; Ferrara, M.; Fiore, F.; Gardelli, C.; Gonzalez Paz, O.; Hazuda, D. J.; Jones, P.; Kinzel, O.; Laufer, R.; Monteagudo, E.; Muraglia, E.; Nizi, E.; Orvieto, F.; Pace, P.; Pescatore, G.; Scarpelli, R.; Stillmock, K.; Witmer, M. V.; Rowley, M. Discovery of raltegravir, a potent, selective orally bioavailable HIV-integrase inhibitor for the treatment of HIV-AIDS infection. *J. Med. Chem.* **2008,** 51, 5843-5855.

135. Gardelli, C.; Nizi, E.; Muraglia, E.; Crescenzi, B.; Ferrara, M.; Orvieto, F.; Pace, P.; Pescatore, G.; Poma, M.; Ferreira Mdel, R.; Scarpelli, R.; Homnick, C. F.; Ikemoto, N.; Alfieri, A.; Verdirame, M.; Bonelli, F.; Paz, O. G.; Taliani, M.; Monteagudo, E.; Pesci, S.; Laufer, R.; Felock, P.; Stillmock, K. A.; Hazuda, D.; Rowley, M.; Summa, V. Discovery and synthesis of HIV integrase inhibitors: development of potent and orally bioavailable N-methyl pyrimidones. *J. Med. Chem.* **2007,** 50, 4953-4975.

136. Markowitz, M.; Morales-Ramirez, J. O.; Nguyen, B. Y.; Kovacs, C. M.; Steigbigel, R. T.; Cooper, D. A.; Liporace, R.; Schwartz, R.; Isaacs, R.; Gilde, L. R.; Wenning, L.; Zhao, J.; Teppler, H. Antiretroviral activity, pharmacokinetics, and tolerability of MK-0518, a novel inhibitor of HIV-1 integrase, dosed as monotherapy for 10 days in treatment-naive HIV-1-infected individuals. *J. Acquir. Immune Defic. Syndr.* **2006,** 43, 509-515.

137. Markowitz, M.; Nguyen, B. Y.; Gotuzzo, E.; Mendo, F.; Ratanasuwan, W.; Kovacs, C.; Prada, G.; Morales-Ramirez, J. O.; Crumpacker, C. S.; Isaacs, R. D.; Gilde, L. R.; Wan, H.; Miller, M. D.; Wenning, L. A.; Teppler, H. Rapid and durable antiretroviral effect of the HIV-1 integrase inhibitor raltegravir as part of combination therapy in treatment-naive patients with HIV-1 infection: results of a 48-week controlled study. *J. Acquir. Immune Defic. Syndr.* **2007,** 46, 125-133.

138. Metifiot, M.; Marchand, C.; Maddali, K.; Pommier, Y. Resistance to integrase inhibitors. *Viruses* **2010,** 2, 1347-1366.

139. Goethals, O.; Van Ginderen, M.; Vos, A.; Cummings, M. D.; Van Der Borght, K.; Van Wesenbeeck, L.; Feyaerts, M.; Verheyen, A.; Smits, V.; Van Loock, M.; Hertogs, K.; Schols, D.; Clayton, R. F. Resistance to raltegravir highlights integrase mutations at codon 148 in conferring cross-resistance to a second-generation HIV-1 integrase inhibitor. *Antiviral Res.* **2011,** 91, 167-176.

140. Ramkumar, K.; Neamati, N. Raltegravir: The evidence of its therapeutic value in HIV-1 infection. *Core Evid.* **2009**, 4, 131-147.

141. Randomized, placebo-controlled, ascending multiple dose study to evaluate the safety, pharmacokinetics, and pharmacodynamics of BMS-707035 in HIV-1 infected subjects; Trial identifier: NCT00397566. http://clinicaltrials.gov/ct2/show/NCT00397566 U.S. National Institutes of Health; Accessed October 28, **2011**.

142. Muraglia, E.; Kinzel, O.; Gardelli, C.; Crescenzi, B.; Donghi, M.; Ferrara, M.; Nizi, E.; Orvieto, F.; Pescatore, G.; Laufer, R.; Gonzalez-Paz, O.; Di Marco, A.; Fiore, F.; Monteagudo, E.; Fonsi, M.; Felock, P. J.; Rowley, M.; Summa, V. Design and synthesis of bicyclic pyrimidinones as potent and orally bioavailable HIV-1 integrase inhibitors. *J. Med. Chem.* **2008,** 51, 861-874.

143. Sato, M.; Motomura, T.; Aramaki, H.; Matsuda, T.; Yamashita, M.; Ito, Y.; Kawakami, H.; Matsuzaki, Y.; Watanabe, W.; Yamataka, K.; Ikeda, S.; Kodama, E.; Matsuoka, M.; Shinkai, H. Novel HIV-1 integrase inhibitors derived from quinolone antibiotics. *J. Med. Chem.* **2006,** 49, 1506-1508.

144. DeJesus, E.; Berger, D.; Markowitz, M.; Cohen, C.; Hawkins, T.; Ruane, P.; Elion, R.; Farthing, C.; Zhong, L.; Cheng, A. K.; McColl, D.; Kearney, B. P. Antiviral activity, pharmacokinetics, and dose response of the HIV-1 integrase inhibitor GS-9137 (JTK-303) in treatment-naive and treatment-experienced patients. *J. Acquir. Immune Defic. Syndr.* **2006,** 43, 1-5.

145. Marinello, J.; Marchand, C.; Mott, B. T.; Bain, A.; Thomas, C. J.; Pommier, Y. Comparison of raltegravir and elvitegravir on HIV-1 integrase catalytic reactions and on a series of drug-resistant integrase mutants. *Biochemistry* **2008,** 47, 9345-9354.

146. Shimura, K.; Kodama, E.; Sakagami, Y.; Matsuzaki, Y.; Watanabe, W.; Yamataka, K.; Watanabe, Y.; Ohata, Y.; Doi, S.; Sato, M.; Kano, M.; Ikeda, S.; Matsuoka, M. Broad antiretroviral activity and resistance profile of the novel human immunodeficiency virus integrase inhibitor elvitegravir (JTK-303/GS-9137). *J. Virol.* **2008,** 82, 764-774.

147. Bar-Magen, T.; Sloan, R. D.; Donahue, D. A.; Kuhl, B. D.; Zabeida, A.; Xu, H.; Oliveira, M.; Hazuda, D. J.; Wainberg, M. A. Identification of novel mutations responsible for resistance to MK-2048, a second-generation HIV-1 integrase inhibitor. *J. Virol.* **2010,** 84, 9210-9216.

148. Antiviral activity of S/GSK1349572, the only once-daily, unboosted integrase inhibitor in clinical development, evaluated in phase 2 study. http://www.gsk.com/media/pressreleases/2009/2009_pressrelease_10080.htm Glaxo Smith Kline; Accessed October 28, **2011**.

149. Jones, G. S.; Yu, F.; Zeynalzadegan, A.; Hesselgesser, J.; Chen, X.; Chen, J.; Jin, H.; Kim, C. U.; Wright, M.; Geleziunas, R.; Tsiang, M. Preclinical evaluation of GS-9160, a novel inhibitor of human immunodeficiency virus type 1 integrase. *Antimicrob. Agents Chemother.* **2009,** 53, 1194-1203.

150. Kawasuji, T.; Fuji, M.; Yoshinaga, T.; Sato, A.; Fujiwara, T.; Kiyama, R. 3-Hydroxy-1,5-dihydro-pyrrol-2-one derivatives as advanced inhibitors of HIV integrase. *Bioorg. Med. Chem.* **2007,** 15, 5487-5492.

151. Lee, S.U.; Park, J.H.; Kwon, T. H.; Yoo, Y. J.; Lee, Y. J.; Shin, C. G.; Yoo, K. H.; Lee, Y. S. Synthesis and HIV-1 integrase inhibitory activities of 4-hydroxy-5-azacoumarin 3-carboxamides. *Bull. Korean Chem. Soc.* **2007**, 28, 1510-1514.

152. Patil, S.; Kamath, S.; Sanchez, T.; Neamati, N.; Schinazi, R. F.; Buolamwini, J. K. Synthesis and biological evaluation of novel 5(H)-phenanthridin-6-ones, 5(H)-phenanthridin-6-one diketo acid, and polycyclic aromatic diketo acid analogs as new HIV-1 integrase inhibitors. *Bioorg. Med. Chem.* **2007,** 15, 1212-1228.

153. Zhao, H.; Neamati, N.; Sunder, S.; Hong, H.; Wang, S.; Milne, G. W.; Pommier, Y.; Burke, T. R., Jr. Hydrazide-containing inhibitors of HIV-1 integrase. *J. Med. Chem.* **1997,** 40, 937-941.

154. Sriram, D.; Yogeeswari, P.; Senchani, G.; Banerjee, D. Newer tetracycline derivatives: synthesis, anti-HIV, antimycobacterial activities and inhibition of HIV-1 integrase. *Bioorg. Med .Chem. Lett.* **2007,** 17, 2372-2375.

155. Di Santo, R.; Costi, R.; Roux, A.; Miele, G.; Crucitti, G. C.; Iacovo, A.; Rosi, F.; Lavecchia, A.; Marinelli, L.; Di Giovanni, C.; Novellino, E.; Palmisano, L.; Andreotti, M.; Amici, R.; Galluzzo, C. M.; Nencioni, L.; Palamara, A. T.; Pommier, Y.; Marchand, C. Novel quinolinonyl diketo acid derivatives as HIV-1 integrase inhibitors: design, synthesis, and biological activities. *J. Med. Chem.* **2008,** 51, 4744-4750.

156. Barreca, M. L.; Ferro, S.; Rao, A.; De Luca, L.; Zappala, M.; Monforte, A. M.; Debyser, Z.; Witvrouw, M.; Chimirri, A. Pharmacophore-based design of HIV-1 integrase strand-transfer inhibitors. *J. Med. Chem.* **2005,** 48, 7084-7088.

157. Brzozowski, Z.; Slawinski, J.; Saczewski, F.; Sanchez, T.; Neamati, N. Synthesis, anti-HIV-1 integrase, and cytotoxic activities of 4-chloro-N-(4-oxopyrimidin-2-yl)-2-mercaptobenzenesulfonamide derivatives. *Eur. J. Med. Chem.* **2008,** 43, 1188-1198.

158. Brzozowski, Z.; Saczewski, F.; Slawinski, J.; Sanchez, T.; Neamati, N. Synthesis and anti-HIV-1 integrase activities of 3-aroyl-2,3-dihydro-1,1-dioxo-1,4,2-benzodithiazines. *Eur. J. Med. Chem.* **2009,** 44, 190-196.

159. He, Q. Q.; Zhang, X.; Wu, H. Q.; Gu, S. X.; Ma, X. D.; Yang, L. M.; Zheng, Y. T.; Chen, F. E. Synthesis and biological evaluation of HQCAs with aryl or benzyl substituents on N-1 position as potential HIV-1 integrase inhibitors. *Bioorg. Med. Chem.* **2011,** 19, 5553-5558.

160. Johns, B. A.; Kawasuji, T.; Weatherhead, J. G.; Boros, E. E.; Thompson, J. B.; Garvey, E. P.; Foster, S. A.; Jeffrey, J. L.; Miller, W. H.; Kurose, N.; Matsumura, K.; Fujiwara, T. Combining symmetry elements results in potent naphthyridinone (NTD) HIV-1 integrase inhibitors. *Bioorg. Med. Chem. Lett.* **2011,** 21, 6461-6464.

161. Serafin, K.; Mazur, P.; Bak, A.; Laine, E.; Tchertanov, L.; Mouscadet, J. F.; Polanski, J. Ethyl malonate amides: a diketo acid offspring fragment for HIV integrase inhibition. *Bioorg. Med. Chem.* **2011,** 19, 5000-5005.

162. Zhao, X. Z.; Maddali, K.; Metifiot, M.; Smith, S. J.; Vu, B. C.; Marchand, C.; Hughes, S. H.; Pommier, Y.; Burke, T. R., Jr. Development of tricyclic hydroxy-1H-pyrrolopyridine-trione containing HIV-1 integrase inhibitors. *Bioorg. Med. Chem. Lett.* **2011,** 21, 2986-2990.

163. Bodiwala, H. S.; Sabde, S.; Gupta, P.; Mukherjee, R.; Kumar, R.; Garg, P.; Bhutani, K. K.; Mitra, D.; Singh, I. P. Design and synthesis of caffeoyl-anilides as portmanteau inhibitors of HIV-1 integrase and CCR5. *Bioorg. Med. Chem.***2011,** 19, 1256-1263.

164. Billamboz, M.; Bailly, F.; Lion, C.; Touati, N.; Vezin, H.; Calmels, C.; Andreola, M. L.; Christ, F.; Debyser, Z.; Cotelle, P. Magnesium chelating 2-hydroxyisoquinoline-1,3(2H,4H)-diones, as inhibitors of HIV-1 integrase and/or the HIV-1 reverse transcriptase ribonuclease H domain: discovery of a novel selective inhibitor of the ribonuclease H function. *J. Med. Chem.* **2011,** 54, 1812-1824.

165. Billamboz, M.; Bailly, F.; Lion, C.; Calmels, C.; Andreola, M. L.; Witvrouw, M.; Christ, F.; Debyser, Z.; De Luca, L.; Chimirri, A.; Cotelle, P. 2-hydroxyisoquinoline-1,3(2H,4H)-diones as inhibitors of HIV-1 integrase and reverse transcriptase RNase H domain: influence of the alkylation of position 4. *Eur. J. Med. Chem.* **2011,** 46, 535-546.

166. Johnson, T. W.; Tanis, S. P.; Butler, S. L.; Dalvie, D.; Delisle, D. M.; Dress, K. R.; Flahive, E. J.; Hu, Q.; Kuehler, J. E.; Kuki, A.; Liu, W.; McClellan, G. A.; Peng, Q.; Plewe, M. B.; Richardson, P. F.; Smith, G. L.; Solowiej, J.; Tran, K. T.; Wang, H.; Yu, X.; Zhang, J.; Zhu, H. Design and synthesis of novel N-hydroxy-dihydronaphthyridinones as potent and orally bioavailable HIV-1 integrase inhibitors. *J. Med. Chem.* **2011,** 54, 3393-3417.

167. Vandurm, P.; Guiguen, A.; Cauvin, C.; Georges, B.; Le Van, K.; Michaux, C.; Cardona, C.; Mbemba, G.; Mouscadet, J. F.; Hevesi, L.; Van Lint, C.; Wouters, J. Synthesis, biological evaluation and molecular modeling studies of quinolonyl diketo acid derivatives: new structural insight into the HIV-1 integrase inhibition. *Eur. J. Med. Chem.* **2011,** 46, 1749-1756.

168. Tang, J.; Maddali, K.; Metifiot, M.; Sham, Y. Y.; Vince, R.; Pommier, Y.; Wang, Z. 3-Hydroxypyrimidine-2,4-diones as an inhibitor scaffold of HIV integrase. *J. Med. Chem.* **2011,** 54, 2282-2292.

169. De Luca, L.; De Grazia, S.; Ferro, S.; Gitto, R.; Christ, F.; Debyser, Z.; Chimirri, A. HIV-1 integrase strand-transfer inhibitors: design, synthesis and molecular modeling investigation. *Eur. J. Med. Chem.* **2011,** 46, 756-764.

170. Nagasawa, J. Y.; Song, J.; Chen, H.; Kim, H. W.; Blazel, J.; Ouk, S.; Groschel, B.; Borges, V.; Ong, V.; Yeh, L. T.; Girardet, J. L.; Vernier, J. M.; Raney, A. K.; Pinkerton, A. B. 6-Benzylamino 4-oxo-1,4-dihydro-1,8-naphthyridines and 4-oxo-1,4-dihydroquinolines as HIV integrase inhibitors. *Bioorg. Med. Chem.Lett.* **2011,** 21, 760-763.

171. Ma, K.; Wang, P.; Fu, W.; Wan, X.; Zhou, L.; Chu, Y.; Ye, D. Rational design of 2-pyrrolinones as inhibitors of HIV-1 integrase. *Bioorg. Med. Chem.Lett.* **2011,** 21, 6724-6727.

172. Tanis, S. P.; Plewe, M. B.; Johnson, T. W.; Butler, S. L.; Dalvie, D.; DeLisle, D.; Dress, K. R.; Hu, Q.; Huang, B.; Kuehler, J. E.; Kuki, A.; Liu, W.; Peng, Q.; Smith, G. L.; Solowiej, J.; Tran, K. T.; Wang, H.; Yang, A.; Yin, C.; Yu, X.; Zhang, J.; Zhu, H. Azaindole N-methyl hydroxamic acids as HIV-1 integrase inhibitors-II. The impact of physicochemical properties on ADME and PK. *Bioorg. Med. Chem. Lett.* **2010,** 20, 7429-7434.

173. Hadi, V.; Koh, Y. H.; Sanchez, T. W.; Barrios, D.; Neamati, N.; Jung, K. W. Development of the next generation of HIV-1 integrase inhibitors: pyrazolone as a novel inhibitor scaffold. *Bioorg. Med. Chem. Lett.* **2010,** 20, 6854-6857.

174. Le, G.; Vandegraaff, N.; Rhodes, D. I.; Jones, E. D.; Coates, J. A.; Thienthong, N.; Winfield, L. J.; Lu, L.; Li, X.; Yu, C.; Feng, X.; Deadman, J. J. Design of a series of bicyclic HIV-1 integrase inhibitors. Part 2: azoles: effective metal chelators. *Bioorg. Med. Chem. Lett.* **2010,** 20, 5909-5912.

175. Ferrara, M.; Fiore, F.; Summa, V.; Gardelli, C. Development of 2-pyrrolidinyl-N-methyl pyrimidones as potent and orally bioavailable HIV integrase inhibitors. *Bioorg. Med. Chem.Lett.* **2010,** 20, 5031-5034.

176. Maurin, C.; Lion, C.; Bailly, F.; Touati, N.; Vezin, H.; Mbemba, G.; Mouscadet, J. F.; Debyser, Z.; Witvrouw, M.; Cotelle, P. New 2-arylnaphthalenediols and triol inhibitors of HIV-1 integrase--discovery of a new polyhydroxylated antiviral agent. *Bioorg. Med. Chem.* **2010,** 18, 5194-5201.

177. Ferro, S.; De Luca, L.; Barreca, M. L.; De Grazia, S.; Christ, F.; Debyser, Z.; Chimirri, A. New chloro, fluorobenzylindole derivatives as integrase strand-transfer inhibitors (INSTIs) and their mode of action. *Bioorg. Med. Chem.* **2010,** 18, 5510-5518.

178. Fan, X.; Zhang, F. H.; Al-Safi, R. I.; Zeng, L. F.; Shabaik, Y.; Debnath, B.; Sanchez, T. W.; Odde, S.; Neamati, N.; Long, Y. Q. Design of HIV-1 integrase inhibitors targeting the catalytic domain as well as its interaction with LEDGF/p75: a scaffold hopping approach using salicylate and catechol groups. *Bioorg. Med. Chem.* **2011,** 19, 4935-4952.

179. Sharma, H.; Patil, S.; Sanchez, T. W.; Neamati, N.; Schinazi, R. F.; Buolamwini, J. K. Synthesis, biological evaluation and 3D-QSAR studies of 3-keto salicylic acid chalcones and related amides as novel HIV-1 integrase inhibitors. *Bioorg. Med. Chem.* **2011**, 19, 2030-2045.

180. Zwaagstra, M. E.; Timmerman, H.; Tamura, M.; Tohma, T.; Wada, Y.; Onogi, K.; Zhang, M. Q. Synthesis and structure-activity relationships of carboxylated chalcones: a novel series of *cysLT*$_1$ (LTD_4) receptor antagonists. *J. Med. Chem*. **1997**, 40, 1075-1089.

181. Pannecouque, C.; Pluymers, W.; Van Maele, B.; Tetz,V.; Cherepanov, P.; De Clercq, E.; Witvrouw, M.; Debyser, Z. New class of HIV integrase inhibitors that block viral replication in cell culture. *Curr. Biol*. **2002**, 12, 1169-1177.

182. Stuyver, L. J.; Lostia, S.; Adams, M.; Mathew, J. S.; Pai, B. S.; Grier, J.; Tharnish, P. M.; Choi, Y.; Chong, Y.; Choo, H.; Chu, C. K.; Otto, M. J.; Schinazi, R. F. Antiviral activities and cellular toxicities of modified 2′,3′-dideoxy-2′,3′-didehydrocytidine analogues. *Antimicrob. Agents Chemother*. **2002**, 46, 3854-3860.

183. Schinazi, R. F.; Sommadossi, J. P.; Saalmann, V.; Cannon, D. L.; Xie, M. Y.; Hart, G. C.; Smith, G. A.; Hahn, E. F. Activity of 3′-azido-3′-deoxythymidine nucleotide dimmers in primary lymphocytes infected with human immunodeficiency virus type 1. *Antimicrob. Agents Chemother*. **1990**, 34, 1061-1067.

184. Sommadossi, J. P.; Carlisle, R.; Schinazi, R. F.; Zhou, Z. Uridine reverses the toxicity of 3′-azido-3′-deoxythymidine in normal human granulocyte macrophage progenitor cells in vitro without impairment of antiretroviral activity. *Antimicrob. Agents Chemother*. **1988**, 32, 997-1001.

185. Gu, X. H.; Yu, H.; Jacobson, A. E.; Rothman, R. B.; Dersch, C. M.; George, C.; Flippen-Anderson, J. L.; Rice, K. C. Design, synthesis, and monoamine transporter binding site affinities of methoxy derivatives of indatraline. *J. Med. Chem.* **2000,** 43, 4868-4876.

186. deSolms, S. J.; Ciccarone, T. M.; MacTough, S. C.; Shaw, A. W.; Buser, C. A.; Ellis-Hutchings, M.; Fernandes, C.; Hamilton, K. A.; Huber, H. E.; Kohl, N. E.; Lobell, R. B.; Robinson, R. G.; Tsou, N. N.; Walsh, E. S.; Graham, S. L.; Beese, L. S.; Taylor, J. S. Dual protein farnesyltransferase-geranylgeranyltransferase-I inhibitors as potential cancer chemotherapeutic agents. *J. Med. Chem.* **2003,** 46, 2973-2984.

187. Kaiser, F.; Schwink, L.; Velder, J.; Schmalz, H. G. Studies towards the total synthesis of mumbaistatin: synthesis of highly substituted benzophenone and anthraquinone building blocks. *Tetrahedron* **2003**, 59, 3201-3217.

188. Ohkanda, J.; Buckner, F. S.; Lockman, J. W.; Yokoyama, K.; Carrico, D.; Eastman, R.; de Luca-Fradley, K.; Davies, W.; Croft, S. L.; Van Voorhis, W. C.; Gelb, M. H.; Sebti, S. M.; Hamilton, A. D. Design and synthesis of peptidomimetic protein farnesyltransferase inhibitors as anti-Trypanosoma brucei agents. *J. Med. Chem.* **2004,** 47, 432-445.

189. Mewshaw, R. E.; Edsall, R. J., Jr.; Yang, C.; Manas, E. S.; Xu, Z. B.; Henderson, R. A.; Keith, J. C., Jr.; Harris, H. A. ERbeta ligands. 3. Exploiting two binding orientations of the 2-phenylnaphthalene scaffold to achieve ERbeta selectivity. *J. Med. Chem.* **2005,** 48, 3953-3979.

190. Xu, J.; Durbin, P. W.; Kullgren, B.; Ebbe, S. N.; Uhlir, L. C.; Raymond, K. N. Synthesis and initial evaluation for in vivo chelation of Pu(IV) of a mixed octadentate spermine-based ligand containing 4-carbamoyl-3-hydroxy-1-methyl-2(1H)-pyridinone and 6-carbamoyl-1-hydroxy-2(1H)-pyridinone. *J. Med. Chem.* **2002,** 45, 3963-3971.

191. Yokel, R. A.; Fredenburg, A. M.; Durbin, P. W.; Xu, J.; Rayens, M. K.; Raymond, K. N. The hexadentate hydroxypyridinonate TREN-(Me-3,2-HOPO) is a more orally active iron chelator than its bidentate analogue. *J. of Pharm. Sci.* **2000**, 89, 545-555.

192. Chua, A. C.; Ingram, H. A.; Raymond, K. N.; Baker, E. Multidentate pyridinones inhibit the metabolism of nontransferrin-bound iron by hepatocytes and hepatoma cells. *Eur. J. Biochem.* **2003,** 270, 1689-1698.

193. Besong, G.; Billen, D.; Dager, I.; Kocienski, P.; Sliwinski, E.; Tai, L. R.; Boyle, F. T. A synthesis of (aR,7S)-(-)-*N*-acetylcolchinol and its conjugate with a cyclic RGD peptide. *Tetrahedron* **2008**, 64, 4700-4710.

194. Jang, S. B. Polymer bound palladium-catalyzed cross-coupling of organoboron compounds with organic halides and organic triflates. *Tetrahedron Lett.* **1997**, 38, 1793-1796.

195. Roidl, G.; Enkelmann, V.; Adams, R. D.; Bunz, U. H. An alternative synthesis of Volhardt's [1,2-diethynyl-3.4-bis(trimethylsilyl)cyclobutadiene] cyclopentadienyl cobalt and selective formation of its dimer. *J. Organomet. Chem.* **1999**, 578, 144-149.

196. Furstner, A.; Mamane, V. Flexible synthesis of phenanthrenes by a $PtCl_{(2)}$-catalyzed cycloisomerization reaction. *J. Org. Chem.* **2002,** 67, 6264-6267.

197. Kim, Y. H.; Lee, H.; Kim, Y. J.; Kim, B. T.; Heo, J. N. Direct one-pot synthesis of phenanthrenes via Suzuki-Miyaura coupling/aldol condensation cascade reaction. *J. Org. Chem.* **2008,** 73, 495-501.

198. Jiang, X. H.; Song, L. D.; Long, Y. Q. Highly efficient preparation of aryl beta-diketo acids with tert-butyl methyl oxalate. *J. Org. Chem.* **2003,** 68, 7555-7558.

199. Bucher, G.; Halupka, M.; Kolano, C.; Schade, O.; Sander, W. Characterization of alkoxycarbonyl radicals by step-scan time-resolved infrared spectroscopy. *Eur. J. Org. Chem.* **2001**, 3, 545-552.

200. Dixon, S.; Smondyrev, A.; Knoll, E.; Rao, S; Shaw, D.; Friesner, R. PHASE a new engine for pharmacophore perception, 3D QSAR model development, and 3D database screening: 1. Methodology and prelimnary results. *J. Comput. Aided Mol. Des*. **2006**, 20, 647-671.

201. Kuo, C. L.; Assefa, H.; Kamath, S.; Brzozowski, Z.; Slawinski, J.; Saczewski, F.; Buolamwini, J. K.; Neamati, N. Application of CoMFA and CoMSIA 3D-QSAR and docking studies in optimization of mercaptobenzenesulfonamides as HIV-1 integrase inhibitors. *J. Med. Chem*. **2004**, 47, 385-399.

202. Clark, M.; Cramer, I. R. D. The probability of chance correlation using partial least squares (PLS) *Quant. Struct. Act. Relat*. **1993**, 12, 137-145.

203. Zhu, Z.; Buolamwini, J. K. Constrained NBMPR analogue synthesis, pharmacophore mapping and 3D-QSAR modeling of equilibrative nucleoside transporter 1 (ENT1) inhibitory activity. *Bioorg. Med. Chem.* **2008,** 16, 3848-3865.

204. Telvekar, V.; Kundaikar, H.; Patel, K.; Chaudhari, H. 3-D QSAR and molecular docking studies on aryl benzofuran-2-yl ketoxime derivatives as candida albicans N-myristoyl transferase inhibitors. *QSAR Comb. Sci.* **2008**, 27, 1193-1203.

205. Pasquini, S.; Mugnaini, C.; Tintori, C.; Botta, M.; Trejos, A.; Arvela, R. K.; Larhed, M.; Witvrouw, M.; Michiels, M.; Christ, F.; Debyser, Z.; Corelli, F. Investigations on the 4-quinolone-3-carboxylic acid motif. 1. Synthesis and structure-activity relationship of a class of human immunodeficiency virus type 1 integrase inhibitors. *J. Med. Chem.* **2008,** 51, 5125-5129.

206. Yuan, H.; Parrill, A. L. QSAR studies of HIV-1 integrase inhibition. *Bioorg. Med. Chem.* **2002,** 10, 4169-4183.

207. Gupta, P.; Roy, N.; Garg, P. Docking-based 3D-QSAR study of HIV-1 integrase inhibitors. *Eur. J. Med. Chem.* **2009,** 44, 4276-4287.

208. Lu, P.; Wei, X.; Zhang, R. CoMFA and CoMSIA 3D-QSAR studies on quionolone caroxylic acid derivatives inhibitors of HIV-1 integrase. *Eur. J. Med. Chem.* **2010,** 45, 3413-3419.

209. Kuo, C. L.; Assefa, H.; Kamath, S.; Brzozowski, Z.; Slawinski, J.; Saczewski, F.; Buolamwini, J. K.; Neamati, N. Application of CoMFA and CoMSIA 3D-QSAR and docking studies in optimization of mercaptobenzenesulfonamides as HIV-1 integrase inhibitors. *J. Med. Chem.* **2004,** 47, 385-399.

210. Buolamwini, J. K.; Assefa, H. CoMFA and CoMSIA 3D QSAR and docking studies on conformationally-restrained cinnamoyl HIV-1 integrase inhibitors: exploration of a binding mode at the active site. *J. Med. Chem.* **2002,** 45, 841-852.

211. Tang, J.; Maddali, K.; Pommier, Y.; Sham, Y. Y.; Wang, Z. Scaffold rearrangement of dihydroxypyrimidine inhibitors of HIV integrase: Docking model revisited. *Bioorg. Med. Chem. Lett.* **2010,** 20, 32757-32759.

212. Engelman, A.; Craigie, R. Identification of conserved amino acid residues critical for human immunodeficiency virus type 1 integrase function in vitro. *J. Virol.* **1992,** 66, 6361-6369.

213. Lins, R. D.; Adesokan, A.; Soares, T. A.; Briggs, J. M. Investigations on human immunodeficiency virus type 1 integrase/DNA binding interactions via molecular dynamics and electrostatics calculations. *Pharmacol. Ther.* **2000,** 85, 123-131.

214. Halgren, T. A.; Murphy, R. B.; Friesner, R. A.; Beard, H. S.; Frye, L. L.; Pollard, W. T.; Banks, J. L. Glide: a new approach for rapid, accurate docking and scoring. 2. Enrichment factors in database screening. *J. Med. Chem.* **2004,** 47, 1750-1759.

215. Huang, N.; Kalyanaraman, C.; Irwin, J. J.; Jacobson, M. P. Physics-based scoring of protein-ligand complexes: enrichment of known inhibitors in large-scale virtual screening. *J. Chem. Inf. Model.* **2006**, 46, 243-253.

216. Tounge, B. A.; Reynolds, C. H. Calculation of the binding affinity of beta-secretase inhibitors using the linear interaction energy method. *J. Med. Chem.* **2003,** 46, 2074-2082.

217. Hou, T.; Wang, J.; Li, Y.; Wang, W. Assessing the performance of the MM/PBSA and MM/GBSA methods. 1. The accuracy of binding free energy calculations based on molecular dynamics simulations. *J. Chem. Inf. Model.* **2011,** 51, 69-82.

218. Aqvist, J.; Medina, C.; Samuelsson, J. E. A new method for predicting binding affinity in computer-aided drug design. *Protein Eng.* **1994,** 7, 385-391.

219. Stjernschantz, E.; Marelius, J.; Medina, C.; Jacobsson, M.; Vermeulen, N. P.; Oostenbrink, C. Are automated molecular dynamics simulations and binding free energy calculations realistic tools in lead optimization? an evaluation of the linear interaction energy (LIE) method. *J. Chem. Inf. Model.* **2006,** 46, 1972-1983.

220. Delelis, O.; Thierry, S.; Subra, F.; Simon, F.; Malet, I.; Alloui, C.; Sayon, S.; Calvez, V.; Deprez, E.; Marcelin, A. G.; Tchertanov, L.; Mouscadet, J. F. Impact of Y143 HIV-1 integrase mutations on resistance to raltegravir in vitro and in vivo. *Antimicrob. Agents Chemother.* **2010,** 54, 491-501.

221. RACHEL. http://tripos.com/data/SYBYL/RACHEL_072505.pdf Tripos Inc.; Accessed November 6, **2011**.

222. Kollman, P. Free energy calculations: applications to chemical and biochemical phenomena. *Chem. Rev*. **1993,** 93, 2395-2417.

223. Beveridge, D. L.; DiCapua, F. M. Free energy via molecular simulation: applications to chemical and biomolecular systems. *Annu. Rev. Biophys. Biophys. Chem.* **1989,** 18, 431-492.

224. Hou, T.; Wang, J.; Li, Y.; Wang, W. Assessing the performance of the MM/PBSA and MM/GBSA methods. 1. The accuracy of binding free energy calculations based on molecular dynamics simulations. *J. Chem. Inf. Model.* **2011,** 51, 69-82.

225. Cramer, R. D., 3rd; Patterson, D. E.; Bunce, J. D. Recent advances in comparative molecular field analysis (CoMFA). *Prog. Clin. Biol. Res.* **1989,** 291, 161-165.

226. Klebe, G.; Abraham, U.; Mietzner, T. Molecular similarity indices in a comparative analysis (CoMSIA) of drug molecules to correlate and predict their biological activity. *J Med. Chem.* **1994,** 37, 4130-4146.

227. Clark, M.; Cramer, R. D., III. The probability of chance correlation using partial least squares (PLS). *Quant. Struct.-Act. Relat.* **1993**, *12*, 137-145.

VITA

Horrick Sharma was born in Nagpur, India in 1977. He did his Bachelor of Pharmacy from the University of Rajasthan in 2002. He also received a degree of Master of Pharmaceutical Chemistry from the University of Manipal in 2005. He joined graduate school at the University of Tennessee Health Science Center, Memphis in the fall of 2006.